UCGE Reports
Number 20305

Department of Geomatics Engineering

Ultra-Tight GPS/Reduced IMU for Land Vehicle Navigation

(URL: http://www.geomatics.ucalgary.ca/graduatetheses)

By

Debo Sun

March 2010

UNIVERSITY OF CALGARY

Ultra-Tight GPS/Reduced IMU for Land Vehicle Navigation

by

Debo Sun

A THESIS

SUBMITTED TO THE FACULTY OF GRADUATE STUDIES

IN PARTIAL FULFILMENT OF THE REQUIREMENTS FOR THE

DEGREE OF DOCTOR OF PHILOSOPHY

DEPARTMENT OF GEOMATICS ENGINEERING

CALGARY, ALBERTA

MARCH 2010

Your file Votre référence
ISBN: 978-0-494-62174-5
Our file Notre référence
ISBN: 978-0-494-62174-5

Abstract

The navigation system of a vehicle plays an important role in the vehicle's safety and control. Such a system can be realized through the integration of a Global Positioning System (GPS) receiver and an inertial measurement unit (IMU) to provide more accurate navigation information than either system alone. To reduce the cost and volume of such systems, a reduced IMU (RIMU) consisting of only one vertical gyro and two or three accelerometers is used to integrate with a GPS receiver, resulting in three types of GPS/RIMU integration strategies, namely loose, tight and ultra-tight (UT). When the phase lock loops (PLLs) of the GPS receiver in a tight system are aided with the Doppler shift from the integrated system, the tight system is termed as tight integration with loop aiding (TLA).

In this dissertation, the RIMU mechanization, TLA GPS/RIMU, and UT GPS/RIMU are thoroughly researched and evaluated with field vehicle test data. The novel elements of the work include (i) an innovative local terrain predictor (LTP) algorithm for RIMU, (ii) an innovative adaptive loop filter (ALF) for TLA GPS/RIMU, and (iii) two innovative algorithms – namely a cascaded PLL plus a frequency discriminator (CaPF) composite loop and a reconfigurable tracking loop (RTL) – for UT GPS/RIMU. Furthermore, two kinds of UT systems – a vector delay lock loop plus a vector frequency lock loop (VDF) and a vector delay lock loop plus a cascaded PLL (VDCaP) – are implemented.

Test results show that all of the above innovative algorithms are valid, and the three types of GPS/RIMU (i.e. loose, TLA, and UT) work well. Specifically, the LTP method can

reduce the three dimensional (3D) root mean square (RMS) velocity error by more than 80% compared to without LTP case; the ALF algorithm can reduce the 3D RMS velocity error by up to 19% compared to constant noise bandwidth loop filters; the VDF and VDCaP systems work well in land vehicle navigation, and the CaPF and RTL algorithms can potentially improve the navigation performance of the UT system.

Acknowledgements

I would like to express my sincere gratitude to my supervisor, Dr. M. Elizabeth Cannon, for her invaluable support, guidance and encouragement throughout my studies and research. I really appreciate that she gave me the opportunity to study in the Position, Location And Navigation (PLAN) group.

I would like to extend my heartfelt gratitude to my co-supervisor, Dr. Mark G. Petovello, for his valuable helps and advices. I am also highly indebted to Dr. Gérard Lachapelle. As my first co-supervisor, he guided my studies and research in my first one and half years and helped me in many ways.

I would further like to extend my sincere thanks to Dr. Cillian O'Driscoll, Jared Bancroft, Tao Lin, and other members and ex-members of the PLAN group for their help in various ways. My special thanks must go to Dr. Guojiang Gao, Dr. Jiancheng Gao, Dr. Ali Broumandan, Dr. Florence Macchi, Dr. Cyrille Gernot, Aiden Morrison, Tao Li, Richard Ong, Kannan Muthuraman, Vahid Dehghanian, Pejman Kazemi, Peng Xie, Wang Da, Ping Luo, Wei Cao, for graciously sharing their time with me and their support.

Most of all, I thank my family for their love and greatest support, and I would like to dedicate this dissertation to my wife Lisa and my lovely daughter Jennifer.

Table of Contents

List of Tables

List of Figures

List of Symbols, Abbreviations and Nomenclature

Symbols	Definition
$(\bullet)(s)$	Laplace transform of signal $(\bullet)$ or transfer function
$(\bullet)_{Dis}$	Discriminator output of GPS receiver
$\dot{(\bullet)}$	Time derivative of quantity $(\bullet)$
$\ddot{(\bullet)}$	Second time derivative of quantity $(\bullet)$
$\overline{(\bullet)}$	Time average of quantity $(\bullet)$
$\widetilde{(\bullet)}$	Quantity $(\bullet)$ with error
$\widehat{(\bullet)}$	Estimate of quantity $(\bullet)$
$\Delta(\bullet)$	Change in quantity $(\bullet)$
$\delta(\bullet)$	Perturbation of quantity $(\bullet)$
$[(\bullet)\times]$	Skew-symmetric matrix form of vector $(\bullet)$
$\mathbf{0}_{n\times n}$	Zero matrix with dimension $n\times n$
$\mathbf{A}_j(g)$	Rotation matrix about j-axis by angle g
$b_{(\bullet)}$	Accelerometer bias in axis $(\bullet)$
$\mathbf{b}$	Accelerometer bias vector
B_n	Noise bandwidth
c	Speed of light
C/N_0	Carrier-to-noise-power density ratio
$d_{(\bullet)}$	Gyro drift in axis $(\bullet)$
$\mathbf{d}$	Gyro drift vector
D	Early-to-late correlator spacing of code discriminator
$\mathbf{E}$	Skew-symmetric matrix of attitude error vector $\boldsymbol{\varepsilon}$
f_d	Carrier Doppler shift
f_{da}	Carrier Doppler shift aiding
f_{dm}	Carrier Doppler shift measurement
f_{LF}	Doppler error output of loop filter
f_T	Transmitted signal frequency
$\mathbf{f}$	Specific force vector
$\mathbf{F}$	Skew-symmetric matrix form of vector $\mathbf{f}$
g	Acceleration of gravity
$\mathbf{g}^e$	Gravity vector
$\mathbf{G}^i$	Gravitational acceleration vector
h	Geodetic altitude
$\mathbf{H}$	Measurement matrix of Kalman filter
I	GPS in-phase signal
$\mathbf{I}_{n\times n}$	Unit matrix with dimension $n\times n$

L	Number of discriminator outputs in a measurement update period of integration Kalman filter
M	Geodetic meridian radius
N	Geodetic prime vertical radius
O_ρ	GPS satellite orbital error
p	Vehicle pitch
$\mathbf{P}_{(\cdot)}(-)$	Prediction error covariance matrix of subscripted quantity of integration Kalman filter
Q	GPS quadraphase signal
r	Geometric range between user and GPS satellite
r	Vehicle roll
$\mathbf{r}^a$	Vector $\mathbf{r}$ in frame a
$\mathbf{r}$	Position vector
$\mathbf{R}_a^b$	Rotation matrix from frame a to b
$\dot{t}_u$	GPS receiver clock drift rate
T	Measurement update period of integration Kalman filter
$T_{(\cdot)}$	Threshold of quantity $(\cdot)$
δt_u	GPS receiver clock offset
δt_s	GPS satellite clock offset
T_{PIT}	Predetection integration time of GPS receiver
$v_{(\cdot)}$	Velocity in axis $(\cdot)$
$\mathbf{v}$	Velocity vector
$\mathbf{v}_u$	User velocity vector
$\mathbf{V}$	GPS satellite velocity vector
$Var(g)$	Variance of quantity g
$w_{(\cdot)}$	Noise of subscripted quantity
$\mathbf{W}_{(\cdot)}$	Noise vector of subscripted quantity
$\mathbf{X}$	State vector of integration Kalman filter
$\mathbf{Z}$	Measurement vector of integration Kalman filter
α	Inverse of correlation time of a first-order GM process
$\boldsymbol{\varepsilon}$	Attitude error vector
$\varepsilon_{(\cdot)}$	Attitude error in axis $(\cdot)$
$\varepsilon_{(\cdot)}$	Noise of subscripted quantity
$\boldsymbol{\kappa}$	User-to-satellite line-of-sight unit vector
λ	Wavelength of signal
λ	Geodetic longitude
ξ	Damping ratio of second-order system
ρ_i	GPS pseudorange of i th satellite
$\sigma_{(\cdot)}$	Standard deviation of subscripted quantity
$\sigma^2_{(\cdot)}$	Variance of subscripted quantity

τ	code phase of DLL
ϕ	Carrier phase measurement of GPS receiver
φ	Geodetic latitude
φ	Carrier phase of PLL
ψ	Vehicle azimuth
$\mathbf{\Omega}^a_{pq}$	Skew-symmetric matrix form of vector $\boldsymbol{\omega}^a_{pq}$
$\omega_{(\bullet)}$	Rotation rate in axis $(\bullet)$
ω_e	Rotation rate of the earth
ω_n	Undamped natural frequency of tracking loop
$\boldsymbol{\omega}^a_{pq}$	Vector of rotation rates of frame q, relative to frame p, expressed in frame a

Abbreviations	**Definition**
2A1G	Two horizontal accelerometers plus one vertical gyro
3A1G	Three accelerometers plus one vertical gyro
3D	Three dimensions
ALF	Adaptive loop filter
CaPF	Cascaded PLL plus FLL discriminator
CaPLL	Cascaded PLL
CNB	Constant noise bandwidth
CNBLF	Constant noise bandwidth loop filter
CTL	Carrier tracking loop
DaDLL	Doppler-aided DLL
DaPLL	Doppler-aided PLL
DGPS	Differential GPS
DLL	Delay lock loop
DR	Dead reckoning
EKF	Extended Kalman filter
FD	Full dimension
FLL	Frequency lock loop
GM	Gaussian Markov
GPS	Global positioning system
IF	Intermediate frequency
IMU	Inertial measurement unit
INS	Inertial navigation system
LKF	Linearized Kalman filter
LTP	Local terrain predictor
LVN	Land vehicle navigation
LVNS	Land vehicle navigation system
M&E	Mechanization and error
MEMS	Micro-electro-mechanical system
NCO	Numerically controlled oscillator
OCXO	Oven controlled crystal oscillator
PIT	Predetection integration time

PLI	Phase lock indicator
PLL	Phase lock loop
RMS	Root mean square
PPS	Pulse-per-second
PRN	Pseudo-random noise
PSD	Power spectral density
PVT	Position, velocity and time
RIMU	Reduced inertial measurement unit
RR	Random ramp
RTK	Real time kinematic
RTL	Reconfigurable tracking loop
SBTL	Scalar-based tracking loop
SBTS	Scalar-based tracking scheme
SCTL	Scalar carrier tracking loop
SV	Space vehicle
TCXO	Temperature compensated crystal oscillator
TLA	Tight integration with loop aiding
UKF	Unscented Kalman filter
UT	Ultra-tight
VBTL	Vector-based tracking loop
VBTS	Vector-based tracking scheme
VCTL	Vector carrier tracking loop
VDCaP	VDLL plus cascaded PLL
VDCaPF	VDLL plus CaPF
VDF	VDLL plus VFLL
VDLL	Vector delay lock loop
VDP	VDLL plus VPLL
VFLL	Vector frequency lock loop
VPLL	Vector phase lock loop
ZUPT	Zero velocity update

Chapter One: Introduction

With recent automobile technology development, vehicle safety and control have been given more attention both in civil and military applications. To this end, land vehicle navigation systems (LVNSs) play an important role because they can provide necessary information for vehicle navigation and control (Allen et al 2009), and thus make a vehicle safer, more comfortable, and easier to operate**.** An LVNS can be obtained through the integration of a Global Positioning System (GPS) receiver and an inertial measurement unit (IMU) or with vehicle sensors, to provide more accurate navigation information than either system alone. In this dissertation, different kinds of GPS/reduced IMU integration systems such as tight GPS/reduced IMU with Doppler loop aiding and ultra-tight (UT) GPS/reduced IMU, both of which can be used as an LNVS, are investigated in order to provide useful information for practical LVNS development.

1.1 Background

GPS/IMU integration systems have been used in many areas, such as flight guidance, vehicle navigation and geodetic surveying. With continuing technology development, there exists a growing demand for small, low cost, reliable and high precision GPS receivers or navigators. The combination of modern GPS and inertial navigation technology makes this kind of GPS receiver possible. Any GPS/IMU system generally contains four elements: an IMU, a GPS receiver, an integration strategy, and a navigation filter. Each of these is discussed briefly below.

1.1.1 Inertial Measurement Unit

An inertial measurement unit is a cluster of instruments (gyroscopes and accelerometers) that measure angular rates and linear accelerations. Combining an IMU with navigation

software, an inertial navigation system (INS) is obtained. An INS is a dead reckoning system which depends on accelerometer and gyro measurements to calculate changes in position, velocity and attitude. It is self-contained and can provide accurate position and velocity over short time periods, but it drifts over time (El-Sheimy 2007; Titterton & Weston 2004; Farrell & Barth 1999). Generally, an INS consists of three orthogonal accelerometers and three orthogonal gyros. The gyro measurements are used to calculate attitude while the accelerometer measurements are used to calculate velocity and position.

In land vehicle navigation, however, in order to reduce the system's cost and volume, it is desired to use a minimum set of hardware components or inertial sensors For example, two horizontal accelerometers and one vertical gyro could be used (Allen et al 2009; Sun et al 2008; Niu et al 2007b; Syed et al 2007). This kind of IMU with less than three gyros and/or less than three accelerometers is herein called a "reduced IMU". For an LVNS, a reduced IMU (RIMU) usually consists of only one vertical gyro and two or three accelerometers, which are often substituted with on vehicle sensors such as a yaw rate sensor and G-sensors (Gao 2007b; Rezaei & Sengupta 2007; Gao et al 2006).

1.1.2 GPS Receiver

In a conventional GPS receiver, generally two kinds of tracking loop are used, namely a code correlation loop or a delay lock loop (DLL) and a carrier Doppler removal loop consisting of one or both of a phase lock loop (PLL) and a frequency lock loop (FLL). The PLL or FLL is for Doppler removal, whereas the DLL is for code correlation. Both tracking loops work interactively. In order to maintain tracking in high dynamic environments, both the order and the noise bandwidth of the PLL in a conventional

receiver are required to be large (Ward et al 2006), such as for a second order loop with a noise bandwidth of more than 18 Hz (Babu & Wang 2005). Even in low dynamic environments, the noise bandwidth is required to be about 5 to 12 Hz for a second order loop. But if the Doppler can be computed from the inertial solution (and knowledge of the satellite position and velocity), it can be used to aid the tracking loops, thus allowing the noise bandwidth of the PLL to be reduced to 3 Hz or less while still tracking in high dynamic environment (Petovello et al 2007; Babu & Wang 2005). As a result, both the tracking and the navigation performance of such an inertial-aided receiver can be improved (Petovello et al 2007).

In order to further improve the receiver's tracking performance, a vector-based tracking scheme can be applied both in the code and carrier loops. In the code correlation loop, the vector-based tracking loop (VBTL) is called vector delay lock loop (VDLL), and in the carrier Doppler removal loop it is called vector phase lock loop (VPLL) for a PLL and vector frequency lock loop (VFLL) for an FLL. In the VBTL concept, the phase and frequency/Doppler (of the code or carrier, as appropriate) of the numerically controlled oscillator (NCO) are predicted using the receiver's navigation solution. In this way, satellites with strong signals can help track satellites with weak signals. As a result, once a navigation solution is available, all tracking loops will remain in lock, even for those with weak signal conditions, and short signal outages may be bridged (Lashley & Bevly 2009a; Lashley & Bevly 2009b; Spilker Jr.1996). On the other hand, since all satellites are intimately related in VBTLs, any error in one space vehicle's (SV's) channel can potentially adversely affect other channels (Petovello et al 2008a).

1.1.3 GPS/IMU Integration Strategies

Since GPS and INS are complementary, they can be integrated and a higher navigation performance can be achieved (Petovello 2003; Greenspan 1996). There are three GPS/INS (or GPS/IMU) integration strategies, namely loose, tight and ultra-tight (Bullock et al 2006; Greenspan 1996; Gebre-Egziabher 2007). In loose integration, a GPS receiver's navigation solution (position and velocity output) is integrated with an INS, thus the GPS receiver and INS can operate independently. In tight integration, a GPS receiver's raw data measurement (generally pseudorange and Doppler shift measurement) is integrated with an INS. In this case, the GPS receiver does not necessarily provide position and velocity information by itself. In the ultra-tight approach, sometimes called deep or deeply coupled integration (Crane 2007; Soloviev et al 2004a; Gustafson & Dowdle 2003), the GPS receiver has no individual tracking loops. The individual tracking loops are replaced by a GPS/INS navigator or VBTLs such as a VDLL and/or VFLL (Gebre-Egziabher 2007; Bullock et al 2006; Van Dierendonck 1996). Effectively, the GPS and IMU are no longer independent sensors.

Further to the above, the tight integration approach is sometimes classified in the literature into two sub-types: tight and alternative tight (Gebre-Egziabher 2007). Sometimes the alternative tight GPS/INS is called an inertial-aided GPS receiver. The alternative tight means the GPS receiver's tracking loops receive Doppler aiding information from the INS. In this dissertation, this approach is called tight with loop aiding or tight loop aiding (TLA). Both TLA and UT integration systems have many

advantages, such as noise suppression, anti-jamming capability and improved navigation performance (Lashley & Bevly 2009b; Gao 2007a; Petovello et al 2007).

As with a full IMU, a reduced IMU can also have the same three kinds of integration strategies: loose, tight (tight and TLA), and ultra-tight. But for a GPS/reduced IMU, there is only limited research, and most is about loose or tight integration (Xing & Gebre-Egziabher 2009; Sun et al 2008; Niu et al 2007b). Research about TLA and UT GPS/reduced IMU is rare (Petovello et al 2007). Compared with a full IMU, the key difference with a reduced IMU is that since there are no horizontal gyros, the pitch and roll cannot be calculated or observed directly from the inertial data and the navigation performance is thus affected by local terrain variations. As a result, the integration of GPS/reduced IMU needs to be adjusted or redesigned compared to a full IMU.

1.1.4 Navigation Filter

In GPS/INS (or GPS/IMU) integration, generally a navigation filter is employed for blending GPS and INS information (Grewal & Andrews 2001; Farrell & Barth 1999). It is used to estimate the errors of GPS and INS in the integration system. Once these errors are estimated and compensated, the system's navigation performance will be improved. Usually a Kalman filter is used as the navigation filter because it is a time domain filter with an iterative structure well suited for running on a computer. Since a conventional Kalman filter is derived from linear systems, when an integration system is linear, it can work very well. But in practical cases, as is the case for an INS, the system is rarely perfectly linear although its error model can be approximated using linear equations. The underlying assumption in this approach is that the attitude error of the INS is

appropriately small. In this light, nonlinear estimation techniques or nonlinear Kalman filters need to be reviewed.

In nonlinear integration systems, such as tight GPS/INS and UT GPS/INS, nonlinear Kalman filters need to be employed, such as a linearized Kalman filter (LKF), an extended Kalman filter (EKF), and an unscented Kalman filter (UKF) (Xing & Gebre-Egziabher 2009; Wendel et al 2005; Gelb1974). For a GPS receiver, if its measurement output is position and velocity information, its measurement equations are linear. If the measurements are pseudorange and Doppler shift (or in-phase I and quadraphase Q signals), as will be discussed later in this dissertation, the measurement equations are nonlinear. Therefore, tight and UT integration systems are nonlinear systems, and generally an EKF is employed for data fusion. Prior to using a Kalman filter, its process noise covariance matrix, $\mathbf{Q}$, and measurement noise covariance, $\mathbf{R}$, must be determined or known. In practice, it may be difficult to know, or even suppose, these values. In this case, an adaptive Kalman filter, whose $\mathbf{Q}$ and/or $\mathbf{R}$ can be estimated online or whose filter gain is estimated online directly while without need to estimate the $\mathbf{Q}$ and/or $\mathbf{R}$, needs to be used for data processing (Mohamed & Schwarz 1999; Gelb1974).

1.2 Overview and Limitations of Previous Work

Applying a TLA and/or UT GPS/reduced IMU in land vehicle navigation is where current research is focused. Although there is much research about TLA and UT using full IMUs (Sivananthan & Weitzen 2009; Lashley et al 2008a; Petovello et al 2008a; Soloviev et al 2007), research with reduced IMUs is seldom seen. It is expected that some research results for a GPS/ full set IMU can be applied to a GPS/reduced IMU. However,

for the integration of a reduced IMU, there are still many problems that remain unsolved, such as the mechanization equation and error model choice for a reduced IMU, the PLL noise bandwidth determination of an inertial-aided GPS receiver, and the preferable configuration of an UT GPS/reduced IMU. This dissertation focuses on the TLA and UT integration with a reduced IMU. As will be seen, some results for the reduced IMU can also be applied to full IMUs, such as the PLL noise bandwidth computation for TLA system, and the configuration design and analysis for UT system.

1.2.1 Reduced IMU

Although there are a few configurations for a reduced IMU, such as one vertical gyro plus three or two accelerometers (Iqbal et al 2008; Niu et al 2007b; Daum et al 1994), one vertical gyro plus one forward accelerometer (Phuyal 2004), and one vertical gyro plus one odometer (Vlcek et al 1993), this dissertation focuses on the former since many new model vehicles are already equipped with horizontal G-sensors and yaw rate sensors for vehicle safety control (Gao 2007b; Rezaei & Sengupta 2007), which can be used as accelerometers and a vertical gyro. Using the G-sensors and yaw rate sensor as a reduced IMU can both save cost and reduce the volume of an LVNS, that is, almost no extra cost and volume are needed for the reduced IMU.

In reduced IMUs comprised of two or three accelerometers and one vertical gyro, since these configurations are based on the supposition that roads are relatively flat such that horizontal gyros and (in some cases) one vertical accelerometer provide relatively little information (Niu et al 2007b). However, in reality, these sensors do provide critical information and their omission inevitably degrades the performance of the navigation

system. Specifically, if a reduced IMU has only one vertical gyro, since there are no horizontal gyros, the pitch and roll cannot be calculated or observed directly from the inertial data and the navigation performance is thus affected by local terrain variations. Similarly, if fewer than three accelerometers are used, full knowledge of the vehicle's acceleration is unavailable. Both situations introduce errors in the navigation system.

In order to overcome the disadvantages of reduced IMUs, integrating them with other navigation systems or constraints is a means of improving performance; for example, GPS/reduced IMU integration (Xing & Gebre-Egziabher 2009; Nui et al 2007b; Phuyal 2004) and GPS/reduced IMU with vehicular constraints or odometer measurement (Li et al 2009; Iqbal et al 2008; Syed et al 2007). For reduced IMUs, the focus of this dissertation is their mechanization equations and error models, rather than the use of vehicular constraints or the inclusion of odometer measurements. Although previous work in this area has provided a few kinds of mechanization equations and error models, such as dead reckoning (DR) type (Xing & Gebre-Egziabher 2009; Iqbal et al 2008; Vlcek et al 1993) and full dimension type (Nui et al 2007b), it is hard to say that these mechanization equations and error models can mostly or completely satisfy the requirements of a GPS/reduced IMU for vehicle safety and control because they both have some drawbacks which may degrade the performance for a reduced IMU-based system. For DR type, roads are supposed to be completely flat, so pitch and roll are zero in the mechanization equations and corresponding error model. This type imposes too strong constraints on the model. For full dimension type, the mechanization equations and error model of a full set IMU are used as those of reduced IMUs, so pitch and roll

values in the mechanization equations and error model cannot be constrained anymore. Neither model can match the real situations that the pitch and roll of a vehicle are determined mostly by the local terrain, which introduces errors in the navigation system.

1.2.2 GPS Receiver

In LVNS, in order to improve the tracking performance and the measurement quality of a GPS receiver, the receiver can be aided with a full set IMU or a reduced IMU. In this dissertation, focus is on a reduced IMU-aided GPS receiver (i.e. TLA GPS/reduced IMU) and UT GPS/reduced IMU. For a GPS-only receiver, it is generally required to have the abilities of weak signal tracking and anti-jamming (Yu 2007; Petovello & Lachapelle 2006a; Humphreys et al 2005; Psiaki 2001). In order to obtain such abilities, a standard GPS receiver has to be changed to include new functions or algorithms (Im et al 2007; Psiaki & Jung 2002). Herein, a GPS receiver obtains these abilities through inertial Doppler aiding for PLL or UT integration, which are more efficient than the GPS-only case in anti-jamming and weak signal tracking (Lashley & Bevly 2008a; Petovello et al 2008a; Im et al 2007). In land vehicle navigation (LVN), because the GPS receiver aided with a reduced IMU or on-vehicle sensors has some advantages over not only a GPS-only receiver but also loose and tight GPS/reduced IMUs, which will be discussed in this dissertation, it can be envisioned that this kind of receiver will be popular in LVN in the near future.

1.2.3 TLA GPS/Reduced IMU

In TLA GPS/reduced IMU, since the PLL of the GPS receiver is aided with Doppler shift information, it offers some advantages over GPS-only receivers including a more accurate navigation solution (especially for velocity and thus position), improved

tracking ability for high dynamics and enhanced anti-jamming performance (Sivananthan & Weitzen 2009; Kim et al 2007; Petovello et al 2007; Gautier & Parkinson 2003).

In general, in any TLA GPS/IMU system (with a full set or reduced IMU), each PLL tracking loop is controlled by a loop filter whose order and noise bandwidth impact the performance of the tracking loop, regardless if the loop is being aided with inertial data or not. With Doppler aiding from an inertial system, the noise bandwidth of the loop filters of the PLLs can be narrowed more than in a GPS-only case because the inertial system removes most of the user dynamics (Chiou et al 2008; Alban et al 2003; Jwo 2001). This results in improved noise suppression within the receivers (Petovello et al 2007, Alban et al 2003). However, the loop noise bandwidth cannot be made arbitrarily small and is limited by the navigation solution error of the GPS/reduced IMU and the receiver's oscillator errors (Chiou 2005; Gebre-Egziabher et al 2005). To this end, for a constant tracking loop noise bandwidth, the bandwidth is generally selected to accommodate the largest signal dynamics resulting from the combined effect of the navigation solution and oscillator errors. Because the navigation solution error varies with time, noise suppression is weakened when the error of the GPS/reduced IMU is small (in comparison to the largest expected error). This problem is exacerbated with a reduced IMU because the roll and pitch parameters cannot be directly observed resulting in navigation solution errors that change with the local terrain and vehicle orientation changes (Sun et al 2008).

However, there is no method or formula to calculate the noise bandwidth according to the navigation performance of a TLA GPS/reduced IMU. Only a few works provided some

useful analyses for the phase error of a Doppler-aided PLL (Chiou et al 2007; Gebre-Egziabher et al 2005), which are helpful in calculating the noise bandwidth according to the navigation performance. As such, in a TLA GPS/reduced IMU, how to choose the noise bandwidth is still an open problem. It is known that with Doppler aiding the noise bandwidth of the PLLs can be reduced, but the extent to which this is possible is as yet unknown. These are fundamental problems in the design of a TLA GPS/reduced IMU.

All previous research involving TLA systems focuses on full IMUs and research with reduced IMUs is rare. Actually, the TLA with reduced IMU is obviously different from the full IMU case, especially for the reduced IMU configuration with only two horizontal accelerometers and one vertical gyro (called the 2A1G configuration). In this configuration, the vertical acceleration cannot be measured and the user dynamics in the vertical direction cannot be effectively removed. As a result, the noise bandwidth cannot be narrowed as much as a TLA with a full IMU. Even for the reduced IMU configuration with three accelerometers and one vertical gyro (called the 3A1G configuration), since the pitch and roll parameters cannot be directly observed, the user dynamics cannot be removed as much as with a full IMU. This is because even for the 3A1G configuration, its attitude error is still larger than that of a full IMU with the same grade inertial sensors resulting in larger unknown user dynamics (Sun et al 2008), thus affecting the noise bandwidth reduction and TLA system performance.

1.2.4 UT GPS/Reduced IMU

In UT GPS/IMU integration, the tracking loops of the GPS receiver are controlled by the navigation solution of the system thus resulting in vector tracking schemes, such as

VDLL for code correlation and VFLL for carrier Doppler removal (Lashley et al 2008b; Petovello et al 2008a; Crane 2007; Spilker Jr.1996). As a result, UT GPS/IMU integration has some potential advantages over GPS-only receivers such as a more accurate navigation solution, improved weak signal tracking, enhanced anti-jamming ability, and more rapid signal recovery after a satellite blockage (Kennedy & Rossi 2008; Lashley & Bevly 2008a; Im et al 2007; Kim et al 2007). As with a full IMU, UT GPS/reduced IMU has the same advantages, but the extent of the performance improvement is different or low because the user dynamics cannot be removed as much as for the full set IMU, which will be discussed in the dissertation.

In a UT GPS/reduced IMU, the tracking loops of the GPS receiver are implemented with VBTLs. Code tracking is implemented with VDLL and carrier tracking is implemented with either VFLL or vector phase lock loop (VPLL). Since, compared to PLL, VFLL can decrease velocity estimation quality, and increase the complexity in estimating navigation bits (Kiesel et al 2007), using VFLL for carrier Doppler removal is not very popular when carrier phase lock can be obtained. Generally a VFLL or FLL is used for Doppler removal only after acquisition but before phase lock is obtained (Ward et al 2006). Following the VFLL or FLL the Doppler removal is usually implemented with a PLL or VPLL. Since a VPLL has a demanding requirement for position accuracy, it is quite hard to implement (Crane 2007). For example, for an L1 carrier signal, its wavelength is 19 cm. In order to implement a VPLL, the calculated pseudorange error for each channel should be controlled within 19/4 cm, resulting in a similar position accuracy requirement for a GPS/reduced IMU. Because of the difficulties in implementing a pure VPLL, an

approximate VPLL can be implemented with a cascaded scheme, whose carrier NCOs are controlled by both the local filter and the navigation filter (Petovello et al 2008a; Crane 2007; Ohlmeyer 2006).

Any GPS receiver must have both a code correlation function and a carrier Doppler removal function (Borre et al 2007; Ward et al 2006; Misra & Enge 2001). Each of the functions can be implemented with different tracking schemes such as a vector-based tracking scheme (VBTS) or a scalar-based tracking scheme (SBTS). If the code correlation function is implemented with VBTS, with different carrier Doppler removal function implementations, the following vector-based GPS receivers are possible:

- VDLL plus VFLL (called VDF): It is straightforward to implement, but estimating navigation bits is complicated.
- VDLL plus VPLL (called VDP): It is hard to implement.
- VDLL plus cascaded PLL (called VDCaP): It is straightforward to implement.

Because of the difficulties in implementing a VPLL, this dissertation focuses on the integration of a GPS receiver with a VDLL plus VFLL configuration and a reduced IMU (RIMU) (i.e. UT GPS/RIMU with VDF), and the integration of a GPS receiver with VDLL plus cascaded PLL configuration and a reduced IMU (i.e. UT GPS/RIMU with VDCaP).

Although there have been many investigations about UT integration of GPS with full IMUs (Sivananthan & Weitzen 2009; Petovello et al 2008a; Crane 2007), investigations

with reduced IMUs are limited. Certainly, many investigations for UT with full IMUs can provide significant references for the corresponding reduced IMU approach. However, for UT GPS/RIMU, there is still a lot of work remaining to be done, such as researching an innovative configuration for a vector-based GPS receiver, which can bear most advantages of both the VFLL and cascaded PLL, research for a new strategy applied to GPS outages to improve GPS signal recovery in GPS/RIMU, and the performance evaluation for UT GPS/RIMU, which can be used to provide significant references for practical LVNS development.

1.3 Research Objectives and Contributions

From the above review of GPS/IMU integration, it can be seen that previous research on TLA and UT GPS/reduced IMU is limited. Even for a reduced IMU, its mechanization equations and error model still need to be innovated. Therefore, the research described herein includes reduced IMU, TLA GPS/RIMU, and UT GPS/RIMU. The focus is on improving the navigation performance, the continuity, and the consistency of TLA and UT GPS/RIMU, and enhancing vehicle safety and control. This latter aspect is one which many previous studies did not consider explicitly. The difference between a TLA and UT system in LVN is also addressed in this dissertation and comparisons for the two systems are made, such as navigation performance comparison, system configuration comparison, and system stability comparison.

With regard to the demands of future LVNS development and the limitations of previous work, the main objectives of this dissertation are to develop innovative algorithms and/or configurations for reduced IMU, TLA, and UT GPS/RIMU to improve LVNS

performance and to investigate different types of TLA and UT approaches to provide helpful results for LVNS development. More specific objectives are outlined as follows:

1. *Develop a set of mechanization equations and a corresponding error model for a reduced IMU to improve the navigation performance of GPS/reduced IMU.* As stated earlier, in the reduced IMU case, because there are no horizontal gyros, the pitch and roll cannot be calculated or observed directly from the inertial data, and the navigation performance is thus affected by local terrain variations. However, the GPS data inherently contains some information regarding the terrain (i.e., from the computation of the vehicle's position). With this in mind, an INS error model that incorporates the local terrain will be developed to improve the navigation performance of the GPS/RIMU system.
2. *Develop a proper PLL loop filter for a TLA GPS/reduced IMU to improve system performance.* In a TLA system, since the PLL of the GPS receiver is aided with the Doppler shift calculated from the navigation solution of the GPS/RIMU system (and satellite information), the noise bandwidth of the loop filters of the PLLs can be narrowed more than in a GPS-only case. Since the loop noise bandwidth cannot be made arbitrarily small and is limited by the navigation solution error of the GPS/RIMU and the receiver's oscillator errors, methods of choosing the noise bandwidth for the PLL loop filter are investigated in order to improve signal tracking, signal reacquisition and overall navigation solution performance. Specifically, the bandwidth can be selected according to the performance of the integration system and the quality of the receiver's oscillator.

3. *Design new algorithms/configurations for a UT GPS/reduced IMU to improve system performance.* In a UT GPS/RIMU, the tracking loops of the GPS receiver are implemented with VBTS. For the receiver with VDCaP, code correlation is implemented with VDLL, and Doppler removal is implemented with a cascaded PLL. In a cascaded PLL, when the PLL is not locked, it may not provide better Doppler measurements than an FLL discriminator. In this light, an innovative algorithm/configuration will be developed to overcome the drawback of the cascaded PLL and provide more reliable Doppler measurement in both the PLL locked and PLL unlocked cases, thus improving the performance of the UT GPS/RIMU. On the other hand, during a partial GPS outage, in which there are less than four satellites in view, the navigation solution error of the GPS/RIMU will increase and may become too large to maintain lock with VBTLs. In this case, the receiver's tracking scheme may need to be switched to a scalar or traditional approach in order to maintain lock on the satellites still in view. As a result, the satellites still in view can keep tracking and the performance of the GPS/RIMU can be improved.
4. *Evaluate the performance of a TLA GPS/reduced IMU.* For a TLA system, with Doppler aiding, the noise bandwidth of the Doppler-aided PLL can be narrowed to improve tracking and navigation solution performance. These two performance indices are investigated using many test runs with vehicle test data under different GPS conditions, including open sky and foliage conditions. Many evaluations are conducted to investigate the effects of IMU grades and reduced IMU

configurations on the performance of the TLA system, and to verify the noise bandwidth determination for a proper PLL loop filter.

5. *Evaluate the performance of a UT GPS/reduced IMU.* In a UT system, with different tracking schemes for carrier Doppler removal, different types of vector-based receivers can be obtained, such as VDF and VDCaP. These two UT systems are investigated first using test runs with vehicle test data. Then evaluations are conducted to verify the new algorithms/configurations of UT GPS/RIMU presented in item 3. Furthermore, comparisons among different tracking schemes are made to investigate the effects of tracking schemes on the performance of the UT systems. Finally, a UT system is compared with a TLA system in both theory and test results to investigate differences in both their signal tracking ability and navigation performance, which can provide useful information for the choice of an LVNS scheme in practice.

In realizing the above objectives, several contributions are made in this dissertation. The major contributions are summarized as follows:

1. Development of a local terrain predictor (LTP) algorithm in the GPS/RIMU to help estimate the pitch and roll of the reduced IMU and thus to improve the navigation performance of the GPS/RIMU in both GPS normal and outage conditions.
2. Development of an adaptive loop filter (ALF) for Doppler-aided PLL following the phase error analysis of the Doppler-aided PLL in a TLA GPS/RIMU. For the

ALF, its noise bandwidth can be adjusted according to the performance of the integration system, the quality of the receiver's oscillator, and the satellites information. With the ALF, both the navigation performance and the PLL tracking ability of the TLA GPS/RIMU can be improved.

3. Development of a composite Doppler removal loop, which is comprised of a cascaded PLL and an FLL discriminator. This can overcome the disadvantage of the cascaded PLL, and provide more reliable Doppler measurement in both the PLL locked and PLL unlocked cases. Thus a vector-based GPS receiver with a VDLL plus a cascaded PLL and an FLL discriminator (CaPF) composite loop is obtained, which can improve the navigation performance of UT GPS/RIMU.
4. Development of a reconfigurable tracking loop for UT GPS/RIMU, which can be applied in the partial GPS outage case. This kind of reconfigurable loop can switch between VDLL and DLL, and switch between CaPF and PLL according to the navigation performance of the integration system when a partial GPS outage occurs. As a result, both the signal tracking ability and the navigation performance of the GPS/RIMU are improved.
5. Evaluation of the performance of a TLA and a UT GPS/RIMU with vehicle test data. Many test runs are conducted to investigate the signal tracking ability and navigation performance of the TLA GPS/RIMU under both GPS strong and weak signal cases. For a UT GPS/RIMU, different types of vector-based GPS receivers are investigated, such as VDF, VDCaP, and VDLL plus a cascaded PLL and an FLL discriminator (VDCaPF). Finally, TLA and UT integration systems are

compared both in theory and through test results to explore their differences in LVN performance.

1.4 Dissertation Outline

This dissertation covers issues related to LVNS development including reduced IMU, TLA and UT GPS/RIMU. It contains six chapters and two appendices with the remaining chapters organized as follows.

Chapter Two gives an overview of the navigation systems related to LVN, including INS, GPS, and GPS/INS integration systems. The basic concepts, principles, and primary equations of these navigation systems are introduced in this chapter, which can facilitate understanding of the contents of the subsequent chapters.

In Chapter Three, a local terrain predictor (LTP) is presented for reduced IMU error modeling resulting in a set of innovative mechanization equations and error model for a reduced IMU. This set of innovative mechanization equations and error model is derived and compared in theory with other sets of mechanization equations and error model of a reduced IMU to identify its advantages. This innovative algorithm of a reduced IMU is fundamental to the following research on the TLA and UT GPS/RIMU. Following the theoretical research of the reduced IMU, a vehicle test for data collection, which can be used for the performance evaluation of different kinds of TLA and UT systems, is introduced. Then the test results of loose GPS/RIMU with an LTP are presented to verify the LTP algorithm. The results of other reduced IMU algorithms are also displayed in order to compare the performance of different reduced IMU algorithms.

In Chapter Four, an adaptive loop filter (ALF) is presented for the Doppler-aided PLL following the phase error analysis of the Doppler-aided PLL in the TLA GPS/RIMU. In this chapter, the traditional PLL loop filter and phase error are introduced. Then, the individual phase errors in the Doppler-aided PLL are analyzed, and their equations are derived. Based on this analysis, the total phase error of the Doppler-aided PLL is obtained and the ALF is designed. Following the ALF design, the test results of the TLA GPS/RIMU are displayed. First, results from the data of a linear translation stage test are shown to illustrate the performance of the TLA system in both strong and weak GPS signal cases. The results of the TLA system from the vehicle test data are then presented, including the results under different GPS conditions, such as open sky and foliage. The results with different PLL noise bandwidths, such as constant and adaptive, are also given and compared to verify the innovative ALF algorithm.

In Chapter Five, two innovative algorithms/configurations for UT GPS/RIMU are presented. One is a composite Doppler removal loop, i.e CaPF. The other is a reconfigurable tracking loop for UT GPS/RIMU. In order to design the innovative algorithms/configurations, first the VDLL, VFLL, and cascaded PLL are detailed and analyzed. Then based on the characteristics of the cascaded PLL and FLL discriminator, the CaPF is presented. Further based on the characteristics of the VBTLs and traditional tracking loops, the reconfigurable tracking loop is designed. Following the UT system analysis and design, the UT and TLA systems are analyzed and compared in terms of system configuration, stability, and navigation performance. After the theoretical analysis

and system design, the test results of the UT GPS/RIMU with vehicle test data are presented. First, the results of the UT GPS/RIMU with VDF are displayed followed by the results of the UT system with VDCaP. Then the results of the UT GPS/RIMU with VDCaPF are given. Further with simulated partial GPS outages, the test results of the UT system with reconfigurable tracking loops are presented. Finally the test results of the UT and TLA systems are compared to identify the differences and similarities of the two systems.

Chapter Six concludes the major results of the previous chapters, and makes recommendations for future work.

In the appendices, the mechanization equations and error model of full IMU, and the individual phase errors of Doppler-aided PLL are included.

Chapter Two: Overview of Land Vehicle Navigation Systems

For land vehicle navigation, many position and location methods can be used, such as dead reckoning, wireless location, and image/vision-based location methods (e.g. Britt & Bevly 2009; Mattern et al 2008; Soloviev 2008; Sönmez & Bingöl 2008). Dead reckoning calculates position through continuously adding relative position changes to a known initial position in a navigation frame, thus the subsequent positions always rely on the previous point's information. As a result, the position error increases with time. It is the main drawback of the dead reckoning method. INS and systems with an odometer plus a magnetic compass are typical examples of dead reckoning systems. In contrast to dead reckoning, wireless location, including satellite location and terrestrial location, directly determines absolute coordinates of an unknown position using measurements to fixed reference points without taking into account previous positions. Thus its position error does not increase with time, but is related to the measurement errors and the geometry of the fixed reference points relative to the user. Unlike dead reckoning and wireless location, the image/vision-based navigation approach is closely related to photogrammetry (i.e. surveying using photographic imagery) in geometric fundamentals (Hofmann-Wellenhof et al 2003). Since different positioning methods have different error characteristics, navigation systems such as INS and GPS, developed from different positioning methods, have correspondingly different position error characteristics. In order to overcome the drawback of each individual navigation system, integrated systems such as GPS/INS are usually employed, thus achieving more accurate and reliable navigation performance. Based on the focus of this dissertation, GPS, INS, and their integration are introduced in this chapter.

2.1 Reference Frames

Prior to introducing navigation systems, it is necessary to define a series of reference frames that are commonly used in land vehicle navigation systems. The following coordinate frames are used in this text:

- *Inertial frame* (i-frame), denoted as $(o, x, y, z)_i$, is a fixed coordinate frame with the centre of the Earth as its origin o_i. Its z axis, z_i, is parallel to the spin axis of the Earth, x_i points to the mean vernal equinox, and y_i is determined by x_i and z_i in a right-handed system.
- *Earth-fixed frame* (e-frame), denoted as $(o, x, y, z)_e$, coincides with the *i*-frame at the origin but rotates with the Earth rate. Its z axis, z_e, is parallel to z_i, x_e points to the mean meridian of Greenwich, and y_e is determined by x_e and z_e in a right-handed system.
- *Local level frame* (ℓ-frame), denoted as $(o, x, y, z)_\ell$, is an east, north, up rectangular coordinate system, which is called ENU. Its origin, o_ℓ, is at the location of the navigation system and on the Earth's surface, x_ℓ points east, y_ℓ points north, and z_ℓ points vertically upwards.
- *Body frame* (b-frame), denoted as $(o, x, y, z)_b$, is rigidly attached to the vehicle of interest, usually at a fixed point such as the centre of gravity. The x_b, y_b and z_b axes point in the right, forward and up directions, respectively.
- *Alternative level frame* ($\ell 1$-frame), denoted as $(o, x, y, z)_{\ell 1}$, is another local level frame which has the same origin and vertical axis with those of ℓ-frame, but the

directions of other two axes ($x_{\ell 1}$ and $y_{\ell 1}$) are determined by the directions of the corresponding two axes x_b and y_b. This frame is used as an intermediate frame to link the local terrain (pitch and roll) and the attitude error of a reduced IMU.

Corresponding to the frames, some quantities are often used in the following equation derivations, and defined as: $\mathbf{r}^a$ denotes a vector in frame *a*, $\mathbf{R}_a^b$ denotes a rotation matrix from frame *a* to *b*, and $\boldsymbol{\omega}_{pq}^a$ denotes a vector of rotation rates of frame *q*, relative to frame *p*, expressed in frame *a*.

2.2 Inertial Navigation System

The operation of inertial navigation is based on the laws of classical mechanics as formulated by Sir Isaac Newton (Rana & Joay 2006). Newton's first law states that a body in motion tends to maintain its motion unless disturbed by an external force acting on the body. His second law states that this force produces a proportional acceleration of the body. If the acceleration can be measured and converted to a navigation frame with appropriate transformations, then in the navigation frame, a single integration yields velocity and a second integration provides change in position. Acceleration can be determined using a device known as an accelerometer, and an INS usually contains three such devices mounted orthogonally. In order to obtain appropriate orientation transformations for acceleration, gyroscopic sensors (or simply gyros) are needed. Generally, three orthogonal gyros are needed to obtain full knowledge of the orientation of accelerometers. A full six-degree of freedom IMU ("full IMU") therefore consists of three orthogonal accelerometers and three gyros. On the other hand, sometimes less than

three gyros and/or accelerometers can be used for navigation, forming a reduced IMU. Both of the systems are introduced in the following sections.

2.2.1 Full IMU System

A full IMU consists of three orthogonal accelerometers and three orthogonal gyros. These accelerometers and gyros can be mounted together on either a platform or a vehicle directly, resulting in two different kinds of navigation systems: gimballed and strapdown. This dissertation focuses on the latter.

In a strapdown system, the sensor assembly is directly mounted onto the vehicle and follows all motions performed by the vehicle reference. The accelerometers measure the specific force $\mathbf{f}^b$ (i.e., force per unit mass) along the axes of the body frame, whereas the gyros sense the angular rate $\boldsymbol{\omega}_{ib}^b$ of the body frame relative to the inertial frame. These measurements are used to calculate the vehicle's navigation information with a set of navigation equations. Navigation equations of a system can be derived in different frames – herein called the navigation frame – such as the inertial frame, Earth-fixed frame, and local level frame. Since this dissertation focuses on land vehicle navigation, in order to facilitate analysis, the local level frame is chosen as the navigation frame.

2.2.1.1 Navigation Equations

In order to derive the navigation equations in the local level frame, the navigation equations in the inertial frame need to be introduced first. The fundamental relationship is the specific force equation in the *i*-frame:

$$\ddot{\mathbf{r}}^i = \mathbf{f}^i + \mathbf{G}^i \tag{2.1}$$

where, $\ddot{\mathbf{r}}^i$ is the acceleration of the vehicle, $\mathbf{r}$ is the position vector of the point P with respect to o_i shown in Figure 2.1, $\mathbf{f}^i$ is the specific force, and $\mathbf{G}^i$ is the gravitational acceleration. The first integral of Equation (2.1) gives the velocity vector $\mathbf{v}^i$, and

$$\begin{cases} \dot{\mathbf{v}}^i = \mathbf{f}^i + \mathbf{G}^i \\ \dot{\mathbf{r}}^i = \mathbf{v}^i \end{cases} \tag{2.2}$$

Equation (2.2) contains two linear differential equations with constant coefficients. Using these, velocity and position can be computed.

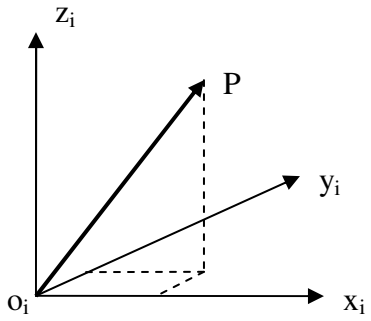

Figure 2.1 Position Vector in Inertial Frame

Based on the above navigation equations in the i-frame, the corresponding equations in the ℓ-frame can be derived. However, additional steps are required. Effectively, in order to obtain the navigation equations in the ℓ-frame, the specific-force equation in the e-frame is developed first, and then transformed to the ℓ-frame. This procedure is applied as follows.

From the relationship between the position vector in the e-frame and i-frame:

$$\mathbf{r}^i = \mathbf{R}_e^i \mathbf{r}^e \tag{2.3}$$

where $\mathbf{R}_e^i$ is the transformation matrix or rotation matrix, which rotates the e-frame into i-frame. And the $\mathbf{R}_e^i$ is determined as the solution to the differential equation

$$\dot{\mathbf{R}}_e^i = \mathbf{R}_e^i \mathbf{\Omega}_{ie}^e \tag{2.4}$$

where $\mathbf{\Omega}_{ie}^e$ is the skew-symmetric matrix

$$\mathbf{\Omega}_{ie}^e = \left[\boldsymbol{\omega}_{ie}^e \times \right] \tag{2.5}$$

This matrix is formed from the elements of the vector $\boldsymbol{\omega}_{ie}^e$ which represents the turn rate of the e-frame with respect to the i-frame. If $\boldsymbol{\omega}_{pq}^a = \left(\omega_{pqx}^a \quad \omega_{pqy}^a \quad \omega_{pqz}^a \right)^T$, $\mathbf{\Omega}_{pq}^a = \begin{bmatrix} 0 & -\omega_{pqz}^a & \omega_{pqy}^a \\ \omega_{pqz}^a & 0 & -\omega_{pqx}^a \\ -\omega_{pqy}^a & \omega_{pqx}^a & 0 \end{bmatrix}$. Through a series of derivations, the acceleration vector $\ddot{\mathbf{r}}^e$ is obtained (Hofmann-Wellenhof et al 2003)

$$\ddot{\mathbf{r}}^e = \mathbf{g}^e + \mathbf{f}^e - 2\mathbf{\Omega}_{ie}^e \dot{\mathbf{r}}^e \tag{2.6}$$

where $\mathbf{f}^e$ is the specific force vector in the e-frame, $\mathbf{g}^e$ is the gravity vector and equal to the gravitational vector $\mathbf{G}^e$ minus the centrifugal acceleration $\mathbf{\Omega}_{ie}^e \mathbf{\Omega}_{ie}^e \mathbf{r}^e$, i.e.

$$\mathbf{g}^e = \mathbf{G}^e - \mathbf{\Omega}_{ie}^e \mathbf{\Omega}_{ie}^e \mathbf{r}^e \tag{2.7}$$

Subsequently, Equation (2.6) is transformed to the ℓ-frame using the relationship between $\mathbf{v}^\ell$ and $\dot{\mathbf{r}}^e$

$$\dot{\mathbf{r}}^e = \mathbf{R}_\ell^e \mathbf{v}^\ell \tag{2.8}$$

Finally, the navigation equations in the ℓ-frame are obtained as (Titterton & Weston 2004; Hofmann-Wellenhof et al 2003)

$$\begin{aligned}\dot{\mathbf{v}}^{\ell} &= \mathbf{g}^{\ell} + \mathbf{f}^{\ell} - 2(\boldsymbol{\Omega}_{i\ell}^{\ell} + \boldsymbol{\Omega}_{ie}^{\ell})\mathbf{v}^{\ell} \\ \dot{\mathbf{r}}^{\ell} &= \mathbf{D}^{-1}\mathbf{v}^{\ell}\end{aligned} \tag{2.9}$$

where $\mathbf{D}^{-1}$ is a matrix which transfers velocity in the ℓ-frame into a position variation rate in the ℓ-frame (see Appendix A), and the position is expressed with curvilinear geodetic coordinates (latitude, longitude, and height). The specific force, $\mathbf{f}^{\ell}$, can be obtained from the accelerometer measurement $\mathbf{f}^{b}$, namely

$$\mathbf{f}^{\ell} = \mathbf{R}_{b}^{\ell}\mathbf{f}^{b} \tag{2.10}$$

where $\mathbf{R}_{b}^{\ell}$ is the rotation matrix describing the attitude of the vehicle. It is computed from the gyro data using numerical integration of (Hofmann-Wellenhof et al 2003)

$$\dot{\mathbf{R}}_{b}^{\ell} = \mathbf{R}_{b}^{\ell}\boldsymbol{\Omega}_{\ell b}^{b} \tag{2.11}$$

The detailed navigation equations are shown in Appendix A.

2.2.1.2 Error Model

In inertial systems, navigation error is induced by a variety of factors such as the inertial sensors, numeric computations, and initial values. Among these sources, the inertial sensors introduce the main error. In order to understand the navigation performance of the INS, the dynamic behaviour of the navigation system error is further analyzed below.

In the ℓ-frame, perturbing the second equation of Equation (2.9) yields the linearized position error dynamics (e.g. El-Sheimy 2007; Farrell & Barth 1999)

$$\delta\dot{\mathbf{r}}^{\ell} = -\mathbf{D}^{-1}\mathbf{D}_{r}\delta\mathbf{r}^{\ell} + \mathbf{D}^{-1}\delta\mathbf{v}^{\ell} \tag{2.12}$$

where $\mathbf{D}_r$ is a coefficient matrix, and $-\mathbf{D}^{-1}\mathbf{D}_r$ is defined in Appendix A. In a similar way, perturbing the first equation of Equation (2.9) yields the linearized velocity error equation (El-Sheimy 2007; Farrell & Barth 1999)

$$\delta\dot{\mathbf{v}}^{\ell} = \mathbf{A}\delta\mathbf{r}^{\ell} + \mathbf{B}\delta\mathbf{v}^{\ell} - \mathbf{F}^{\ell}\boldsymbol{\varepsilon}^{\ell} + \mathbf{R}_b^{\ell}\delta\mathbf{f}^{b} + \delta\mathbf{g}^{\ell} \tag{2.13}$$

where $\mathbf{A}$, $\mathbf{B}$, and $\mathbf{F}^{\ell}$ are matrices defined in Appendix A, and $\mathbf{F}^{\ell}$ is the skew-symmetric matrix form of the specific force vector $\mathbf{f}^{\ell}$. $\boldsymbol{\varepsilon}^{\ell}$ is attitude error, $\delta\mathbf{f}^{b}$ is accelerometer measurement error, and $\delta\mathbf{g}^{\ell}$ is the gravity computational error. From Equation (2.13), it can be seen that the velocity error variation is not only related to the position and velocity error, but also related to attitude error, specific force, and accelerometer measurement error.

The attitude error is defined as the misalignment caused by measurement, computational, and initialization errors. For small angles of misalignment, the computed transformation matrix can be written as (Titterton & Weston 2004)

$$\tilde{\mathbf{R}}_b^{\ell} = (\mathbf{I} + \mathbf{E}^{\ell})\mathbf{R}_b^{\ell} \tag{2.14}$$

where $\mathbf{I}$ is a 3×3 unit matrix, $\mathbf{E}^{\ell}$ is the skew-symmetric matrix of the attitude error $\boldsymbol{\varepsilon}^{\ell}$, and $\mathbf{R}_b^{\ell}$ is the true transformation matrix. Starting from Equation (2.14), through a series of differentiation and approximation operations, the attitude error equation is obtained as (Titterton & Weston 2004)

$$\dot{\boldsymbol{\varepsilon}}^{l} = \mathbf{P}\delta\mathbf{r}^{l} + \mathbf{Q}\delta\mathbf{v}^{l} - \boldsymbol{\Omega}_{il}^{l}\boldsymbol{\varepsilon}^{l} + \mathbf{R}_b^{l}\delta\boldsymbol{\omega}_{ib}^{b} \tag{2.15}$$

where matrices $\mathbf{P}$ and $\mathbf{Q}$ are defined in Appendix A, and $\delta\boldsymbol{\omega}_{ib}^{b}$ is the gyro measurement error. From Equation (2.15), it can be seen that the attitude error variation is induced not only by the gyro measurement error but also by the position, velocity, and attitude errors.

In fact, for an INS, the gyro measurement error is the main factor causing attitude errors, especially for low accuracy IMUs such as micro-electro-mechanical systems (MEMSs). The attitude error and accelerometer measurement error are the main sources inducing velocity errors. Therefore, it is important to model the sensor errors and include them in INS error model to improve the navigation performance. Generally, inertial sensor errors include some or all of the following components (Titterton & Weston 2004): a) fixed or repeatable terms; b) temperature-induced variations; c) switch-on to switch-on variations; d) in-run variations (i.e. variations with time or vehicle's motions). A detailed error model may contain many terms and be too complicated to use in practical systems. As a result, in general a simplified error model of inertial sensors is often used. For instance, the error model for both gyros and accelerometers is expressed as the sum of four terms: a first-order Gaussian Markov (GM) process (in-run variations), white noise (in-run variations), random constant (switch-on to switch on variations), and a scale-factor error (in-run variations) (Godha 2006; Grewal et al 2001). To reduce the Kalman filter computation of a GPS/INS system, the error model of inertial sensors can be further simplified as a first-order GM process plus a white noise component (Godha 2006). In this case, the gyro error model (for one axis) is expressed as

$$\begin{aligned} \delta\omega_{ib}^{b} &= d + w_{\omega} \\ \dot{d} &= -\alpha d + w_{d} \end{aligned} \tag{2.16}$$

where $\delta\omega_{ib}^{b}$ is the gyro measurement error, d is gyro drift, w_{ω} is gyro measurement noise, α is the inverse of the correlation time of the process, and w_d is the driving noise. Similarly, the accelerometer error model is written as

$$\begin{aligned} \delta f^{b} &= b + w_{f} \\ \dot{b} &= -\beta b + w_{b} \end{aligned} \tag{2.17}$$

where δf^{b} is the accelerometer measurement error, b is the accelerometer bias, w_b is white noise, β is the inverse of correlation time, and w_b is the driving noise. Further details on the INS error model equations are shown in Appendix A.

2.2.2 Reduced IMU System

A reduced IMU consists of less than three gyros and/or less than three accelerometers, resulting in incomplete acceleration and/or rotation rate measurements. As a result, the navigation performance of a reduced IMU is degraded compared to a full IMU with the same grade inertial sensors (Sun et al 2008; Nui et al 2007b). For land vehicle navigation, usually one vertical gyro and two or three accelerometers are used in a reduced IMU as shown in Figure 2.2 (Sun et al 2008; Nui et al 2007b), producing two reduced IMU configurations: 3A1G and 2A1G. These two configurations are based on the assumption that roads are relatively flat such that horizontal gyros and (in some cases) one vertical accelerometer provide relatively little information (Niu et al 2007b). But in practice, roads are not flat. Slopes and tilts always exist, inevitably introducing navigation errors

with a reduced system. The reason that slopes and tilts introduce navigation errors in a reduced IMU is explained in the following.

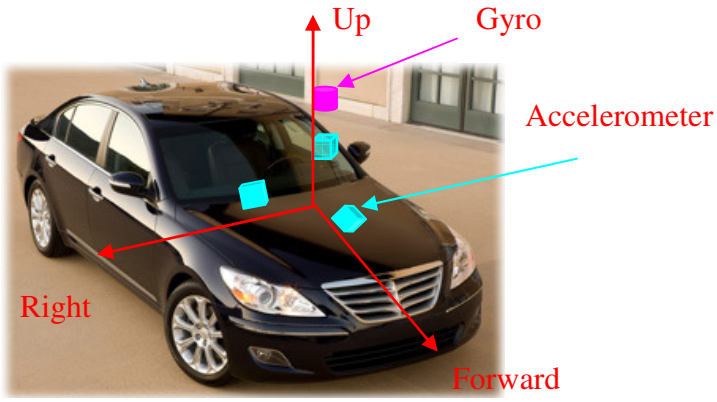

Figure 2.2 Reduced IMU Configuration

In inertial navigation, originally, a gimballed platform was used to carry the sensor assembly in order to isolate the assembly from the angular motions of the vehicle (Hofmann-Wellenhof et al 2003). The gyros of the assembly track the rotations of the platform and drive servomotors to align the platform to the local level frame (if the local level frame is the navigation frame). If the platform and the local level frames are completely coincident, the acceleration in each axis of the ℓ-frame can be exactly measured by the corresponding accelerometers of the assembly (without considering the sensor errors). Otherwise the acceleration in the ℓ-frame cannot be completely measured by the corresponding accelerometers. The accelerometer measurement has error induced by the cross product of the specific force and the attitude error vectors; the bigger the attitude error, the greater the accelerometer measurement error, and the greater the navigation error. Similar conclusions can be obtained from strapdown systems. In a

strapdown system, the platform is implemented with a rotation matrix (i.e., $\mathbf{R}_b^\ell$ if ℓ-frame is navigation frame). For a reduced IMU, since there are no horizontal gyros, its platform (or $\mathbf{R}_b^\ell$) cannot be adjusted to be completely coincident with the ℓ-frame. Actually, the platform mostly follows the local terrain around its two horizontal axes. As a result, the attitude error of the reduced IMU depends on local terrain variations, and so does the navigation error. Since reduced IMU displays different characteristics from the full IMU, its mechanization equations and error model need to be discussed, as shown in Chapter Three.

2.3 GPS Receiver

A GPS receiver is a device that receives GPS signals for determining the user's position and velocity. Generally, a GPS receiver consists of five parts or functions: GPS signal receiving, signal conditioning, signal acquisition, signal tracking, and navigation processing (Borre et al 2007; Misra & Enge 2001). Although each part is important, based on the focus of this dissertation, the following mainly introduces the last two parts.

2.3.1 GPS Receiver Configuration

A generic GPS receiver functional configuration is shown in Figure 2.3 (Ward et al 2006; Raquet 2004). In this figure, RF denotes radio frequency, IF denotes intermediate frequency, and LO denotes local oscillator. Figure 2.3 contains a GPS antenna, front end part, an oscillator, signal processing part, and navigation processing part. Among these parts, the antenna is for GPS signal receiving. After signal receiving, the front end part implements signal conditioning, including signal amplification, frequency down conversion, and signal sampling. Then the signal processing part implements signal acquisition and tracking functions. Herein, the signal acquisition carries out a global

search for approximate values of the code phase and Doppler shift. After the acquisition algorithm has significantly reduced the code and Doppler errors, signal tracking commences. The main purpose of tracking is to refine the code phase and Doppler shift values, continue to track the signals, and demodulate the navigation data. Signal tracking can provide pseudorange, Doppler shift, and carrier phase measurements. Once these measurements from at least four satellites are available, the navigation processing part starts the calculation of the user's position, velocity and time (PVT). During the above processes, the oscillator and frequency synthesizer generate signals to control the frequency down conversion and signal processing. Furthermore, the user can control both the signal processing and navigation processing through interrupts. Generally, a GPS receiver contains several channels, such as 12 channels. Each channel consists of the circuitry or software (for software receiver) necessary to track the signal from one single GPS satellite.

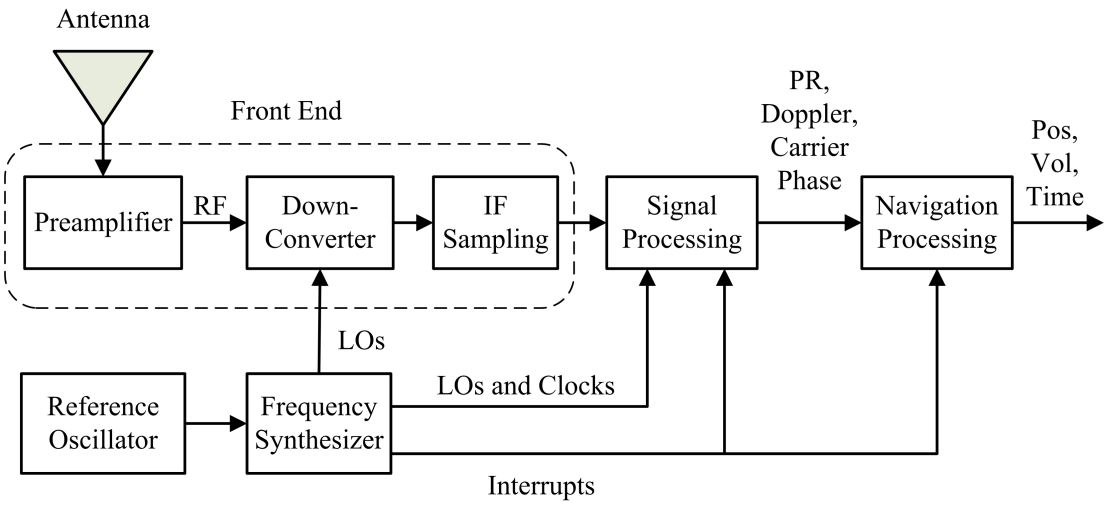

Figure 2.3 GPS Receiver Functional Configuration

2.3.2 GPS Receiver Scalar-Based Tracking Loops

GPS signal tracking can be implemented with either a scalar-based tracking scheme (SBTS) or a vector-based tracking scheme (VBTS). With SBTS, each channel of the receiver has its own tracking loops that operate independently of other channels (i.e., the loops are closed locally). Accordingly, the locally-closed tracking loops are called scalar-based tracking loops (SBTLs). Generally, with SBTS, each channel has two of this kind of locally-closed SBTLs: one is a delay lock loop (DLL), the other is a carrier tracking loop (CTL) or carrier Doppler removal loop consisting of one or both of a phase lock loop (PLL) and a frequency lock loop (FLL). In order to implement both code and carrier wipeoff functions, a GPS receiver must have both a DLL and a CTL (either a PLL or a FLL, or both), as shown in Figure 2.4 (Ward et al 2006; Raquet 2004). In the figure, "E" stands for "early", "P" stands for "prompt", and "L" stands for "late". I is in-phase signal and Q is quadraphase signal. Specifically, Figure 2.4 illustrates that the input signal is first multiplied with a carrier replica to wipe off the carrier wave from the signal ("Doppler Removal"); then the signal is multiplied with a code replica to remove the code from the signal ("Correlation"), and provides the navigation message obtained from $I_{3j}(P)$ (for more information, please see Borre et al (2007)). In this dissertation, the pseudo-random noise (PRN) code is C/A code, and the carrier wave is L_1 GPS signal with the frequency $f_{L1} = 1575.42$ MHz.

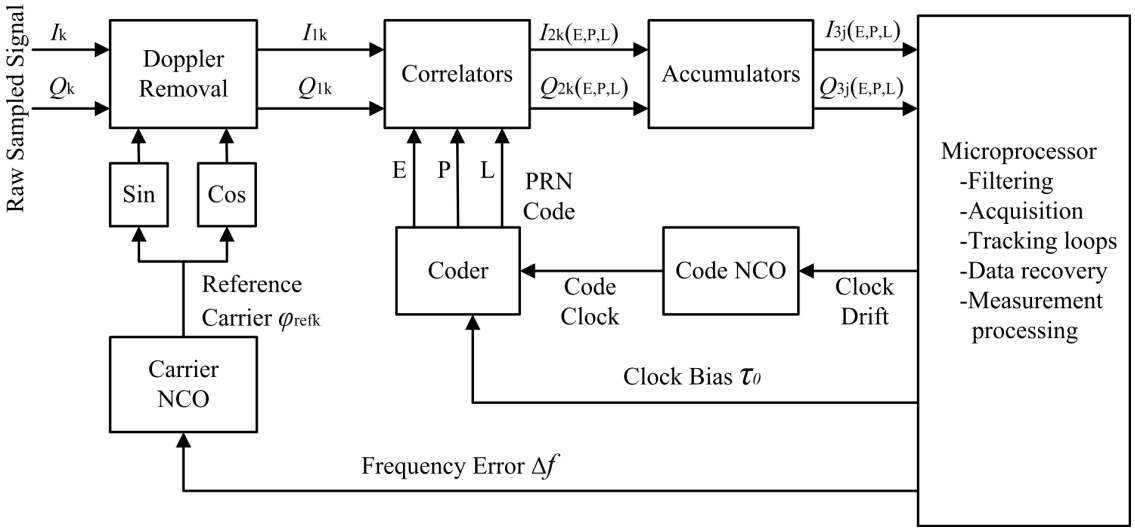

Figure 2.4 Scalar-Based Tracking Loops of GPS Receiver (One Channel)

In a CTL, when there is excess Doppler error, generally an FLL operated with a wide bandwidth is used because the FLL is more robust (Ward et al 2006). With the Doppler error decreasing, the FLL will gradually reduce its bandwidth and finally transition into a wideband PLL. Subsequently, the PLL will gradually narrow its bandwidth to the steady state model of operation. PLLs are considered as the desired steady state tracking model because they can not only produce the most accurate Doppler measurements, but also provide the most error-free data demodulation compared to the FLLs (Ward et al 2006). However, the FLLs fulfill the carrier wipeoff process by replicating the approximate frequency. They have wider frequency pull-in ranges, and are easier to acquire lock compared to the PLLs. So they are preferable in cases such as large Doppler error and high dynamics, where it is difficult to acquire and maintain signal lock using PLLs.

Both the DLL and the CTL are sophisticated systems, but either system can be modeled as a control system to facilitate system analysis (Misra & Enge 2001). In particular, for both a DLL and a Costas PLL, either system is modeled as a linear phase lock loop like the one shown in Figure 2.5 (Alban et al 2003; Misra & Enge 2001). In Figure 2.5, $R(s)$ is the input phase (either carrier or code), $\hat{R}(s)$ is the output phase, $E(s) = R(s) - \hat{R}(s)$ is the actuating error, $N(s)$ is noise or disturbance, $G_p(s) = 1/s$ is the transfer function of the NCO, $F(s)$ is the Doppler shift and $G_c(s)$ is the controller or loop filter. For a Doppler-aided DLL, generally a first-order loop filter is used, i.e. $G_c(s) = k_p$, where k_p is a constant (Ward et al 2006). For a Doppler-aided PLL, usually a second-order loop filter is used (Ward et al 2006), i.e. $G_c(s) = \left(2\xi\omega_n s + \omega_n^2\right)/s$, where $\xi = 0.707$ is the damping ratio of the system and ω_n is the un-damped natural frequency. Without Doppler aiding, the order of the loop filters should be higher than that with Doppler aiding (Ward et al 2006; Babu & Wang 2005). For an FLL, just like the PLL, it can be modeled as a control system as well, and has a similar transfer function as the PLL if the input signal of the FLL is frequency.

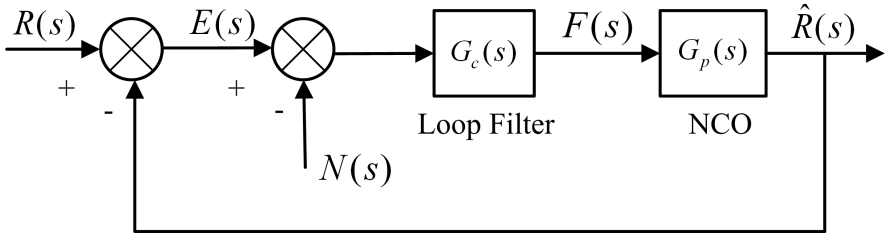

Figure 2.5 Block Diagram of Linearized Phase Lock Loop (One Channel)

In SBTLs, the measurement error or tracking error of a loop can be induced by numerous sources such as the loop's nonlinearity and the receiver's dynamics (Ward et al 2006). These sources induce measurement errors in the following way: first each of the sources produces an input error or noise; then this input error propagates in the loop, generating a measurement error. Consequently, the magnitude of this measurement error is not only related to the magnitude of the input error, but also related to the loop's noise bandwidth. In a PLL, there are numerous sources of phase measurement errors. However, it is sufficient to consider only the dominant error sources such as thermal noise, oscillator noise, and receiver dynamics. The formulae calculating these source-induced phase errors are given in Appendix B.

2.3.3 GPS Receiver Vector-Based Tracking Loops

When VBTS is applied in GPS signal tracking, the tracking loops are termed vector-based tracking loops (VBTLs). In contrast to SBTLs, VBTLs of a GPS receiver are closed via the navigation solution coming from either the GPS-only or the GPS/INS integration system. Thus the tracking loops of each channel are not independent, i.e. the loops of different channels are coupled through the navigation solution or navigation loop. Like SBTLs, there are also two types of VBTLs: one is vector delay lock loop (VDLL), the other is vector carrier tracking loop (VCTL) consisting of one or both of a vector phase lock loop (VPLL) and a vector frequency lock loop (VFLL).

A vector-based GPS receiver can be composed of a VDLL and either a VCTL or a scalar carrier tracking loop (SCTL) (or simply CTL). An example of a vector-based GPS receiver consisting of a VDLL and a VFLL is shown in Figure 2.6. From Figure 2.6, it

can be seen that in each channel, both the code NCO and the carrier NCO are controlled by the output of the GPS/INS integration system. The pseudorange error and carrier Doppler error directly come from the corresponding discriminators. There are no locally-closed tracking loops. Correspondingly the noise in a tracking loop does not propagate through a locally-closed loop.

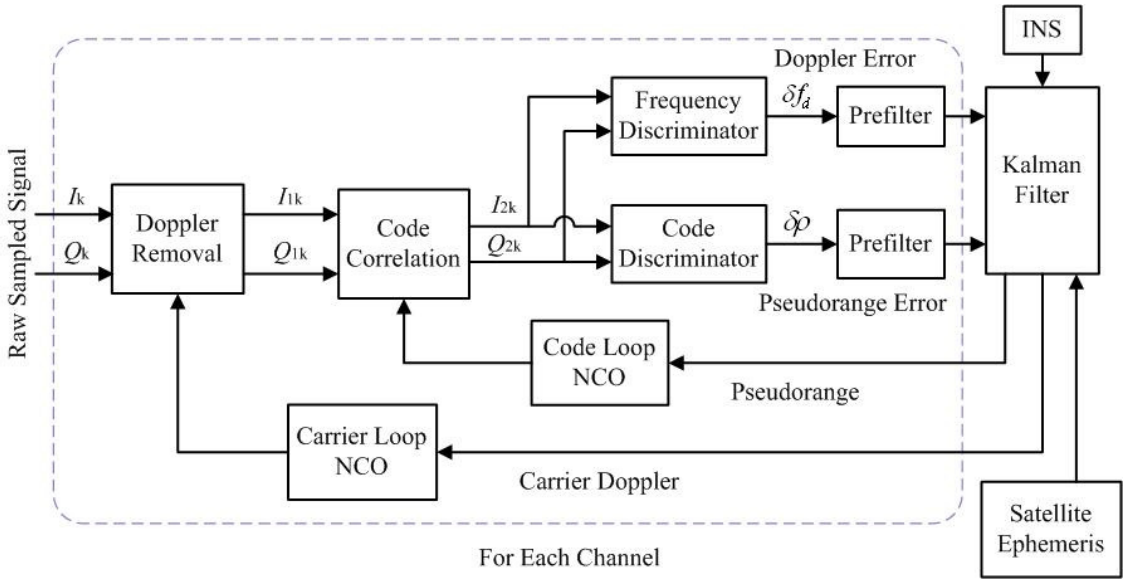

Figure 2.6 Vector-Based Tracking Loops of GPS Receiver (One Channel)

Like SBTLs, VBTLs also can be modeled as a linear control loop for one channel, but this loop is broken or open. Figure 2.7 takes a VDLL as an example to illustrate the block diagram of a VBTL. From Figure 2.7, it can be seen that the code NCO is controlled with Doppler aiding obtained from the navigator of the receiver, and reset frequently with the code phase that is also obtained from the navigator. The code phase measurement $\hat{\tau}_m$ equals the output of the NCO plus the filtered output of the code discriminator, and τ_m is the input code phase. Figure 2.7 is a discrete system, where T_{PIT} is the predetection

integration time (PIT). This figure is drawn with reference to the block diagram of the discrete linearized model of a DLL as shown in Misra & Enge (2001).

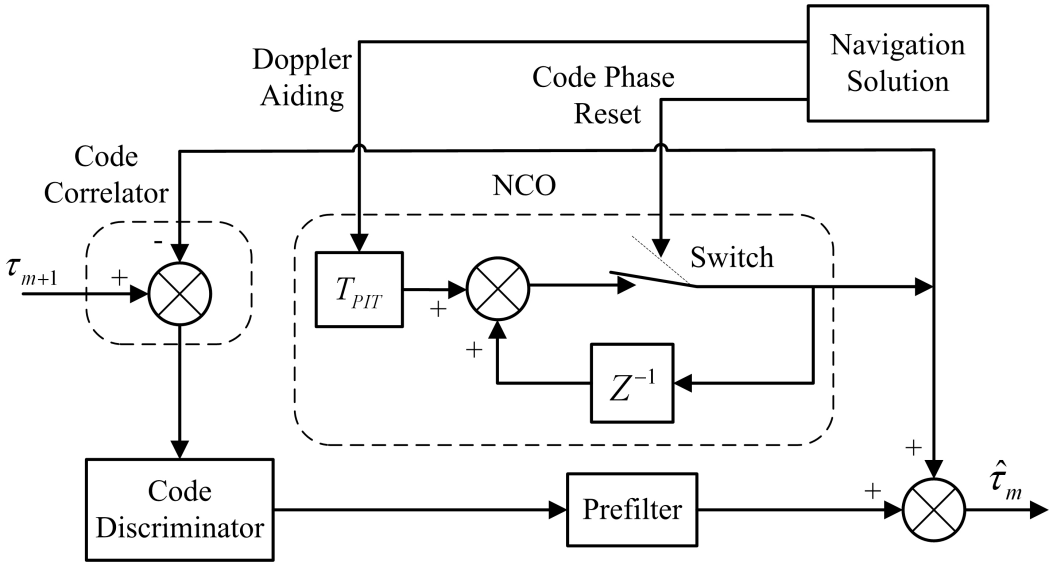

Figure 2.7 Block Diagram of VDLL's Lock Loop (One Channel)

2.3.4 GPS Receiver Measurements

Generally, a GPS receiver can provide two types of measurements: one from code tracking called a pseudorange, the other from carrier phase tracking called the carrier phase. At the same time, carrier phase tracking gives an estimate for pseudorange rate, called Doppler frequency or Doppler shift. In a GPS receiver, the basic measurement is the transit time of the signal from a satellite to the receiver. The corresponding pseudorange is defined as the transit time multiplied by the speed of light. Since there are various factors degrading the measurement accuracy of the transit time, the pseudorange measurement inevitably contains errors. Accounting for various measurement errors, the measured pseudorange can be written as (Lachapelle 2006; Misra & Enge 2001)

$$\rho = r + O_\rho + c(\delta t_u - \delta t_s) + I_\rho + T_\rho + \varepsilon_\rho \tag{2.18}$$

where the unit of ρ is metres, O_ρ is orbital error, δt_u and δt_s are receiver and satellite clock offsets respectively (herein advance is positive; delay is negative), c is the speed of light, I_ρ and T_ρ are ionospheric and tropospheric delays respectively, ε_ρ is noise, r is geometric range, written as

$$r = \sqrt{(X - x_u)^2 + (Y - y_u)^2 + (Z - z_u)^2} \tag{2.19}$$

where (x_u, y_u, z_u) is the position of the user, (X, Y, Z) is the position of a satellite, which is calculated from the ephemeris.

The carrier phase measurement is much more precise than code phase, but is an ambiguous measurement of the signal transit time. Like code phase, carrier phase measurements also contain errors. Accounting for various measurement errors, the carrier phase measurement can be expressed as (Lachapelle 2006; Misra & Enge 2001)

$$\phi = r + O_\rho + c(\delta t_u - \delta t_s) + \lambda M - I_\rho + T_\rho + \varepsilon_\phi \tag{2.20}$$

where the unit of ϕ is metres, λ is wavelength, M is integer cycle ambiguity, ε_ϕ is noise, and the remaining parameters have the same meaning as in Equation (2.18). In the CTL of a GPS receiver, the Doppler shift is measured continuously. It is produced by both the relative motion of the satellite with respect to the user and the receiver clock drift. Its measurement can be written as (Kaplan et al 2006; Misra & Enge 2001)

$$f_d = -f_T \frac{(\mathbf{V} - \mathbf{v}_u) \cdot \boldsymbol{\kappa}}{c} - f_T \dot{t}_u + \varepsilon_d \tag{2.21}$$

where the unit of f_d is Hz, $\mathbf{V}$ is the satellite velocity vector, $\mathbf{v}_u$ is the user velocity vector, $\boldsymbol{\kappa}$ is the user-to-satellite line-of-sight unit vector, f_T is the transmitted signal

frequency (for L_1 signal, $f_{L1} = 1575.42\,\text{MHz}$), $\dot{t}_u$ is receiver clock drift rate (herein it is positive if the user clock is running fast), and ε_d is noise.

2.3.5 Estimation of Position, Velocity, and Time

Once GPS measurements are obtained, the user's position, velocity, and time can be estimated. In the following, only pseudorange and Doppler shift measurements are used to estimate the PVT. First, from the pseudorange measurement, the user's position and receiver clock offset can be obtained. From Equation (2.18), most errors such as satellite clock offset, ionospheric delay, and tropospheric delay can be modeled and corrected first. After the correction, substituting Equation (2.19) into Equation (2.18) yields the pseudorange measurement of *i*th satellite

$$\rho_i = \sqrt{(X_i - x_u)^2 + (Y_i - y_u)^2 + (Z_i - z_u)^2} + c\delta t_u + \tilde{\varepsilon}_{\rho i} \tag{2.22}$$

where $\tilde{\varepsilon}_{\rho i}$ is the noise after the pseudorange error correction. In order to determine the user's three-dimensional position (x_u, y_u, z_u) and the clock offset δt_u, at least four satellites' pseudorange measurements are needed. With four measurements, four corresponding equations can be obtained with Equation (2.22). Then the position and clock offset can be solved.

A simple approach to solving the four equations is to linearize them about an approximate user position, and solve iteratively. Let $\hat{\mathbf{x}}_u = (\hat{x}_u \quad \hat{y}_u \quad \hat{z}_u)^T$ and $\delta\hat{t}_u$ be the estimates of the position and clock offset. Approximating the pseudorange equation with a first-order Taylor series yields

$$\rho_i - \hat{\rho}_i = -\frac{X_i - \hat{x}_u}{\hat{r}_i}\delta x_u - \frac{Y_i - \hat{y}_u}{\hat{r}_i}\delta y_u - \frac{Z_i - \hat{z}_u}{\hat{r}_i}\delta z_u + c\Delta t_b + \tilde{\varepsilon}_{\rho i} \tag{2.23}$$

where $i = 1, 2, \cdots, N$, where N is the number of satellites, $\delta x_u = x_u - \hat{x}_u$, $\delta y_u = y_u - \hat{y}_u$, $\delta z_u = z_u - \hat{z}_u$, $\Delta t_b = \delta t_u - \delta \hat{t}_u$, $\hat{\rho}_i$ is expressed as

$$\hat{\rho}_i = \hat{r}_i + c\delta \hat{t}_u \tag{2.24}$$

and $\hat{r}_i$ is

$$\hat{r}_i = \sqrt{(X_i - \hat{x}_u)^2 + (Y_i - \hat{y}_u)^2 + (Z_i - \hat{z}_u)^2}\ . \tag{2.25}$$

Once at least four linearized equations as Equation (2.23) are obtained, the four unknowns δx_u, δy_u, δz_u, and Δt_b can be solved using a least-squares algorithm (Misra & Enge 2001; Axelrad & Brown 1996). Finally, the user's position and the receiver clock offset can be obtained.

Similar to the position estimation with pseudorange, velocity and clock drift can be estimated with Doppler shift. Starting from Equation (2.21) , the pseudorange rate is defined as

$$\dot{\rho} = -c \cdot f_d / f_T \tag{2.26}$$

Then the measurement of pseudorange rate for *i*th satellite is written as

$$\dot{\rho}_i = (\mathbf{V}_i - \mathbf{v}_u) \cdot \boldsymbol{\kappa}_i + c \cdot \dot{t}_u - \varepsilon_{\dot{\rho} i} \tag{2.27}$$

where $\varepsilon_{\dot{\rho}i} = c \cdot \varepsilon_{di} / f_T$, $\mathbf{V}_i = \begin{pmatrix} V_{ix} & V_{iy} & V_{iz} \end{pmatrix}^T$, $\mathbf{v}_u = \begin{pmatrix} v_{ux} & v_{uy} & v_{uz} \end{pmatrix}^T$, and $\boldsymbol{\kappa}_i = \begin{pmatrix} \frac{X_i - \hat{x}_u}{\hat{r}_i} & \frac{Y_i - \hat{y}_u}{\hat{r}_i} & \frac{Z_i - \hat{z}_u}{\hat{r}_i} \end{pmatrix}^T$, the parameters in $\boldsymbol{\kappa}_i$ are defined in Equation (2.23).

Rearranging Equation (2.27) yields

$$\dot{\rho}_i - \mathbf{V}_i \cdot \boldsymbol{\kappa}_i = -\mathbf{v}_u \cdot \boldsymbol{\kappa}_i + c \cdot \dot{t}_u - \varepsilon_{\dot{\rho}i} \tag{2.28}$$

When at least four pseudorange rate equations as Equation (2.28) are obtained, the four unknowns v_{ux} , v_{uy} , v_{uz} , and $\delta \dot{t}_u$ can be solved with least-squares algorithm. If the user's dynamics is modeled as a linear equation, PVT can be solved using a Kalman filter with the measurements of pseudorange and pseudorange rate (Axelrad & Brown 1996).

2.4 GPS/IMU Integration System

As mentioned in Chapter One, there are three kinds of GPS/INS integration systems, namely loose, tight and ultra-tight integration. And for tight integration, the system is further divided into two sub-types: tight and TLA system (see Chapter One). These systems are introduced in the following.

2.4.1 Loose Integration System

In loose GPS/INS integration, the GPS receiver outputs position and velocity information which is integrated with the INS as shown in Figure 2.8. As shown, A is attitude, $\delta \mathbf{X}_{INS}$ denotes the INS error state.

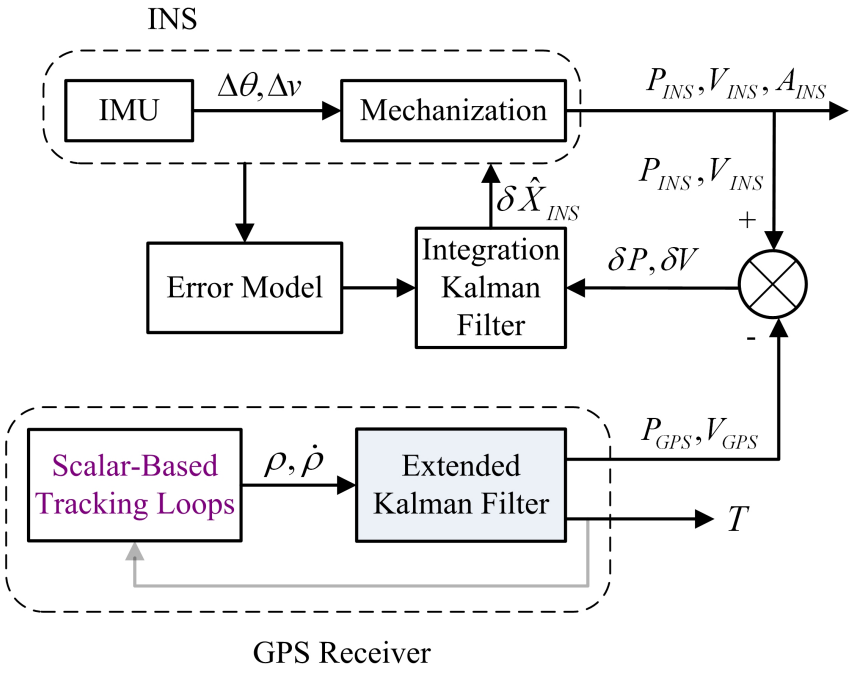

Figure 2.8 Loose GPS/INS Integration Block Diagram

From Figure 2.8, it can be seen that the GPS receiver has an extended Kalman filter responsible for navigation processing. The integration filter implemented with an extended Kalman filter is used for the information fusion of the integration system. The output of the integration filter is used to correct the INS with a closed-loop scheme (through $\delta\hat{\mathbf{X}}_{INS}$). Since the measurements of the integration filter are position and velocity error, the measurement equation is linear and written as

$$\mathbf{Z}_{k+1} = \mathbf{H}\mathbf{X}_{k+1} + \boldsymbol{\eta}_{k+1} \tag{2.29}$$

where $\mathbf{Z}_{k+1} = (\delta\mathbf{P}_{k+1} \quad \delta\mathbf{V}_{k+1})^T$, $\boldsymbol{\eta}_{k+1}$ is measurement noise, $\mathbf{X}_{k+1}$ is the state vector, and $\mathbf{X}_{k+1} = \delta\mathbf{X}_{INS}(k+1)$. $\mathbf{H} = \begin{bmatrix} \mathbf{I}_{3\times3} & \mathbf{0}_{3\times3} & \mathbf{0}_{3\times(n-6)} \\ \mathbf{0}_{3\times3} & \mathbf{I}_{3\times3} & \mathbf{0}_{3\times(n-6)} \end{bmatrix}$, where $\mathbf{I}_{3\times3}$ is a 3×3 unit matrix, $\mathbf{0}_{3\times3}$ is a 3×3 zero matrix, n is the dimension of the state. If the state equation is expressed as

$$\mathbf{X}_{k+1} = \boldsymbol{\Phi}_k \mathbf{X}_k + \mathbf{G}_k \mathbf{W}_k \tag{2.30}$$

an extended Kalman filter can be obtained (Gelb 1974). In Equation (2.30), $\mathbf{W}_k$ is the state process noise. Since Equation (2.30) is a linearized equation (Titterton & Weston 2004) and the INS error correction in the integration system is implemented with a feedback loop or closed loop, the implemented integration filter is an extended Kalman filter (Grewal & Andrews 2001; Farrell & Barth 1999).

2.4.2 Tight and Ultra-Tight Integration Systems

In tight GPS/INS integration, the GPS receiver outputs raw data measurements, i.e. pseudorange, carrier phase, and carrier Doppler. Generally pseudorange and carrier Doppler measurement are used to integrate with the INS as shown in Figure 2.9 (if carrier phase is to be used, its cycle ambiguities need to be solved). In Figure 2.9, $\delta\mathbf{X}_{GPS}$ denotes the error state of the GPS receiver. The integration filter is an extended Kalman filter. The measurement equation is nonlinear and written as

$$\mathbf{Z}_{k+1} = \mathbf{h}(\mathbf{X}_{k+1}) + \boldsymbol{\eta}_{k+1} \tag{2.31}$$

where $\mathbf{Z}_{k+1} = (\delta\rho_1(k+1) \quad \delta\dot{\rho}_1(k+1) \quad \cdots \quad \delta\rho_N(k+1) \quad \delta\dot{\rho}_N(k+1))^T$, where N is the tracked satellite number, k denotes discrete time, $\delta\rho_i = \rho_i - \hat{\rho}_i$ and $\delta\dot{\rho}_i = \dot{\rho}_i - \mathbf{V}_i \cdot \boldsymbol{\kappa}_i$, $i = 1, 2, \cdots, N$, are expressed as Equations (2.23) and (2.28) respectively. If the state equation is expressed as Equation (2.30), and the state

$\mathbf{X}_{k+1} = \left(\delta\mathbf{X}_{INS}^{T}(k+1) \quad \delta\mathbf{X}_{GPS}^{T}(k+1)\right)^{T}$, an extended Kalman filter can be obtained (Gelb 1974). In tight integration system, since both the dynamics and measurement equations of the integration filter are nonlinear, for Kalmen filter implementation, one would have to use extended Kalman filtering (Grewal et al 2001).

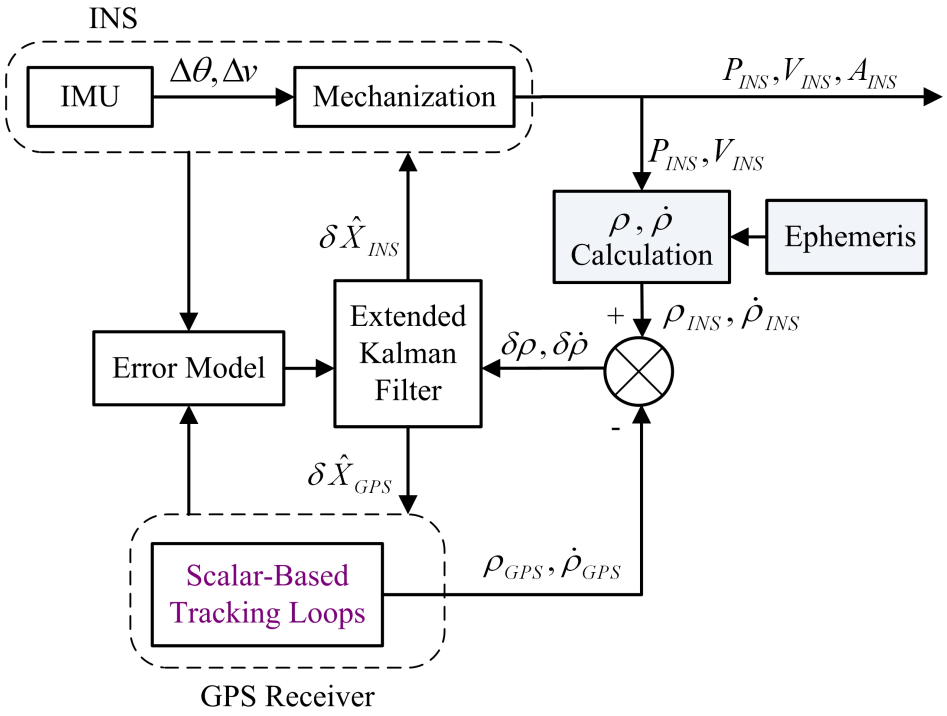

Figure 2.9 Tight GPS/INS Integration Block Diagram

The block diagram of TLA GPS/INS integration is shown in Figure 2.10. As discussed in Chapter One, in the TLA system, the PLLs of the GPS receiver accept Doppler shift aiding calculated from the navigation solution of the integration system and satellite information. Comparing Figure 2.10 and Figure 2.9, it can be seen that the only difference between the TLA and tight systems is that in the TLA system, the GPS receiver's PLLs are aided with the Doppler shift.

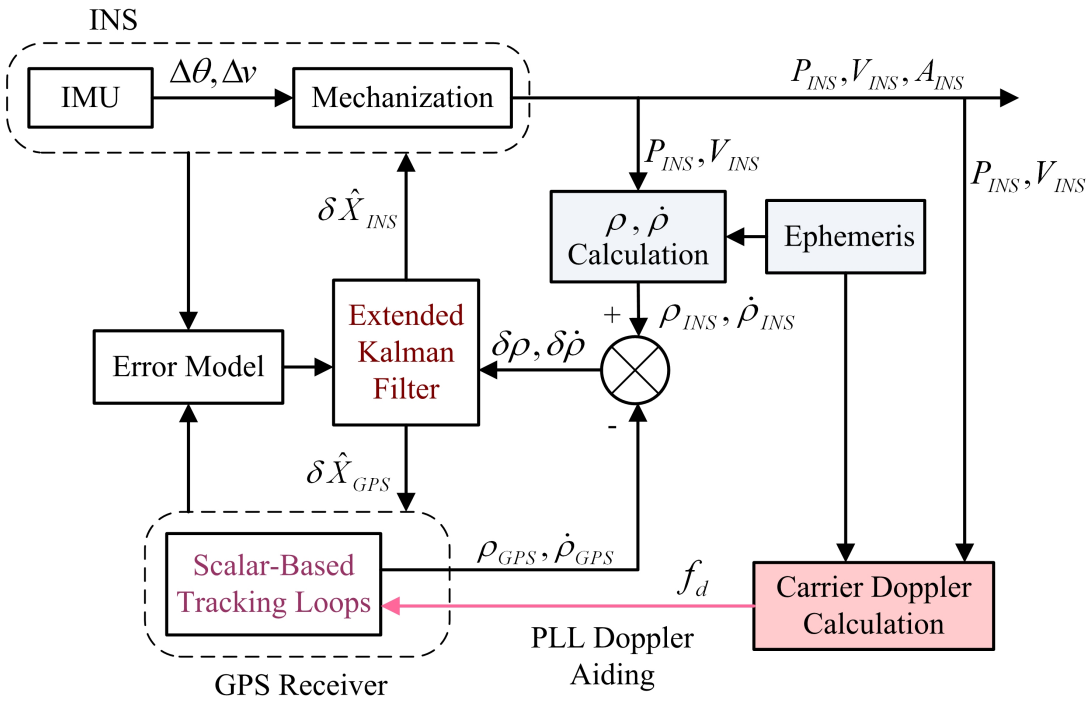

Figure 2.10 TLA GPS/INS Integration Block Diagram

The block diagram of UT GPS/INS integration is shown in Figure 2.11. From Figure 2.11, it can be seen that the tracking loops of the receiver are vector-based whereas those in TLA and tight system are scalar-based. The code phase and Doppler shift calculated from the INS and satellite ephemeris are used to control both the code NCO and carrier NCO to implement vector-based tracking. In the UT system, the pseudorange and carrier Doppler are used as the measurements in the integration system (Lashley & Bevly 2008a; Pany et al 2005). Sometimes the in-phase *I* and quadraphase *Q* signals of the receiver, which are used as the input of the discriminators in a scalar-based receiver, are used as measurements for a UT system directly (Crane 2007; Ohlmeyer 2006). The *I* and *Q* signals are generated in the front-end part of any GPS receiver. In this part, the GPS

signal is down-converted and separated into two constituents: in-phase *I* and quadraphase *Q*. These two components are orthogonal to each other and used in the signal acquisition and tracking part of the receiver (Lachapelle 2006; Ward et al 2006).

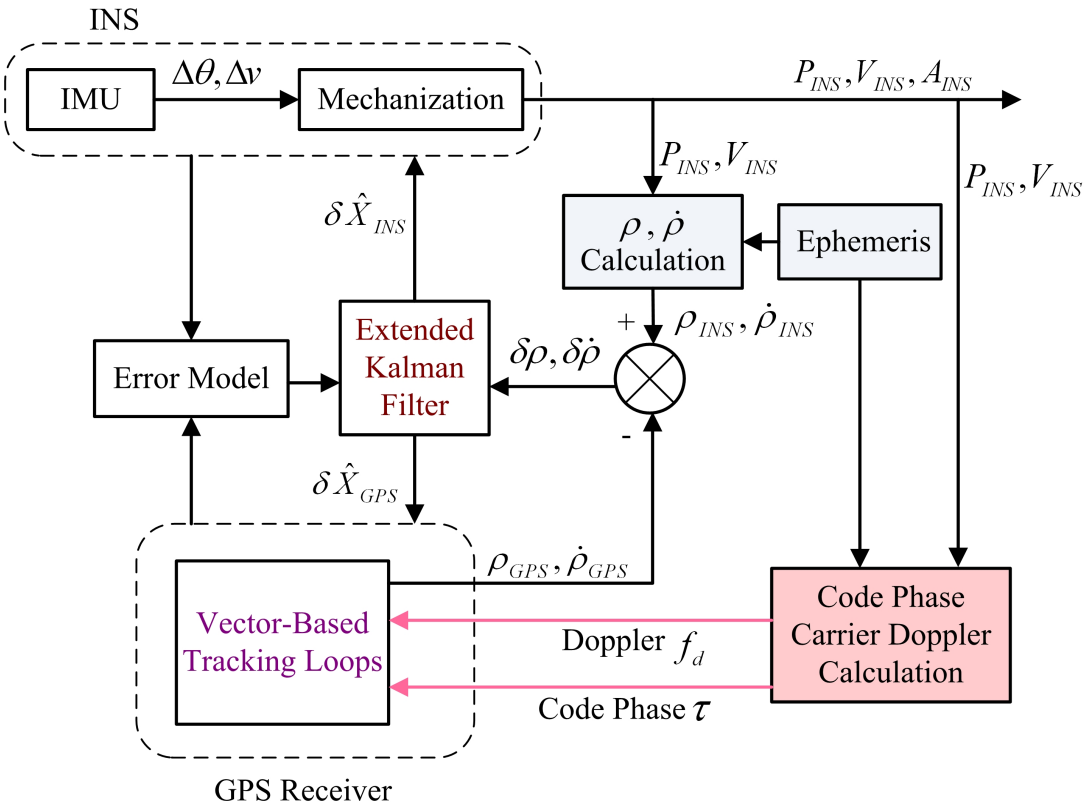

Figure 2.11 UT GPS/INS Integration Block Diagram

Chapter Three: Mechanization of Reduced IMU

As discussed in Chapter Two, generally there are two reduced IMU (RIMU) configurations used in land vehicle navigation, namely 3A1G (i.e. three accelerometers plus one vertical gyro) and 2A1G (i.e. two horizontal accelerometers plus one vertical gyro). Since there are no horizontal gyros in the reduced IMUs, their rotation measurements are incomplete (for the 2A1G case, so is the acceleration measurement), resulting in degraded navigation performance (Sun et al 2008; Niu et al 2007b). Owing to the fact that reduced IMUs display different characteristics from full IMUs, their mechanization equations and error models are reviewed in this chapter.

This chapter begins with the development of a local terrain predictor (LTP) method for an RIMU to improve the navigation performance of a GPS/RIMU, resulting in a set of innovative mechanization equations and error model. This set of equations and error model and other two sets of mechanization equations and error model for RIMU (i.e. dead reckoning and full dimension type) are compared to identify their advantages and disadvantages. Following the theoretical research, a field vehicle test, conducted to collect IMU and GPS data for post-mission processing, is described. An evaluation of the LTP method is then performed with the field data, and finally a comparison of the three sets of mechanization equations and error model is made with tests using the real data.

3.1 Mechanization of RIMU with a Local Terrain Predictor

In inertial navigation, a full six degree of freedom IMU consists of three orthogonal accelerometers and three orthogonal gyros. As a result, the acceleration and rotation of the vehicle mounted with the IMU are completely measured. By contrast, in a reduced

IMU where there is only one vertical gyro, the pitch and roll cannot be measured. Similarly, if fewer than three accelerometers are used, such as in the 2A1G configuration, full knowledge of the vehicle's acceleration is unavailable. Both situations introduce errors in the navigation system.

In order to overcome the disadvantages of RIMUs, integrating them with other navigation systems or constraints is a means of improving performance. For example, GPS/RIMU (Niu et al 2007b; Phuyal 2004) and GPS/RIMU with vehicular constraints (Li et al 2009; Syed et al 2007) have previously been studied. Herein, a local terrain predictor is presented to help estimate the pitch and roll of the RIMU and thus to improve navigation performance. The LTP method can be envisaged as an error modeling method for RIMUs that compensates for terrain-induced pitch and roll variations. It does not increase the measurement variables of GPS/RIMU, but changes the navigation equations and error model of the RIMU. Since this dissertation only focuses on two RIMU configurations, i.e. 3A1G and 2A1G, with the LTP, the navigation equations and error models of the two configurations are investigated below.

3.1.1 Derivation of Navigation Equations of RIMU

The derivation of navigation equations is based on the 3A1G configuration, and can be developed from the navigation equations of a full IMU as shown in Equation (A.1) in Appendix A. Furthermore, only the attitude equation needs to be derived, as below. For details on notation, please refer to Appendix A. The following development closely follows that in Sun et al (2008) and as such many of the intermediate steps of the derivations are omitted in the interest of brevity.

First, for a land vehicle navigation system, the rotation matrix from the b-frame to the ℓ-frame can be expressed as (Petovello 2003)

$$\mathbf{R}_b^{\ell} = \mathbf{A}_z(\psi)\mathbf{A}_x(-p)\mathbf{A}_y(-r) \tag{3.1}$$

where ψ is azimuth, p is pitch, r is roll, and $\mathbf{A}_j(\varpi)$, $j = x, y, z$, $\varpi = p, r, \psi$, is a rotation matrix about j-axis by angle ϖ. Through a series of derivations with Equation (3.1), the following is obtained (Sun et al 2008)

$$\mathbf{A}_z(-\psi)\dot{\mathbf{R}}_b^{\ell}\mathbf{A}_y(r)\mathbf{A}_x(p) = \begin{bmatrix} 0 & \dot{\psi} - \dot{r}\sin p & \dot{r}\cos p \\ -\dot{\psi} + \dot{r}\sin p & 0 & -\dot{p} \\ -\dot{r}\cos p & \dot{p} & 0 \end{bmatrix} = [\boldsymbol{\Theta}\times] \tag{3.2}$$

where

$$\boldsymbol{\Theta} = \begin{bmatrix} \dot{p} \\ \dot{r}\cos p \\ -\dot{\psi} + \dot{r}\sin p \end{bmatrix} \tag{3.3}$$

From Equation (A.1), $\dot{\mathbf{R}}_b^{\ell} = \mathbf{R}_b^{\ell}(\boldsymbol{\Omega}_{ib}^b - \boldsymbol{\Omega}_{i\ell}^b)$. Substituting this equation and Equation (3.1) into Equation (3.2), and through a series of derivations, the following is obtain (Sun et al 2008)

$$\boldsymbol{\Theta} = (\boldsymbol{\omega}_{ib}^{\ell 1} - \boldsymbol{\omega}_{i\ell}^{\ell 1}) \tag{3.4}$$

where

$$\boldsymbol{\omega}_{ib}^{\ell 1} = \mathbf{R}_b^{\ell 1}\boldsymbol{\omega}_{ib}^b = \mathbf{A}_x(-p)\mathbf{A}_y(-r)\begin{bmatrix} \omega_{ibx}^b \\ \omega_{iby}^b \\ \omega_{ibz}^b \end{bmatrix} = \begin{bmatrix} \omega_{ibx}^b \cos r + \omega_{ibz}^b \sin r \\ \omega_{ibx}^b \sin p \sin r + \omega_{iby}^b \cos p - \omega_{ibz}^b \sin p \cos r \\ -\omega_{ibx}^b \cos p \sin r + \omega_{iby}^b \sin p + \omega_{ibz}^b \cos p \cos r \end{bmatrix} \tag{3.5}$$

$$\boldsymbol{\omega}_{i\ell}^{\ell 1} = \mathbf{A}_z(-\psi)\boldsymbol{\omega}_{i\ell}^{\ell} = \mathbf{A}_z(-\psi)\begin{bmatrix}\omega_{i\ell x}^{\ell}\\ \omega_{i\ell y}^{\ell}\\ \omega_{i\ell z}^{\ell}\end{bmatrix} = \begin{bmatrix}\omega_{i\ell x}^{\ell}\cos\psi - \omega_{i\ell y}^{\ell}\sin\psi\\ \omega_{i\ell x}^{\ell}\sin\psi + \omega_{i\ell y}^{\ell}\cos\psi\\ \omega_{i\ell z}^{\ell}\end{bmatrix} \tag{3.6}$$

and where $\boldsymbol{\omega}_{ib}^{b}$ and $\boldsymbol{\omega}_{i\ell}^{\ell}$ are defined in Appendix A, $\boldsymbol{\omega}_{ib}^{b}$ is the measurement of gyros, and $\mathbf{R}_b^{\ell 1} = \mathbf{A}_x(-p)\mathbf{A}_y(-r)$. Substituting Equations (3.5) and (3.6) into Equation (3.4) yields

$$\begin{cases}\dot{p} = \omega_{ibx}^{b}\cos r + \omega_{ibz}^{b}\sin r - \left(\left(\dfrac{-v_n}{M+h}\right)\cos\psi - \left(\dfrac{v_e}{N+h} + \omega_e\cos\phi\right)\sin\psi\right)\\ \dot{r}\cos p = \omega_{ibx}^{b}\sin p\sin r + \omega_{iby}^{b}\cos p - \omega_{ibz}^{b}\sin p\cos r\\ \qquad\qquad -\left(\left(\dfrac{-v_n}{M+h}\right)\sin\psi + \left(\dfrac{v_e}{N+h} + \omega_e\cos\phi\right)\cos\psi\right)\\ -\dot{\psi} + \dot{r}\sin p = -\omega_{ibx}^{b}\cos p\sin r + \omega_{iby}^{b}\sin p + \omega_{ibz}^{b}\cos p\cos r - \left(\dfrac{v_e\tan\phi}{N+h} + \omega_e\sin\phi\right)\end{cases} \tag{3.7}$$

where the velocity components v_e, v_n, meridian radius M, prime vertical radius N, height h, latitude φ, and rotation rate of the earth ω_e are defined in Appendix A. Therefore, the azimuth rate equation is obtained from Equation (3.7) as

$$\dot{\psi} - \dot{r}\sin p = \omega_{ibx}^{b}\cos p\sin r - \omega_{iby}^{b}\sin p - \omega_{ibz}^{b}\cos p\cos r + \left(\frac{v_e\tan\varphi}{N+h} + \omega_e\sin\varphi\right) \tag{3.8}$$

From Equation (3.7), it can be seen that since ω_{ibx}^{b} and ω_{iby}^{b} are unknown (not measured), pitch and roll cannot be calculated. Because pitch and roll are generally small in land vehicle applications, they can be considered as error terms and will therefore be modeled accordingly. However, for the mechanization equations, they are assumed to be zero, that is, $p = 0, r = 0$. With this assumption, the azimuth rate equation and attitude direction cosine matrix can be obtained from Equations (3.8) and (3.1), respectively, and written as

$$\begin{cases} \dot{\psi} = -\omega_{ibz}^{b} + \left(\dfrac{v_e \tan\phi}{N+h} + \omega_e \sin\phi \right) \\ \mathbf{R}_b^{\ell} = \mathbf{A}_z(\psi) \end{cases} \tag{3.9}$$

Substituting Equation (3.9) into Equation (A.1), the navigation equations of RIMU (3A1G) are obtained, see Equation (3.19).

3.1.2 Derivation of Error Model of RIMU

The corresponding error model of the RIMU (3A1G) needs to be derived from the full IMU error equations given in Equation (A.6) (see Appendix A). In order to facilitate the derivations, in the following, $\mathbf{W}_f$ and $\mathbf{W}_\omega$ of Equation (A.6) (i.e. accelerometer and gyro measurement noise, respectively) are ignored in the derivation. It does not affect the derivation, and the two terms can be added back after the derivation. The position error model and accelerometer bias model of the 3A1G are the same as those of Equation (A.6), but the other error state models (i.e., velocity, attitude and gyro biases) are derived in below.

First, the attitude error model is derived. Recall that in Equation (3.9) the pitch and roll are assumed to be zero and considered as error terms. However, for land applications, the pitch and roll are primarily determined by the local terrain and since this terrain can be expressed as a first-order Gaussian Markov (GM) process (Kuchar 2001), the pitch and roll can also be expressed as first-order GM processes

$$\begin{cases} \dot{p} = -\alpha_p p + w_p \\ \dot{r} = -\alpha_r r + w_r \end{cases} \tag{3.10}$$

where α_p, α_r are the inverse of correlation time of the process, and w_p, w_r are driving noise terms. The definition of the azimuth rate error is

$$\delta\dot{\psi} = \dot{\tilde{\psi}} - \dot{\psi} \tag{3.11}$$

where $\dot{\psi}$ is the 'true' azimuth rate which can be obtained from Equation (3.8), $\dot{\tilde{\psi}}$ is azimuth rate with error and can be obtained from Equation (3.9). Substituting Equation (3.8) and the azimuth rate equation of Equation (3.9) into Equation (3.11), and through a series of derivations and approximations, the following is obtained (Sun et al 2008)

$$\delta\dot{\psi} \approx d_z + w_\psi \tag{3.12}$$

where w_ψ is the equivalent white noise corrupting the drift, d_z is the drift of vertical gyro, defined as

$$d_z = \omega_{ibz}^b - \tilde{\omega}_{ibz}^b \tag{3.13}$$

where $\tilde{\omega}_{ibz}^b$ is the vertical gyro measurement, ω_{ibz}^b is true rotation rate about z_b. The vertical gyro drift, d_z, can be modeled as a first-order GM process

$$\dot{d}_z = -\alpha_d d_z + w_d \tag{3.14}$$

where α_d is the inverse of the correlation time and w_d is the driving noise.

Next, in order to link the attitude error of the RIMU with the local terrain (pitch and roll), the attitude error $\boldsymbol{\varepsilon}^{\ell 1}$ needs to be expressed as a function of the pitch, roll and azimuth errors. Through a series of derivations, the attitude error $\boldsymbol{\varepsilon}^{\ell 1}$ is expressed as (Sun et al 2008)

$$\dot{\boldsymbol{\varepsilon}}^{\ell 1} = \delta\boldsymbol{\Theta} \tag{3.15}$$

where $\boldsymbol{\Theta}$ is defined in Equation (3.3). Since p and r are small angles of only a few degrees, and in the navigation equations, p and r are chosen as zero, Equation (3.15) is approximated as

$$\dot{\boldsymbol{\varepsilon}}^{\ell 1} \approx \begin{bmatrix} \delta\dot{p} \\ \delta\dot{r} \\ -\delta\dot{\psi} \end{bmatrix} = \begin{bmatrix} -\dot{p} \\ -\dot{r} \\ -\delta\dot{\psi} \end{bmatrix} \tag{3.16}$$

Since in the navigation equations, p and r are chosen as zero, $\delta p = 0 - p = -p$, $\delta r = 0 - r = -r$ (estimate value minus truth value). Therefore, $\delta\dot{p} = -\dot{p}$, $\delta\dot{r} = -\dot{r}$ (i.e. Equation (3.16) is satisfied). From Equations (3.10), (3.12) and (3.16), the attitude error model can be written as

$$\begin{bmatrix} \dot{\varepsilon}_x^{\ell 1} \\ \dot{\varepsilon}_y^{\ell 1} \\ \dot{\varepsilon}_z^{\ell 1} \end{bmatrix} = \begin{bmatrix} -\alpha_p & 0 & 0 \\ 0 & -\alpha_r & 0 \\ 0 & 0 & 0 \end{bmatrix} \begin{bmatrix} \varepsilon_x^{\ell 1} \\ \varepsilon_y^{\ell 1} \\ \varepsilon_z^{\ell 1} \end{bmatrix} + \begin{bmatrix} 0 \\ 0 \\ -1 \end{bmatrix} d_z + \begin{bmatrix} w_p \\ w_r \\ w_\psi \end{bmatrix} \tag{3.17}$$

The velocity error model can be obtained from Equation (A.6) as

$$\delta\dot{\mathbf{v}}^{\ell} = \mathbf{B}\delta\mathbf{v}^{\ell} - \mathbf{F}^{\ell}\boldsymbol{\varepsilon}^{\ell} + \mathbf{R}_b^{\ell}\mathbf{b} = \mathbf{B}\delta\mathbf{v}^{\ell} - \mathbf{R}_{\ell 1}^{\ell}\mathbf{F}^{\ell 1}\boldsymbol{\varepsilon}^{\ell 1} + \mathbf{R}_b^{\ell}\mathbf{b} \tag{3.18}$$

Finally, substituting Equations (3.14), (3.17) and (3.18) into Equation (A.6), the error model of RIMU (3A1G), see Equation (3.20), is obtained.

As mentioned above, in the LTP, the pitch and roll are modelled as first-order GM processes. Although the first-order GM models match the practical local terrain well, the error between the GM model and the actual local terrain still exists. This is because the GM model is obtained from the statistics of large local terrain data set (Kuchar 2001). For

a section of finite-length road, the local terrain and the GM model may be different. In this light, the error in local terrain modeling needs to be considered in the velocity error model, i.e. Equation (3.18). From Equation (3.18), it can be seen that if the error in local terrain modeling is $\delta\boldsymbol{\varepsilon}^{\ell 1}$, it will produce an acceleration error $\mathbf{R}_{\ell 1}^{\ell}\mathbf{F}^{\ell 1}\delta\boldsymbol{\varepsilon}^{\ell 1}$ in $\delta\dot{\mathbf{v}}^{\ell}$, and $\mathbf{R}_{\ell 1}^{\ell}\mathbf{F}^{\ell 1}\delta\boldsymbol{\varepsilon}^{\ell 1} \approx \mathbf{R}_{\ell 1}^{\ell}\begin{bmatrix} -g\eta_r & -g\eta_p & 0 \end{bmatrix}^T = \mathbf{R}_{\ell 1}^{\ell}\boldsymbol{\eta}_{pr}$, if $\delta\boldsymbol{\varepsilon}^{\ell 1} = \begin{bmatrix} \eta_p & \eta_r & 0 \end{bmatrix}^T = \boldsymbol{\eta}_{pr}$, where g is gravity acceleration, η_p and η_r are pitch and roll modeling errors (caused by error in the local terrain model, not by errors in estimating δp and δr), respectively. Since $\mathbf{R}_{\ell 1}^{\ell}\boldsymbol{\eta}_{pr}$ looks like an accelerometer bias or accelerometer measurement noise in Equation (3.18) (if accelerometer measurement noises are considered, as shown in Equation (A.6), and $\mathbf{R}_{\ell 1}^{\ell}\boldsymbol{\eta}_{pr} = \mathbf{R}_{b}^{\ell}(\mathbf{R}_{\ell 1}^{b}\boldsymbol{\eta}_{pr})$), in practice, this term can be combined into the accelerometer white noise or the accelerometer bias. This is implemented by setting the covariance of either the accelerometer white noise or the accelerometer bias to be slightly larger than its actual value in the Kalman filter of a GPS/RIMU (especially for high accuracy accelerometers). This can be seen as a compensation for the term $\mathbf{R}_{\ell 1}^{\ell}\boldsymbol{\eta}_{pr}$ which does not appear in the error model of the RIMU. Doing so obviates the need to model $\boldsymbol{\eta}_{pr}$, which is fortunate since modeling for $\boldsymbol{\eta}_{pr}$ is difficult.

3.1.3 Equation Summary for 3A1G Configuration

The navigation equations, which are summarized from Equations (3.9) and (A.1), are as follows

$$\begin{cases} \dot{\mathbf{r}}^{\ell} = \mathbf{D}^{-1}\mathbf{v}^{\ell} \\ \dot{\mathbf{v}}^{\ell} = \mathbf{R}_b^{\ell}\mathbf{f}^b - (2\boldsymbol{\Omega}_{ie}^{\ell} + \boldsymbol{\Omega}_{e\ell}^{\ell})\mathbf{v}^{\ell} + \mathbf{g}^{\ell} \\ \dot{\psi} = -\omega_{ibz}^b + \left(\dfrac{v_e \tan\phi}{N+h} + \omega_e \sin\phi\right) \\ \mathbf{R}_b^{\ell} = \mathbf{A}_z(\psi) \end{cases} \tag{3.19}$$

where ψ is azimuth, $\mathbf{A}_z(\psi)$ is a rotation matrix about the z-axis by angle ψ, and the other variables and parameters are defined in Equations (3.9) and (A.1).

The corresponding error model, which is summarized from Equations (3.14), (3.17), (3.18), and (A.6), is given by

$$\begin{bmatrix} \delta\dot{\mathbf{r}}^{\ell} \\ \delta\dot{\mathbf{v}}^{\ell} \\ \dot{\boldsymbol{\varepsilon}}^{\ell 1} \\ \dot{d}_z \\ \dot{\mathbf{b}} \end{bmatrix} = \begin{bmatrix} \mathbf{0}_{3\times3} & \mathbf{D}^{-1} & \mathbf{0}_{3\times3} & \mathbf{0}_{3\times1} & \mathbf{0}_{3\times3} \\ \mathbf{0}_{3\times3} & \mathbf{B} & -\mathbf{R}_{\ell 1}^{\ell}\mathbf{F}^{\ell 1} & \mathbf{0}_{3\times1} & \mathbf{R}_b^{\ell} \\ \mathbf{0}_{3\times3} & \mathbf{0}_{3\times3} & \boldsymbol{\Gamma}_{\varepsilon} & \mathbf{M}_d & \mathbf{0}_{3\times3} \\ \mathbf{0}_{1\times3} & \mathbf{0}_{1\times3} & \mathbf{0}_{1\times3} & -\alpha_d & \mathbf{0}_{1\times3} \\ \mathbf{0}_{3\times3} & \mathbf{0}_{3\times3} & \mathbf{0}_{3\times3} & \mathbf{0}_{3\times1} & -\boldsymbol{\Lambda} \end{bmatrix} \begin{bmatrix} \delta\mathbf{r}^{\ell} \\ \delta\mathbf{v}^{\ell} \\ \boldsymbol{\varepsilon}^{\ell 1} \\ d_z \\ \mathbf{b} \end{bmatrix} + \begin{bmatrix} \mathbf{0}_{3\times1} \\ \mathbf{R}_b^{\ell}\mathbf{W}_f \\ \mathbf{W}_{\varepsilon} \\ w_d \\ \mathbf{W}_b \end{bmatrix} \tag{3.20}$$

where $\mathbf{R}_{\ell 1}^{\ell} = \mathbf{A}_z(\psi)$, $\mathbf{F}^{\ell 1} = \mathbf{R}_b^{\ell 1}[\mathbf{f}^b \times]$ is a skew-symmetric matrix. $\boldsymbol{\Gamma}_{\varepsilon} = diag(-\alpha_p \quad -\alpha_r \quad 0)$, $\mathbf{M}_d = [0 \quad 0 \quad -1]^T$. Other variables and parameters are defined in Equations (3.14), (3.17), (3.18), and (A.6).

3.1.4 Mechanization and Error Model of 2A1G Configuration

In this configuration, there are two horizontal accelerometers and one vertical gyro. The acceleration and rotation information are therefore both incomplete, and the difference between the 2A1G and 3A1G configurations is that in the former the vertical specific force needs to be calculated.

Suppose the specific force can be expressed as $\mathbf{f}^{\ell} = [f_e \quad f_n \quad g + \delta f_u]^T$ in the local level frame (ℓ-frame), where g is gravity acceleration and δf_u is the vehicle's true vertical acceleration, f_e and f_n are specific forces in east and north, respectively. So in the body frame (b-frame), specific force can be expressed as

$$\mathbf{f}^b = \begin{bmatrix} f_x^b & f_y^b & f_z^b \end{bmatrix}^T = \mathbf{R}_{\ell}^b \mathbf{f}^{\ell} \tag{3.21}$$

Substituting $\mathbf{R}_{\ell}^b$, which can be obtained from Equation (3.1) with $\mathbf{R}_{\ell}^b = (\mathbf{R}_b^{\ell})^T$, into Equation (3.21) yields (Sun et al 2008)

$$\begin{aligned} f_z^b = {} & f_e(\cos\psi \sin r - \sin\psi \sin p \cos r) + f_n(-\sin\psi \sin r - \cos\psi \sin p \cos r) \\ & + g \cos p \cos r + \delta f_u \cos p \cos r \end{aligned} \tag{3.22}$$

Since pitch, roll and δf_u are generally small (most of δf_u is less than $g/10$ and behaves like noise), and in most vehicle navigation applications, f_e and f_n are much less than g, Equation (3.22) can be simplified as

$$f_z^b \approx g \cos p \cos r \tag{3.23}$$

Since the approximation error of Equation (3.23) is related to the local terrain, which is expressed as a first-order GM process, the approximation error of Equation (3.23) is therefore also expressed as a first-order GM process

$$\dot{b}_z = -\beta_z b_z + w_{fz} \tag{3.24}$$

where β_z is the inverse of the correlation time of b_z, w_{fz} is the driving noise of b_z.

Substituting Equation (3.23) into Equation (3.19), the navigation equations of 2A1G are obtained, which have the same form as Equation (3.19) except that the vertical

acceleration in the body frame needs to be calculated with Equation (3.23) and the best available estimates of the pitch p and roll r. Substituting Equation (3.24) into Equation (3.20), the corresponding error model of 2A1G is obtained, which has the same form as Equation (3.20) except for the vertical accelerometer bias term. Although the vertical accelerometer bias has the same expression in both 3A1G and 2A1G, it has different parameters or meanings in the two error models. In 3A1G, the bias model comes from the actual vertical accelerometer, but in 2A1G it comes from the vertical acceleration calculation error, which is related to the local terrain.

3.2 Comparison of Three Types of RIMU Mechanizations and Corresponding Error Models

In the following, the term "RIMU mechanization and corresponding error model" is simplified as "RIMU M&E equations", where "M&E" means "mechanization and error". In addition to the above LTP type of RIMU M&E equations obtained with the LTP method, there are other two types of RIMU M&E equations that are often used in practice. These two types of RIMU M&E equations are called dead reckoning (DR) type and full dimension (FD) type, respectively. The DR type is given in Xing & Gebre-Egziabher (2009), Iqbal et al (2008), and Rogers (1999), and the FD type is given in Nui et al (2007b). Since the main differences among the three types of M&E equations are in their error models, the comparison among them is made primarily in this context. In order to compare all three types of RIMU M&E equations (LTP, DR and FD), the DR and FD type mechanizations and their corresponding error models are introduced first. In the following, for the sake of convenience, the three types of RIMU M&E equations are termed as LTP, DR, and FD M&E equations.

3.2.1 DR Mechanization and Corresponding Error Model

The DR method is generally used in 2A1G case or an odometer plus a vertical gyro case (Xing & Gebre-Egziabher 2009; Iqbal et al 2008; Farrell & Barth 1999). In order to completely compare the three types of M&E equations, not only the DR M&E equations for 2A1G but also those for 3A1G are given in here. In the DR method, the pitch and roll are assumed to be zero in both the mechanization equations and error model of an RIMU (Xing & Gebre-Egziabher 2009; Iqbal et al 2008). Accordingly, the DR mechanization equations used in this chapter are obtained as Equation (3.19), and for 3A1G, the vertical specific force f_z^b comes from the vertical accelerometer measurement; for 2A1G, $f_z^b = g$. These DR mechanization equations are slightly different from the traditional mechanization equations of a DR system (Xing & Gebre-Egziabher 2009; Farrell & Barth 1999). For example, Equation (3.19) will become the traditional mechanization equations of a DR system (2A1G) (Xing & Gebre-Egziabher 2009; Farrell & Barth 1999) if the following three modifications for Equation (3.19) are made: first the terms $(2\boldsymbol{\Omega}_{ie}^{\ell} + \boldsymbol{\Omega}_{e\ell}^{\ell})\mathbf{v}^{\ell}$, $\mathbf{g}^{\ell}$, and $\left(\frac{v_e \tan\phi}{N+h} + \omega_e \sin\phi\right)$ are removed from Equation (3.19); second, the matrix $\mathbf{D}^{-1}$ of Equation (3.19) is assumed to be a unit matrix; and finally the height, vertical velocity, and acceleration are not considered in Equation (3.19).

The corresponding error model for 2A1G can be obtained from Equation (3.20). From this equation, velocity error can be written as

$$\delta\dot{\mathbf{v}}^{\ell} = \mathbf{B}\delta\mathbf{v}^{\ell} + \mathbf{R}_b^{\ell}(\mathbf{b} - \mathbf{R}_{\ell 1}^{b}\mathbf{F}^{\ell 1}\boldsymbol{\varepsilon}^{\ell 1}) + \mathbf{R}_b^{\ell}\mathbf{W}_f \tag{3.25}$$

Integrating Equation (3.16) and assuming that both sides have same initial values yield

$$\boldsymbol{\varepsilon}^{\ell 1} = \begin{bmatrix} -p \\ -r \\ -\delta\psi \end{bmatrix} = \begin{bmatrix} -p \\ -r \\ 0 \end{bmatrix} + \begin{bmatrix} 0 \\ 0 \\ -\delta\psi \end{bmatrix} = \boldsymbol{\theta}_{pr} + \boldsymbol{\theta}_{\psi} \tag{3.26}$$

where $\boldsymbol{\theta}_{pr} = \begin{bmatrix} -p & -r & 0 \end{bmatrix}^T$, $\boldsymbol{\theta}_{\psi} = \begin{bmatrix} 0 & 0 & -\delta\psi \end{bmatrix}^T$. Substituting Equation (3.26) into the term $\mathbf{R}_{\ell 1}^{b}\mathbf{F}^{\ell 1}\boldsymbol{\varepsilon}^{\ell 1}$ of Equation (3.25) yields

$$\mathbf{R}_{\ell 1}^{b}\mathbf{F}^{\ell 1}\boldsymbol{\varepsilon}^{\ell 1} = \mathbf{F}^{b}\boldsymbol{\varepsilon}^{\ell 1} = \mathbf{F}^{b}\boldsymbol{\theta}_{pr} + \mathbf{F}_{xy}^{b}\delta\psi \tag{3.27}$$

where $\mathbf{F}^{b} = \left[\mathbf{f}^{b}\times\right]$, $\mathbf{f}^{b} = \begin{bmatrix} f_x^b & f_y^b & f_z^b \end{bmatrix}^T$, and $\mathbf{F}_{xy}^{b} = \begin{bmatrix} -f_y^b & f_x^b & 0 \end{bmatrix}^T$. Substituting Equation (3.27) into Equation (3.25) yields

$$\delta\dot{\mathbf{v}}^{\ell} = \mathbf{B}\delta\mathbf{v}^{\ell} - \mathbf{R}_{b}^{\ell}\mathbf{F}_{xy}^{b}\delta\psi + \mathbf{R}_{b}^{\ell}\mathbf{b}_{com} + \mathbf{R}_{b}^{\ell}\mathbf{W}_{f} \tag{3.28}$$

where $\mathbf{b}_{com}$ is

$$\mathbf{b}_{com} = \mathbf{b} - \mathbf{F}^{b}\boldsymbol{\theta}_{pr}. \tag{3.29}$$

From Equation (3.29), it can be seen that the effect of the local terrain (pitch and roll) on the velocity error is combined into the accelerometer bias. The new accelerometer bias $\mathbf{b}_{com}$ effectively contains both the true accelerometer bias and the effect of the local terrain.

Finally, the corresponding error model for 2A1G is expressed as

$$\begin{bmatrix} \delta\dot{\mathbf{r}}^{\ell} \\ \delta\dot{\mathbf{v}}^{\ell} \\ \delta\dot{\psi} \\ \dot{d}_z \\ \dot{\mathbf{b}}_{com} \end{bmatrix} = \begin{bmatrix} \mathbf{0}_{3\times3} & \mathbf{D}^{-1} & \mathbf{0}_{3\times1} & \mathbf{0}_{3\times1} & \mathbf{0}_{3\times3} \\ \mathbf{0}_{3\times3} & \mathbf{B} & -\mathbf{R}_b^{\ell}\mathbf{F}_{xy}^{b} & \mathbf{0}_{3\times1} & \mathbf{R}_b^{\ell} \\ \mathbf{0}_{1\times3} & \mathbf{0}_{1\times3} & \mathbf{0}_{1\times1} & 1 & \mathbf{0}_{1\times3} \\ \mathbf{0}_{1\times3} & \mathbf{0}_{1\times3} & \mathbf{0}_{1\times1} & -\alpha_d & \mathbf{0}_{1\times3} \\ \mathbf{0}_{3\times3} & \mathbf{0}_{3\times3} & \mathbf{0}_{3\times1} & \mathbf{0}_{3\times1} & -\mathbf{\Lambda}_{com} \end{bmatrix} \begin{bmatrix} \delta\mathbf{r}^{\ell} \\ \delta\mathbf{v}^{\ell} \\ \delta\psi \\ d_z \\ \mathbf{b}_{com} \end{bmatrix} + \begin{bmatrix} \mathbf{0}_{3\times1} \\ \mathbf{R}_b^{\ell}\mathbf{W}_f \\ w_{\psi} \\ w_d \\ \mathbf{W}_{bcom} \end{bmatrix} \tag{3.30}$$

where $\mathbf{\Lambda}_{com} = diag(\beta_{comx} \;\; \beta_{comy} \;\; \beta_{comz})$ are the inverse of the correlation times of $\mathbf{b}_{com}$, and $\mathbf{W}_{bcom}$ are driving noises of $\mathbf{b}_{com}$ (assumed to be first-order GM processes). Combining the effect of the local terrain into the accelerometer bias term is reasonable because both of them can be expressed as a first-order GM process, but with different correlation times. Because of the different correlation time, modeling for the composite bias is difficult. Combining the local terrain into the accelerometer bias means that in the Kalman filter of a GPS/RIMU, if the variance of the accelerometer bias is chosen as larger than its actual value, the effect of the local terrain will likely be absorbed in the accelerometer bias term. In Equation (3.30), the position error, velocity error and accelerometer bias each have three dimensions (3D). This is because the vertical errors (position, velocity, and acceleration) caused by the local terrain is considered in the error model. For 3A1G, its corresponding error mode has the same form as Equation (3.30) except that its vertical accelerometer bias model only comes from the vertical accelerometer error characteristics with no contribution from the local terrain.

3.2.2 FD Mechanization and Corresponding Error Model

The FD type of mechanization equations and corresponding error model are given in Nui et al (2007b), and have the same form as those of a full IMU (see Appendix A), as the name implies. The differences in mechanization between an RIMU and a full IMU are their input signals. In a full IMU, all the input signals for the mechanization equations are

real signals obtained from actual accelerometers and gyros. But in an RIMU, such as in a 2A1G, the measurements of the rotation rates around two horizontal axes are supposed to be zero, and the measurement of the specific force in vertical direction is supposed to be gravity acceleration (i.e. g). This is because there are no horizontal gyros and vertical accelerometer. In their corresponding error models, all the senor error models of the full IMU comes from actual sensors, whereas some senor error models of the 2A1G are fictitious. For example, the error models for two horizontal gyros and one vertical accelerometer are chosen as a Gaussian white noise with large variance value (Nui et al 2007b). For 3A1G case, both the vertical specific force measurement and vertical accelerometer error model come from the actual vertical accelerometer.

3.2.3 Comparison of Three Types of Mechanizations and Corresponding Error Models

All three sets of mechanization equations come from the full IMU equations based on the assumption that the pitch and roll are zero. And the DR and LTP mechanization equations are the simplified form of FD equations. Correspondingly, all three sets of equations are very similar. The only difference between the LTP mechanization and the other two mechanizations is that in LTP mechanization, the vertical specific force is $\hat{f}_z^b = g\cos\hat{p}\cos\hat{r}$, as shown in Equation (3.23), whereas in the DR and FD equations, $\hat{f}_z^b = g$.

In contrast, the three error models show some important differences. The main characteristics for each are summarized below.

The key characteristics of the DR error model are:

- It has 11 states (three position errors, three velocity errors, one azimuth error, one vertical gyro drift, and three accelerometer biases).
- The effect of the local terrain (pitch and roll) on velocity error is combined into horizontal accelerometer biases.
- As a result of the previous point, modeling of the composite bias is difficult since the actual accelerometer bias and the local terrain have different correlation times.
- It has strong constraints on horizontal attitude error (i.e. pitch and roll are chosen as zero). This may degrade the performance of a GPS/RIMU when the composite bias cannot be modeled properly (since its modeling is difficult, as discussed above).

The key characteristics of the LTP error model are:

- It has 13 states (three position errors, three velocity errors, three attitude errors, one vertical gyro drift, and three accelerometer biases).
- Local terrain model (pitch and roll) is introduced into the RIMU error model and used to compensate the velocity error, thus improving performance.
- Every variable in the error model has a clear concept. In particular, from the LTP model, it can be seen clearly that the horizontal attitude error is roughly equal to the pitch and roll, and the azimuth error is affected by the local terrain.
- Factors related to unmodeled errors/noises are clear, and it is relatively easy to determine the covariance of process noise. In particular, the noise in the azimuth error equation is related to the local terrain, as shown in Equation (3.12), and its variance calculation needs to consider the local terrain factor.

- It has reasonable constraints (i.e. with local terrain) on horizontal attitude error which is roughly equal to the pitch and roll.

The key characteristics of the FD error model are:

- It has 15 states (three position errors, three velocity errors, three attitude errors, three gyro drifts, and three accelerometer biases).
- The modeling of horizontal attitude errors is not reasonable. Since the rotation rates around two horizontal axes are modeled as white noise with large variances, the horizontal attitude error is effectively a random walk, not a first-order GM process. Owing to the fact that the variance of a random walk process can become infinite as time approaches infinity (Gelb 1974), the variances of the horizontal attitude errors can become very large with time increasing (in a quarter of a Schuler period). This means that although the actual horizontal attitude error may be only few degrees (for pitch and roll), the RIMU error model is able to give unreasonably large estimates of pitch and roll. From this point, the modeling for horizontal attitude error is considered unreasonable.
- It has no constraints (from local terrain or environment) on horizontal attitude errors, just like in a full IMU (for a full IMU, generally its horizontal attitude error reaches the maximum value in a quarter of a Schuler period (Farrell & Barth 1999)). And the variances of the measurement noises for horizontal rotation rates are chosen to be on the order of a few deg/s. This may degrade the performance of a GPS/RIMU.

3.3 Field Vehicle Test

In order to evaluate the above algorithms, a field vehicle test was conducted in a suburban area of Calgary, Alberta in October 2007. Data from the field test was collected and stored for post-mission processing. Details regarding the test are given below.

3.3.1 Test Setup, Route Selection, and Data Collection

Two grades of IMUs were used during the test: a tactical-grade IMU (Honeywell HG1700 AG11, or simply "HG1700") and a micro-electro-mechanical system (MEMS)-grade IMU (Crista IMU). For the HG1700 IMU, the gyro drift is 1 deg/h and the accelerometer bias is 1 milli-g (NovAtel 2009; Petovello 2003). For the Crista IMU, the gyro turn on drift is 2000-5000 deg/h, noise is 200-300 deg/h/$\sqrt{\text{Hz}}$, and the accelerometer turn on bias and noise are 0.3-0.5 m/s^2 and 0.003-0.004 g/$\sqrt{\text{Hz}}$, respectively (CCT 2006; Godha 2006). Data from both IMUs was logged at a rate of 100 Hz. A NovAtel SPAN system was used to log GPS pseudorange, Doppler shift and carrier phase measurements at a rate of 1 Hz, and for HG1700 IMU data collection (NovAtel 2009). The Crista IMU data was time tagged using the pulse-per-second (PPS) signal of the SPAN system's GPS receiver, and logged to a computer. The time tagging was implemented as follows: the PPS signal was fed into the Crista IMU which then reported its time relative to the last PPS received. The remaining one second ambiguity is then easily determined in post-mission. GPS intermediate frequency (IF) data was collected with an IF data collection system consisting of a NovAtel Euro-3M card. An oven controlled crystal oscillator (OCXO), namely a Symmetricom 1000B, was used to

drive the front-end. The key specifications of the OCXO are: frequency: 5 MHz, short term stability: $<1.0\times10^{-12}$, ageing per day: $<1.0\times10^{-10}$ (Symmetricom 2007).

Figure 3.1 is the vehicle test setup. In this figure, antenna A is for GPS IF data collection, and antenna B is for NovAtel SPAN system. Figure 3.2 is data collection block diagram. The left panel of this figure is for IMU and GPS raw data collection (i.e. pseudorange, Doppler shift and carrier phase). Data collected from this block was used for reference solution generation and RIMU mechanization research. The right panel in Figure 3.2 is for IF data collection. The collected IF data, as well as the IMU data collected in the left panel, is used for TLA and UT GPS/RIMU integration research (with a software GPS receiver), which will be conducted in the following chapters. In this field test, two test routes were selected for data collection, as shown in Figure 3.3 and Figure 3.4. Figure 3.3 is the route map of the open sky test. Figure 3.4 is the route map of the foliage test. Actually, the environment of the open sky test is a mostly open sky with a few periods containing foliage.

The open sky test lasted more than 20 minutes and was used for all the evaluations in this dissertation. The foliage route lasted about 14 minutes and was only used for TLA and UT GPS/RIMU integration research. A GPS base station was used in this test for differential GPS (DGPS) purposes.

Figure 3.1 Vehicle Test Setup

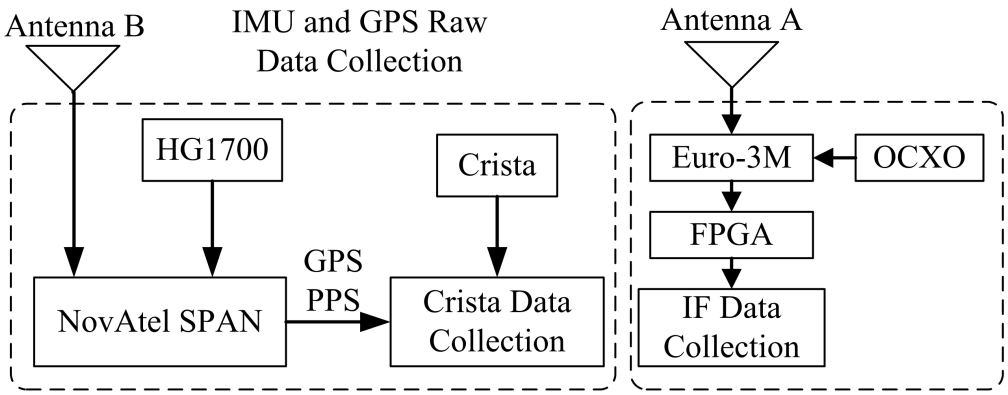

Figure 3.2 Data Collection Block Diagram

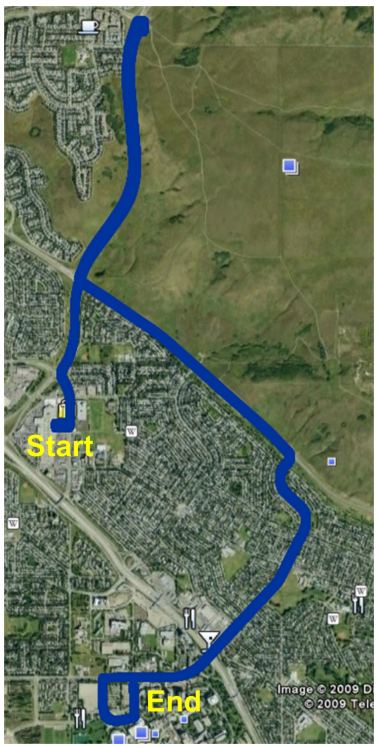

Figure 3.3 Route Map of Open Sky Test

Figure 3.4 Route Map of Foliage Test

3.3.2 GPS Availability, Test Trajectory, and Reference Velocity and Attitude

Only the open sky test route is used for the RIMU mechanization work presented in this chapter. The test route is divided into two sections: section A, whose environment is near open sky case, and section B, whose environment contains a bit of foliage (see Figure 3.4).

The GPS availability of the open sky test is shown in Figure 3.5. From this figure, it can be seen that in section A, in most cases, the number of tracked GPS satellites is seven or eight. Only during a few very short periods does the number of tracked satellites (or space vehicles – SVs) drop below seven. As such, it is concluded that there are no naturally occurring GPS outages in section A. In contrast to section A, in section B there are a few periods in which the number of tracked satellites is less than four, and sometimes there are only one or two tracked satellites. In other words, there are clearly naturally occurring GPS outages in section B. Generally, if there are only 1-3 tracked satellites, the outage is called partial GPS outage and if there are no satellites tracked, the outage called complete outage (Greenspan 1996).

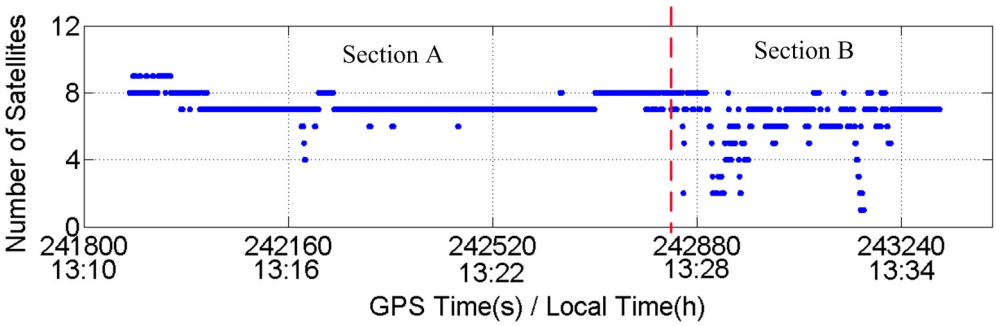

Figure 3.5 Number of Tracked Satellites in Open Sky Test

The trajectory of the open sky test is shown in Figure 3.6. This figure shows that the distance change in the south-north direction is about 5 km and about 2 km in the east-west direction. The vertical variation is more than 100 m. Figure 3.7 shows the velocity profile with the maximum horizontal velocity being about 25 m/s and the maximum vertical velocity being less than 2 m/s. The reference attitude solution is shown in Figure 3.8. As expected, the azimuth solution roughly shows the orientation of the road on which the vehicle moves. In contrast, pitch and roll generally show the slope of the road (some vehicle-specific attitude variations are also included, but these are expected to be small compared to the terrain variations and have relatively short duration). In the open sky test, the pitch and roll mostly range between -3 and 3 degrees. The maximum absolute pitch and roll are 4 and 5 degrees, respectively. The root mean square (RMS) of the pitch and roll for the entire test are both 2.1 degrees. For section A, the pitch and roll RMS is 2.2 degrees and 2.0 degrees, respectively. In the following discussions, the term "local terrain" will mean pitch and roll variations only (not azimuth).

The reference solution was obtained using a differential GPS solution integrated with the HG1700 IMU. It is assumed that the reference solution has a similar accuracy level with that in Godha (2006), which is also generated using a DGPS/HG1700 IMU system: the RMS of the position error of the reference solution in each direction is about 0.23 m, the RMS of velocity accuracy 0.015 m/s in each direction, and the RMS of attitude accuracy is 0.03 degrees in pitch and roll and 0.17 degrees in azimuth.

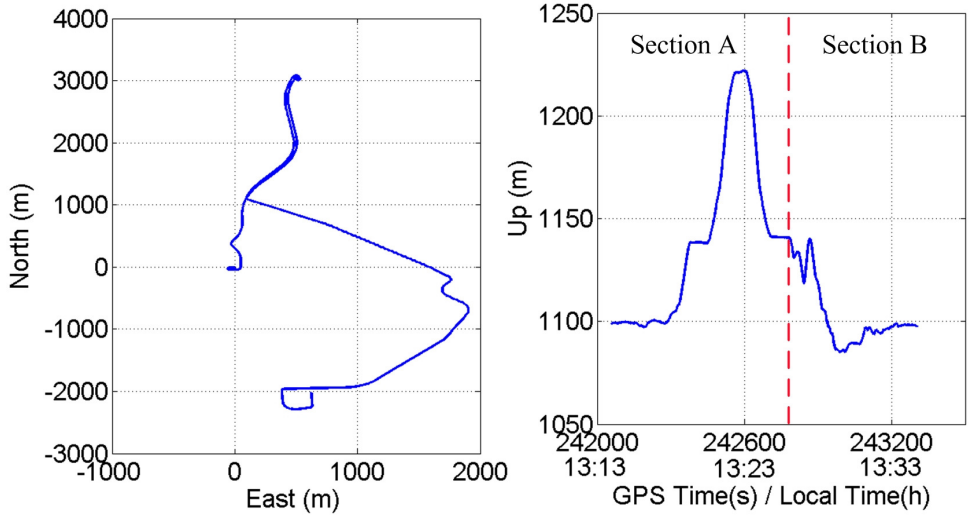

Figure 3.6 Trajectory of Open Sky Test

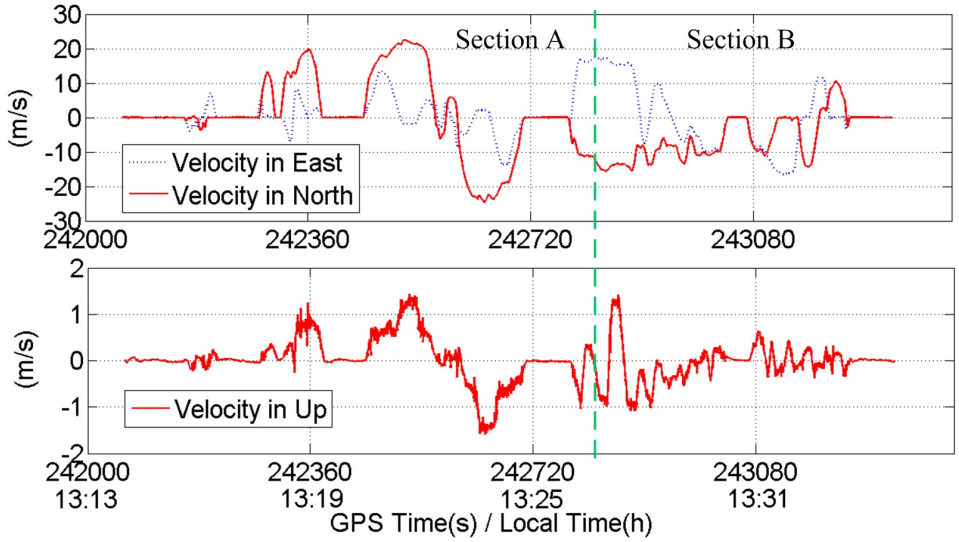

Figure 3.7 Reference Velocity of Open Sky Test

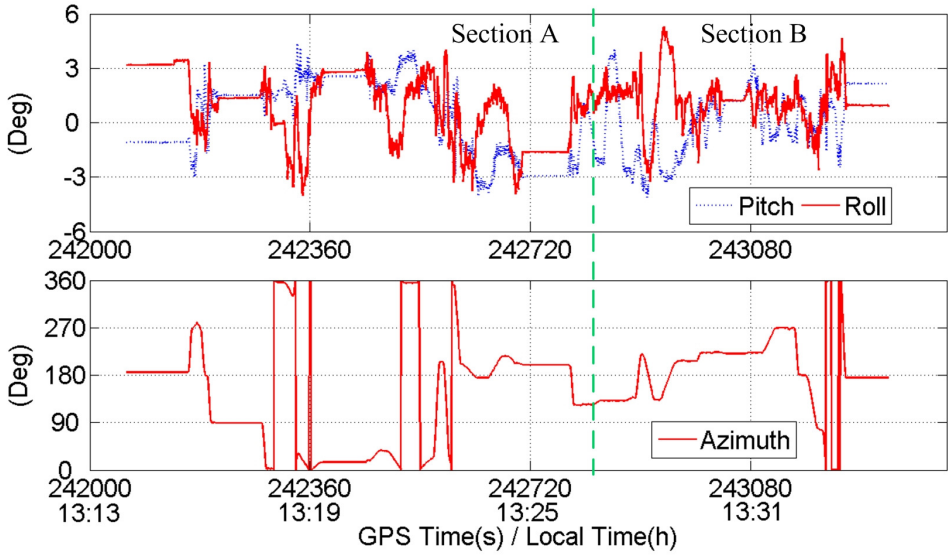

Figure 3.8 Reference Pitch, Roll and Azimuth of Open Sky Test

3.4 Data Processing

The data processing strategy is shown in Figure 3.9. A loose integration strategy was adopted to simplify development and to assess algorithm performance. In loose integration, an extended Kalman filter was used, as discussed in Chapter Two. In each reduced IMU configuration (details below), both the tactical and MEMS-grade IMUs were used. The GPS-only solution was obtained with GPS solution software (C³NAVG²™) developed in the PLAN group at the University of Calgary. The GPS measurement update rate of the Kalman filter was 1 Hz and the integrated solution output rate was 10 Hz. For assessing the benefit of the GPS/RIMU with an LTP, in order to simplify analysis, only route section A (near open sky case) was used. However, for comparing the three types of RIMU M&E equations, in order to give a complete and fair result, both sections A and B were used. For the sake of simplicity, only the MEMS IMU was used for the comparison.

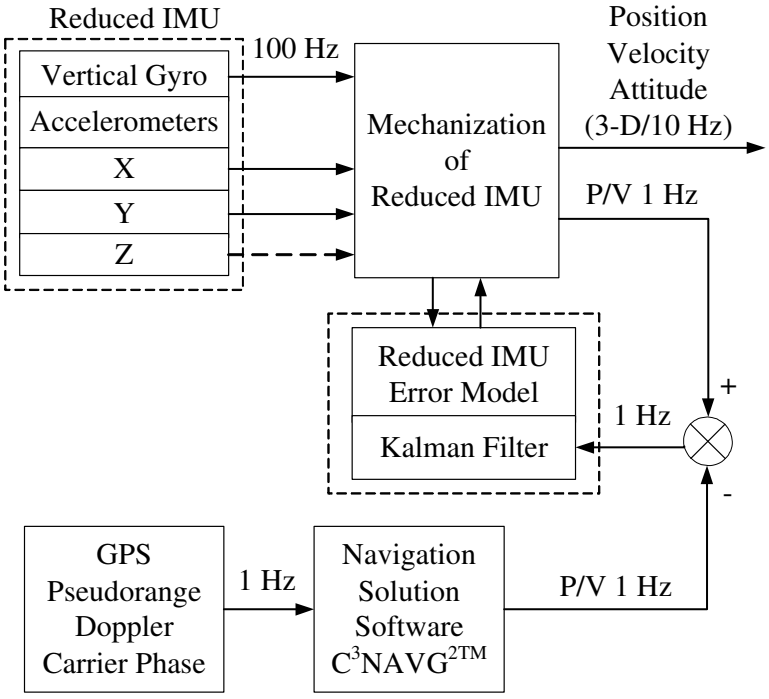

Figure 3.9 Data Processing Block Diagram

3.5 Evaluation of GPS/RIMU with an LTP

In order to verify the LTP method and to evaluate the performance of the GPS/RIMU with an LTP, a series of tests were performed using different IMU configurations. In particular, both RIMU configurations (3A1G and 2A1G) were tested using each grade of IMU (tactical and MEMS), for a total of four combinations. All RIMUs are integrated with GPS using a loose coupling strategy. In the following test, the correlation times of the first-order GM models for pitch and roll are chosen as 10 s, and the variance of the driving noise was chosen as $2\alpha_p\sigma_p^2$ (or $2\alpha_r\sigma_r^2$ for roll), where α_p is the inverse of correlation time and σ_p^2 is the variance of the pitch.

3.5.1 GPS/3A1G Integration

Figure 3.10 shows the velocity and attitude errors of GPS/3A1G (HG1700) with LTP, and Figure 3.11 is the velocity and attitude errors of GPS/3A1G (Crista) with LTP. Statistics from the two figures are shown in Table 3.1 and it can be seen that the RMS of the pitch and roll errors for both the HG1700 and Crista IMU are less than 0.8 degrees from the actual local terrain values, i.e. the pitch and roll RMS are 2.2 degrees and 2.0 degrees, respectively. This means that the LTP can help to estimate the pitch and roll, suggesting the model is valid in the GPS/3A1G case. Furthermore, comparing the performance of the HG1700 and Crista IMUs from Table 3.1, it can be seen that the lower grade IMU (Crista) has poorer performance. The azimuth error using the Crista is near twice that when using the HG1700. Azimuth accuracy is affected by the grade of the IMU since the azimuth is calculated from the vertical gyro measurement. But the difference in the pitch and roll errors between the two systems is comparatively small. With the HG1700 IMU, the pitch and roll errors are only reduced about 20% compared to the Crista IMU. This is because the pitch and roll are affected less by the grade of the IMU since they are computed primarily from the terrain model, which is the same in both cases. The east and north velocity errors of the two systems are the same. This may be explained with the following two possible reasons: the first is that because the Crista IMU has lower pitch and roll estimation accuracy, some of its pitch and roll information is “estimated out” in its horizontal accelerometer biases, as discussed in Sun et al (2008). The second is that the pitch and roll estimation accuracy difference between the two grade IMUs is too small to result in an obvious difference in east and north velocity estimation. So the total effect from the Crista IMU on horizontal velocity is the same or

almost same with that from the HG1700. In contrast, the vertical velocity error is affected by the grade of the IMU since the vertical velocity is calculated from the vertical accelerometer measurement. Finally, from Figure 3.10 and Figure 3.11, it can be seen that the velocity error is related to the attitude error, especially to the pitch and roll errors. Specifically, when pitch and/or roll have large errors, the velocity error increases.

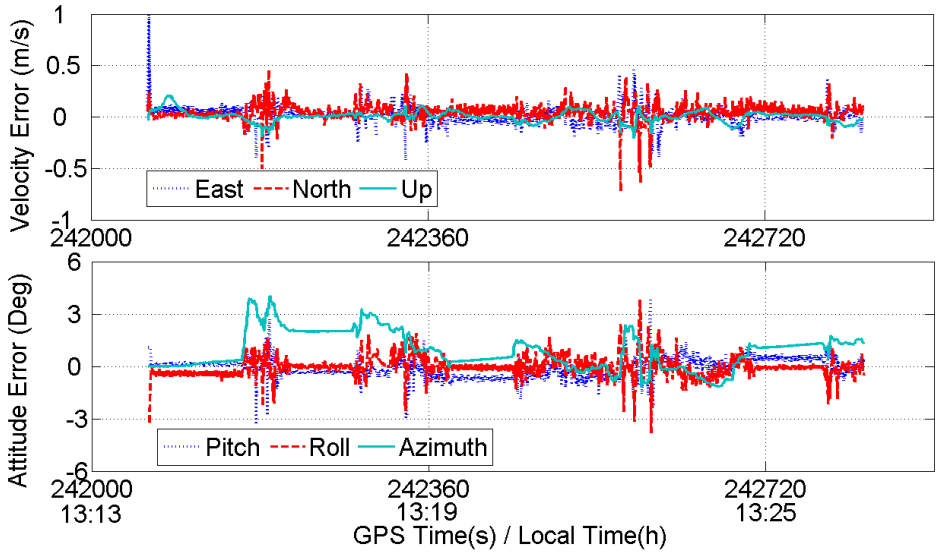

Figure 3.10 Velocity and Attitude Errors of GPS/3A1G (HG1700) with LTP

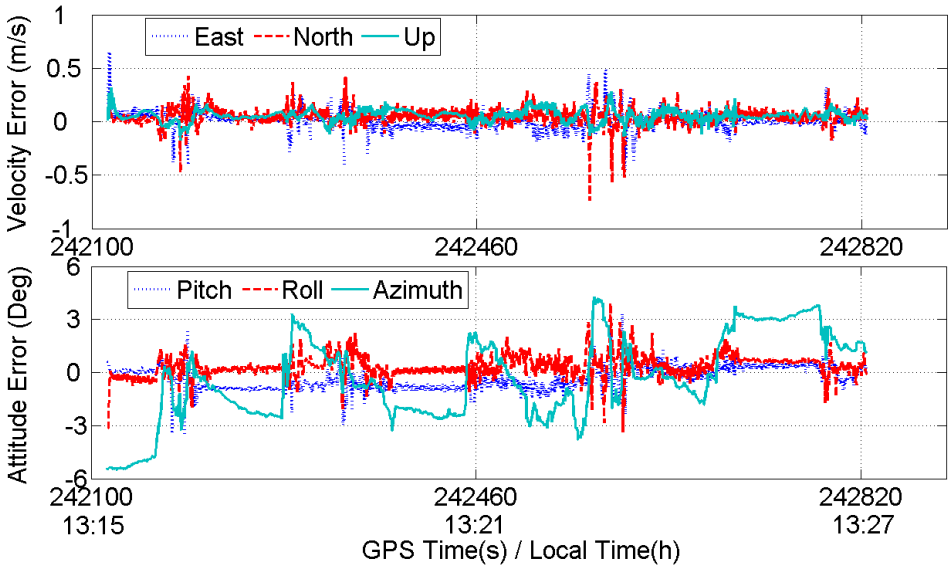

Figure 3.11 Velocity and Attitude Errors of GPS/3A1G (Crista) with LTP

Table 3.1 Attitude and Velocity Error Statistics of GPS/3A1G with LTP

Reduced IMU	RMS Attitude Error (Deg)			RMS Velocity Error (m/s)		
	Pitch	Roll	Azimuth	East	North	Up
3A1G (HG1700)	0.57	0.58	1.38	0.08	0.08	0.05
3A1G (Crista)	0.72	0.70	2.38	0.08	0.08	0.08

3.5.2 GPS/2A1G Integration

As before, both HG1700 and Crista IMU were used in this configuration. The test results for both IMUs are shown in Figure 3.12 and Figure 3.13, respectively. The statistics of test results for both IMUs are listed in Table 3.2.

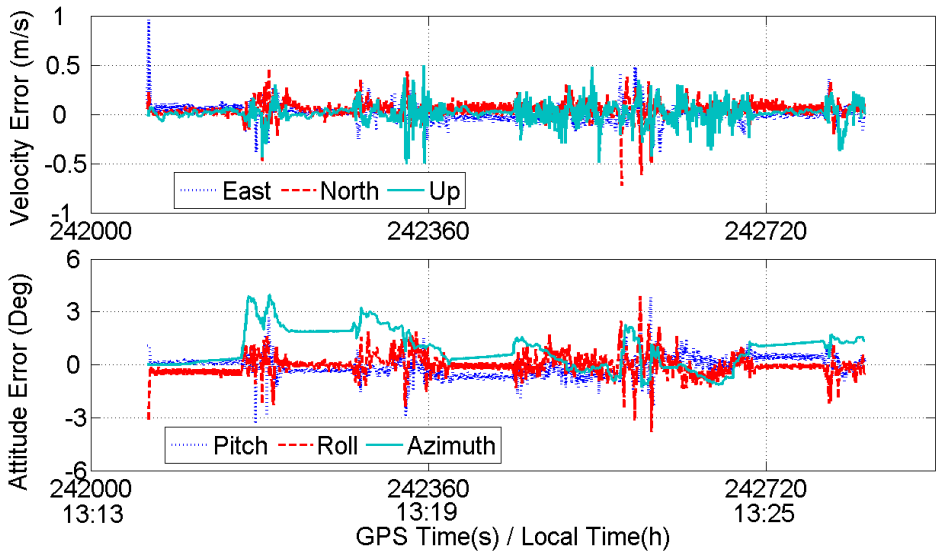

Figure 3.12 Velocity and Attitude Errors of GPS/2A1G (HG1700) with LTP

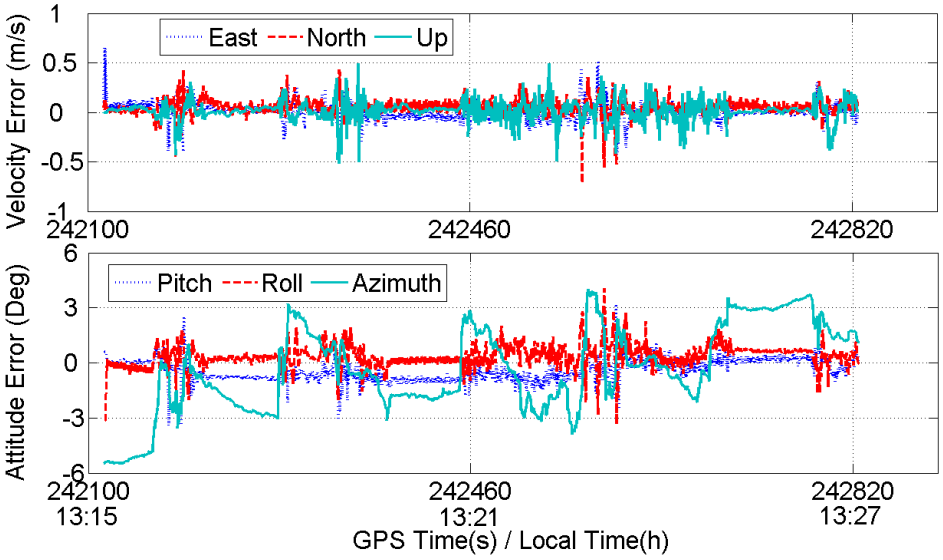

Figure 3.13 Velocity and Attitude Errors of GPS/2A1G (Crista) with LTP

Table 3.2 Attitude and Velocity Error Statistics of GPS/2A1G with LTP

Reduced IMU	RMS Attitude Error (Deg)			RMS Velocity Error (m/s)		
	Pitch	Roll	Azimuth	East	North	Up
2A1G (HG1700)	0.57	0.59	1.35	0.08	0.08	0.09
2A1G (Crista)	0.71	0.70	2.38	0.08	0.08	0.09

From the statistics, it can be seen that the pitch and roll RMS errors for both the HG1700 and Crista IMUs are reduced greatly from the local terrain variation, just as in GPS/3A1G case. This suggests that the LTP is valid in the GPS/2A1G case as well. Further, from Table 3.2, it can be seen that the Crista RIMU has larger attitude errors than the HG1700 RIMU, as expected. As with the 3A1G configuration, the azimuth error of the GPS/2A1G (Crista) is almost twice that of the GPS/2A1G (HG1700) and the pitch and roll errors of the HG1700 IMU are only reduced about 20% compared to the Crista IMU for the same reasons as before. From Table 3.2, it also can be seen that the two grades of IMUs have the same velocity error. For the east and north velocity errors, the reason for this result is the same as with the 3A1G configuration. But for the vertical velocity error, the reason is that the vertical accelerations for both grades of IMUs are calculated from the same formula as in the 2A1G configuration, which has no vertical accelerometer (and thus is not a function of IMU quality). Finally, from Figure 3.12 and Figure 3.13, it can be seen that velocity error is related to attitude error, as in the 3A1G configuration.

For both 3A1G and 2A1G configurations, if the pitch and roll values of the GPS/RIMU were fixed to zero (i.e. no LTP) (just like the DR error model when the effect of the local terrain on the velocity error is not considered in the accelerometer bias), the velocity error increases greatly, especially for horizontal velocities, and so does the azimuth error, as shown in Table 3.3. Comparing this table with Table 3.1 and Table 3.2, it can be seen that the LTP can reduce the 3D RMS velocity error by more than 80 % for both 3A1G and 2A1G. This means the LTP method is valid.

Through the comparison of GPS/3A1G and GPS/2A1G, two conclusions are obtained (Sun et al 2008). First, the two configurations (3A1G and 2A1G) have almost the same attitude result for a given grade of IMU. Second, the horizontal velocity errors are not affected by the configuration or the vertical accelerometer, only the vertical velocity error is affected by the configuration. When the tradeoff between cost and performance is considered, the 2A1G configuration may be a reasonable choice for vehicular applications.

Table 3.3 Attitude and Velocity Error Statistics of GPS/RIMU (Crista) without LTP

Reduced IMU	RMS Attitude Error (Deg)			RMS Velocity Error (m/s)		
	Pitch	Roll	Azimuth	East	North	Up
3A1G (Crista)	2.17	1.99	15.90	0.69	0.74	0.13
2A1G (Crista)	2.17	1.99	15.90	0.69	0.74	0.09

3.5.3 GPS Outage Test

To assess the performance of the GPS/RIMU system with an LTP during a GPS outage, a series of GPS outage tests were conducted. In the outage tests, both grades of IMUs and both RIMU configurations were used. Ten 30 s long GPS outages (complete) were simulated in the data by artificially omitting the satellites during post-mission processing. These outages were carefully selected to represent varying vehicle dynamics, including stops, periods of acceleration/deceleration, and constant velocity.

During an outage, the "GPS/RIMU with LTP" approach assumes that the pitch and roll estimates are almost constant values (they vary slightly because of the first-order GM process model with long correlation time (500 s) used). In contrast, the "GPS/RIMU

without an LTP" assumes that the pitch and roll estimates are zero during GPS outage. In the tests, the RMS of position or velocity error is calculated from the following equation

$$RMS(t_i) = \sqrt{\frac{1}{10}\sum_{j=1}^{10}\left(x_j(t_i) - x_r(t_i)\right)^2} \tag{3.31}$$

where t_i is GPS outage duration (from 0 to 30 s), $x_j(t_i)$ is the output (position or velocity) of reduced IMU in the *j*th GPS outage at t_i and $x_r(t_i)$ is the reference solution at t_i.

Results of the MEMS IMU are shown in Figure 3.14 and Figure 3.15 (the tactical IMU has similar results and are therefore not shown). Figure 3.14 shows the horizontal position and velocity errors of two configurations of GPS/RIMU (Crista) with and without an LTP. Figure 3.15 shows the corresponding vertical position and velocity errors. For the vertical position, since the GPS/RIMU has a larger bias (about 4 m) from standalone GPS compared to the reference solution, in order to facilitate the analysis this bias is removed when calculating the RMS of the vertical position error with Equation (3.31). From Figure 3.14 and Figure 3.15, it can be seen that the position and velocity RMS errors are a function of time since the last GPS measurement. Furthermore, Figure 3.14 shows that for the Crista IMU under both configurations, both the horizontal position and velocity error of the GPS/RIMU with an LTP are about half those of the GPS/RIMU without an LTP, respectively. Figure 3.15 shows that both the vertical position and velocity error are reduced only marginally or remain at the same level when an LTP is applied.

In order to facilitate the comparison, the RMS position errors at the end of the GPS outage are summarized in Table 3.4. From this table, it can be seen that, for the GPS/RIMU without an LTP, the horizontal position errors for different grades of IMU (HG1700 and Crista) and different RIMU configurations (3A1G and 2A1G) are almost the same and range from 219 to 223 m. This is consistent with the earlier analysis: the horizontal position error is mainly determined by the local terrain when there is no LTP used during GPS outage. With an LTP, the horizontal position errors for different IMU grades and different configurations are greatly reduced, as shown in Table 3.4. From this table, it can be seen that with an LTP, even though the grade and configuration of the RIMUs are different, they have similar results. Specifically, the RMSs of the horizontal position errors for all IMUs and configurations are almost the same (from 103 to 104 m), which is less than half the error without an LTP. Like the position errors, the horizontal velocity errors of the GPS/ RIMU with an LTP are also reduced, and the extent of the reduction for both position and velocity errors is similar (in terms of percentage), as shown in Figure 3.14. For the vertical position error, Table 3.4 shows that it is reduced only slightly, if at all, with an LTP for all the IMUs and configurations. The vertical velocity error is similarly reduced, as shown in Figure 3.15. A detailed analysis for these results is given in Sun et al (2008). All these test results show that the LTP is valid during a GPS outage.

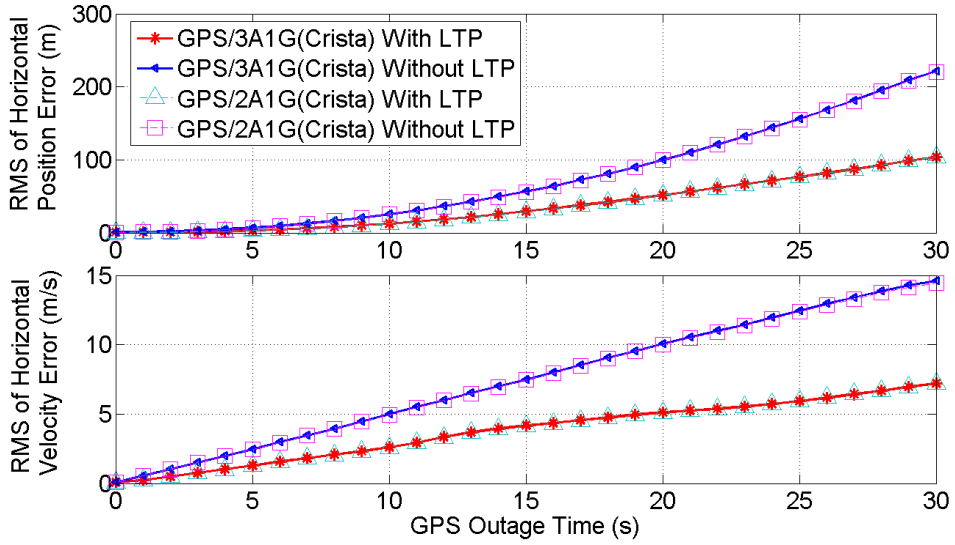

Figure 3.14 Horizontal Position and Velocity Error Comparison between GPS/RIMU (Crista) with and without LTP

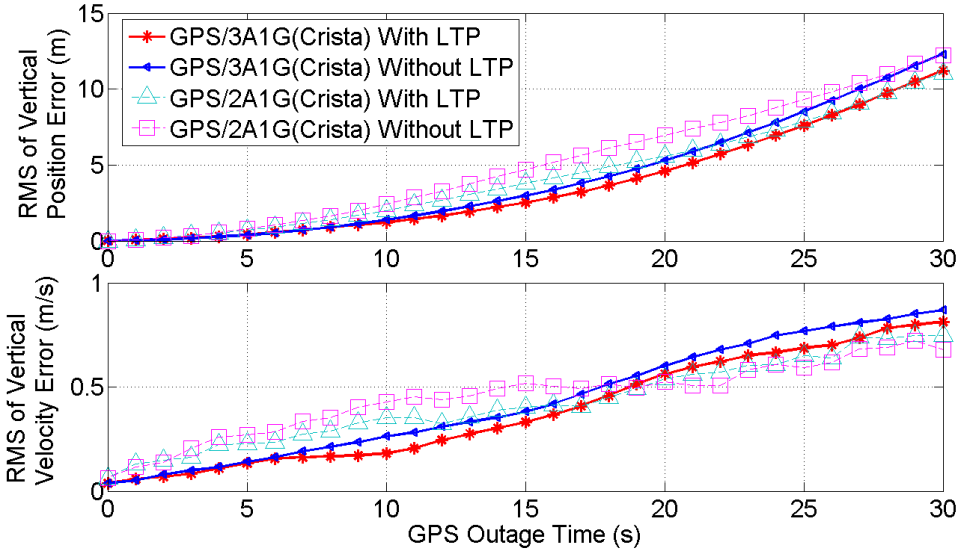

Figure 3.15 Vertical Position and Velocity Error Comparison between GPS/RIMU (Crista) with and without LTP

Table 3.4 Horizontal and Vertical Position Error Comparison between GPS/RIMU with and without LTP at The End of GPS Outage

Reduced IMU	RMS Position Error (m)			
	Horizontal		Vertical	
	LTP	No LTP	LTP	No LTP
3A1G (HG1700)	104	219	10	15
2A1G (HG1700)	104	223	12	12
3A1G (Crista)	103	221	11	12
2A1G (Crista)	103	220	11	12

3.5.4 Summary

With the GPS/RIMU with an LTP, a series of system configuration tests were conducted to verify the LTP method. Following the system configuration tests, some GPS outage tests were conducted. Based on the test results, the following conclusions are drawn:

- The LTP method is valid. With the LTP, pitch and roll were estimated, and velocity error was reduced, especially for horizontal velocity error, it was reduced by more than 80% for both 3A1G and 2A1G MEMS IMU compared to without LTP.
- During GPS outages, the LTP method reduced position and velocity errors.
- During GPS outages with an LTP, the horizontal position and velocity errors of different grade IMUs and different configurations were reduced greatly, but the vertical position and velocity errors were reduced only slightly or remained the same.

Given the above, 2A1G may be a better configuration when cost and performance are considered. In conclusion, LTP is a valid attitude error model (for pitch and roll) for RIMU, and can improve the navigation performance of a GPS/RIMU.

3.6 Evaluation of Three Types of RIMU M&E Equations

In order to compare the performance of the three types of mechanizations and their error models, another series of tests were performed using only the Crista system. Specifically, for each mechanization, two GPS/RIMU systems, namely the GPS/3A1G and GPS/2A1G, were tested using sections A and B of the data. Consequently, there are four sets of results for each mechanization.

In order to obtain a fair comparison between the different types of M&E equations, the process noise parameters and covariance of each error model must be chosen properly. In practice, this is difficult since for different error models the process noise parameters have different interpretations, especially for those noises which are not related to or do not come from actual sensors (e.g., related to local terrain). Herein, process noise terms that are not related to a particular sensor are called noise without a corresponding sensor. Furthermore, it is understood that the covariances of these noises can only be obtained approximately because they are related to some unknown factors. For example, the horizontal rotation rate noises are related to the rates of pitch and roll, which are hard to be known precisely without horizontal gyros. In this light, the comparison of the different types of M&E equations below can be seen as approximate, but still instructive. In the following tests, the covariance of each corresponding error model is chosen as the best value that we can have. It is obtained through several parameter selection trials.

3.6.1 Test Results with Section A (Near Open Sky Case)

First, GPS/3A1G (Crista) and GPS/2A1G (Crista) were tested using different M&E equations with data from section A. The test results are summarized in Table 3.5 for

3A1G, and Table 3.6 for 2A1G. From Table 3.5, it can be seen that for the 3A1G case, the three types of M&E equations have similar results under the near open sky case except that the DR model can not estimate pitch and roll. For the 2A1G case, similar conclusions can be drawn from Table 3.6. For the DR model, the test results show that although it can not estimate pitch and roll, it still has a similar azimuth and velocity estimation accuracy with those of the LTP model. This is because the effect of the local terrain (pitch and roll) on the velocity error is modeled as an accelerometer bias, and is estimated in this term. Consequently, the estimated accelerometer bias in this case is not the true accelerometer bias but instead is a composite bias, as shown in Equation (3.29). If the pitch and roll are not modeled in the accelerometer bias term (i.e. the accelerometer bias model comes from the actual accelerometer), they will not be estimated, resulting in navigation errors, as shown in Table 3.3. Comparing Table 3.3 with Table 3.5 and Table 3.6, it can be seen that when pitch and roll are not estimated in accelerometer bias, both the azimuth and velocity estimation error will increase several times (about eight-fold for both azimuth and horizontal velocity error), compared to the case where pitch and roll are estimated in the accelerometer bias. For the GPS/RIMU with an LTP or FD model, its pitch and roll information comes from the GPS solution because neither the LTP nor the FD model can provide the local terrain information directly.

Table 3.5 Velocity and Attitude Error Statistics of GPS/3A1G (Crista) with Data from Section A

3A1G Mechanization	RMS Attitude Error (Deg)			RMS Velocity Error (m/s)		
	Pitch	Roll	Azimuth	East	North	Up
DR	N/A	N/A	2.24	0.08	0.08	0.08
LTP	0.72	0.70	2.38	0.08	0.08	0.08
FD	0.61	0.74	2.48	0.08	0.09	0.07

Table 3.6 Velocity and Attitude Error Statistics of GPS/2A1G (Crista) with Data from Section A

2A1G Mechanization	RMS Attitude Error (Deg)			RMS Velocity Error (m/s)		
	Pitch	Roll	Azimuth	East	North	Up
DR	N/A	N/A	2.24	0.08	0.08	0.09
LTP	0.71	0.70	2.38	0.08	0.08	0.09
FD	0.61	0.71	2.50	0.08	0.09	0.09

3.6.2 Test Results with Section B (Near Foliage Case)

The GPS/3A1G and GPS/2A1G configurations were tested using different types of M&E equations with data from section B. The test results are summarized in Table 3.7 for 3A1G, and Table 3.8 for 2A1G. From Table 3.7, it can be seen that for 3A1G case, the DR and LTP model have similar results except that the DR model can not estimate pitch and roll. But for the FD model, both its attitude and velocity errors are much greater than those of the LTP. In particular, the velocity error is more than twice that of the LTP. For the 2A1G case, similar conclusions can be obtained from Table 3.8 except for the vertical velocity error. The vertical velocity error of the FD is less than that of the LTP, which is contrary to the result of 3A1G case. This can be explained with Figure 3.16, the vertical velocity error of the 3A1G and 2A1G cases with the FD model and under near foliage case. From this figure, it can be seen that a large vertical velocity error (more than 1.5 m/s) in the 3A1G case, which appears between GPS time 242800 and 242980 s, is not present in the 2A1G case, resulting in a smaller RMS vertical velocity error. Consequently, the RMS vertical velocity error of the 2A1G is less than that of the 3A1G, as shown in Table 3.7 and Table 3.8, although the vertical velocity error of the 3A1G is much less than that of the 2A1G in most cases, as shown in Figure 3.16. As a result, in 2A1G, the vertical velocity error of the FD is less than that of the LTP. The reason for

that with the FD error model, the large vertical velocity error in 3A1G case disappears in 2A1G case is explained as follows: in this partial outage (between GPS time 242800 and 242980 s), the tracked SVs have high elevation angles (one SV's elevation is about 80 degrees), thus providing relatively accurate vertical information (for both position and velocity). In this case, since the GPS/2A1G takes more vertical information from the GPS than the GPS/3A1G does (since 2A1G has no vertical accelerometer), the large vertical velocity error that may arise in the 2A1G case is corrected by GPS. As a result, the GPS/2A1G does not produce any large vertical velocity error during this partial GPS outage.

With respect to the performance comparison between the FD and LTP model (or FD and LTP M&E equations), as concluded above, the FD model has greater attitude and velocity error than the LTP does. This is because in the FD model, there is no constraint on horizontal attitude errors, and the variances of the measurement noises of horizontal rotation rates are chosen to be on the order of a few deg/s, as discussed in Section 3.2. Consequently, the GPS/RIMU with FD model takes more navigation information from the GPS than the system with the LTP model does, especially during partial GPS outages (because there is no constraint in FD model). Since there are several partial GPS outages in the near foliage test, the performance of the GPS/RIMU with FD model is degraded by the poor GPS solutions, and the degradation is more serious than that with LTP model. Thus the FD model has greater attitude and velocity error than the LTP does.

Table 3.7 Velocity and Attitude Error Statistics of GPS/3A1G (Crista) with Data from Section B

3A1G Mechanization	RMS Attitude Error (Deg)			RMS Velocity Error (m/s)		
	Pitch	Roll	Azimuth	East	North	Up
DR	N/A	N/A	3.55	0.35	0.31	0.10
LTP	0.56	0.75	3.61	0.35	0.32	0.12
FD	0.81	0.99	5.30	0.80	0.80	0.26

Table 3.8 Velocity and Attitude Error Statistics of GPS/2A1G (Crista) with Data from Section B

2A1G Mechanization	RMS Attitude Error (Deg)			RMS Velocity Error (m/s)		
	Pitch	Roll	Azimuth	East	North	Up
DR	N/A	N/A	3.55	0.35	0.31	0.26
LTP	0.55	0.77	3.66	0.35	0.32	0.26
FD	0.68	1.02	5.31	0.81	0.76	0.15

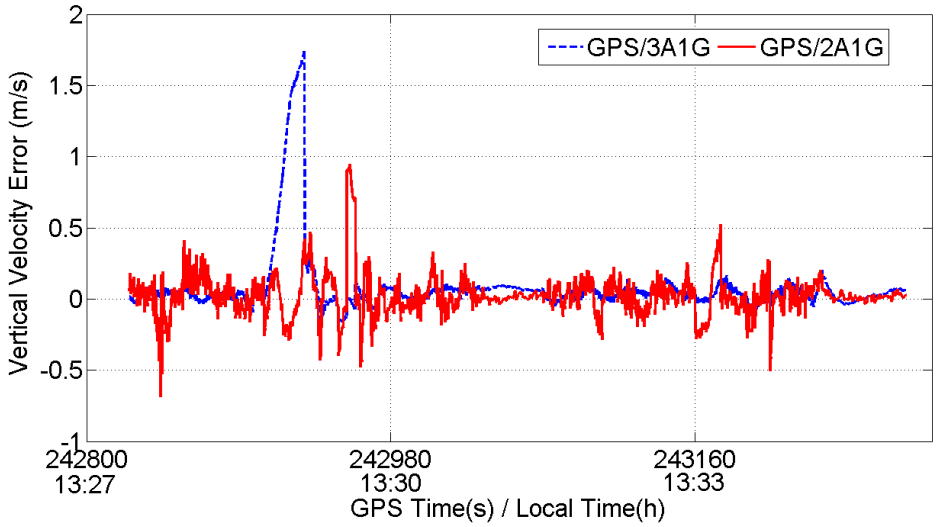

Figure 3.16 Vertical Velocity Error of GPS/RIMU (Crista) with FD Model in Section B

3.6.3 Summary and Discussion

From the above test results, it can be concluded that both the DR and LTP M&E equations (or model) perform well in both the near open sky and the near foliage case except that the DR model cannot estimate pitch and roll. But the FD model only performs well in the near open sky case. This is because the FD model has no constraint

on horizontal attitude errors. Thus the GPS/RIMU with FD model takes more navigation information from the GPS than the system with LTP model does. When the navigation information provided by the GPS is poor, such as in the near foliage case, the FD model will perform poorly, i.e. with larger navigation errors (velocity and attitude) than the LTP model.

The reason the DR model can achieve a similar performance with that of the LTP is that the effect of the local terrain (pitch and roll) on the velocity error is modeled and estimated in the accelerometer bias term. If the pitch and roll are not estimated in the accelerometer bias term, both the azimuth and velocity error of the DR model increase about eight-fold. In conclusion, compared to the LTP model, the DR model can achieve a similar performance only if the pitch and roll are estimated in the accelerometer bias term (a composite bias). Compared to the LTP model, the FD model can achieve a similar performance in the near open sky case, but in the near foliage case, its performance is much inferior to that of the LTP except for the vertical velocity in the 2A1G configuration.

3.7 Summary

In this chapter, in order to overcome the disadvantages of RIMUs, an LTP method was developed for RIMU to obtain a set of innovative mechanization equations and error model. This M&E equations were compared with other two types of M&E equations (namely DR and FD type) to investigate their relative performance. After the theoretical research, a series of tests for GPS/RIMU were conducted with real test data to verify the

LTP method, and to compare the performance of the three types of M&E equations. From these tests, the following conclusions are drawn:

- The LTP method is valid, and can improve the navigation performance of a GPS/RIMU in both GPS available and unavailable cases.
- With an LTP, pitch and roll were estimated, and velocity error was reduced, especially for horizontal velocity error. The 3D RMS velocity error was reduced by more than 80% compared to without LTP case.
- 2A1G may be a better configuration for GPS/RIMU (loose) when cost and performance are considered because with a vertical accelerometer, only the vertical velocity error of the GPS/3A1G was reduced (about 11% for MEMS IMU).
- Compared to LTP model, the DR model can achieve a similar performance only if the pitch and roll are estimated in the accelerometer bias term (a composite bias); otherwise its performance is much degraded.
- Compared to the LTP model, the FD model achieved a similar performance in the near open sky case. But in the near foliage case, its performance was much inferior. Specifically, the 3D RMS velocity error of the GPS/3A1G (Crista) with FD model was more than twice that of the system with the LTP model.

Chapter Four: TLA GPS/Reduced IMU

As discussed in Chapter One, in a tight GPS/RIMU, if the GPS receiver's tracking loops, especially PLLs, receive Doppler aiding from the INS obtained from the RIMU, the tight integration system is called tight with loop aiding (TLA), i.e. TLA GPS/RIMU. In a TLA GPS/RIMU, the noise bandwidth of the loop filters of the PLLs can be narrowed more than in a GPS-only case (Chiou et al 2007; Petovello et al 2007; Gebre-Egziabher et al 2005; Chiou 2005). As a result, the TLA integration system offers some advantages over GPS-only receivers including a more accurate navigation solution (especially for velocity and thus position), improved tracking ability for high dynamics and good anti-jam performance (Kim et al 2007; Petovello et al 2007; Chiou et al 2004; Hamm et al 2004). Since the TLA system's performance can be improved through narrowing the noise bandwidth of the PLL loop filters, in order to design a TLA system, the following two problems must be solved: how narrow can the noise bandwidth be and how much can the system performance be improved through a Doppler aiding? To answer these two questions, this chapter conducts a thorough assessment on the TLA GPS/RIMU system in terms of the tracking ability of the GPS receiver and the navigation performance of the TLA system when the loop filter noise bandwidth is adjusted.

In this chapter, first the TLA GPS/RIMU is introduced. Then the phase error of a PLL with Doppler aiding is analyzed. Based on the phase error analysis, the formulae, which can be used to calculate the noise bandwidth of a Doppler-aided PLL, are given. Then an adaptive PLL loop filter – or simply an adaptive loop filter (ALF) – is designed to exploit the greatest potential ability of the Doppler-aided PLL to improve the performance of the

TLA GPS/RIMU. Following the theoretical research, a test conducted with a translation stage on the roof of a building is described first. The translation stage provides motions for the test. Then an assessment of the potential benefits of a TLA GPS/RIMU is performed with the translation stage test data. Further an assessment with real data collected in the field vehicle test, as described in Chapter Three, is made to identify the advantages of TLA system. Finally, an evaluation of the TLA GPS/RIMU with and without ALFs is performed using the vehicle test data.

4.1 TLA GPS/RIMU

In a TLA GPS/RIMU system, the key point is how the GPS receiver uses a PLL aided with a Doppler value calculated from the integrated navigation solution and satellite information to improve its performance. In the TLA system, two reduced IMU configurations are considered: 3A1G and 2A1G. Their navigation equations and error models are given in Chapter Three. The configuration of the TLA GPS/RIMU is shown in Figure 4.1, which gives more detailed information for the Doppler aided PLL than does Figure 2.10 – the block diagram of TLA GPS/INS integration. It is noted in Figure 4.1 that the "Tight Integration" box contains an extended Kalman filter to integrate both the GPS (pseudorange and Doppler shift) and IMU data. The Doppler aiding rate for the tracking loops is equal to the IMU measurement rate, i.e. the output rate of the Kalman filter for Doppler aiding calculation. The Doppler aiding value is calculated from Equation (2.21). It consists of two parts: one comes from the relative motion of the satellite with respect to the user; the other from the receiver clock drift.

In the TLA GPS/RIMU system, the Doppler-aided PLL can be modeled as a control system (Alban et al 2003; Misra & Enge 2001), as shown in Figure 4.1 (right panel). In order to facilitate the analysis of the phase errors induced by Doppler aiding *error*, the true Doppler, $F_d(s)$, is removed from the block diagram of Doppler-aided PLL, resulting in Figure 4.2, the block diagram of Doppler aiding error propagation. In this figure, phase error $\delta\varphi_r(s) = \varphi_r(s) - F_d(s)/s$ and Doppler aiding error $\Delta F_d(s) = F_{dc}(s) - F_d(s)$ are inputs and $\delta\varphi(s) = \varphi(s) - F_d(s)/s$ is output, where $\varphi_r(s)$ is PLL input phase, $\varphi(s)$ is output phase, $F_{dc}(s)$ is the calculated Doppler aiding. With reference to Figure 4.2, $N(s)$ is noise, $G_p(s) = 1/s$ is the transfer function of the numerically controlled oscillator (NCO), and $G_c(s) = \left(2\xi\omega_n s + \omega_n^2\right)/s$ is the transfer function of a second-order loop filter, where $\xi = 0.707$ is the damping ratio of the system and ω_n is the un-damped natural frequency. Furthermore, $\delta\varphi_r(t) = 0$ cannot affect the system analysis since it is assumed that the phase error induced by system dynamics only comes from the Doppler aiding error. From control system theory (e.g., Nise 2000; Ogata 1997), the phase error induced by Doppler aiding error is obtained from Figure 4.2 as follows

$$\delta\varphi(s) = \frac{s}{s^2 + 2\xi\omega_n s + \omega_n^2}\Delta F_d(s) \tag{4.1}$$

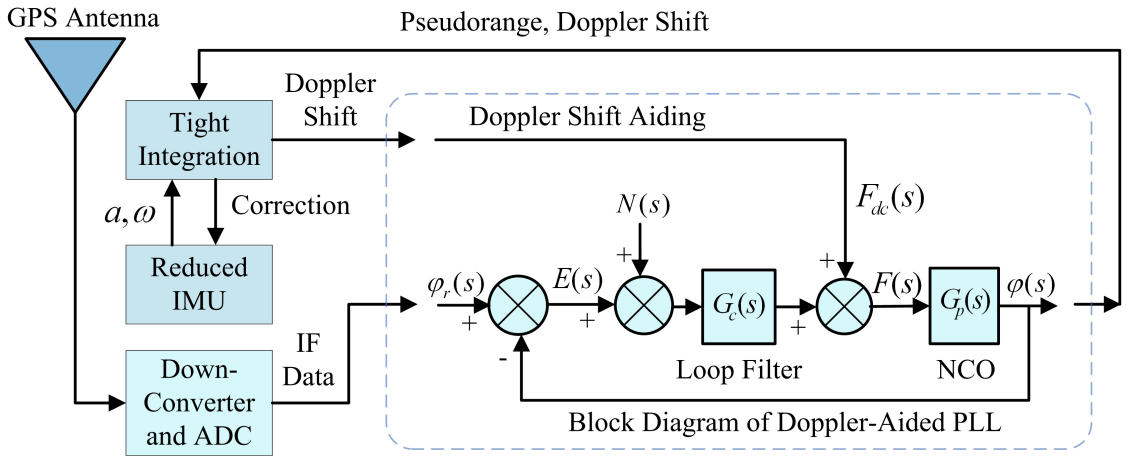

Figure 4.1 Configuration of TLA GPS/RIMU

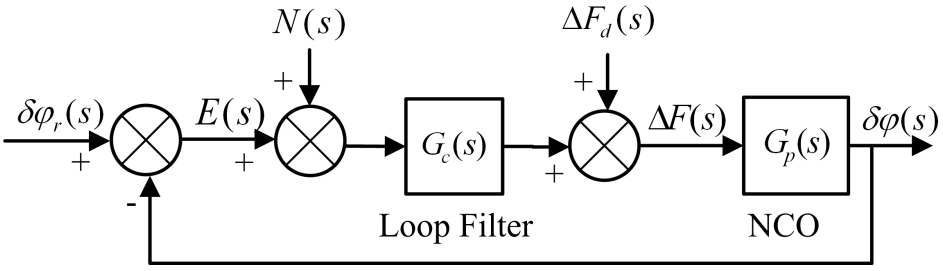

Figure 4.2 Block Diagram of Doppler Aiding Error Propagation

4.2 Phase Error of Doppler-Aided PLL in TLA GPS/RIMU

In a TLA GPS/RIMU, the phase error of the Doppler-aided PLL is, to some extent, different from the traditional PLL because Doppler aiding not only removes most user dynamics, but also introduces some additional frequency errors. In light of this, the phase error of Doppler-aided PLL needs to be reviewed.

4.2.1 Individual Phase Errors in Doppler-Aided PLL

There are many possible error sources in a Doppler-aided PLL. To simplify the analysis, only the following main sources are considered herein (see Appendix B for details):

- Thermal noise (see Equation (B.1))
- Allan deviation oscillator phase jitter (see Equation (B.2))

- Vibration-induced oscillator phase jitter (see Equation (B.3))
- Doppler aiding error-induced phase errors

In the context of this thesis, the last error source is of primary interest and, to this end, it is assumed that the Doppler error of the GPS/RIMU consists of the combination of a series of piecewise first-order Gauss-Markov (GM) processes and a series of piecewise random ramps (RRs). The reasons for doing so are twofold: first, a series of piecewise GM and RR processes well match the Doppler error observed in most cases because of the error characteristics of GPS/RIMU; second, using only these two types of Doppler errors can facilitate system analysis. In GPS/RIMU integration, if the attitude error is small and noisy, the resulting Doppler error will look like a first-order GM process, which is produced mostly by the GPS measurement and the reduced IMU attitude error. Otherwise, the Doppler error may contain a first-order GM process, and a random ramp mainly induced by the reduced IMU attitude error. For example, the velocity error of the GPS/3A1G, as shown in Figure 4.20, can be expressed as a first-order GM process. Its correlation function can be approximately expressed as $R(\tau) = R_0 e^{-\beta|\tau|}$, for east and north velocity error, $R_0 \approx 1.9e^{-3}$ (m/s)^2, $\beta \approx 1/5$ (1/s), respectively; for vertical velocity error, $R_0 \approx 1.0e^{-3}$ (m/s)^2, $\beta \approx 1/4$ (1/s). The equations corresponding to the Doppler aiding-induced phase errors of interest in this chapter are given below.

Random ramp-induced phase error is obtained from Equation (B.4), and given as

$$\theta_{RR} = 360\frac{A_{RR}}{\omega_n^2} \text{ (degrees)} \tag{4.2}$$

where A_{RR} is the amplitude (slope) of the random ramp (Hz/s). First-order GM-induced phase jitter is obtained from Equation (B.10), and given as

$$\sigma_{\varphi GM} = 360 \cdot \sqrt{\frac{e^{\alpha T} \cdot \sigma_w^2}{\omega_n^4 + \gamma^4} \left(\frac{\gamma^2}{2\sqrt{2}\omega_n} + \frac{\omega_n}{2\sqrt{2}} - \frac{\gamma}{2} \right)} \text{ (degrees)} \tag{4.3}$$

where $\gamma = \alpha\sqrt{e^{\alpha T}}$, and from Equation (B.8),

$$\sigma_w = \sigma_{GM} \sqrt{(1 - e^{-2\alpha T}) / T} \tag{4.4}$$

where σ_{GM} is the standard deviation of the GM process (Hz), α is the reciprocal of the correlation time (1/s), and T is the measurement update period of the Kalman filter for GPS/RIMU (s).

4.2.2 Total Phase Error in Doppler-Aided PLL

Based on the above individual phase errors, the total phase error (1-sigma) of the Doppler-aided PLL can be expressed as

$$\sigma_{PLL} = \sqrt{\sigma_{tPLL}^2 + \sigma_v^2 + \sigma_{Arx}^2 + \sigma_{Asv}^2 + \sigma_{\varphi GM}^2} + \frac{\theta_{RR}}{3} \tag{4.5}$$

where σ_{tPLL} , σ_v , $\sigma_{\varphi GM}$, and θ_{RR} are thermal noise, oscillator vibration phase jitter, Doppler aiding GM phase jitter, and Doppler aiding RR phase error, respectively, and σ_{Arx} and σ_{Asv} are respectively the receiver and satellite Allan phase jitters. σ_{tPLL} and σ_v are defined in Equations (B.1) and (B.3), respectively. σ_{Arx} and σ_{Asv} are defined in Equation (B.2). $\sigma_{\varphi GM}$ and θ_{RR} are defined in Equations (4.3) and (4.2), respectively. The RR phase error is considered as a dynamic stress error (much like the dynamic stress error in a standard tracking loop), so it appears outside the square root in Equation (4.5) (Ward et al 2006). In Equation (4.5), the thermal noise, oscillator Allan phase jitter,

oscillator vibration phase jitter, and Doppler aiding error-induced phase error are considered to be independent. Furthermore, the Doppler aiding GM phase jitter and Doppler aiding RR phase error are assumed to be independent to simplify the analysis of Doppler aiding error-induced phase error. It is noted that Equation (4.5) is applicable to any Doppler-aided PLL. Furthermore, if the parameters for calculating the total phase error with Equation (4.5) are known, according to the PLL tracking threshold $\sigma_{PLL} \leq 15$ (degrees) (Ward et al 2006) (i.e. if $\sigma_{PLL} \leq 15$ (degrees), the PLL is considered to be locked), the minimum noise bandwidth of Doppler-aided PLL can be obtained with Equation (4.5). Since σ_{PLL} is a nonlinear function of the noise bandwidth, as shown in Equation (4.5) (also discussed in Ward et al (2006) and Gebre-Egziabher et al (2005)), there are no analytical solutions for the noise bandwidth. Therefore, a search strategy is needed to obtain the minimum noise bandwidth solution. If the noise bandwidth solution is obtained in real time and applied to the PLL loop filter simultaneously, an adaptive loop filter with varying noise bandwidth can be obtained.

4.3 Adaptive PLL Loop Filter for TLA GPS/RIMU

In general, each PLL tracking loop of a GPS receiver is controlled by a loop filter whose order and noise bandwidth impact the performance of the tracking loop (Ward et al 2006). In a TLA GPS/RIMU integration, the noise bandwidth can be narrowed more than in a GPS-only case resulting in improved noise suppression within the receiver (Petovello et al 2007, Alban et al 2003). However, the loop noise bandwidth cannot be made arbitrarily small and is limited by the navigation solution error of the GPS/RIMU and the receiver's oscillator errors (Gebre-Egziabher et al 2005), as shown in Equation (4.5). Since the navigation solution error varies (see Chapter Three), the loop filter with a

constant noise bandwidth cannot optimally accommodate signal dynamics resulting from the navigation solution. In this light, an adaptive PLL loop filter capable of adjusting its bandwidth would be beneficial, as it would still be able to accommodate large navigation errors, but would provide improved performance during periods when the navigation solution errors are small.

However, to date, there has not been a method or formula to calculate the noise bandwidth according to the navigation performance of a TLA GPS/RIMU. How to choose the noise bandwidth is thus an open problem that is addressed herein. In order to solve this problem, based on the phase error analysis given in Gebre-Egziabher et al (2005) and Chiou (2005), the phase error sources for the GPS/RIMU are analyzed, and formulae for calculating these phase errors are derived in Appendix B. Following the phase error analysis, a novel adaptive PLL loop filter is developed. Generally, it is straightforward to manipulate the loop bandwidth because it is easier to maintain a stable loop during transitions compared to manipulating the loop order (Lee et al 2007; Hsieh & Sobelman 2005; Mao et al 2004). For adjusting the noise bandwidth of an adaptive loop filter, some information can be used to calculate the noise bandwidth, such as carrier to noise power density (C/N_0), elevation angle of the satellite, and the vehicle's acceleration (Lee et al 2007). Actually in Lee et al (2007), the noise bandwidth only takes on two values (i.e. a wide noise bandwidth and a narrow noise bandwidth) according to the C/N_0, elevation, and acceleration. This method is quite coarse.

4.3.1 Evaluation of Doppler Aiding Uncertainty for TLA GPS/RIMU

From Equation (4.5) (i.e. the total phase error of Doppler-aided PLL), it can be seen that the Doppler aiding error (as computed from the integrated navigation solution) affects the total phase error of the PLL. Therefore, in order to calculate the total phase error and design the ALF, the Doppler aiding uncertainty resulting from the navigation uncertainty is derived first below.

The Doppler aiding error uncertainty can be calculated from the GPS/RIMU navigation solution uncertainty. Specifically, the navigation solution uncertainty – as obtained from the integrated navigation solution Kalman filter predicted covariance matrix, $\mathbf{P}(-)$ – is used to compute the Doppler aiding uncertainty, which is then used to adapt the tracking loop. In order to link $\mathbf{P}(-)$ with real GPS measurements, an adaptive algorithm for calculating $\mathbf{P}(-)$ is used as follows (Mohamed & Schwarz 1999)

$$\mathbf{P}_k(-) = \mathbf{P}_{k-1}(+) + \hat{\mathbf{Q}}_{k-1} \tag{4.6}$$

where the process noise covariance is adapted using

$$\hat{\mathbf{Q}}_k = \eta \cdot \hat{\mathbf{Q}}_{k-1} + (1-\eta) \cdot \mathbf{K}_{k-1} \boldsymbol{\upsilon}_{k-1} \boldsymbol{\upsilon}_{k-1}^T \mathbf{K}_{k-1}^T \tag{4.7}$$

where $0 < \eta < 1$ is a weighting factor, $\mathbf{K}_{k-1}$ is the Kalman filter gain, $\boldsymbol{\upsilon}_{k-1} = \mathbf{z}_{k-1} - \mathbf{H}_{k-1}\mathbf{X}_{k-1}(-)$ is the innovation sequence of the Kalman filter, where $\mathbf{z}_{k-1}$ is the measurement, $\mathbf{H}_{k-1}$ is measurement matrix, $\mathbf{X}_{k-1}(-)$ is the predicted state vector. The initial value $\hat{\mathbf{Q}}_0$ is chosen as the best estimate of $\mathbf{Q}$ based on system and error characteristics.

Suppose the diagonal elements (sub-matrices in diagonal) of the $\mathbf{P}(-)$ are $\mathbf{P}_{\delta r}(-)$, $\mathbf{P}_{\delta v}(-)$, $\mathbf{P}_{\varepsilon}(-)$, $\mathbf{P}_{d}(-)$, and $\mathbf{P}_{b}(-)$, where $\mathbf{P}_{(g)}(-) = E\left[(\mathbf{g}(-))(\mathbf{g}(-))^{T}\right]$, $\delta\mathbf{r}(-)$ denotes predicted position error, $\delta\mathbf{v}(-)$ denotes predicted velocity error, $\boldsymbol{\varepsilon}(-)$ denotes predicted attitude error, $\mathbf{d}(-)$ denotes predicted gyro drift, and $\mathbf{b}(-)$ denotes predicted accelerometer bias. Once $\mathbf{P}(-)$ is obtained, the velocity error sub-matrix $\mathbf{P}_{\delta v}(-)$ can be extracted. $\mathbf{P}_{\delta v}(-)$ is then used to compute the Doppler aiding uncertainty caused by the velocity error of the TLA GPS/RIMU as

$$\sigma_{fd}^{2} = \frac{\hat{\boldsymbol{\kappa}}^{T}\mathbf{P}_{\delta v}(-)\hat{\boldsymbol{\kappa}}}{\lambda_{1}^{2}} \tag{4.8}$$

where $\lambda_1 = c / f_{L1}$, c is the speed of light, f_{L1} is the transmitted frequency, and $\boldsymbol{\kappa}$ is the unit vector from the user to SV. The position error is assumed small enough that $\hat{\boldsymbol{\kappa}} \approx \boldsymbol{\kappa}$ (this is reasonable for position errors less than several hundred metres). Similar to the above, the variance of the Doppler rate caused by the integrated system's acceleration error is given as

$$\sigma_{afd}^{2} = \frac{\hat{\boldsymbol{\kappa}}^{T}\mathbf{P}_{\delta a}(-)\hat{\boldsymbol{\kappa}}}{\lambda_{1}^{2}} \tag{4.9}$$

where $\delta\mathbf{a}(-) = \delta\dot{\mathbf{v}}(-)$ is the predicted acceleration error. The calculation of $\mathbf{P}_{\delta a}(-)$ is derived in Equation (4.10). In a reduced IMU, since $\delta\dot{\mathbf{v}} \approx -\mathbf{R}_{\ell 1}^{\ell}\mathbf{F}^{\ell 1}\boldsymbol{\varepsilon}^{\ell 1} + \mathbf{R}_{b}^{\ell}\mathbf{b}$ (see Equation (3.18)), then

$$\mathbf{P}_{\delta a}(-) = \mathbf{R}_{\ell 1}^{\ell}\mathbf{F}^{\ell 1}\mathbf{P}_{\varepsilon}(-)(\mathbf{F}^{\ell 1})^{T}(\mathbf{R}_{\ell 1}^{\ell})^{T} + \mathbf{R}_{b}^{\ell}\mathbf{P}_{b}(-)(\mathbf{R}_{b}^{\ell})^{T} \tag{4.10}$$

where $\boldsymbol{\varepsilon}^{\ell 1}$ is attitude error in the $\ell 1$-frame, $\mathbf{F}^{\ell 1} = \left[\mathbf{R}_b^{\ell 1}\mathbf{f}^b \times\right]$ is a skew-symmetric matrix, where $\mathbf{f}^b$ is specific force in the b-frame, $\mathbf{R}_{\ell 1}^{\ell}$ is a rotation matrix, and $\mathbf{b}$ is the accelerometer bias. The ℓ-frame is the local level frame (east, north, and up) and the $\ell 1$-frame is an alternative level frame (see Section 2.1 for details). Once $\mathbf{P}(-)$ is known, the sub-matrices $\mathbf{P}_{\varepsilon}(-)$ and $\mathbf{P}_b(-)$ can be extracted and $\mathbf{P}_{\delta a}(-)$ is calculated using Equation (4.10).

For one SV channel, once σ_{fd}^2 is obtained, the Doppler aiding-induced phase jitter can be calculated. Recall that the Doppler error of TLA GPS/RIMU is assumed to be the combination of a series of piecewise first-order GM processes and a series of piecewise random ramps. The objective therefore is to relate the values of σ_{fd}^2 and σ_{afd} from above to the variance of the first-order GM process in Equation (4.4) (i.e., σ_{GM}^2) and to the amplitude of the RR error in Equation (4.2) (i.e., A_{RR}). It is pointed out that there is no rigorous method to accomplish this. However, as will be shown later, the following approximations work well in practice

$$\sigma_{GM}^2 \approx \sigma_{fd}^2 \tag{4.11}$$

$$A_{RR} \approx 3\sigma_{afd} \tag{4.12}$$

The first equation states the GM variance for each satellite is approximately equal to the Doppler uncertainty for that satellite. The second equation considers the 3σ (>99%) Doppler rate uncertainty to be a good upper bound of the slope of the random ramp.

It is noted that for a GPS/RIMU, the velocity error has different characteristics in the horizontal and vertical directions (see Section 3.5 for details). The Doppler aiding uncertainty caused by the velocity error of the TLA GPS/RIMU is therefore separated accordingly. The horizontal and vertical Doppler aiding uncertainties are assumed to have different correlation times for the GM process. In this context, the Doppler aiding uncertainty caused by horizontal velocity error is given as

$$\sigma_{fdxy}^2 = \frac{\hat{\boldsymbol{\kappa}}^T \mathbf{P}_{\delta vxy}(-)\hat{\boldsymbol{\kappa}}}{\lambda_1^2} \tag{4.13}$$

where $\delta\mathbf{v}_{xy}(-) = \begin{bmatrix}\delta v_x(-) & \delta v_y(-) & 0\end{bmatrix}^T$. Similarly, the Doppler aiding uncertainty caused by vertical velocity error is

$$\sigma_{fdz}^2 = \frac{\hat{\boldsymbol{\kappa}}^T \mathbf{P}_{\delta vz}(-)\hat{\boldsymbol{\kappa}}}{\lambda_1^2} \tag{4.14}$$

where $\delta\mathbf{v}_z(-) = \begin{bmatrix}0 & 0 & \delta v_z(-)\end{bmatrix}^T$. Once σ_{fdxy}^2 and σ_{fdz}^2 are obtained, σ_{GMxy}^2 and σ_{GMz}^2 – the variances of the first-order GM – can be calculated using Equation (4.11). Then, using Equation (4.3), the phase jitters $\sigma_{\varphi GMxy}$ and $\sigma_{\varphi GMz}$ induced by σ_{fdxy}^2 and σ_{fdz}^2 respectively can be calculated. Finally, the total phase jitter caused by GM Doppler aiding uncertainty is

$$\sigma_{\varphi GM}^2 = \sigma_{\varphi GMxy}^2 + \sigma_{\varphi GMz}^2 \tag{4.15}$$

Having developed a means of approximating the different error components in a TLA GPS/RIMU system, the following section looks at how the ALF is designed.

4.3.2 Adaptive PLL Loop Filter Design

As suggested in Chiou (2005), a second-order loop filter is used in the Doppler-aided PLL of the TLA GPS/RIMU. A second-order loop filter has two parameters; the damping ratio, ξ, and the natural frequency, ω_n. When $\xi = 0.707$, the system has not only the almost minimum coefficient between noise bandwidth and natural frequency, i.e. noise bandwidth $B_n = 0.53\omega_n$ (the minimum coefficient is 0.5 (Stensby 1997)), but also an optimal dynamic performance of the system, i.e. the system's overshoot and settling time are both small (Best 2007; Ogata 1997) . As a result, in the adaptive loop filter developed here, only the noise bandwidth is adjusted.

In a TLA GPS/RIMU, the total phase error variation with the noise bandwidth is shown in Figure 4.3. From this figure, it can be seen that when the GPS signal is strong (C/N_0 = 45 dB-Hz), the total phase error will increase with decreasing noise bandwidth. When the C/N_0 is decreased to 30 dB-Hz, the total phase error still has a similar variation tendency as in the strong signal case. In contrast, when the C/N_0 is further decreased to 20 dB-Hz (i.e. the GPS signal is very weak), the total phase error has a minimum value at a particular noise bandwidth value, and it is always greater than 15 degrees. For the results shown, the predetection integration time (PIT) was 20 ms, and similar conclusions can be drawn for other PIT values.

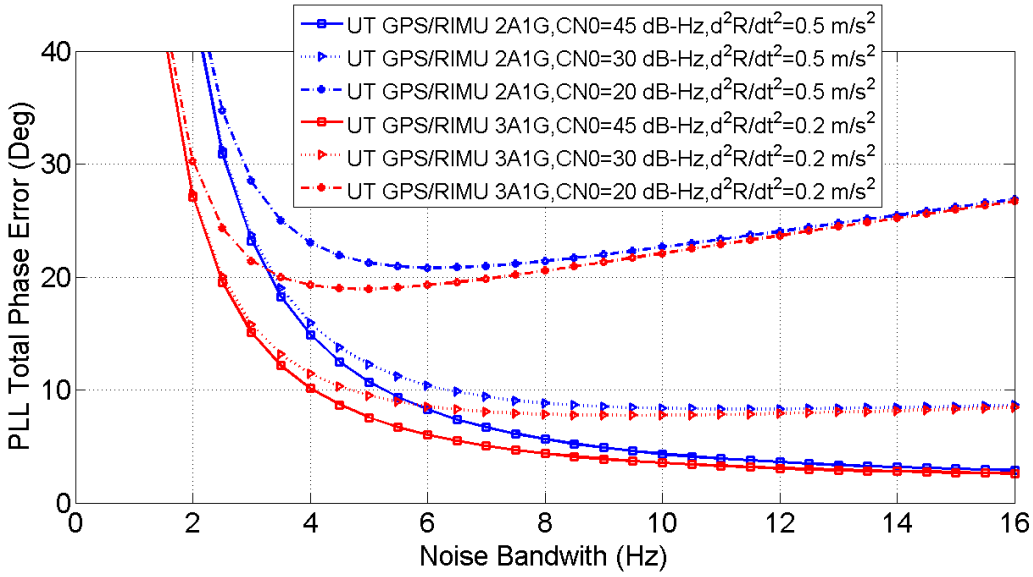

Figure 4.3 Total PLL Phase Error Variation with Noise Bandwidth

Given the above, the selection of the tracking loop's noise bandwidth was made according to two criteria:

- For a strong signal (i.e. a signal for which the total phase error is less than 15 deg at a noise bandwidth of 10 Hz – see the middle and the bottom curves in Figure 4.3) the lowest bandwidth for which the total PLL error is less than 15 deg is selected. The motivation here is that as long as the total PLL error meets this requirement, the tracking loop is considered to be tracking the phase of the signal (Ward et al 2006) and so by minimizing the loop bandwidth the overall Doppler error is also minimized.
- For a weak signal (i.e. a signal for which the total phase error exceeds 15 deg at a noise bandwidth of 10 Hz – see the top curves in Figure 4.3) the bandwidth that

minimizes the total PLL error is selected to allow the PLL the maximum possibility to be locked.

Based on the relationship between total phase error and noise bandwidth, the noise bandwidth search flowchart is given in Figure 4.4.

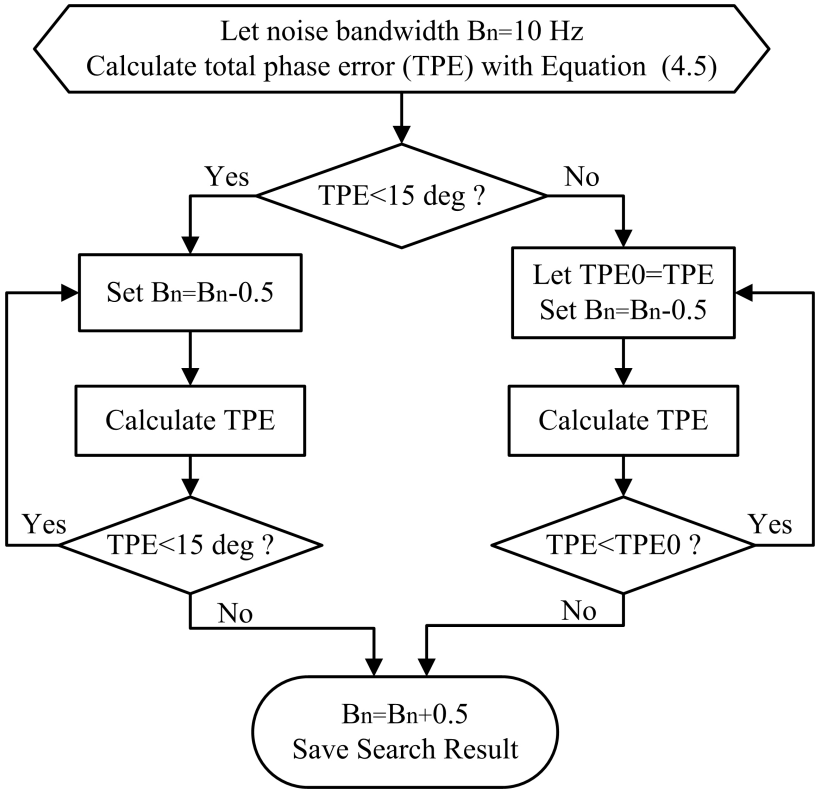

Figure 4.4 Noise Bandwidth Search Flowchart

4.4 Test Description

To explore the advantages of TLA GPS/RIMU and to verify the ALF algorithm, two kinds of tests were conducted to collect data for post-mission processing: one is translation stage test, which is only used for TLA system research; the other is field vehicle test, which was described in Chapter Three and will be used for both TLA system and the ALF research.

4.4.1 Translation Stage Test

The translation stage test was conducted on the roof of the engineering building at the University of Calgary in March 2007. The roof is a relatively benign signal environment (i.e., little multipath and few obstructions). So it can provide an ideal or near ideal environment to investigate the advantages of TLA GPS/RIMU. In this test, motion was provided with a precise translation stage (Anorad, relative precision at the micrometre level) that was approximately level. The precise motion allowed for a controlled motion profile to be generated and used as a reference solution. The maximum acceleration generated for the test was 1.9 m/s^2 (this is the most the table could generate). A picture of the test setup is shown in Figure 4.5. A Honeywell HG1700 IMU (described in Section 3.3) and a GPS antenna were installed on the translation stage. The HG1700 IMU is part of the NovAtel SPAN system (see Section 3.3 for details). For time tagging purposes, the SPAN system's receiver was fed data from a separate (static) antenna. The RF signal from the antenna mounted to the translation stage was passed through a variable signal attenuator and then to an IF data collection system consisting of a NovAtel Euro-3M card (see Section 3.3 for details). The attenuator attenuated the signal at a rate of 1 dB/s for 40 s before the end of the test. An OCXO, namely a Symmetricom 1000B (see Section 3.3 for details), was used to drive the front-end (for more details, see Petovello et al (2007)).

Figure 4.5 Translation Stage Test Setup

A skyplot of the translation stage test is shown in Figure 4.6. From this figure, it can be seen that there were eight SVs in view with an elevation greater than 5 degrees. The reference velocity of the stage motion in forward-backward direction is shown in Figure 4.7. It is obtained from the INS plus zero velocity update (ZUPT) since GPS measurements (i.e. pseudorange and Doppler shift) were unavailable in this test. The velocities of the stage in both vertical and lateral direction were very small (less than 0.02 m/s). Furthermore, all the dynamics were in forward-backward direction, which was approximately in a north/south direction.

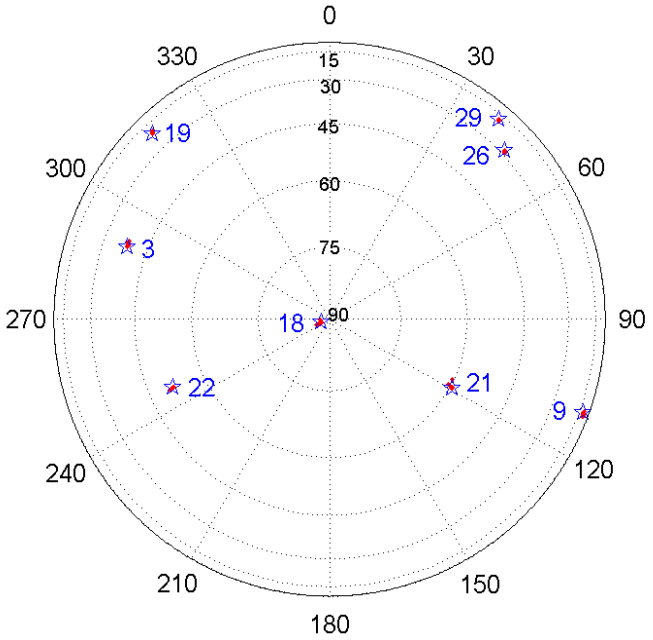

Figure 4.6 GPS Satellite Skyplot of Translation Stage Test

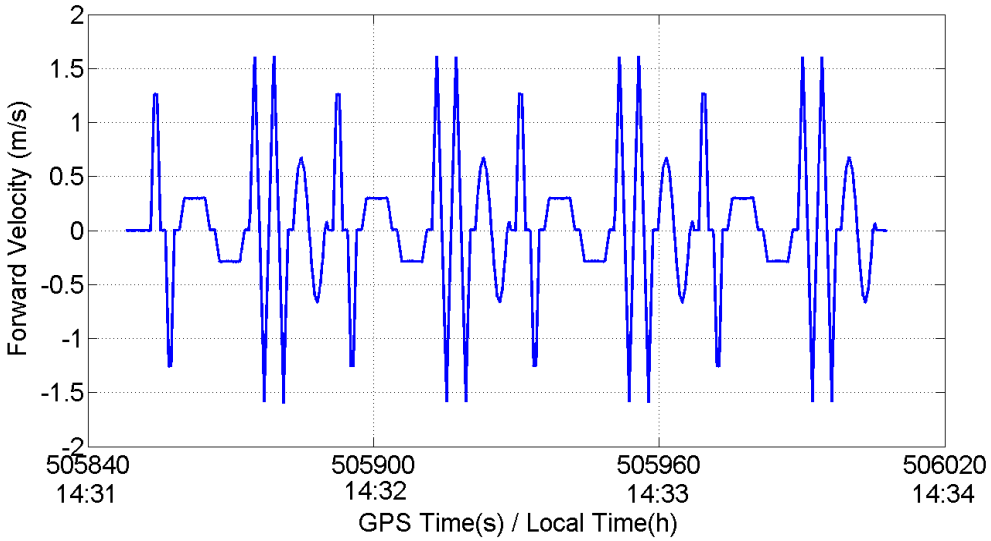

Figure 4.7 Reference Velocity of Stage Motion in Forward Direction

4.4.2 Field Vehicle Test

The field vehicle test was described in Section 3.3. As mentioned in that section, there were two test routes in the vehicle test: one was an open sky route, the other was in

foliage. Only the section A of the open sky test (which contains mostly open sky data), as well as the foliage route, was used for the TLA system research. In the following, the term “open sky route” will only mean the section A of the open sky route.

4.4.2.1 Open Sky Test

For the open sky test, its test trajectory, reference velocity, and attitude are shown in Figures 3.6 to 3.8, respectively. Its GPS satellite skyplot and signal C/N_0 variations are shown in Figure 4.8 and Figure 4.9, respectively. Figure 4.8 shows that in the open sky test there are seven SVs in view with an elevation greater than 5 degrees. From Figure 4.9, it can be seen that the carrier to noise power densities (C/N_0) of the satellites in the open sky test are high and vary by less than 5 dB-Hz for most satellites most of time. Only the C/N_0 of PRN 27 is low, but still more than 40 dB-Hz most of time. The C/N_0 of PRN 11 has some large, but very short attenuations.

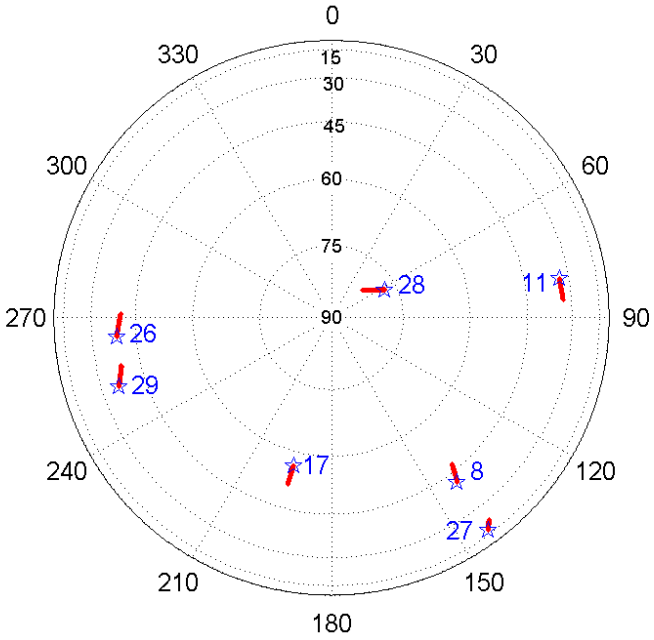

Figure 4.8 GPS Satellite Skyplot of Open Sky Test

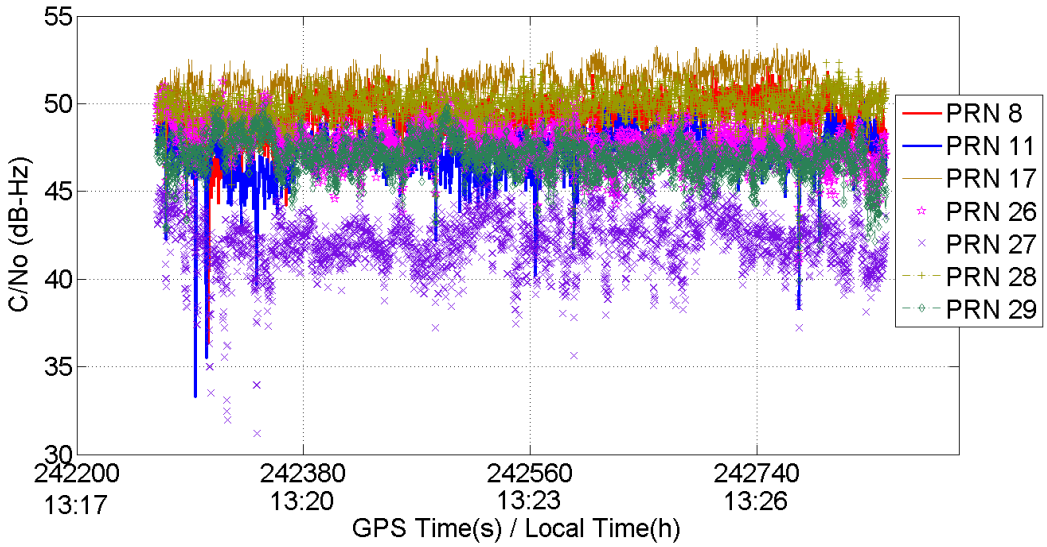

Figure 4.9 Satellite C/N_0 Variations of Open Sky Test

4.4.2.2 Foliage Test

In the foliage test, the test trajectory, reference velocity, and attitude are shown in Figure 4.10, Figure 4.11, and Figure 4.12, respectively. Figure 4.10 shows that the distance traveled in the south-north direction was more than 2 km, and about 2 km in the east-west direction. The vertical variation was more than 15 m. Figure 4.11 shows that the maximum horizontal velocity was about 15 m/s, and the maximum vertical velocity about 0.8 m/s. From Figure 4.12, it can be seen that the pitch mostly ranged between -2 and 2 degrees, and the roll mostly between 0 and 4 degrees. The RMSs of the pitch and roll were about 1.0 and 2.1 degrees, respectively.

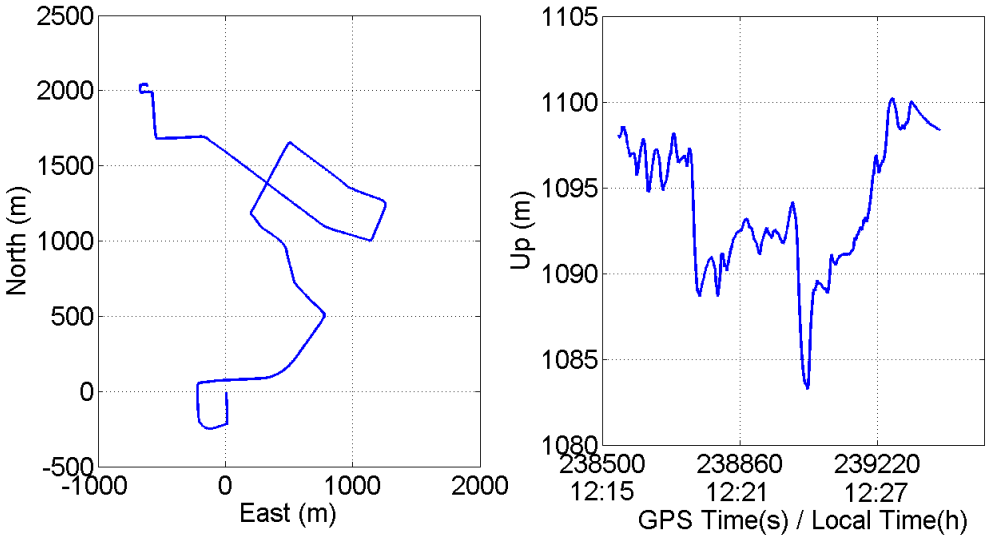

Figure 4.10 Trajectory of Foliage Test

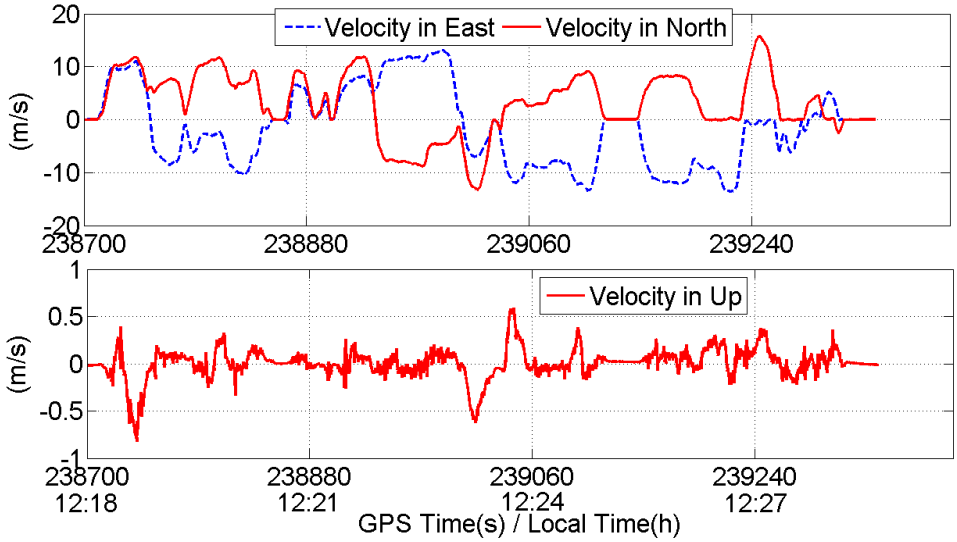

Figure 4.11 Reference Velocity of Foliage Test

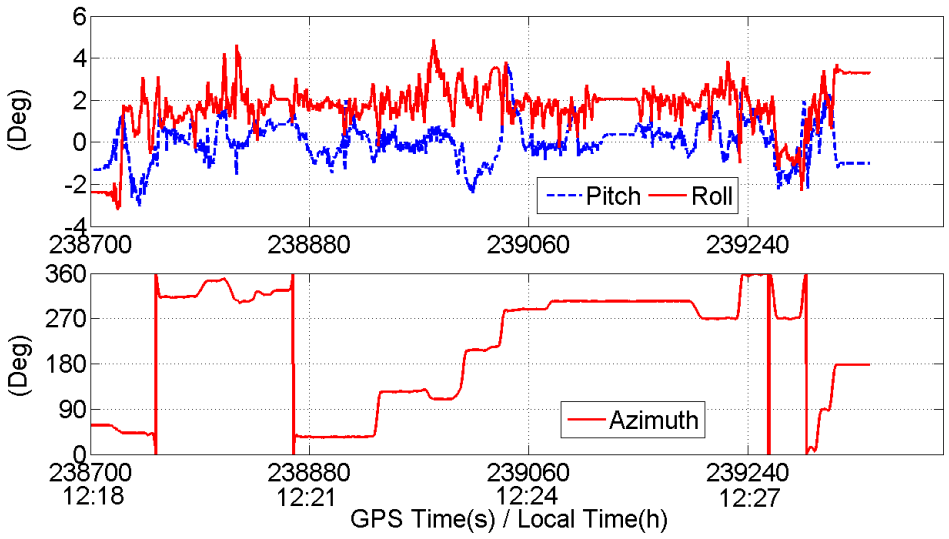

Figure 4.12 Reference Pitch, Roll and Azimuth of Foliage Test

The GPS satellite skyplot and C/N_0 variations of the foliage test are shown in Figure 4.13 and Figure 4.14, respectively. From Figure 4.13, it can be seen that there were nine SVs in view with an elevation greater than five degrees. Figure 4.14 shows that the C/N_0 variations of satellites are dramatic, and can reach as much as 20 dB-Hz.

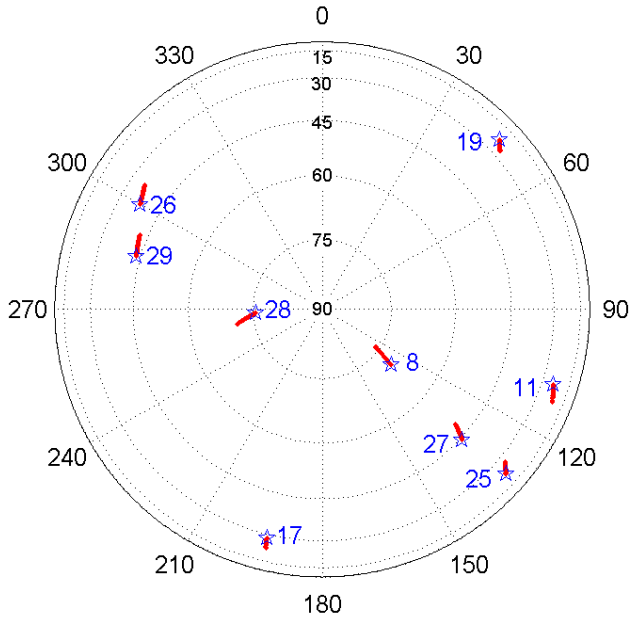

Figure 4.13 GPS Satellite Skyplot of Foliage Test

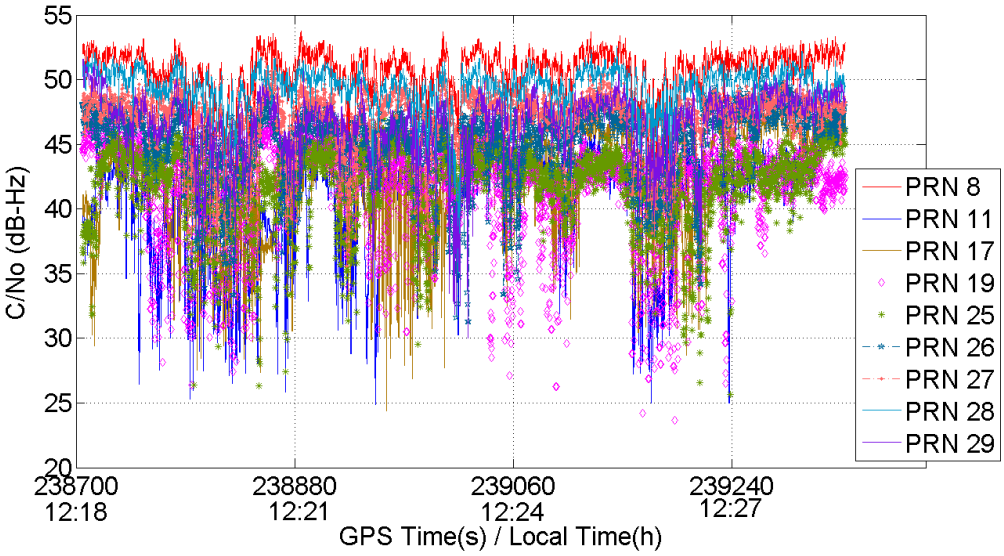

Figure 4.14 Satellite C/N_0 Variations of Foliage Test

4.5 Data Processing and Test Scenario

Data processing was performed with the TLA GPS/RIMU software developed from the University of Calgary's GSNRx™ software receiver (Petovello et al 2008b). In order to

implement TLA GPS/RIMU integration, the GSNRx™ software receiver was modified by the author of this dissertation to include IMU data processing, and to implement the TLA architecture, as shown in Figure 4.1. Based on the research of this dissertation, only the receiver's GPS L1 C/A code post-mission capabilities were used. For the translation stage test data, a 2A1G (HG1700) configuration was used. Its mechanization equations and corresponding error model were developed based on the stage test conditions, and given in Petovello et al (2007).

For the vehicle test data, two RIMU configurations (i.e. 3A1G and 2A1G) were used for each grade of IMU (tactical and MEMS). In addition to assessing the performance of the TLA GPS/RIMU, the performance of TLA GPS/RIMU with ALFs was evaluated. For the purpose of this work, the TLA GPS/RIMU software was further modified by the author of this dissertation to include the adaptive loop filter architecture described in Section 4.3.2. The receiver's output rate was set to 10 Hz and the IMU data was processed at 100 Hz. In order to facilitate comparison, the GPS measurement noise variance (used to compute the navigation solution) was the same for all tests, i.e. 100 (m^2) for pseudorange, 0.04 $(m/s)^2$ for pseudorange rate.

A necessary part for implementing the ALF algorithm described in Section 4.3.2 is to properly model the oscillator errors. To this end, the Allan parameters of the OCXO oscillator used were chosen from Table B.1. The power curve of the random vibration for calculating vibration-induced oscillator phase jitter was chosen from Table B.2 and multiplied by 0.01. This scaling was necessary to yield a good approximation with the

real power spectral density (PSD) curve shown in Figure 4.15, which is obtained from the vehicle test data described in Section 3.3. This is because the test in this dissertation is for a land vehicle, but Table B.2 was obtained from a test for a turbojet transport aircraft (Gebre-Egziabher et al 2005). As per Gebre-Egziabher et al (2005), the Allan parameters of the satellite oscillator were chosen as those of a temperature compensated crystal oscillator (TCXO) multiplied by 0.01. With reference to Figure 4.15, the "spline" stands for the cubic spline fit interpolation method provided by Matlab.

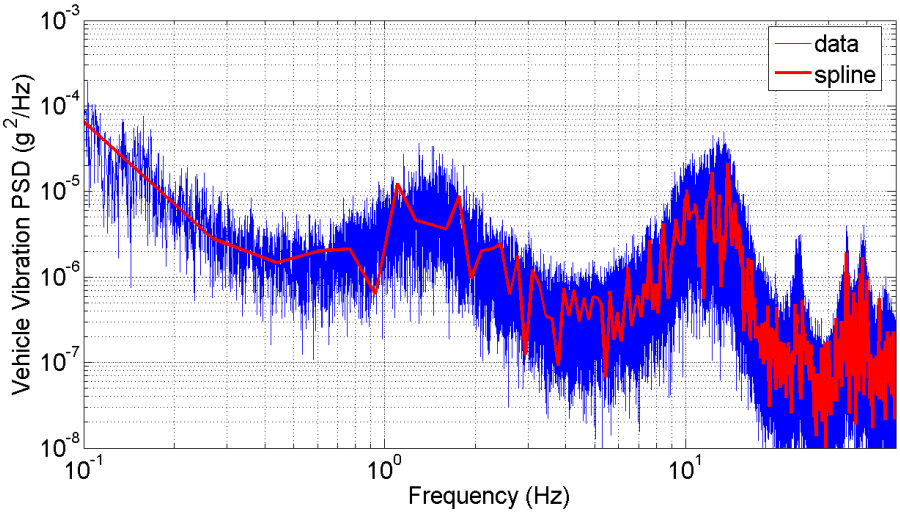

Figure 4.15 Power Curve of Vehicle's Random Vibration

4.6 Evaluation of TLA GPS/RIMU

The evaluation of the TLA GPS/RIMU is performed with both the translation stage test data and the vehicle test data. Thus the advantages of the TLA system can be investigated completely, i.e. in both ideal (or near ideal) and real situations. To identify the TLA system's advantages, the test results of the TLA system are compared with those of corresponding tight system (i.e. no Doppler aiding for the GPS receiver). In order to simplify analysis, only some representative test results are shown in the following.

4.6.1 Test Results with Translation Stage Test Data

With translation stage test data, the TLA GPS/RIMU (for the translation stage test, only 2A1G (HG1700) is used) is investigated from two aspects: PLL tracking performance and system navigation performance. To investigate the PLL tracking performance, PRN 19 is chosen as an example. The reason for choosing PRN 19 is that PRN 19 has the largest or near largest sensitivity to the stage motion since it has a low elevation angle (about 21 degrees), and is the closest satellite with an azimuth in the north-south direction (its azimuth is about 317 degrees, see Figure 4.6). The tracking performances of the TLA and tight system for PRN19 are shown in Figure 4.16. In this figure, the phase lock indicator is a value which is equal to the normalized estimate of the cosine of twice the carrier phase error and is used to show the phase lock situation (Van Dierendonck 1996). The phase lock indicator falls in the range of ±1, with +1 indicating perfect phase tracking. From Figure 4.16, it can be seen that even though the two systems of TLA and tight have the same PLL noise bandwidth (4 Hz), compared to the tight system, the TLA system can improve the tracking performance. That is, the phase lock indicator (PLI) has a value nearer to one, and the Doppler shift has a smaller error. From Figure 4.16, it also can be seen that the C/N_0 is attenuated at about GPS time 505960 s. Actually the GPS signal is attenuated at GPS time 505956 s, and the attenuation is increased at a rate of 1 dB/s to a maximum of 40 dB. The C/N_0 curve shows that the TLA system can give a valid C/N_0 estimate for longer time (i.e. for the signal with lower C/N_0). This means that the TLA system can track the signal with lower C/N_0.

The forward velocity errors of the TLA and tight system are shown in Figure 4.17. From this figure, it can be seen that the TLA system has much smaller velocity error, specifically for TLA system, the RMS forward velocity error is 0.02 m/s; for tight system, it is 0.20 m/s. More test results and analyses for the translation stage test were given in Petovello et al (2007), and some conclusions were obtained as follows: the velocity solution obtained from the TLA GPS/2A1G (HG1700) is about 60-90% more accurate than the corresponding tight system solution. Furthermore, the TLA GPS/2A1G (HG1700) is found to provide roughly 5 dB of sensitivity improvement relative to tight GPS/2A1G (HG1700).

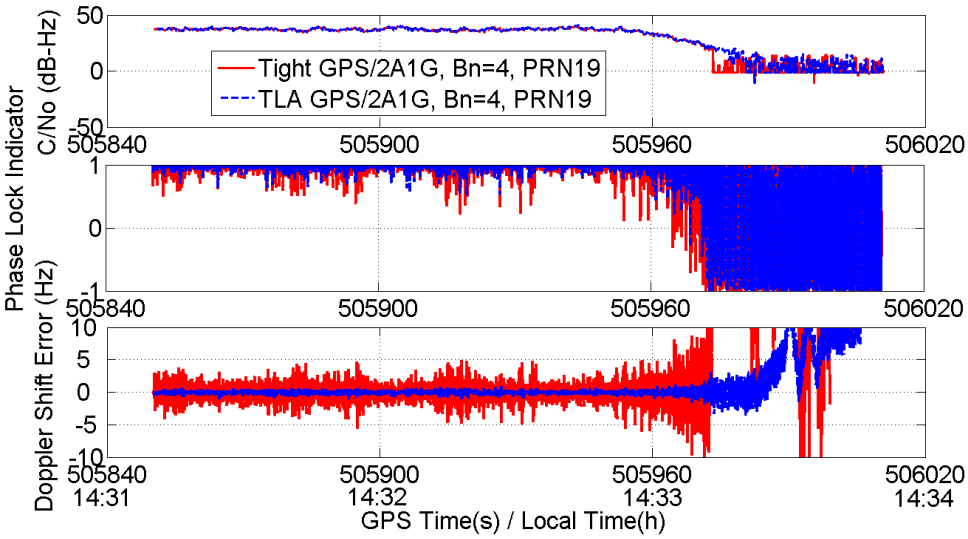

Figure 4.16 Tracking Performance Comparison of TLA and Tight GPS/2A1G (HG1700) for PRN19

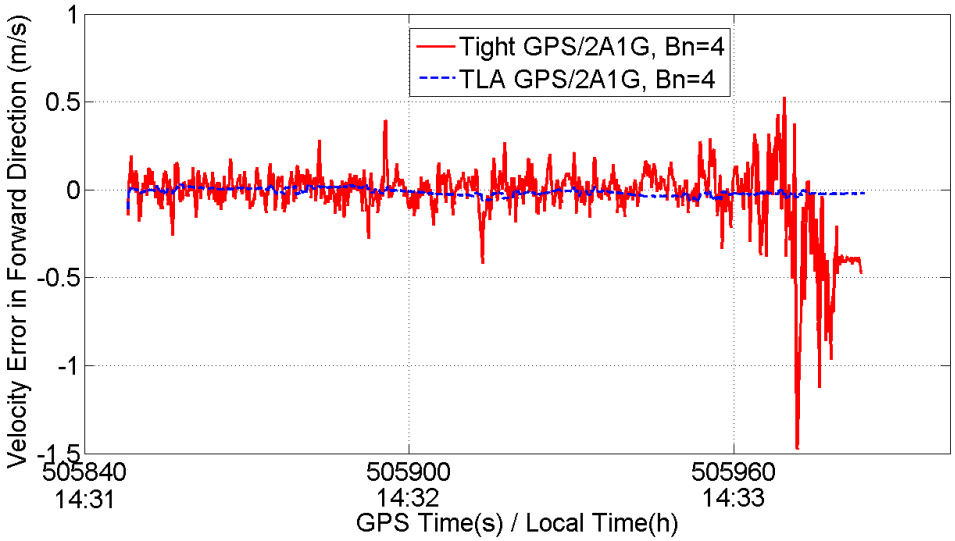

Figure 4.17 Forward Velocity Errors of TLA and Tight GPS/2A1G (HG1700)

4.6.2 Test Results with Vehicle Test Data

With vehicle test data, the TLA GPS/RIMU is evaluated both in terms of the number of SVs used in the navigation solution and the system navigation performance. The number of SVs used in the navigation solution also can be used as a criterion to assess the tracking performance, i.e. generally, the more SV's used in the navigation solution, the better the tracking performance. In order to simplify analysis, only the test results of GPS/3A1G (Crista) are shown in the following. To investigate the advantages of the TLA system, the test results of the TLA system and the corresponding tight system are displayed together. For the TLA GPS/3A1G, a noise bandwidth of 3 Hz was used, and a second-order loop filter was used for the reasons discussed in Section 4.3.2. For the tight GPS/3A1G, the noise bandwidth was set to 8 Hz and a third-order loop was used.

With the open sky data, the number of SVs used in the navigation solution of GPS/3A1G (Crista) is shown in Figure 4.18. The same plot for the foliage data is shown in Figure

4.19. Both of the two figures show that the TLA system has more SVs used in the navigation solution, especially for the foliage case. This means that with Doppler aiding, the tracking performance of the GPS receiver is improved, and the improvement is more obvious in the foliage case. This is because the PLL phase error is more sensitive to the noise bandwidth when the C/N_0 is low. That is, when the C/N_0 is low, narrowing the noise bandwidth can significantly reduce the PLL phase error (Ward et al 2006). This result is consistent with the theory.

The navigation performance of the GPS/3A1G (Crista) is summarized in Table 4.1 for the open sky case, and Table 4.2 for the foliage case. From the two tables, it can be seen that the TLA GPS/3A1G has a better performance than the corresponding tight system in terms of velocity and attitude, especially for velocity. Compared to the tight system, the RMS three-dimensional (3D) velocity error of the TLA system is reduced by 54% for the foliage case; for the open sky case, it is only a bit. In the both cases, both pitch and roll error are reduced a little, if at all, but the azimuth error is noticeably reduced. Specifically in foliage case, the RMS azimuth error of TLA GPS/3A1G (Crista) is reduced by 26% compared to the tight GPS/3A1G (Crista). Furthermore, the attitude error reduction of the TLA system is more obvious in the foliage case than in the open sky case. Also, it can be seen that compared to the foliage case, the open sky test has much smaller velocity error but has a greater pitch error. This is because the two test routes have different local terrain. The position errors of the TLA GPS/3A1G with open sky data and foliage data are summarized in Table 4.3. This table shows that the position errors are only few metres (less than 10 m in 3D) for the both test routes. These values are only used to show

how the magnitude of position errors vary with the two test routes (i.e. the open sky and foliage). These position errors mainly come from the GPS solution. So if the position error needs to be reduced, a DGPS and/or a real time kinematic (RTK) technique needs to be applied.

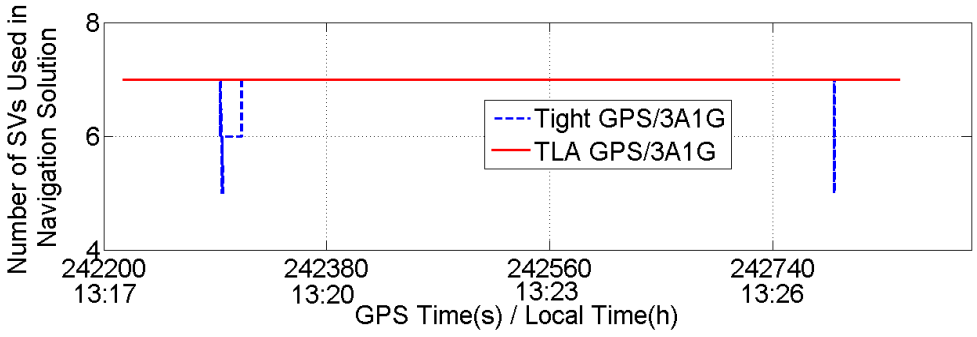

Figure 4.18 Number of SVs Used in Navigation Solution of TLA and Tight GPS/3A1G (Crista) with Open Sky Data

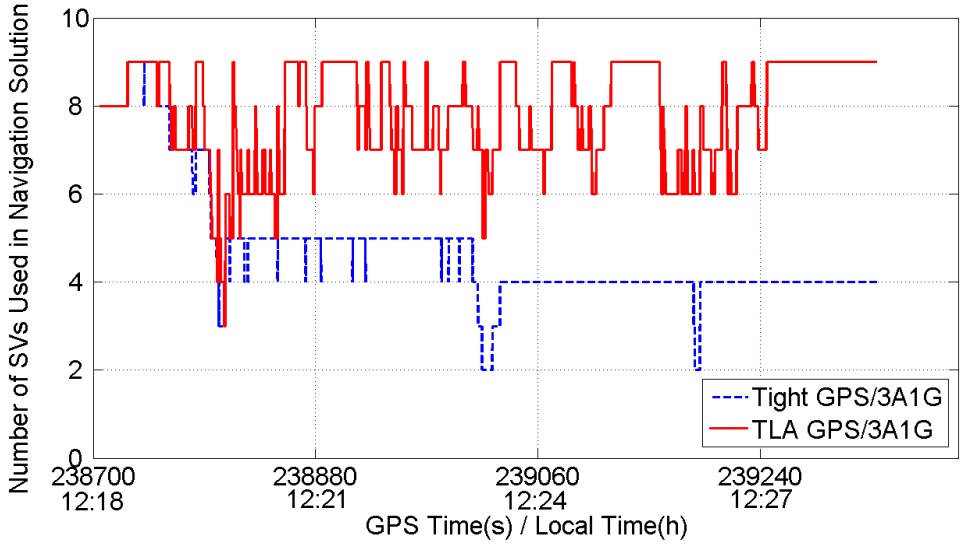

Figure 4.19 Number of SVs Used in Navigation Solution of TLA and Tight GPS/3A1G (Crista) with Foliage Data

Table 4.1 Velocity and Attitude Error of TLA and Tight GPS/3A1G (Crista) with Open Sky Data

Integration Strategy	RMS Attitude Error (Deg)			RMS Velocity Error (m/s)		
	Pitch	Roll	Azimuth	East	North	Up
TLA GPS/3A1G	0.65	0.58	2.54	0.04	0.04	0.03
Tight GPS/3A1G	0.65	0.59	2.96	0.04	0.05	0.04

Table 4.2 Velocity and Attitude Error of TLA and Tight GPS/3A1G (Crista) with Foliage Data

Integration Strategy	RMS Attitude Error (Deg)			RMS Velocity Error (m/s)		
	Pitch	Roll	Azimuth	East	North	Up
TLA GPS/3A1G	0.33	0.63	2.71	0.07	0.08	0.03
Tight GPS/3A1G	0.46	0.76	3.64	0.11	0.18	0.11

Table 4.3 Position Error of TLA GPS/3A1G (Crista)

TLA GPS/3A1G	RMS Position Error (m)		
	East	North	Up
With Open Sky Data	0.83	1.69	6.27
With Foliage Data	4.18	1.57	7.08

4.6.3 Summary

With both the translation stage test data and the vehicle test data, the performance of the TLA GPS/RIMU was investigated in this section. In order to identify the TLA system's advantages, results of the TLA system were compared with those of the corresponding tight system. Through a series of the performance assessments in terms of tracking ability and navigation solution, the following conclusions can be drawn:

- In both ideal and real situations, i.e. on both the roof of a building and a real road, the TLA GPS/RIMU performed better than the corresponding tight system in terms of tracking ability and navigation solution.

- With Doppler aiding, the tracking performance of the GPS receiver was improved. Specifically, there were more satellites used in the navigation solution, and the Doppler shift measurement error was reduced.
- With Doppler aiding, the navigation performance of the TLA GPS/RIMU was improved, i.e. the 3D RMS velocity error was reduced by 54% (for the foliage case); both the pitch and roll error were reduced a little, if at all, but the azimuth error was more significantly reduced.

4.7 Evaluation of TLA GPS/RIMU with ALFs

Following the evaluation of TLA GPS/RIMU, the evaluation for TLA GPS/RIMU with ALFs is performed with vehicle test data. In the following, the term "TLA GPS/RIMU" means the PLL tracking loops of the GPS receiver have a constant noise bandwidth (CNB) loop filter, whereas the term "TLA GPS/RIMU with ALFs" means that the PLL tracking loops have an adaptive loop filter, as described in Section 4.3.2. The objective of this section is to investigate if the ALF algorithm is valid (i.e., can provide a proper noise bandwidth) and if the performance of the TLA GPS/RIMU with ALFs can be further improved, compared to with the constant noise bandwidth loop filter (CNBLF). For this purpose, in the following tests, both open sky and foliage test data were used for the evaluation of the TLA system with ALFs in terms of tracking and navigation performance improvement. In order to facilitate comparison, for the TLA GPS/3A1G, the (constant) noise bandwidth was chosen as 5 Hz for both grades of IMUs and both test routes (open sky and foliage). This value was selected based on the largest bandwidth computed using the ALF approach (about 5 Hz). In this way, the constant bandwidth results are "optimal", in the sense that the smallest bandwidth that captures the receiver

dynamics is used. Similarly, for the GPS/2A1G system, the CNB was set to 10 Hz based on the maximum computed value of about 10 Hz when the ALF was used. In the following, B_n is used to denote the tracking loop noise bandwidth.

4.7.1 Test Results with Open Sky Test Data

Before investigating the tracking and navigation performance of the TLA system with ALFs, variations in the attitude and velocity error of the TLA system are briefly reviewed.

4.7.1.1 Velocity and Attitude Error

For the TLA GPS/RIMU with ALFs, the velocity and attitude error of the 3A1G (Crista) are shown in Figure 4.20, and the corresponding error for the 2A1G (Crista) are shown in Figure 4.21. From these two figures, it can be seen that the TLA GPS/2A1G has more vertical velocity error, which will be quantified later.

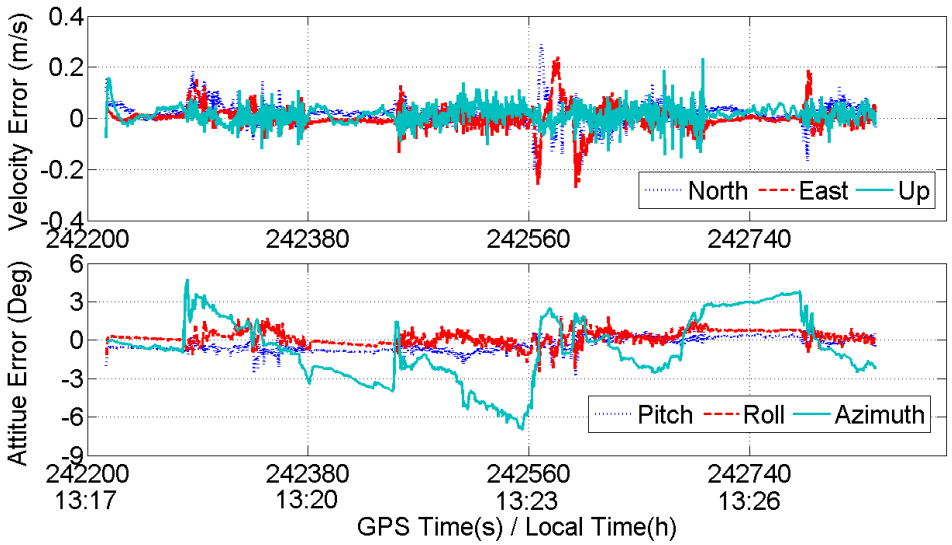

Figure 4.20 Velocity and Attitude Error of TLA GPS/3A1G (Crista) with ALFs and Open Sky Data

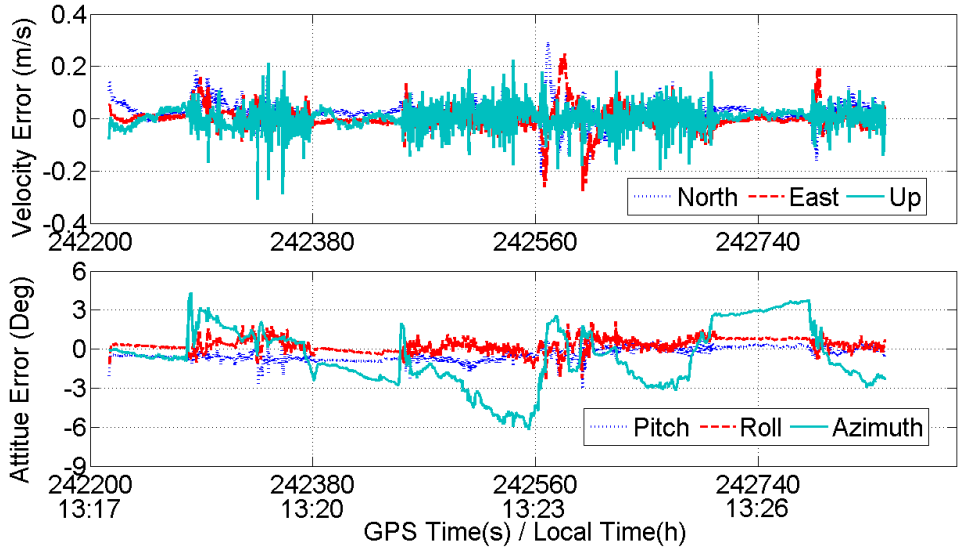

Figure 4.21 Velocity and Attitude Error of TLA GPS/2A1G (Crista) with ALFs and Open Sky Data

4.7.1.2 PLL Tracking Performance Comparison between ALF and CNBLF

In the following, PRN 27 is taken as an example to show the variations of phase lock indicator (PLI), Doppler shift error, and noise bandwidth. The reason for choosing PRN 27 is that it has high sensitivity to the vehicle's motion (most in the horizontal) since it has low elevation angle (about 23-18 degrees), as shown in Figure 4.8. Therefore, with PRN 27 it is easy to investigate not only the effect of the vehicle's dynamics on the noise bandwidth selection, but also the effect of the ALF on PLL tracking performance. The PLI, Doppler shift error, and noise bandwidth of PRN 27 in the TLA system are shown in Figure 4.22 and Figure 4.23. Figure 4.22 shows the tracking performance comparison of the TLA GPS/3A1G (Crista) with and without ALFs ("without ALFs" means "with CNBLFs"). Figure 4.23 shows the same plot for the GPS/2A1G (Crista) configuration.

From Figure 4.22, it can be seen that the Doppler error is reduced for the ALF case. Specifically, the RMS Doppler error with and without ALF is 0.23 Hz and 0.28 Hz, respectively. The phase lock indicator is not obviously improved. In fact, the PLL phase error is not necessarily reduced with the ALF, i.e. the PLI value is not necessarily increased (to approach 1) with the ALF if it is already greater than 0.9 (i.e. the PLL is locked (Ward et al 2006; Van Dierendonck 1996)). This can be explained from the ALF design strategy as given in Section 4.3.2. In the ALF design, when a signal is strong, the lowest bandwidth for which the PLL is locked is selected to minimize the overall Doppler error. As a result, the selected noise bandwidth (or the ALF) only promises to allow the PLL locked, it does not promise to necessarily increase the PLI value (i.e. to reduce the phase error). In addition, it is noted however that the phase lock in Figure 4.22 is occasionally degraded (i.e. PLI is much less than 0.9) over short time periods. This may be caused by unmodeled or unpredicted system errors, such as pitch and roll modeling errors in the reduced IMU and GPS multipath error. Figure 4.22 also shows the calculated noise bandwidth of the ALF for PRN 27, which is smaller than the corresponding constant noise bandwidth, as expected. From Figure 4.23, just like the 3A1G, similar conclusions can be obtained for the 2A1G configuration. Namely, the RMS Doppler error is reduced from 0.54 Hz to 0.26 Hz and the phase lock is improved to some extent. However, it is noted that the noise bandwidth in 2A1G is wider than in the 3A1G case. This is expected because of the unmodeled vertical acceleration when only using two accelerometers.

The RMS Doppler errors for all tracked satellites are summarized in Table 4.4 for the 3A1G, and Table 4.5 for the 2A1G. From these two tables, it can be seen clearly that with ALF, the Doppler errors are reduced compared to with CNBLF, as expected. In Table 4.5, for PRN 11, its RMS Doppler error with CNBLF (B_n=10 Hz) is much bigger than others, i.e. the RMS Doppler error is 1.20 Hz for PRN 11, but the maximum Doppler error is 0.54 for others. This is caused by a few seconds of sudden signal attenuation, resulting in an about 10 Hz frequency jump in the neighbourhood of GPS time 242300 s. This sudden signal attenuation in PRN11 also caused a Z-count error in navigation data decoding in a stand-alone GPS receiver test.

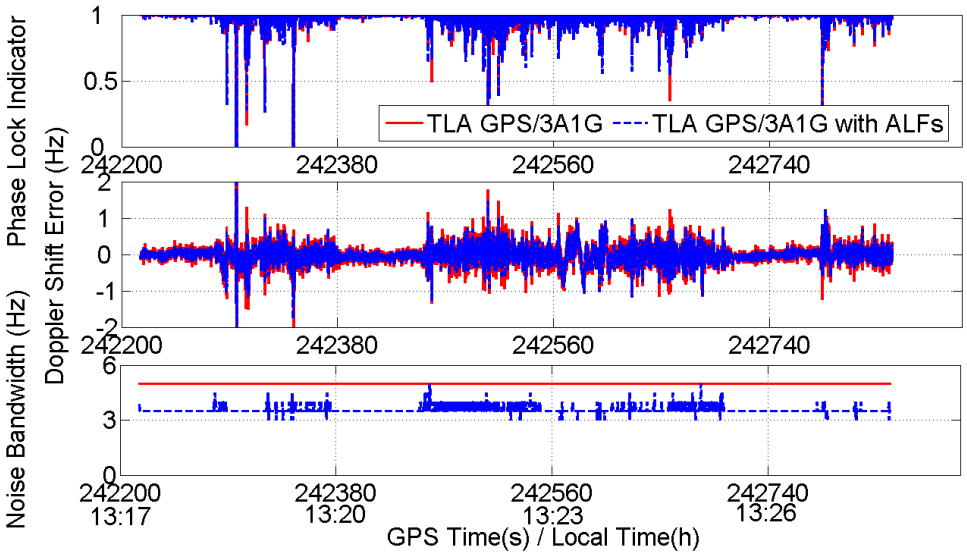

Figure 4.22 Tracking Performance of TLA GPS/3A1G (Crista) with and without ALFs for Open Sky Test and PRN 27

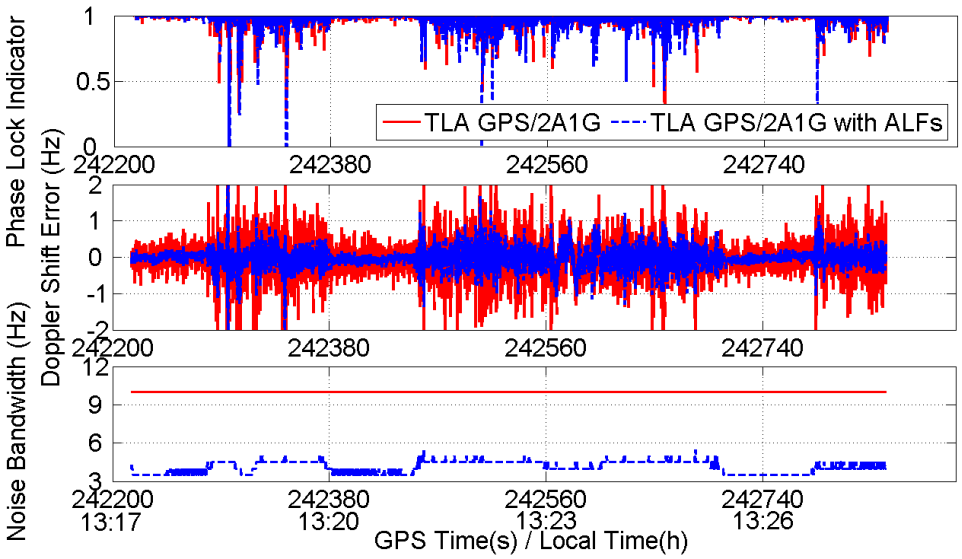

Figure 4.23 Tracking Performance of TLA GPS/2A1G (Crista) with and without ALFs for Open Sky Test and PRN 27

Table 4.4 RMS Doppler Errors of Tracked SVs in TLA GPS/3A1G (Crista) with and without ALFs for Open Sky Test

Tracking Loop Configuration	RMS Doppler Error per PRN (Hz)						
	8	11	17	26	27	28	29
ALF	0.15	0.19	0.14	0.17	0.23	0.14	0.16
CNBLF (B_n=5Hz)	0.17	0.23	0.15	0.19	0.28	0.16	0.19

Table 4.5 RMS Doppler Errors of Tracked SVs in TLA GPS/2A1G (Crista) with and without ALFs for Open Sky Test

Tracking Loop Configuration	RMS Doppler Error per PRN (Hz)						
	8	11	17	26	27	28	29
ALF	0.18	0.23	0.16	0.19	0.26	0.16	0.19
CNBLF (B_n=10Hz)	0.28	1.20	0.22	0.32	0.54	0.21	0.33

4.7.1.3 Navigation Performance Comparison between ALF and CNBLF

The statistical results of the TLA GPS/RIMU with ALFs are summarized in Table 4.6 and Table 4.7. Table 4.6 is the velocity and attitude error of TLA GPS/RIMU (Crista) with and without ALFs. Table 4.7 shows the same value for the HG1700 IMU. From Table 4.6, it can be seen that for the MEMS IMU, TLA GPS/3A1G with ALFs has

similar navigation performance as with CNBLFs ($B_n = 5$ Hz). Only the north velocity error of the ALF case is a little bit smaller than that of the CNBLF case, but the azimuth error is a little bit larger This is very likely because in the open sky test, the GPS signals are strong as shown in Figure 4.9, so a small reduction in noise bandwidth cannot significantly improve the navigation performance. Similar conclusions can be drawn for the tactical-grade inertial unit (see Table 4.7). The fact that the azimuth error of the 3A1G (Crista) with the ALF is a little bit bigger than that with the CNBLF is possibly caused by the correlated Doppler shift measurement error or occasional factors, such as the vertical gyro drift estimation situation before a stop. This needs to be further investigated with more test data in the future. The reason for choosing the correlated Doppler shift measurement error as a possible source causing a larger azimuth error is explained as follows: the Doppler shift measurement error can be correlated in time when the noise bandwidth of the PLL is narrowed. And the more the noise bandwidth is narrowed, the stronger the measurement error is correlated (Gelb 1974). This can affect the integration Kalman filter's stability or the integration system's performance (Bullock et al 2006).

For the 2A1G configuration, navigation performance can be improved by using the ALF approach compared to the CNBLFs ($B_n = 10$ Hz) approach for both the MEMS and tactical IMUs. For the MEMS IMU, the 3D RMS velocity error of GPS/2A1G with ALFs is reduced by 13%. The pitch and roll errors almost keep the same values, only the

azimuth error is reduced somewhat. For the tactical-grade IMU, similar conclusions can be obtained, with a 3D velocity error reduction of 15%.

Comparing the 3A1G and 2A1G results, it can be seen that the 3A1G case has smaller velocity errors and similar attitude error compared to the 2A1G case. This applies to both grades of IMUs and for both ALF and CNBLF. The improvement with the 3A1G case arises because, no matter whether ALFs are used or not, the system has smaller noise bandwidths because the extra accelerometer is better able to compensate for the receiver dynamics. In turn, the navigation solution performance is improved. It is noted that the improvement with the 3A1G case in the TLA GPS/RIMU is different from that in the loose GPS/RIMU (see Chapter Three). In the TLA GPS/RIMU, the improvement with the 3A1G case comes from not only the vertical accelerometer but also the narrower noise bandwidth of the PLL. As a result, in the TLA GPS/RIMU, not only the vertical velocity error but also the horizontal velocity error is reduced. However, in loose GPS/RIMU (see Tables 3.1 and 3.2), only the vertical velocity error is reduced with 3A1G case. In this light, for TLA GPS/RIMU, the 3A1G configuration is a better choice since it can allow a narrower noise bandwidth, resulting in not only a smaller vertical velocity error but also a smaller horizontal velocity error.

Table 4.6 Velocity and Attitude Error of TLA GPS/RIMU (Crista) with and without ALFs for Open Sky Test

Integration Strategy	RMS Attitude Error (Deg)			RMS Velocity Error (m/s)		
	Pitch	Roll	Azimuth	East	North	Up
TLA GPS/3A1G with ALFs	0.65	0.57	2.59	0.04	0.04	0.03
TLA GPS/3A1G (B_n=5Hz)	0.66	0.57	2.25	0.04	0.05	0.03
TLA GPS/2A1G with ALFs	0.65	0.59	2.37	0.04	0.05	0.04
TLA GPS/2A1G (B_n=10Hz)	0.66	0.59	2.66	0.05	0.05	0.05

Table 4.7 Velocity and Attitude Error of TLA GPS/RIMU (HG1700) with and without ALFs for Open Sky Test

Integration Strategy	RMS Attitude Error (Deg)			RMS Velocity Error (m/s)		
	Pitch	Roll	Azimuth	East	North	Up
TLA GPS/3A1G with ALFs	0.43	0.40	0.46	0.04	0.04	0.03
TLA GPS/3A1G (B_n=5Hz)	0.43	0.40	0.42	0.04	0.04	0.03
TLA GPS/2A1G with ALFs	0.43	0.40	0.47	0.04	0.04	0.04
TLA GPS/2A1G (B_n=10Hz)	0.44	0.42	0.53	0.04	0.05	0.05

4.7.2 Test Results with Foliage Test Data

With foliage test data, TLA GPS/RIMU with ALFs has similar velocity and attitude error variations as with open sky test data. As such, focus is given only to the tracking and navigation performance analysis as in the open sky test.

4.7.2.1 PLL Tracking Performance Comparison between ALF and CNBLF

Figure 4.24 compares the tracking performance of TLA GPS/3A1G (Crista) with and without ALFs for PRN 25. Figure 4.25 shows the same plot for the 2A1G (Crista) case. In this test, PRN 25 is selected for the same reason as in the open sky test, i.e. PRN 25 has low elevation angle (about 30-22 degrees), as shown in Figure 4.13. Its C/N_0 varies dramatically, and it still can keep tracking the signal, as shown in Figure 4.14.

From Figure 4.24 and Figure 4.25, it can be seen that for both 3A1G and 2A1G with ALFs, the Doppler errors are reduced. The improvement of the phase lock indicator is not obvious for 3A1G, but obvious for 2A1G, just like for the open sky test. In this foliage case, the test results of phase lock indicator are explained as follows: in the ALF design, when a signal is weak, the bandwidth that minimizes the total PLL phase error is selected (see Section 4.3.2). As a result, the selected noise bandwidth promises to have a minimum PLL phase error. However, it is noted that when the total phase error vs. noise bandwidth curve is relatively flat in a certain range of noise bandwidth, a small reduction in noise bandwidth cannot decrease the total phase error significantly. In this light, for 3A1G case, since the noise bandwidth reduction in the ALF is small (only 1-2 Hz), the improvement of phase lock indicator is not obvious. The RMS Doppler errors of all tracked satellites are summarized in Table 4.8 for the 3A1G (Crista), and Table 4.9 for the 2A1G (Crista). From these two tables, similar conclusions can be drawn as for the open sky test.

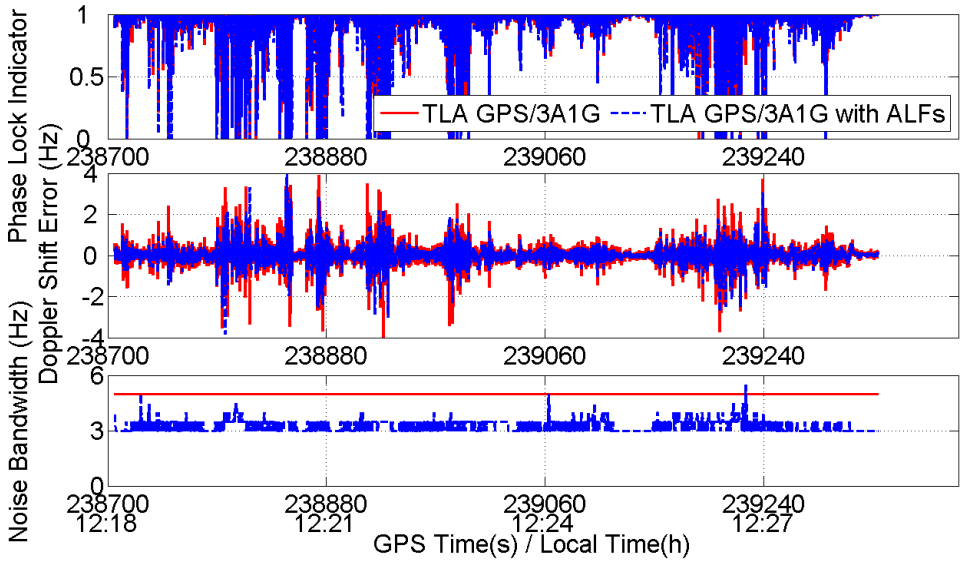

Figure 4.24 Tracking Performance of TLA GPS/3A1G (Crista) with and without ALFs for Foliage Test and PRN 25

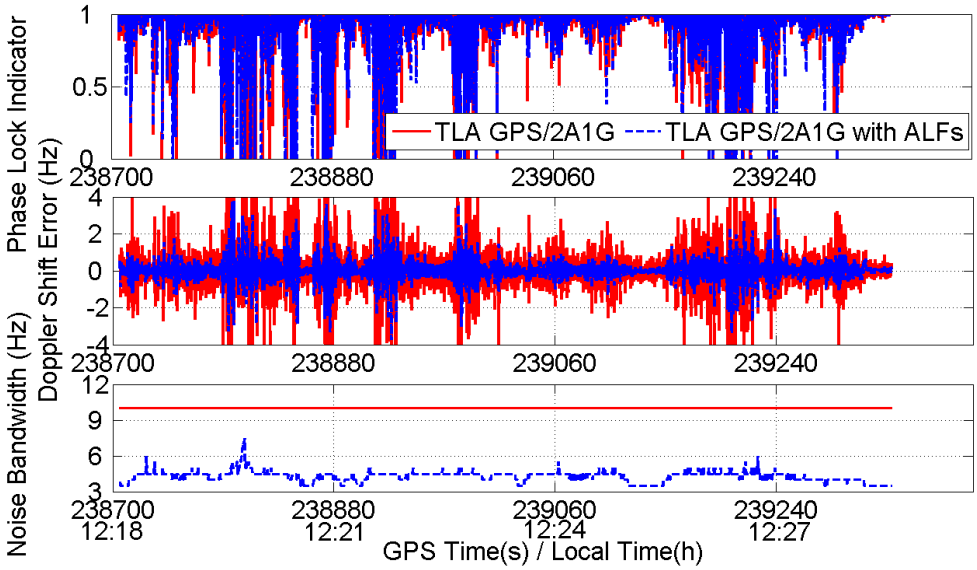

Figure 4.25 Tracking Performance of TLA GPS/2A1G (Crista) with and without ALFs for Foliage Test and PRN 25

Table 4.8 RMS Doppler Errors of Tracked SVs in TLA GPS/3A1G (Crista) with and without ALFs for Foliage Test

Tracking Loop Configuration	RMS Doppler Error per PRN (Hz)								
	8	11	17	19	25	26	27	28	29
ALF	0.14	0.56	0.60	0.67	0.41	0.27	0.20	0.15	0.23
CNBLF (B_n=5Hz)	0.21	0.67	0.71	0.81	0.53	0.38	0.30	0.23	0.33

Table 4.9 RMS Doppler Errors of Tracked SVs in TLA GPS/2A1G (Crista) with and without ALFs for Foliage Test

Tracking Loop Configuration	RMS Doppler Error per PRN (Hz)								
	8	11	17	19	25	26	27	28	29
ALF	0.26	0.60	0.70	0.80	0.49	0.38	0.33	0.27	0.35
CNBLF (B_n=10Hz)	0.44	1.47	1.46	1.60	1.17	0.83	0.64	0.48	0.71

4.7.2.2 Navigation Performance Comparison between ALF and CNBLF

The test results are summarized in Table 4.10 and Table 4.11. Table 4.10 lists the velocity and attitude errors of the MEMS IMU with and without ALFs. Table 4.11 shows the velocity and attitude errors of the tactical-grade IMU with and without ALFs. From Table 4.10, it can be seen that for the MEMS IMU, with ALFs, the 3D RMS velocity error of the 3A1G is reduced by 18%, the pitch and roll error are marginally reduced, and the azimuth error is reduced by 17%. Further, comparing the test results of TLA GPS/3A1G (Crista) with ALFs and with CNBLFs (B_n =3 Hz), as given in Table 4.10 and Table 4.2 respectively, it can be seen that the TLA system with ALFs has similar results as for the system with a CNB of 3 Hz. This noise bandwidth value of 3 Hz is the best that can be obtained for the 3A1G case (for the data collected). It is obtained through a series of noise bandwidth selection trials. This further demonstrates the ALF algorithm is valid and can provide a proper noise bandwidth for the Doppler-aided PLL. For the 2A1G case with ALFs, the 3D RMS velocity error is reduced by 19%, the pitch and roll error are reduced a little bit, and the azimuth error is reduced by 16%.

For the tactical-grade IMU, similar conclusions can be drawn except for the azimuth error. Specifically, for the 3A1G, the 3D RMS velocity error is reduced by 16%; for the 2A1G, the velocity error is reduced by 19%. In the both cases (3A1G and 2A1G), azimuth error

is small and keeps almost the same value (about 0.3 degrees). This results from the fact that the TLA system with the tactical-grade IMU takes much more azimuth information from the IMU (with more accurate azimuth calculation) than from the GPS.

Table 4.10 Velocity and Attitude Error of TLA GPS/RIMU (Crista) with and without ALFs for Foliage Test

Integration Strategy	RMS Attitude Error (Deg)			RMS Velocity Error (m/s)		
	Pitch	Roll	Azimuth	East	North	Up
TLA GPS/3A1G with ALFs	0.33	0.64	2.72	0.07	0.08	0.03
TLA GPS/3A1G (B_n=5Hz)	0.35	0.67	3.28	0.08	0.10	0.04
TLA GPS/2A1G with ALFs	0.43	0.64	3.31	0.08	0.10	0.05
TLA GPS/2A1G (B_n=10Hz)	0.46	0.71	3.93	0.09	0.12	0.08

Table 4.11 Velocity and Attitude Error of TLA GPS/RIMU (HG1700) with and without ALFs for Foliage Test

Integration Strategy	RMS Attitude Error (Deg)			RMS Velocity Error (m/s)		
	Pitch	Roll	Azimuth	East	North	Up
TLA GPS/3A1G with ALFs	0.29	0.59	0.33	0.07	0.08	0.03
TLA GPS/3A1G (B_n=5Hz)	0.31	0.61	0.27	0.08	0.10	0.03
TLA GPS/2A1G with ALFs	0.32	0.63	0.31	0.08	0.10	0.05
TLA GPS/2A1G (B_n=10Hz)	0.37	0.66	0.32	0.09	0.12	0.08

4.7.3 Summary and Discussion

From the above test results, it can be concluded that with ALFs, the PLL tracking performance of the TLA GPS/RIMU can be improved in terms of reducing the Doppler error and providing better phase tracking, especially for the 2A1G case. However, some unmodeled system errors may cause phase lock degradation during short time periods. Compared to the CNBLF case, the navigation performance of the TLA GPS/RIMU with ALFs is also improved. Specifically, the 3D RMS velocity error can be reduced by up to 19%. Similarly, pitch and roll errors also can be reduced, but only slightly. It was also

observed that azimuth error can be reduced by 17% for the MEMS IMU case. Comparing the 3A1G and 2A1G results, it can be concluded that the 3A1G case has smaller velocity error and similar or a little bit smaller attitude error than the 2A1G case (for the foliage test and MEMS IMU, it has smaller azimuth error). This is expected because the GPS/2A1G configuration inherently needs wider noise bandwidths (relative to the 3A1G case), which results in lower navigation performance. It follows therefore, that the 3A1G configuration is preferable. These conclusions are supported by the test results given in Sun et al (2010).

Compared to the open sky test results, the foliage test results show more clearly that the performance of the TLA GPS/RIMU with ALFs were improved relative to the CNBLF case. This implies that the ALF is more efficient in the foliage case (with serious GPS signal attenuations). This can be explained from the fact that when C/N_0 is high (>40 dB-Hz), the thermal phase jitter is small even if the noise bandwidth is wide (Ward et al 2006). Since the above improvements result only from implementing an adaptable noise bandwidth, we conclude that the proposed approach is both valid and effective. Correspondingly, the error model in Equation (4.5) and its underlying assumptions are considered sufficiently appropriate for the application at hand.

Finally, it is noted that the variability of the terrain, the operational environment (e.g., foliage, urban, etc.) and sensor quality will all affect performance of a given system and care should therefore be exercised when extrapolating the above results to other situations/conditions. That said, it is expected the proposed algorithm will still yield

benefits in all cases with appropriate filter tuning, but further testing is required to quantity the level of such improvements.

4.8 Summary

In this chapter, first the TLA GPS/RIMU system was introduced and analyzed. Its PLL phase error was derived. Based on the theoretical analysis, an adaptive PLL loop filter whose noise bandwidth can be adjusted according to the performance of the integration system and GPS signal C/N_0 was designed and applied to a TLA GPS/RIMU. Following the theoretical analysis and the ALF design, first the evaluation for TLA system was conducted with both the translation stage test data and the vehicle test data to investigate the advantages of the TLA system. Then evaluation for TLA system with ALFs was conducted to verify the ALF algorithm. In these evaluations, IMU configurations consisted of either 3A1G or 2A1G and both tactical and MEMS grade IMUs were used. From the evaluation results, some conclusions are drawn as follows:

- In both ideal and real situations, i.e. on both the roof of a building and a real road, the TLA GPS/RIMU performed better than the corresponding tight system in terms of tracking ability and navigation solution.
- With Doppler aiding, the tracking performance of the GPS receiver was improved, with more satellites being tracked, and smaller Doppler shift measurement error.
- With Doppler aiding, the navigation performance of the TLA GPS/RIMU was improved. The 3D RMS velocity error was reduced by 54% (for the foliage case); both the pitch and roll error were reduced a little, if at all, but the azimuth error was reduced obviously. Specifically in foliage case, the RMS azimuth error of

TLA GPS/3A1G (Crista) was reduced by 26% compared to the tight GPS/3A1G (Crista).

- The ALF was valid and provided a proper noise bandwidth for the Doppler-aided PLL of the TLA GPS/RIMU.
- With ALFs, the PLL tracking performance of the TLA GPS/RIMU was improved in terms of reducing the Doppler measurement error and providing better phase tracking, but some unmodeled system errors might cause phase lock degradation.
- With ALFs, the navigation performance of the TLA GPS/RIMU was improved, especially for velocity. The 3D RMS velocity error was reduced by up to 19%. The pitch and roll error was also reduced, but only slightly. The azimuth error was reduced by 17% for MEMS IMU and the foliage test data.
- In TLA GPS/RIMU, the 3A1G case outperformed the 2A1G case since it allowed a narrower noise bandwidth, resulting in not only a smaller vertical velocity error but also a smaller horizontal velocity error.

Chapter Five: Ultra-Tight GPS/Reduced IMU

As discussed in Chapters One and Two, in a UT GPS/IMU integration, the tracking loops of the GPS receiver are controlled by the navigation solution of the system thus resulting in vector-based tracking loops (i.e. VBTLs), namely a VDLL for code correlation and VFLL for carrier Doppler removal (Lashley et al 2008b; Petovello et al 2008a; Spilker Jr.1996). Since the VBTLs are closed via the navigation solution of the UT system, it offers some potential advantages over scalar-based tracking loops (i.e. SBTLs), such as improved weak signal tracking, enhanced anti-jamming ability, and more rapid signal recovery after a satellite blockage (Kennedy & Rossi 2008; Lashley & Bevly 2008a; Im et al 2007; Petovello & Lachapelle 2006a). As a result, the UT system outperforms GPS-only receivers (with SBTLs) in terms of tracking ability and navigation accuracy (Kennedy & Rossi 2008; Lashley & Bevly 2008a). The ultra-tight architectures mentioned in Section 1.2.4, namely VDF (Vector DLL and FLL) and VDCaP (Vector DLL with cascaded PLL), also apply to reduced IMU systems. As with a full IMU, UT GPS/RIMU has the same advantages, but the extent of the performance improvement is expected to be lower because the user dynamics cannot be removed as much as for the full IMU case.

With this in mind, the objectives of this chapter are threefold: 1) investigate the performance of UT GPS/RIMU systems with VDF and with VDCaP, 2) present two innovative algorithms/configurations for UT GPS/RIMU to improve system performance, and 3) compare the UT system with the corresponding TLA system to identify their respective advantages and disadvantages. Based on the above objectives, this chapter is

arranged as follows. First the UT GPS/RIMU is introduced, including the architectures and the implementations of the UT system. Specifically, the UT GPS/RIMU with VDF and UT GPS/RIMU with VDCaP systems are discussed. Second, an innovative algorithm/configuration (i.e. a cascaded PLL and FLL, or CaPF, composite loop) is developed to overcome the drawback of the cascaded PLL, thus producing more reliable Doppler measurements. Further, another innovative algorithm/configuration – reconfigurable tracking loops (RTLs) – for UT GPS/RIMU is developed to improve the system performance in the case when a partial GPS outage occurs. Third, the UT system is compared with the corresponding TLA system to identify their differences in both tracking and navigation performance. Finally, following the above theoretical development, evaluations for UT GPS/RIMU with VDF and UT GPS/RIMU with VDCaP are performed with real data. Further, the test results of UT system and the corresponding TLA system are compared to quantify their differences in tracking and navigation performance.

5.1 UT GPS/RIMU

Any GPS receiver must have both a code tracking loop and a carrier tracking loop (Borre et al 2007; Ward et al 2006). In a UT GPS/RIMU, these two tracking loops are implemented with VBTLs, which are closed via the navigation solution of the UT system. Thus the tracking loops of each channel are not independent, that is, the loops of different channels are coupled through the navigation solution, or navigation loop. The VBTLs can be implemented using either a traditional transfer function method (Kiesel et al 2007; Pany et al 2005) or a state-space method (Petovello et al 2008a; Crane 2007; Ohlmeyer 2006). Furthermore, with the state-space approach, a Kalman filter can be designed and

used for the VBTLs (Petovello et al 2008a; Crane 2007). In this chapter, only the transfer function approach is used. However, it is noted that if all noise sources are properly accounted for, both methods yield the same result. The benefit of the transfer function approach is that it does not require explicit consideration of intermediate states and thus can lead to a simpler analysis. In the UT GPS/RIMU, code tracking can be implemented with a VDLL and carrier tracking can be implemented with either a VFLL or a VPLL. Since a VPLL is quite difficult to implement, as discussed in Chapter One, an approximate VPLL, i.e. a cascaded PLL, is considered. Consequently, two kinds of UT systems are implemented: one is UT GPS/RIMU with VDF (or simply called VDF); the other is UT GPS/RIMU with VDCaP (or simply called VDCaP). These two UT systems are discussed below.

5.1.1 UT GPS/RIMU with VDF

The motivation for researching the VDF is that the VDF is one kind of UT system, which can be used in land vehicle navigation. Accordingly, the VDF research can provide some useful results for practical land vehicle navigation system design. The VDF system has been investigated in many publications including Lashley & Bevly (2008a), Soloviev et al (2007), and Pany & Eissfeller (2006). It is a common configuration for implementing a UT system. In order to understand and design the VDF system, the implementation and the measurement thermal noise of the VDF are discussed as follows.

5.1.1.1 VDF Implementation

In a UT GPS/RIMU with VDF, the code loop is implemented with a VDLL and the carrier loop is implemented with a VFLL. Its block diagram is shown in Figure 5.1. From this figure, it can be seen that both the code NCO and the carrier NCO are controlled by

the output of the integration system (i.e. the output of the integration Kalman filter). The pseudorange prediction error and carrier Doppler prediction error directly come from the corresponding discriminators.

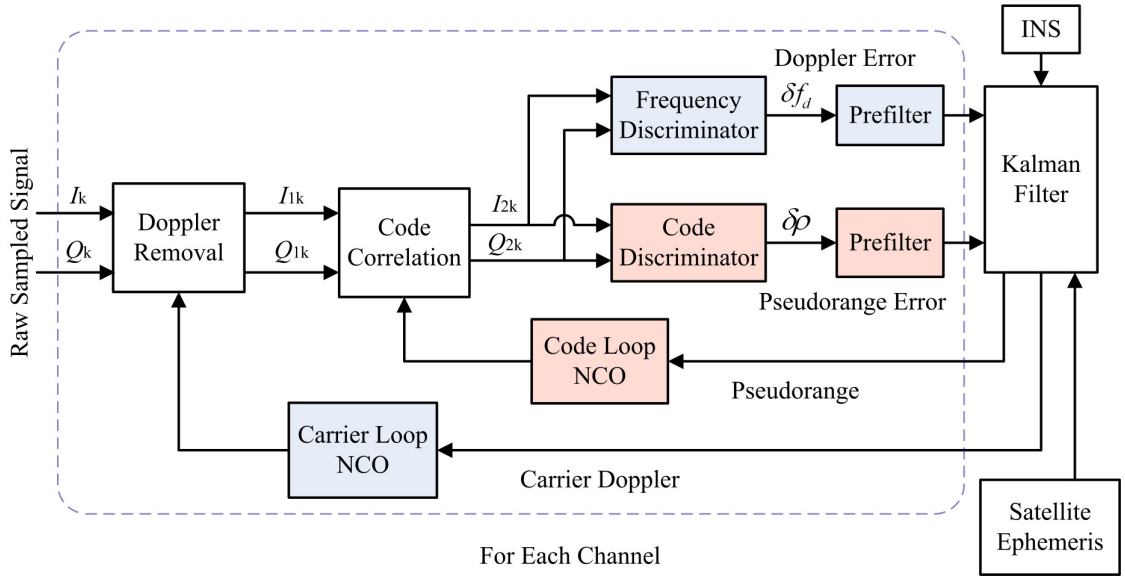

Figure 5.1 Vector-Based Tracking Loops of GPS Receiver (One Channel)

The block diagram of a VDLL is shown in Figure 5.2. With reference to this figure, z^{-1} represents a unit delay in z-transform. From Figure 5.2, it can be seen that in the VDLL, each channel's NCO is only controlled by the code phase and code Doppler, both calculated from the UT system and not the discriminator output. So the individual (channel) tracking loop is open. The code phase and code Doppler used for controlling the code NCO can be calculated with Equations (2.18) and (2.21), respectively. In the calculation, the noise and the unknown (or unmodeled) terms are ignored. Since the Doppler shift calculated from Equation (2.21) is a carrier Doppler, it needs to be transferred to a code Doppler by dividing 1540 (for C/A code and carrier L_1, or, more

generally, the ratio of the carrier frequency to the code chipping rate). In the code NCO, the calculated code phase is used to reset the output of the NCO; the calculated code Doppler is used to control the NCO. The output of the code tracking loop is

$$\rho_m = c \cdot \hat{\tau}_m = \rho_{NCO} + \overline{\rho}_{Dis} \tag{5.1}$$

where ρ_m is pseudorange measurement of the code loop, ρ_{NCO} is the pseudorange output of the NCO, and $\overline{\rho}_{Dis}$ is the smoothed pseudorange error output of the discriminator, where $\rho = c \cdot \tau$, τ is the corresponding code phase (expressed in time), c is the speed of light. In practice, it is generally assumed that $\rho_{NCO} \approx \rho_{Est}$, where ρ_{Est} is the calculated pseudorange.

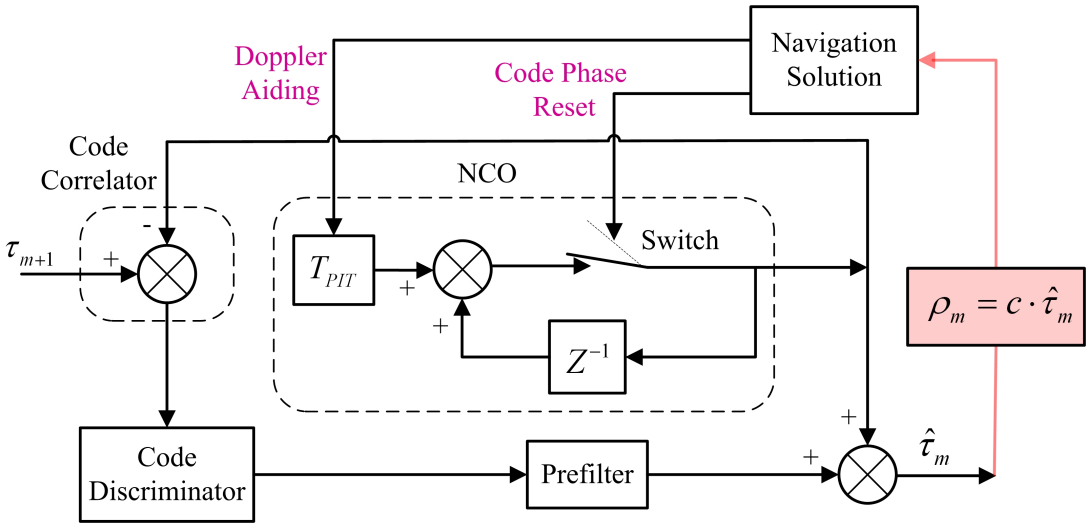

Figure 5.2 Block Diagram of VDLL's Lock Loop (One Channel)

The block diagram of the VFLL is shown in Figure 5.3. φ_r is input carrier phase, φ is output carrier phase, f_{da} is Doppler aiding, $\overline{f}_{Dis}$ is smoothed Doppler error output of the frequency discriminator, and $\hat{f}_d$ is the output of the tracking loop. Figure 5.3 shows that

in the VFLL, each NCO is only controlled by carrier Doppler aiding calculated from the UT system. So the individual (channel) carrier tracking loop is open, just like in the VDLL. The Doppler aiding is the same as that calculated in the VDLL, but expressed as a carrier Doppler (not code Doppler). The output of the frequency tracking loop is

$$f_{dm} = \hat{f}_d = f_{da} + \bar{f}_{Dis} \tag{5.2}$$

where f_{dm} is the carrier Doppler measurement of the frequency loop.

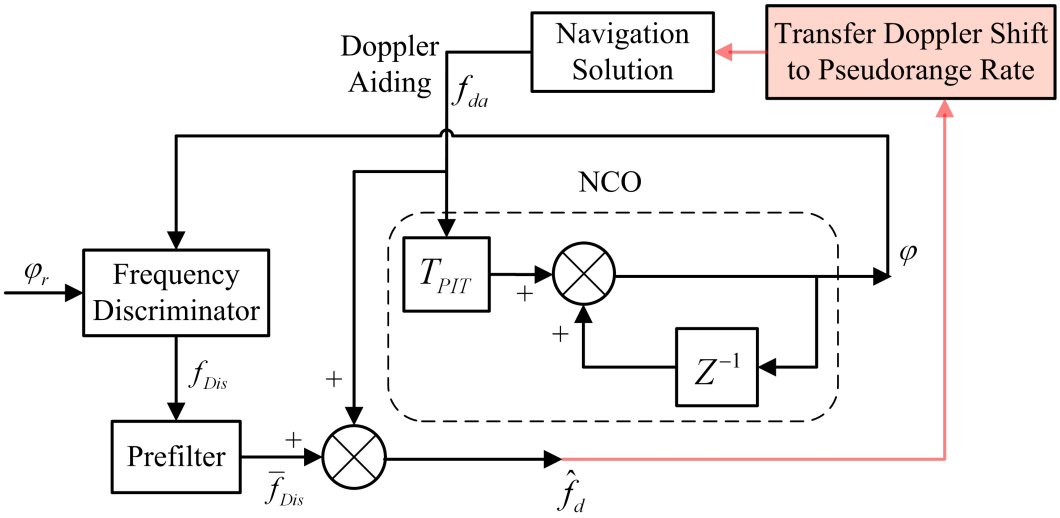

Figure 5.3 Block Diagram of VFLL Tracking Loop (One Channel)

From the block diagrams of VDLL and VFLL, it can be seen that each discriminator (for both VDLL and VFLL) has a prefilter used for smoothing the discriminator's output, thus providing a smoothed estimation error measurement (for pseudorange and Doppler shift). This smoothed error measurement can be used as the measurement to the Kalman filter of the UT GPS/RIMU (see Figure 5.1) since the measurement of the Kalman filter equals the actual measurement value minus the estimated value (see Equation (2.29)). Generally the output rate of the discriminator is high (for example, if the predetection integration

time is $T_{PIT} = 20$ ms, the output rate is 50 Hz), whereas the measurement update rate of the integration Kalman filter is low (for example, the update rate is typically 10 Hz or less). In order to filter the measurement noise of a discriminator, a prefilter is therefore required (each channel has one individual prefilter for code and one individual prefilter for carrier). The prefilter can be implemented with different algorithms, such as an averaging algorithm (Bullock et al 2006), a linear model fitting algorithm (Pany et al 2005), and a Kalman filter algorithm (Lashley et al 2008b; Crane 2007; Petovello & Lachapelle 2006a). To simplify computation, an averaging algorithm is used in this chapter for both VDLL and VFLL.

For the VDLL, the prefilter algorithm is

$$\bar{\rho}_{Dis}(k+1) = \frac{1}{L}\sum_{i=1}^{L}\rho_{Dis}(kL+i) \tag{5.3}$$

where $\bar{\rho}_{Dis}(k+1)$ is the output of the prefilter (i.e. the smoothed pseudorange error output), $\rho_{Dis}(kL+i)$ is the output of the code discriminator (i.e. the input of the prefilter), L is the number of discriminator outputs in a measurement update period of the integration Kalman filter, k is the discrete time of the prefilter's output, $kL+i$ is the discrete time of the discriminator's output. For the VFLL, the averaging algorithm is

$$\bar{f}_{Dis}(k+1) = \frac{1}{L}\sum_{i=1}^{L} f_{Dis}(kL+i) \tag{5.4}$$

where $\bar{f}_{Dis}(k+1)$ is the output of the prefilter, and $f_{Dis}(kL+i)$ is the output of the frequency discriminator (see Figure 5.3).

5.1.1.2 VDF Measurement Noise

The motivations for discussing the VDF measurement noise are twofold: 1) the measurement noise analysis can be used in the performance discussion of the VDF; and 2) the measurement noise analysis also can be used in the performance comparison of the UT and TLA systems. To simplify analysis, only the thermal noises of the VBTLs (i.e. VDLL and VFLL) and the corresponding SBTLs (i.e. DLL and FLL) are discussed and compared in the following.

Since in VDLL and VFLL the individual tracking loops are open, the measurement noise of the discriminators cannot be suppressed through a locally-closed loop (i.e. an individual loop). Fortunately the prefilter is used to filter out some measurement noise of the discriminator. For a code loop, if the variance of the measurement thermal noise of the discriminator (i.e. in the discriminator output) is $\sigma^2_{\rho Dis}$, the variance of the pseudorange measurement thermal noise of the locally-closed loop (i.e. DLL) is (Misra & Enge 2001; Van Dierendonck et al 1992)

$$\sigma^2_{\rho DLL} = 2B_n T_{PIT} \sigma^2_{\rho Dis} \tag{5.5}$$

where B_n is the noise bandwidth of the locally-closed code loop (i.e. a scalar-based tracking loop), and T_{PIT} is predetection integration time. The calculation equation of $\sigma_{\rho DLL}$ is given in Misra & Enge (2001). The variance of the pseudorange measurement thermal noise of the VDLL (for each channel) can be obtained from the prefilter (with averaging algorithm, see Equation (5.3)), and is given as

$$\sigma^2_{\rho VDLL} = \sigma^2_{\rho Dis} / L \tag{5.6}$$

This eqaution is obtained from the assumption that the output noises (at different times) of the discriminator are independent (Misra & Enge 2001). Suppose $T_{PIT} = 20$ ms, $B_n = 0.05$ Hz (for Doppler-aided code loop), and the measurement update rate of the integration Kalman filter is 10 Hz, then $L = 5$ (i.e. Kalman filter update period (100 ms) divided by T_{PIT} (20 ms)), and $2B_nT_{PIT} = 2\times10^{-3} \ll 1/L = 0.2$ (where $2B_nT_{PIT}$ is the coefficient of $\sigma^2_{\rho Dis}$ in Equation (5.5), and $1/L$ is the coefficient of $\sigma^2_{\rho Dis}$ in Equation (5.6)). So compared to a scalar-based code loop (i.e., a DLL), a VDLL has much greater measurement thermal noise.

In a similar way, if the variance of the measurement thermal noise of a frequency discriminator (i.e. in the discriminator output) is σ^2_{fDis}, the variance of the Doppler measurement thermal noise of the FLL is (Misra & Enge 2001)

$$\sigma^2_{fdFLL} = 2B_nT_{PIT}\sigma^2_{fDis} \tag{5.7}$$

The calculation equation of σ_{fdFLL} is given in Equation (5.16). The variance of the measurement thermal noise of the VFLL (for each channel) is

$$\sigma^2_{fdVFLL} = \sigma^2_{fDis} / L \tag{5.8}$$

Again, for $T_{PIT} = 20$ ms, $B_n = 5$ Hz (for a Doppler-aided FLL), and $L = 5$, $2B_nT_{PIT} = 0.2 = 1/L$ is obtained. For these parameters, the VFLL and the FLL have the same measurement noise variance.

5.1.2 UT GPS/RIMU with VDCaP

The motivation for the VDCaP research is the same as that of the VDF research, i.e. the VDCaP is another kind of UT system, which can be used in land vehicle navigation, and the VDCaP research can provide useful information for practical land vehicle navigation system design. Furthermore, for carrier phase loop, a cascaded PLL (CaPLL) outperforms a Doppler-aided PLL (DaPLL) in some cases such as weak GPS signal case, which will be discussed below.

There are quite a few publications discussing the VDCaP approach, such as Petovello et al (2008a), Crane (2007), and Ohlmeyer (2006). Since a PLL outperforms a VFLL or a FLL in terms of Doppler estimation and navigation data bit estimation, i.e. the VFLL or FLL can decrease velocity estimation quality, and increase the complexity in estimating navigation bits (Kiesel et al 2007), the VDCaP is more popular than the VDF in implementing a UT system. It is noted that the conclusion that a VFLL or FLL can decrease velocity estimation quality compared to a PLL should be obtained from the thermal noise and steady state of the tracking loop. If the Doppler jitter caused by both the transient state of the tracking loop and the C/N_0 variations is considered, this conclusion should be amended. In the following, first the implementation of the VDCaP is discussed including the cascaded PLL design. Then the Doppler measurement thermal noise of the VDCaP, which is caused by the discriminator output noise, is derived and compared with that of a VFLL.

5.1.2.1 VDCaP Implementation

The VDCaP has a similar block diagram as that in Figure 5.1. In a UT GPS/RIMU with VDCaP, the code loop is implemented with a VDLL and the carrier loop is implemented with a cascaded PLL. As discussed in some papers such as Petovello et al (2008a), Crane (2007), and Ohlmeyer (2006), the cascaded PLL can be implemented with a local Kalman filter and the carrier NCO is controlled by both the local filter and the navigation filter. Furthermore, the local filter is reinitialized after each navigation filter cycle, i.e. the state variables of the local filter are set to zero after each measurement update of the navigation filter (Crane 2007). In this section, the VDLL of the VDCaP is the same as that of the VDF. The CaPLL is implemented with a traditional tracking loop and is similar to the Doppler-aided PLL discussed in Chapter Four. It differs from the DaPLL because the CaPLL is reset under some conditions, as described in Crane (2007). The block diagram of the CaPLL is shown in Figure 5.4. From this figure, it can be seen that the Doppler measurement of the CaPLL is

$$f_{dm}(k) = \hat{f}_d(k) = f_{da}(k) + f_{LF}(k) \tag{5.9}$$

where f_{LF} is the Doppler error output of the loop filter, k is discrete time. Other variables are defined in Equation (5.2). When the loop filter is reset, the state variables of the filter are set to zero.

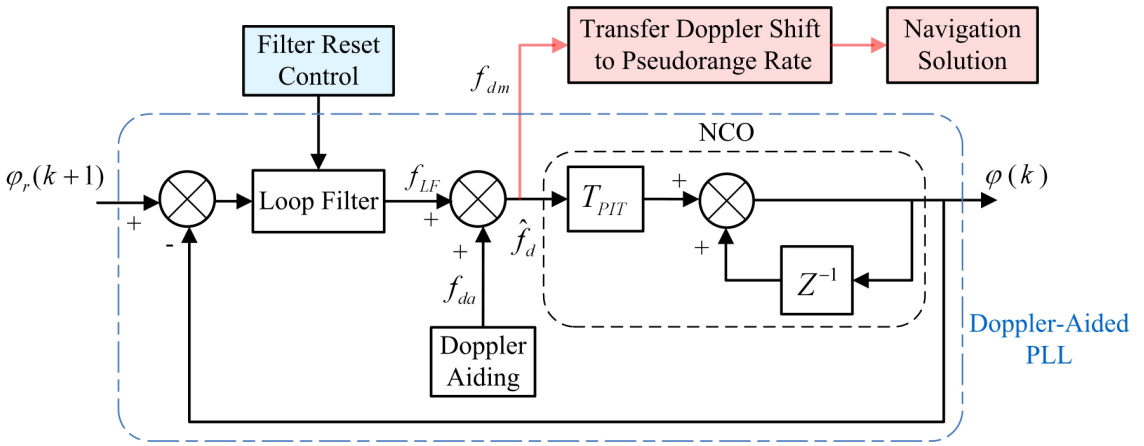

Figure 5.4 Block Diagram of Cascaded PLL (One Channel)

For a second-order loop filter (used in the carrier phase loop in this Chapter), as shown in Figure 5.5, resetting state variables to zero means that $f_{LF}(k)=0$ and $f_{sum}(k)=0$ (see Crane (2007)). With reference to Figure 5.5, $f_{sum}(k)$ is the output of the integrator of the loop filter, and $e_{\varphi}(k)=\varphi_r(k)-\varphi(k-1)$ is the error signal of the system (Misra & Enge 2001), where $\varphi_r(k)$ is the input phase of the phase tracking loop, $\varphi(k-1)$ (for initial state $\varphi(-1)=\hat{\varphi}_r(0)$) is the output phase of the loop. ξ is the damping ratio of the second-order system, ω_n is the undamped natural frequency. The output Doppler of the second-order loop filter, $f_{LF}(k)$, can be written as

$$f_{LF}(k)=f_{sum}(k)+2\xi\omega_n e_{\varphi}(k)=f_{sum}(k-1)+T_{PIT}\omega_n^2 e_{\varphi}(k)+2\xi\omega_n e_{\varphi}(k). \tag{5.10}$$

Before proceeding, it is worth noting that the loop filter is effectively tracking the error in the aided Doppler data. As such, under nominal conditions when the INS is well calibrated, $f_{LF}(k)$ will be close to zero (if Doppler aiding has no error). More generally,

$f_{LF}(k)$ will consist of two parts: one is the Doppler aiding error and the other is an "extra" Doppler which is generated to drive the difference between in the local and incoming *phase* to zero according to the designed control law of the loop (Nise 2000; Ogata 1997). Generally the control law controls the difference between in the local and incoming phase to zero quickly. When the output phase completely follows the incoming phase (i.e. the DaPLL is completely stabilized or in steady state), this extra Doppler value will approach to zero (Ogata 1997). Thus the $f_{LF}(k)$ will be equal or approximately equal to the Doppler aiding error (with very small error).

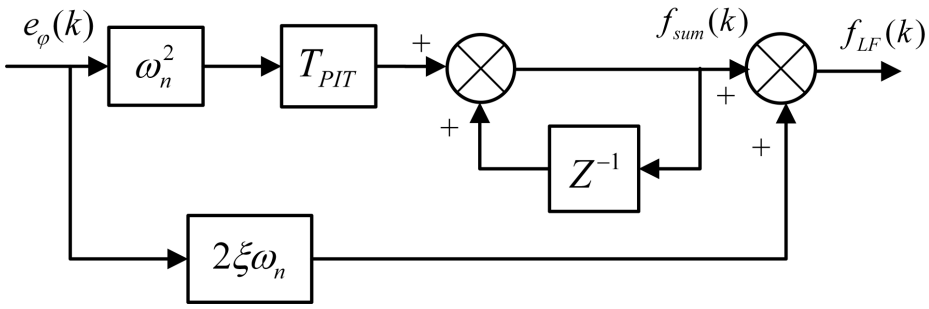

Figure 5.5 Block Diagram of Second-Order Loop Filter

Furthermore, from Equation (5.10), it can be seen that the output of the loop filter is not only related to the output of the integrator of the loop filter, but also related to the error signal $e_\varphi(k)$. In the DaPLL, $f_{LF}(k)$ serves the purpose of both compensating the Doppler aiding error (i.e. the error of f_{da}) and eliminating the error signal $e_\varphi(k)$, as discussed above. If the error signal $e_\varphi(k)$ is caused by the system's dynamics, $f_{LF}(k)$ controls $\varphi(k)$ to follow the $\varphi_r(k+1)$ (see Figure 5.4). In this case, although $f_{LF}(k)$ is not completely equal to the Doppler aiding error (i.e. it contains an extra Doppler value for

controlling the output phase, as discussed above), the loop filter should not be reset. This is because the two parts of $f_{LF}(k)$ are both useful: one is for compensating the Doppler aiding error, the other is for controlling the output phase to converge to the input phase quickly.

On the other hand, if $e_{\varphi}(k)$ is mostly caused by noise (thermal or other noise), $f_{LF}(k)$ will contain another Doppler value, which is caused by the noise alone. If the GPS signal is strong enough, this Doppler noise term can be ignored, like in the above discussion. However, for weak signals, this term can become significant and must be considered. Suppose the Doppler aiding error compensation part of the $f_{LF}(k)$ is $f_{LF,DAE}(k)$, the extra Doppler value for control is $f_{LF,Con}(k)$, and the Doppler noise part is $f_{LF,Noi}(k)$. In some foliage or weak GPS signal cases, frequently $f_{LF,Noi}(k)$ is much larger than $f_{LF,DAE}(k)$ and $f_{LF,Con}(k)$ (especially for wide loop noise bandwidth case), resulting in the phase loop losing lock on the signal. In this case, the $f_{LF}(k)$ might seriously deviate from the $f_{LF,DAE}(k)$. In these cases, resetting the loop filter can constrain the deviation of the $f_{LF}(k)$ from the $f_{LF,DAE}(k)$ (i.e. constrain the term $f_{LF,Noi}(k)$), helping the loop to recover quickly.

From the above analysis, it can be seen that the criteria for the loop filter reset should be carefully designed. The loop filter can be reset after every measurement update of the navigation filter, as discussed in Crane (2007). This can disturb the process of controlling

the output phase $\varphi(k-1)$ to converge to the input phase $\varphi_r(k)$ (see Figure 5.4), resulting in a delay in phase lock. In contrast, in order to overcome this disadvantage, the loop filter can be reset according to the following criteria:

- In a strong signal case, the loop filter is not reset.
- In a weak signal case, when $PLI < T_{PLI}$ and $\left|f_{dm} - f_{da}\right| > T_{fd}$, reset the loop filter. Here, T_{PLI} is a PLI threshold, f_{dm} and f_{da} are defined in Equation (5.2), and T_{fd} is a Doppler error threshold.

In practice, T_{PLI} and T_{fd} should be chosen carefully, for example, $T_{PLI} = 0.3$ and $T_{fd} = 1-2$ Hz (they are empirical values). When the loop filter of a CaPLL is not reset in a test, the CaPLL becomes a DaPLL.

From the above loop filter reset criteria, it can be seen that only in weak signal cases and/or when the loop has lost lock and the deviation of the output of the loop filter from the Doppler aiding error is beyond a certain value should the loop filter be reset. Adopting such an approach will limit the deviation of the output of the loop filter from the Doppler aiding error and help the loop recover quickly from a loss of lock, as discussed above. Consequently, the CaPLL should outperform the DaPLL when the loop filter reset is applied. That is why in some TLA system tests in this dissertation (e.g. foliage test, see Section 5.7.2), the loop filter is also reset according to the same reset criteria as that of the CaPLL.

5.1.2.2 Doppler Measurement Noise

The motivation for discussing the Doppler measurement noise of the CaPLL is that the measurement noise analysis can be used in the navigation performance discussion of the VDCaP, and in the performance comparison of the VDF and VDCaP. To simplify analysis, only the Doppler measurement thermal noise of the CaPLL is discussed and compared with that of the VFLL. Actually, in the Doppler thermal noise analysis, a CaPLL can be equivalent to a PLL (with lower noise bandwidth compared to a PLL without Doppler aiding). From this light, the Doppler measurement thermal noise of a PLL is discussed below.

Compared to an FLL, the Doppler measurement thermal noise of a PLL is smaller (Ward et al 2006). However, a comparison between a PLL and a VFLL has not been performed. Although Kiesel et al (2007) gave the conclusion that a VFLL can decrease velocity estimation quality compared to a PLL, no formula or more information was given. In this section, the Doppler measurement noise comparison of a PLL and a VFLL will be made from theoretical analysis and equations. In order to compare the Doppler measurement noises of a PLL and a VFLL, the Doppler measurement thermal noise variance of the PLL needs to be derived first. To simplify the derivation, a first-order loop is used, as shown in Figure 5.6 (Misra & Enge 2001), since it is not easy to derive the Doppler noise variance directly from a second-order loop. Although using the Doppler noise variance of a first-order loop to replace that of a second-order loop is not perfect in the thermal noise analysis, it still has some instructive significance to the thermal noise analysis of the

second-order loop. In this light, the Doppler thermal noise variance derived from a first-order loop will be used in this chapter.

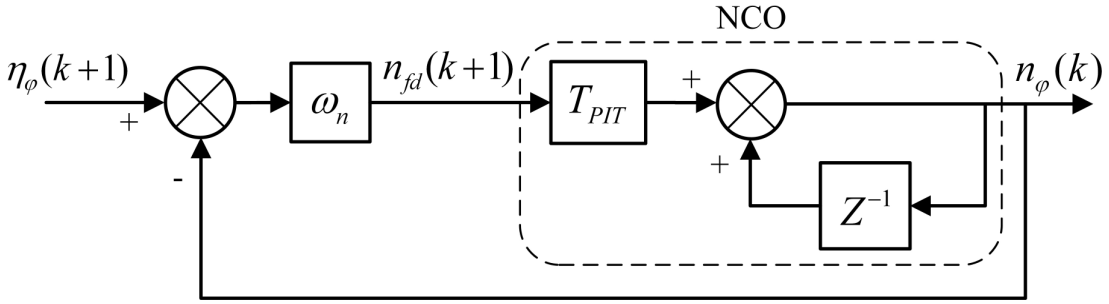

Figure 5.6 Block Diagram of First-Order Phase Lock Loop

In Figure 5.6, η_φ is the discriminator output noise (i.e. thermal noise), n_φ is the loop output noise, and n_{fd} is the Doppler measurement noise. The variance of η_φ is expressed as (Misra & Enge 2001)

$$Var(\eta_\varphi) = \frac{1}{2T_{PIT}C/N_0}\left(1+\frac{1}{2T_{PIT}C/N_0}\right) \tag{5.11}$$

where C/N_0 is the carrier to noise power density. For the phase tracking loop, the variances of the input noise η_φ and the output noise n_φ have the following relationship (Misra & Enge 2001)

$$Var(n_\varphi) = 2B_n T_{PIT} Var(\eta_\varphi) \tag{5.12}$$

Since $\eta_\varphi(k+1)$ and $n_\varphi(k)$ are independent, the variance of $n_{fd}(k+1)$ is obtained as

$$Var(n_{fd}) = \omega_n^2\left(Var(n_\varphi)+Var(\eta_\varphi)\right) = \omega_n^2\left(2B_n T_{PIT} Var(\eta_\varphi)+Var(\eta_\varphi)\right) \tag{5.13}$$

For a first-order loop, $\omega_n = 4B_n$ (Ward et al 2006). Substituting this equation and Equation (5.11) into Equation (5.13) yields

$$Var(n_{fd}) = \frac{16B_n^2}{C/N_0}\left(1+\frac{1}{2T_{PIT}C/N_0}\right)\left(B_n+\frac{1}{2T_{PIT}}\right) \text{ (rad/s)}^2 \tag{5.14}$$

Expressing $Var(n_{fd})$ in Hertz yields

$$\sigma_{fdPLL} = \frac{\sqrt{Var(n_{fd})}}{2\pi} = \frac{2B_n}{\pi}\sqrt{\frac{1}{C/N_0}\left(1+\frac{1}{2T_{PIT}C/N_0}\right)\left(B_n+\frac{1}{2T_{PIT}}\right)} \text{ (Hz)} \tag{5.15}$$

where σ_{fdPLL} is the Doppler measurement thermal noise standard deviation obtained from the first-order PLL.

The analysis now shifts to computing the standard deviation of the Doppler measurement thermal noise for a VFLL. In order to derive the thermal noise standard deviation of the VFLL, the standard deviation of the Doppler measurement thermal noise of an FLL is needed first and can be expressed as (Ward et al 2006)

$$\sigma_{fdFLL} = \frac{1}{2\pi T_{PIT}}\sqrt{\frac{4\zeta_f B_n}{C/N_0}\left[1+\frac{1}{T_{PIT}C/N_0}\right]} \text{ (Hz)} \tag{5.16}$$

where ζ_f is a coefficient that is usually selected as $\zeta_f = 1$ at high C/N_0, and $\zeta_f = 2$ near threshold (Raquet 2004). With Equations (5.7), (5.8) and (5.16), the standard deviation of the Doppler measurement thermal noise of the VFLL is obtained as

$$\sigma_{fdVFLL} = \frac{1}{2\pi T_{PIT}}\sqrt{\frac{2\zeta_f}{L\cdot T_{PIT}C/N_0}\left[1+\frac{1}{T_{PIT}C/N_0}\right]} \text{ (Hz)} \tag{5.17}$$

With Equations (5.15) and (5.17), the Doppler measurement thermal noise standard deviations of the PLL and the VFLL are drawn in Figure 5.7 as a function of tracking loop bandwidth. From this figure, it can be seen that with low C/N_0, the VFLL has much

more Doppler noise compared to the high C/N_0. With high C/N_0, the Doppler noises of both the PLL and VFLL are low. For the VFLL, its measurement noise variance is not related to the noise bandwidth (because the VFLL is an open loop, there is no loop filter in it). This is also evident from Equation (5.17), which is only a function of L (smoothing parameter). But the measurement noise of the PLL increases with the noise bandwidth. Thus if the noise bandwidth of the PLL is greater than a certain value (for a given C/N_0), the measurement noise of the PLL will be greater than that of the VFLL.

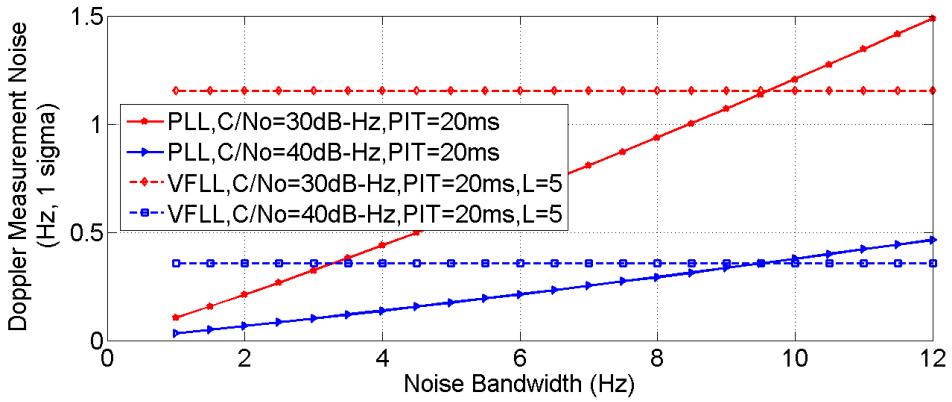

Figure 5.7 Doppler Measurement Noise Variances of PLL and VFLL

5.2 CaPF Composite Loop for UT GPS/RIMU

In order to design the CaPF, first the Doppler measurement error of the CaPLL is analyzed. It is noted that in the following Doppler measurement error analysis, only the DaPLL is considered because the Doppler measurement error analysis for both DaPLL and CaPLL are the same. As discussed in Section 5.1.2.1, the loop filter output of a DaPLL consists of two parts: one is the Doppler aiding error, the other is an extra Doppler value, which is used to control the output phase of the tracking loop to converge to the input phase. This extra Doppler value causes Doppler measurement errors in the

DaPLL and CaPLL cases. In general, the larger the phase errors in the tracking loop (i.e. the input phase minus the output phase), the larger the extra Doppler values, and the larger the Doppler measurement errors. This is a drawback of the DaPLL. Actually the PLL (without Doppler aiding) also has this same drawback.

In order to overcome this drawback of the CaPLL (or just DaPLL), a composite loop, which consists of a CaPLL and an FLL discriminator, is developed in the hope of providing more reliable Doppler measurements in both the PLL locked and unlocked cases, thus improving the performance of the UT GPS/RIMU. This composite loop is termed as CaPF, and the UT system is herein called UT GPS/RIMU with VDCaPF, that is, a VDLL plus a CaPF.

The block diagram of the CaPF is shown in Figure 5.8. With reference to this figure, "Disc." is the abbreviation of "discriminator", f_{dm} is the Doppler measurement output, the "Filter Reset Control" is the same with that of the CaPLL, as shown in Figure 5.4, but the filter reset criteria are different. Specifically, the loop is reset under the following conditions:

- After every measurement update from the navigation filter, when $PLI < T_{PLI} = 0.9$
- In weak signal environments with the 2A1G configuration and when $PLI < T_{PLI} = 0.3$ and $\left| f_{dm} - f_{da} \right| > T_{fd}$ $(T_{fd} = 1 - 2\,\text{Hz})$

The motivation of choosing such loop filter reset criteria is to simulate a VFLL when $PLI < T_{PLI} = 0.9$ in order to obtain a better Doppler measurement. More specifically,

when the PLI is less than 0.9 it suggests the phase is not being tracked very well. If no actions were taken, the tracking loops would adjust to try to drive the phase error to zero, and in the process generate Doppler measurements that are not only related to range rate. Therefore the Doppler measurements are not accurate. If the Doppler measurements are used to update the navigation solution, the navigation performance will be degraded. To avoid this, the loop filter in the CaPF approach is reset such that f_{LF} becomes zero, and correspondingly, the NCO is driven only by the aiding Doppler. If the NCO is only driven by the aiding Doppler, the output of the frequency discriminator is the error in the aiding Doppler value. As will be shown below, this discriminator output can be filtered and added to the aiding Doppler value in order to generate a Doppler measurement that much more closely related to the range rate, that is, they are more accurate. In the process, the expectation would be that the navigation solution is more accurate and thus the aiding Doppler would also become more accurate with the ultimate benefit of improving signal tracking.

However, the loop filter in the CaPF approach is not always reset. It is only reset when the above loop filter reset criteria are satisfied. For example after every measurement update from the navigation filter and when $PLI < 0.9$. If $PLI < 0.9$, at every measurement update time or point, the loop filter is reset. But between two measurement update points, the loop filter is not reset in order to allow the tracking loop a great possibility to be locked. Thus the tracking loop of the CaPF is a DaPLL during two measurement update points, but at the measurement update points, the carrier loop is actually a VFLL. In order to obtain the measurement of Doppler aiding error during two

measurement update points, the Doppler aiding error needs to be calculated and is discussed in the following. It is noted that only when the carrier loop is a VFLL, the output of the frequency discriminator is the error in the aiding Doppler value.

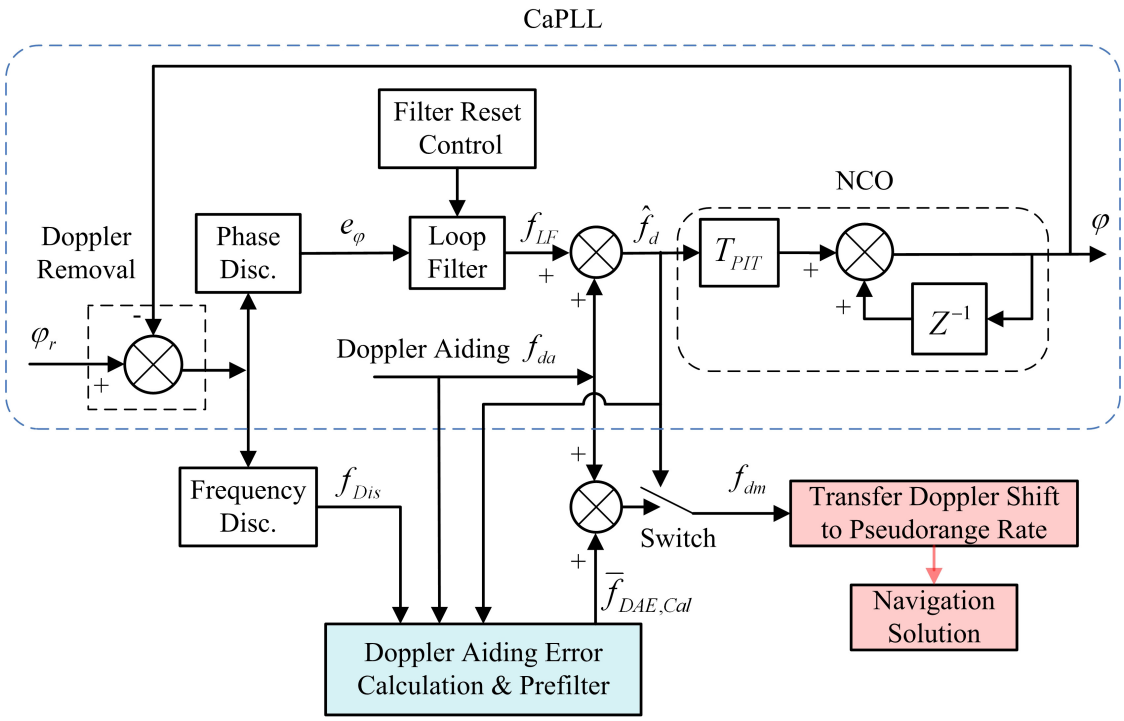

Figure 5.8 Block Diagram of CaPF (One Channel)

From Figure 5.8, it can be seen that the Doppler measurement comes from either the CaPLL or the frequency discriminator, which is controlled by a switch. If the Doppler measurement comes from the CaPLL (the output is switched to upper branch), it is calculated with Equation (5.9); otherwise the Doppler measurement comes from the frequency discriminator (i.e. the Doppler aiding plus the smoothed calculated Doppler aiding error, and the output is switched to lower branch), and is calculated with

$$f_{dm}(k+1) = f_{da}((k+1)L-1) + \frac{1}{L}\sum_{i=1}^{L}\left(f_{Dis}(kL+i) + \left(\hat{f}_d(kL+i-1) - f_{da}(kL+i-1)\right)\right) \tag{5.18}$$

where the term $\left(f_{Dis}(kL+i) + \left(\hat{f}_d(kL+i-1) - f_{da}(kL+i-1)\right)\right)$ is the calculated Doppler aiding error. It is explained as follows.

With reference to Figure 5.8, suppose the Doppler output of the loop filter, f_{LF}, can be expressed as (as discussed in Section 5.1.2.1)

$$f_{LF} = f_{LF,DAE} + f_{LF,Con} \tag{5.19}$$

where $f_{LF,DAE}$ is the Doppler aiding error compensation part of the f_{LF}, and $f_{LF,Con}$ is the extra Doppler value for controlling the phase. Herein the Doppler noise part is ignored. In order to simplify the math, the discrete time is omitted from the expression of the variables. From Equations (5.9) and (5.19), the Doppler measurement of the CaPLL is obtained as

$$\hat{f}_d = f_{da} + f_{LF} = f_{da} + f_{LF,DAE} + f_{LF,Con} \tag{5.20}$$

Subtracting the Doppler aiding value, f_{da}, from both sides of Equation (5.20) yields

$$\hat{f}_d - f_{da} = f_{LF,DAE} + f_{LF,Con} \tag{5.21}$$

Since the Doppler output of the frequency discriminator is the Doppler error, i.e. the input Doppler (true Doppler) minus the output Doppler, then the Doppler output of the frequency discriminator is

$$f_{Dis} = -f_{LF,Con} \tag{5.22}$$

It is noted that the true Doppler is $f_{da} + f_{LF,DAE}$, and the output Doppler of the CaPLL is $f_{da} + f_{LF,DAE} + f_{LF,Con}$ (see Equation (5.20)). So the Doppler error is $-f_{LF,Con}$. Substituting Equations (5.21) and (5.22) into the term $f_{dis} + (\hat{f}_d - f_{da})$ yields

$$f_{Dis} + (\hat{f}_d - f_{da}) = f_{LF,DAE} \tag{5.23}$$

Thus the term $f_{Dis} + (\hat{f}_d - f_{da})$ is the calculated Doppler aiding error.

From Equations (5.18), (5.20) and (5.23), it can be seen that the calculated Doppler measurement with Equation (5.18) equals the Doppler aiding plus the smoothed calculated Doppler aiding error, whereas the Doppler measurement of the CaPLL equals the Doppler aiding plus the Doppler aiding error and the extra Doppler value for control. If the extra Doppler value for control is sufficiently large due, for example, to weak signals or transient state, the Doppler measurement of the CaPLL will have more error than that of Equation (5.18). This often happens in the case where the phase loop has lost lock on the signal. Consequently, the Doppler measurement from the calculation of Equation (5.18) (or just simply called "from the FLL discriminator") can improve the measurement. Stated differently, if the loop has lost lock on the signal, the input to the loop will be mostly noise in weak signal case. Correspondingly, the output of the discriminator will be mostly noise. By filtering the discriminator outputs, the goal is to remove this noise, and thus regain tracking capability.

In contrast, if the phase loop is locked, the extra Doppler value for control should approach zero. Therefore, the Doppler measurement from both the CaPLL and Equation

(5.18) will have the same value. But the Doppler measurement from the CaPLL has smaller thermal noise than that from Equation (5.18) when the noise bandwidth is sufficiently narrow (see Figure 5.7). For this reason, when the phase loop is locked, the Doppler measurement should come from the CaPLL.

In order to take advantage of the Doppler measurement of the frequency discriminator, the Doppler measurement output is switched according to the following criterion: when $PLI \geq T_{PLI} = 0.9$, f_{dm} is switched to CaPLL; else f_{dm} is switched to frequency discriminator. This is because if $PLI < 0.9$, the CaPLL tracking loop is considered unlocked (Ward et al 2006; Van Dierendonck 1996), and the loop filter is reset. If the Doppler measurement comes from Equation (5.18), it will have less Doppler error (i.e. it does not contain the extra Doppler value for control). Thus the carrier loop will simulate a VFLL. It is noted that this CaPF configuration can be used for any UT system, not only for the UT GPS/RIMU.

5.3 Reconfigurable Tracking Loops for UT GPS/RIMU

In a UT system, the NCOs of the VBTLs are controlled by the navigation solution of the UT system. If the navigation solution is not accurate enough to maintain the signal lock, the VBTLs will fail, i.e. all tracking loops will break down. This is the main drawback of VBTLs (Pany & Eissfeller 2006; Pany et al 2005). In contrast, SBTLs are not affected by the navigation solution accuracy of the system. For a SBTL, even if there is no navigation solution obtained, the SBTL can still keep tracking when the GPS signal is strong enough. To overcome the drawback of the VBTLs, the VBTLs should be switched to the corresponding SBTLs when the navigation solution accuracy of the UT system is

sufficiently poor. But the question arises then as to what conditions or criteria should be used to switch the VBTLs to SBTLs? Pany et al (2005) used time to control the switch from VBTLs to SBTLs during a GPS outage. This is not accurate enough for a UT GPS/RIMU because the navigation solution accuracy is not only related to the GPS (or the GPS outage duration time), but also related to the RIMU. From this viewpoint, in this section, the estimated navigation performance of the UT GPS/RIMU is used to control the switch between VBTLs and SBTLs, specifically, the switch between VDLL and DLL, and the switch between CaPF and PLL (no Doppler aiding). Thus a reconfigurable tracking loop, which can switch between VDLL and DLL, and switch between CaPF and PLL, is obtained.

5.3.1 Switch Strategy between VDLL and DLL

In a DLL, the rule-of-thumb tracking threshold is (Ward et al 2006)

$$3\sigma_{DLL} = 3\sigma_{tDLL} + R_e \le D/2 \tag{5.24}$$

where σ_{tDLL} is thermal noise code tracking jitter (1σ), R_e is dynamic stress error in the DLL tracking loop, and D is early-to-late correlator spacing. In a VDLL, since the individual tracking loop is open and the NCO is controlled directly by the navigation solution of the UT system as shown in Figure 5.2, then, with reference to Equation (5.24), the tracking threshold of a VDLL can be written as

$$3\sigma_{VDLL} = 3\sigma_{\rho Est} + c_{\rho Est} \le D/2 \tag{5.25}$$

where σ_{VDLL} is the total pseudorange estimation uncertainty caused by the navigation solution of a UT GPS/RIMU, $\sigma_{\rho Est}$ is the standard deviation of the pseudorange estimation noise, and $c_{\rho Est}$ is an empirical constant to account for unmodeled

pseudorange errors such as multipath and atmosphere delays . More specifically, $c_{\rho Est}$ is the pseudorange error which is not accounted for in the term $\sigma_{\rho Est}$. The units of all variables in Equation (5.25) are metres.

Based on Equation (5.25), the switch strategy between VDLL and DLL is designed such that if $3\sigma_{\rho Est} + c_{\rho Est} \leq D/2$, the code tracking loop is switched to VDLL; else the tracking loop is switched to DLL. This is because if $3\sigma_{\rho Est} + c_{\rho Est} > D/2$, the VDLL may fail.

For a given navigation position error, its projection onto the line-of-sight (LOS) of each satellite is different, resulting in different pseudorange estimation errors for different satellites. For the sake of simplification and to reduce calculations in the receiver, the projection calculation is omitted and the maximum pseudorange error (calculated directly from the navigation position error) is used to control the switch between DLL and VDLL, i.e. only one switch control threshold is applied to all satellites. In practice, $c_{\rho Est}$ can be chosen according to different test environments, for example, in suburban area, $c_{\rho Est}$ can be chosen as 15 metres. This value is used herein because for the vehicle test used in this dissertation, the 3D position error of the GPS position is about 10 metres. It is noted that this value is selected to be larger than its theoretical value in order to make sure the VDLL safely (conservatively) switches to the DLL before it fails. In contrast, $\sigma_{\rho Est}$ can be calculated from the predicted covariance matrix, $\mathbf{P}(-)$, of the integrated navigation

Kalman filter. Suppose $\mathbf{P}_{\delta r}(-) = E\left[\delta\mathbf{r}(-)\delta\mathbf{r}^T(-)\right]$, where $\delta\mathbf{r}(-)$ is navigation position prediction error. In this case, $\mathbf{P}_{\delta r}(-)$ is the sub-matrix of $\mathbf{P}(-)$ corresponding to the position states (see Section 4.3.1 for detail), and can be expressed as

$$\mathbf{P}_{\delta r}(-) = \begin{bmatrix} p_{11}(-) & p_{12}(-) & p_{13}(-) \\ p_{21}(-) & p_{22}(-) & p_{23}(-) \\ p_{31}(-) & p_{32}(-) & p_{33}(-) \end{bmatrix} \tag{5.26}$$

The maximum pseudorange estimation noise variance is given by the sum of the variances as

$$\sigma^2_{\rho Est} = P_{11}(-) + P_{22}(-) + P_{33}(-) \tag{5.27}$$

5.3.2 Switch Strategy between CaPF and PLL

The composite loop (CaPF) is closed with carrier phase. Actually its closed part is a CaPLL. This CaPLL is both aided and reset with the Doppler aiding from the navigation solution (see Section 5.2). With this in mind, if the Doppler aiding is not accurate enough, the CaPLL will fail. Actually, the loop filter reset of the CaPLL is mainly affected by the Doppler aiding error. In Section 5.2, the loop filter reset of the CaPF is discussed only in the normal GPS case, i.e. no GPS outage. If there is a long enough GPS outage in a test, the loop filter reset and the Doppler aiding of the CaPF should stop, and the CaPF should be switched to a pure PLL (i.e. no Doppler aiding).

Actually, the effectiveness of Doppler aiding is mainly affected by the dynamics of the aiding error. In other words, it is the dynamics of the aiding error that causes the Doppler-aided PLL to fail. These dynamics are mainly induced by the attitude error of the

GPS/RIMU and the specific force measured by the RIMU (generally related to the vehicle's dynamics), especially during GPS outages. To illustrate this latter point, suppose the specific force measured by the RIMU is the true specific force, $\mathbf{f}^b$, the true rotation matrix from b-frame to ℓ-frame is $\mathbf{R}_b^\ell$, and the estimated rotation matrix is $\tilde{\mathbf{R}}_b^\ell$. In this case, the dynamics of the Doppler aiding error is given as

$$\delta\mathbf{f}^\ell = \tilde{\mathbf{R}}_b^\ell \mathbf{f}^b - \mathbf{R}_b^\ell \mathbf{f}^b = (\tilde{\mathbf{R}}_b^\ell - \mathbf{R}_b^\ell)\mathbf{f}^b \tag{5.28}$$

From this equation, it can be seen that for a given $\mathbf{f}^b$, the more the attitude error (i.e. $\tilde{\mathbf{R}}_b^\ell - \mathbf{R}_b^\ell$), the more the dynamics of the Doppler aiding error (i.e. $\delta\mathbf{f}^\ell$). For a given grade of inertial sensors, generally a full IMU has a less attitude error than an RIMU. Thus there are less user dynamics left in the Doppler aiding error with a full IMU than with an RIMU. Furthermore, if the accelerometer measurement error, $\delta\mathbf{f}^b$, is considered, the dynamics of the Doppler aiding error should contain another main term, $\mathbf{R}_b^\ell \delta\mathbf{f}^b$.

Generally, a large $\delta\mathbf{f}^\ell$ causes a large velocity error (Doppler aiding error), especially during GPS outages (Farrell & Barth 1999). The Doppler aiding error can be obtained from the pseudorange rate error divided by the signal wavelength (see Equation (2.26)). In this light, only the pseudorange rate error (corresponding to Doppler aiding error) is used to control the switch between CaPF and PLL, thus simplifying the switching criterion. Based on this consideration, the criterion for applying a CaPF is selected as

$$\sigma_{\rho rCaPF} = \sigma_{\rho rEst} \le \gamma\sigma_{\rho rT} \tag{5.29}$$

where $\sigma_{\rho rCaPF}$ (or $\sigma_{\rho rEst}$) is the pseudorange rate uncertainty standard deviation caused by the navigation solution error of a UT GPS/RIMU, $\sigma_{\rho rT}$ is chosen as the pseudorange rate uncertainty standard deviation in the case where there is no GPS outage, and γ is a coefficient. In practice, $\sigma_{\rho rT}$ is chosen according to the performance of the GPS/RIMU, γ is chosen according to the parameters of the tracking loop, such as the loop filter order and noise bandwidth. For example, for vehicle test and MEMS IMU, $\sigma_{\rho rT}$ can be chosen as 0.16 m/s (3D) (this is an empirical value, which was obtained from the test results of Chapter Four), and γ can be chosen as 3 (for a second-order loop filter with a noise bandwidth of 3 Hz for 3A1G case and 8 Hz for 2A1G case). This means that if the pseudorange rate uncertainty standard deviation is more than three times the normal (no GPS outage) pseudorange rate uncertainty standard deviation, it is considered that the CaPF fails.

Based on Equation (5.29), the switch strategy between CaPF and PLL is designed such that if $\sigma_{\rho rCaPF} \le \gamma\sigma_{\rho rT}$, the phase tracking loop is switched to CaPF; else the tracking loop is switched to PLL.

Similar to the pseudorange estimation uncertainty calculation discussed in Section 5.3.1, the projection of the velocity uncertainty onto the line of sight for each satellite is omitted when computing the pseudorange rate estimation uncertainty. Correspondingly, the maximum pseudorange rate uncertainty calculated directly from the navigation velocity error covariance matrix is used to control the switch for every satellite. Specifically,

$\sigma_{\rho rCaPF}$ can be calculated from $\mathbf{P}_{\delta v}(-) = E\left[\delta\mathbf{v}(-)\delta\mathbf{v}^T(-)\right]$, where $\delta\mathbf{v}(-)$ is the navigation velocity prediction error. $\mathbf{P}_{\delta v}(-)$ can be extracted from $\mathbf{P}(-)$ (see Section 4.3.1 for detail), and can be expressed as

$$\mathbf{P}_{\delta v}(-) = \begin{bmatrix} p_{44}(-) & p_{45}(-) & p_{46}(-) \\ p_{54}(-) & p_{55}(-) & p_{56}(-) \\ p_{64}(-) & p_{65}(-) & p_{66}(-) \end{bmatrix} \tag{5.30}$$

Again, the maximum pseudorange rate uncertainty variance is given by the sum of the variances:

$$\sigma^2_{\rho rPF} = P_{44}(-) + P_{55}(-) + P_{66}(-) \tag{5.31}$$

5.3.3 Implementation of Reconfigurable Tracking Loops (RTLs)

Based on the above switching strategies between VDLL and DLL, and between CaPF and PLL, the reconfigurable tracking loops are implemented as shown in Figure 5.9. It is noted that in order to enhance the switch reliability, the switch back from SBTLs to VBTLs is delayed one second from when the switch criterion is satisfied. This can prevent frequent switches when operating near the threshold. This means that once a tracking loop has been switched to a SBTL from a VBTL, its switch back should be done cautiously. Correspondingly, the RTLs are mainly used in GPS outage cases. When there are fewer than four satellites in view, the navigation solution error of the GPS/RIMU might be too large to maintain signal lock using a VBTL approach. In this case, the tracking loops are switched to SBTLs to let the satellites in view keep tracking, thus improving the performance of the GPS/RIMU. Since the satellites in view still keep

tracking, when the loops are switched back to VBTLs, the reacquisition for these satellites is avoided.

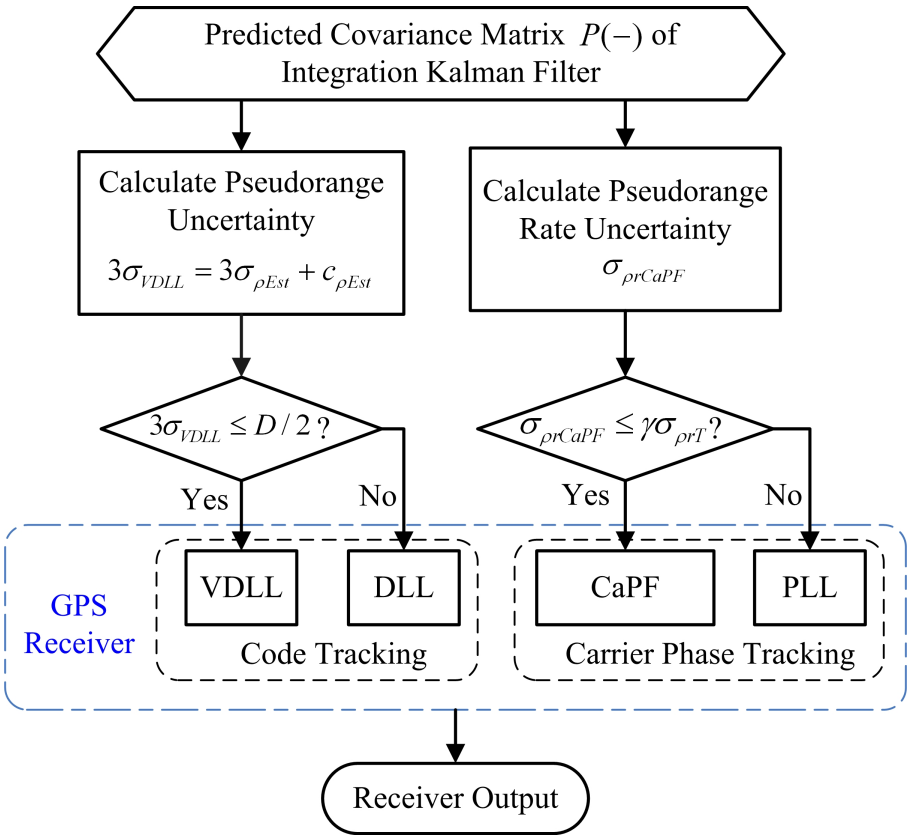

Figure 5.9 Flowchart of Reconfigurable Tracking Loop Implementation

5.4 Theoretical Comparison of UT and TLA GPS/RIMU

From the discussions of UT and TLA GPS/RIMU (see Chapter Four for TLA system), it can be seen that UT and TLA GPS/RIMU are mainly different in the configurations of tracking loops. In the UT system, tracking loops are closed via the navigation solution of the UT system, whereas in the TLA system, tracking loops are closed via their respective outputs. Because of the difficulties in implementing a VPLL, in this chapter a cascaded PLL is used to replace the VPLL in the UT system, resulting in the VDCaP configuration (see Section 5.1.2). In the TLA system, the code loop is a Doppler-aided DLL (DaDLL),

and the carrier loop is a DaPLL. Correspondingly, in the VDCaP approach, the code loop is a VDLL, and the carrier loop is a CaPLL. Owing to the fact that the UT (i.e. VDCaP) and TLA system have a same kind of carrier loops (i.e. phase lock loop), the comparison between UT and TLA systems will be made in the VDCaP and the TLA system (if UT and TLA systems have different kind of carrier loops such as a VFLL for UT system and a DaPLL for TLA system, their comparison is not straightforward, and herein it is not considered).

5.4.1 Comparison in Carrier/Code Tracking Loops

For carrier tracking loop, the DaPLL and the CaPLL are both Doppler-aided PLLs. In the CaPLL case, however, the loop filter is reset according to some criteria (see Section 5.1.2.1). If the Doppler aiding is accurate enough, and the GPS signal is weak, the CaPLL should outperform the DaPLL, at least in theory (see Section 5.1.2.1). This is because the CaPLL can bound the Doppler measurement error, resulting from the loop filter reset. The bounding for the Doppler error can benefit the tracking loop's recovery from temporary loss of lock, but it may disturb the process of the carrier phase convergence, resulting in delay in phase lock, as discussed in Section 5.1.2.1. In this light, the CaPLL underperforms the DaPLL in the case where the GPS signal is strong and/or the Doppler aiding is not accurate enough (if the loop filter is still reset). As mentioned before, if the loop filter of the CaPLL is not reset in a test, the CaPLL becomes a DaPLL.

For the code tracking loop, the UT system uses a VDLL, whereas the TLA system uses a DaDLL. Sometimes the DaDLL is just simply called as DLL because in this dissertation, the DLL is always aided with the code Doppler. For the DaDLL, it is a closed loop, and

can be modeled as a control system (see Section 2.3.2). With code Doppler aiding, the noise bandwidth of the DLL can be narrowed, as discussed in DaPLL (see Chapter Four for detail). So the DaDLL of the TLA system is a feedback control system with low noise bandwidth. In contrast, the VDLL of the UT system can be considered as an open loop (i.e. in the VDLL, the individual tracking loop is open, and the code loop is only closed via the navigation solution of the UT system). The output of the code tracking loop is not fed back directly to control the loop, but is instead fed to the navigation solution. Consequently, the stability and the output of the open loop (i.e. the VDLL) are not only related to the input of the open loop, but also related to the navigation solution of the UT system (i.e. the control of the open loop). With this in mind, the comparison between the VDLL and the DaDLL is made in the following four aspects: 1) pseudorange measurement thermal noise; 2) system stability; 3) multipath alleviating ability; 4) weak signal tracking ability.

The comparisons in the above four aspects are as follows:

- Compared to the VDLL, the DaDLL has a much smaller pseudorange measurement thermal noise since it is aided with the code Doppler, and has low noise bandwidth, as discussed in Section 5.1.1.2. For the given parameters of Section 5.1.1.2, the pseudorange measurement thermal noise variance of the VDLL is one hundred times that of the DaDLL.
- Since the DaDLL is a closed loop, it has the ability to track the signals with unmodelled or unknown parameters such as time delays in code signals (Ogata 1997). But for the VDLL, since it is an open loop, if the unknown time delay of

the tracked signal is more than half of the early-to-late correlator spacing, the VDLL will fail (see Equation (5.25)). Similarly, if the 3D position error of the UT system is more than half of the early-to-late correlator spacing, which usually occurs during partial GPS outages (for a complete GPS outage, there are no satellites in view; this is not considered herein), the VDLL also will fail. From this light, the DaDLL is more stable.

- Since the VDLL is an open loop, it cannot track signals with unmodelled or unknown time delays which is more than half of the early-to-late correlator spacing. A multipath signal can introduce unknown time delays (Misra & Enge 2001). If the unknown time delay is more than half of the early-to-late correlator spacing, the VDLL will not track it, thus removing it from the navigation solution. On the contrary, the DLL is a closed loop, it can track signals with unknown time delays, such as multipath signals. But the DLL can alleviate multipath signals with a narrow correlator (Misra & Enge 2001).
- The VDLL and DaDLL both have a weak signal tracking ability (Lashley & Bevly 2008a; Soloviev et al 2007; Gebre-Egziabher et al 2005). In the VDLL, since its NCO is controlled by the navigation solution of the UT system, it achieves this weak signal tracking ability (Lashley & Bevly 2009b). In contrast, the DaDLL achieves this ability through narrowing its noise bandwidth.

5.4.2 Comparison in System Performance

Based on the above carrier/code tracking loop comparison, the system performance of the UT and TLA GPS/RIMU are compared in terms of tracking ability and navigation performance. The characteristics of the carrier/code tracking loops determine the tracking

ability and the navigation performance of the integration system. If only the difference of UT and TLA system in code loop is considered, the TLA system is more stable than the UT system because the DaDLL is more stable than the VDLL.

In the case where no partial GPS outage happens, the UT and TLA systems are compared as follows. If the GPS signal is strong, the UT and TLA systems are supposed to have similar tracking ability and velocity error. This conclusion is drawn based on the three following facts: first the CaPLL and the DaPLL have similar tracking ability and measurement noise in strong GPS signal case; second it is assumed that in the strong GPS signal case, the calculated pseudorange (for code NCO control) has a small error, thus the VDLL and DaDLL have a similar tracking ability, and; the thermal noise is low in strong GPS signal case (Ward et al 2006). If the GPS signal is weak, both the code and carrier loop of the UT and TLA system will be affected. Comparing the two systems' performance in theory is not straightforward in this case. Accordingly, the performance comparison of the two systems will be performed empirically with test results.

The comparisons for the tracking ability and navigation performance will be quantified later with vehicle test data. Since the evaluation for the multipath alleviating ability needs special experiments, it will be made in future. It is noted that the comparison results above are still applicable to the comparison of the UT and TLA GPS/full IMU systems.

5.5 Test Description and Data Processing

To assess the performance of the UT GPS/RIMU systems and to verify the innovative algorithms/configurations, the same data described in Section 3.3 was used. Data

processing was performed with the UT GPS/RIMU software developed from the TLA GPS/RIMU software. To implement UT GPS/RIMU integration, the TLA GPS/RIMU software was modified to include the vector tracking architectures, as discussed in Sections 5.1 to 5.3. It is noted that the TLA GPS/RIMU software was originally developed from the University of Calgary's GSNRx™ software receiver (see Section 4.5). In the data processing, two RIMU configurations (i.e. 3A1G and 2A1G) were used in the assessment of the UT GPS/RIMU. To simplify analysis, only MEMS IMU data was used in the assessment.

In UT system tests, the GPS pseudorange measurement noise variance (used to compute the navigation solution) was chosen as 400 (m^2) for open sky data, 900 (m^2) for foliage data. The pseudorange rate measurement noise variance was chosen as 0.04 $(m/s)^2$ for both sets of data. For TLA system tests, the pseudorange measurement noise variance was chosen as 100 (m^2), and the pseudorange rate variance was chosen the same as that of the UT system test, for both sets of test data. The reason for choosing larger pseudorange noise variance for the UT system is that the pseudorange measurement of the UT system comes from a VDLL, and the VDLL has more measurement thermal noise than the DaDLL of the TLA system (see Section 5.1). Furthermore, since the C/N_0 of GPS signal of the foliage data varies dramatically (see Figure 4.14), its pseudorange noise variance is chosen as larger than that of the open sky data. In contrast, to facilitate comparison, the pseudorange rate variance for all tests was chosen as the same. For Doppler-aided PLL, the noise bandwidth was chosen as 3 Hz for 3A1G, and 8 Hz for 2A1G. These were the best values that could be obtained through a series of noise

bandwidth selection trials. For CaPLL, the loop filter is only reset in the foliage test and 2A1G configuration. In other cases, the loop filter of the CaPLL is not reset, resulting in a DaPLL. In the tests, the output rate of the integration system was 10 Hz, and PIT was 20 ms.

5.6 Evaluation of UT GPS/RIMU

In the following, the UT GPS/RIMU systems will be evaluated in terms of tracking ability and navigation performance. The tracking ability of the GPS receiver is assessed using the number of SVs used in the navigation solution, as applied in Section 4.6. First the UT systems of VDF and VDCaP are evaluated and compared. Then the innovative algorithms such as CaPF and RTL are investigated.

5.6.1 Evaluation of GPS/RIMU with VDF

With the open sky data, the velocity and attitude error of the UT GPS/RIMU (Crista) with VDF have similar plots as those in Figure 4.20 for 3A1G and in Figure 4.21 for 2A1G. The number of satellites used in the navigation solution is seven for both 3A1G and 2A1G in all the time. That means all the SVs are being used. The statistical results of the UT GPS/RIMU (Crista) with VDF are summarized in Table 5.1. This table shows that for both RIMU configurations (i.e. 3A1G and 2A1G), the RMS velocity error in each direction is less than 0.05 m/s; the pitch and roll error are about 0.6 degrees, respectively; and the azimuth error is less than 2.2 degrees.

Table 5.1 Velocity and Attitude Error of UT GPS/RIMU (Crista) with VDF and Open Sky Data

Integration Strategy	RMS Attitude Error (Deg)			RMS Velocity Error (m/s)		
	Pitch	Roll	Azimuth	East	North	Up
UT GPS/3A1G	0.65	0.56	1.68	0.04	0.05	0.03
UT GPS/2A1G	0.63	0.59	2.13	0.04	0.05	0.04

For the foliage data, the velocity and attitude error variations of the UT system with VDF are shown in Figure 5.10 for 3A1G, and Figure 5.11 for 2A1G. From these two figures, it can be seen that the 2A1G has more vertical velocity error, which is consistent with the results in Chapters Three and Four. Figure 5.12 displays the number of SVs used in the navigation solution. It shows that although there are nine SVs in view, sometimes only eight SVs are used in the navigation solution for both 3A1G and 2A1G. The SV that is not used in the navigation solution calculation is rejected by an innovation sequence test. Table 5.2 summarizes the statistical results of the UT system. From this table, it can be seen that for both RIMU configurations, the RMS velocity error in each direction is less than 0.07 m/s; the RMS pitch error is less than 0.4 degrees, the RMS roll error is about 0.6 degrees; and the RMS azimuth error is about 3.0 degrees. Further, comparing Table 5.1 and Table 5.2, it can be seen that with foliage data, the UT system has more velocity and azimuth error, as is expected. It is not appropriate to compare the pitch/roll error of the two sets of data because the two test routes have different local terrain.

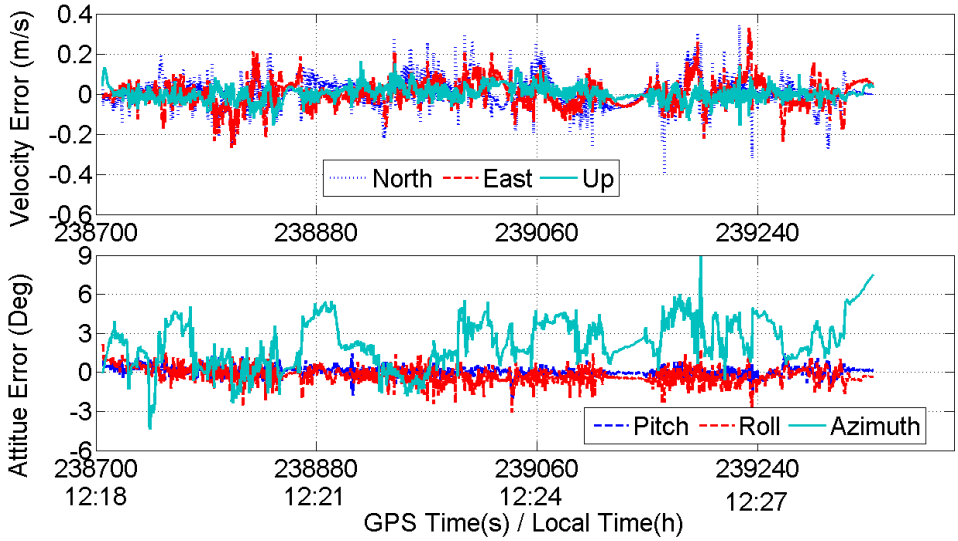

Figure 5.10 Velocity and Attitude Error of UT GPS/3A1G (Crista) with VDF and Foliage Data

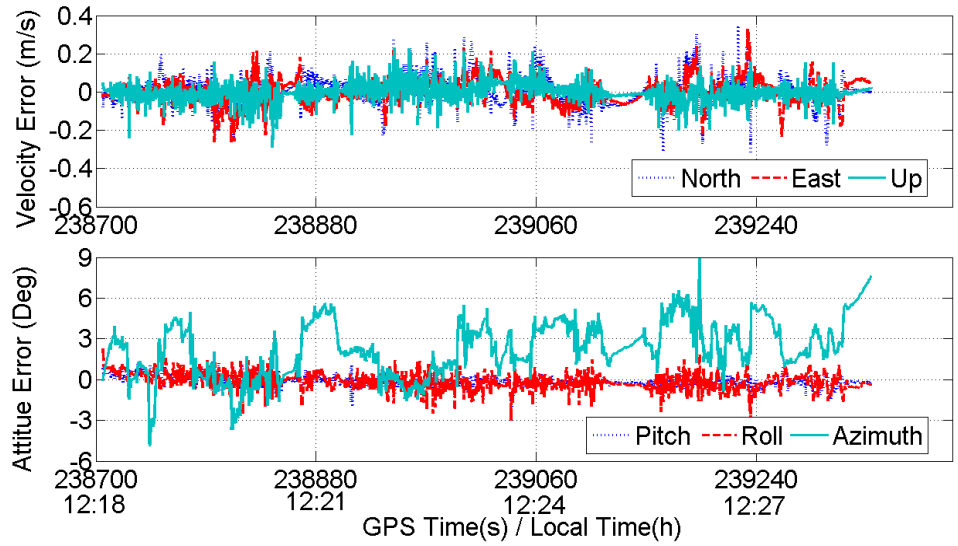

Figure 5.11 Velocity and Attitude Error of UT GPS/2A1G (Crista) with VDF and Foliage Data

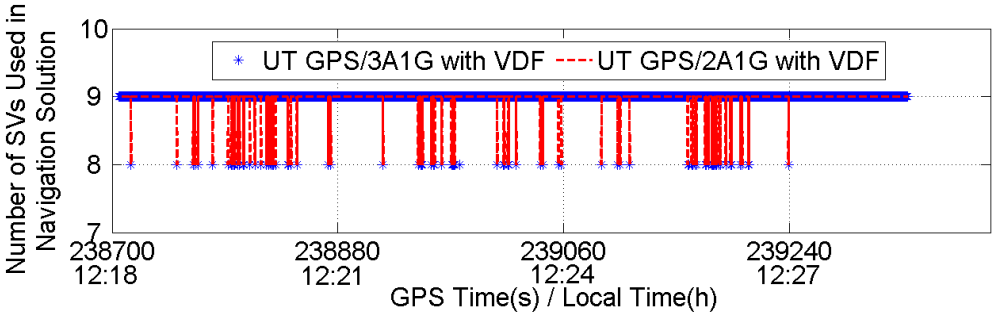

Figure 5.12 Number of SVs Used in Navigation Solution of UT GPS/RIMU (Crista) with VDF and Foliage Data

Table 5.2 Velocity and Attitude Error of UT GPS/RIMU (Crista) with VDF and Foliage Data

Integration Strategy	RMS Attitude Error (Deg)			RMS Velocity Error (m/s)		
	Pitch	Roll	Azimuth	East	North	Up
UT GPS/3A1G	0.34	0.62	2.91	0.06	0.07	0.03
UT GPS/2A1G	0.39	0.60	3.04	0.06	0.07	0.05

5.6.2 Evaluation of GPS/RIMU with VDCaP

The UT system with VDCaP has the similar velocity and attitude error variations as those in the VDF with the same RIMU configuration and test data. Thus in the following only the number of SVs used in the navigation solution and the statistical results are shown.

With open sky data, for 3A1G case, all the SVs in view (seven) are used in the navigation solution. For the 2A1G case, occasionally one SV is rejected from the navigation solution, as shown in Figure 5.13 (the rejected SV is PRN 11, its signal has some sudden signal attenuations, as discussed in Section 4.7.1). The RMS errors of the UT system with VDCaP are summarized in Table 5.3. From this table, it can be seen that the velocity error in each direction is less than 0.04 m/s for 3A1G, and less than 0.05 m/s for 2A1G;

the pitch and roll error are about 0.6 degrees for both RIMU configurations; and the azimuth error is about 2.5 degrees for 3A1G and 1.8 degrees for 2A1G.

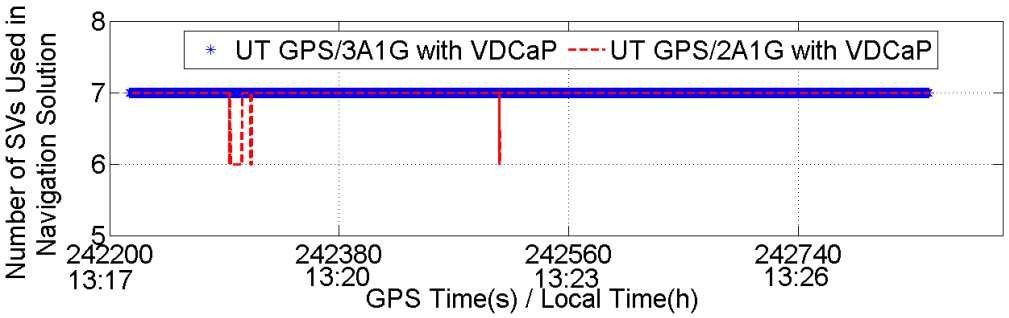

Figure 5.13 Number of SVs Used in Navigation Solution of UT GPS/RIMU (Crista) with VDCaP and Open Sky Data

Table 5.3 Velocity and Attitude Error of UT GPS/RIMU (Crista) with VDCaP and Open Sky Data

Integration Strategy	RMS Attitude Error (Deg)			RMS Velocity Error (m/s)		
	Pitch	Roll	Azimuth	East	North	Up
UT GPS/3A1G	0.65	0.58	2.53	0.04	0.04	0.03
UT GPS/2A1G	0.65	0.58	1.78	0.04	0.05	0.04

With the foliage data, the number of SVs used in the navigation solution is shown in Figure 5.14. It can be seen that with VDCaP, 3A1G configuration has more SVs used in navigation solution than 2A1G does. Furthermore, in both 3A1G and 2A1G, a few of SVs in view are rejected from the navigation solution. The RMS errors are summarized in Table 5.4. From this table, it can be seen that the velocity error can reach as large as 0.09 m/s for 3A1G (in the north direction), and 0.11 m/s for 2A1G (also in the north direction). The pitch error is less than 0.5 degrees, and the roll error less than 0.7 degrees for both RIMU configurations. The azimuth error is about 2.70 degrees for the 3A1G case and 3.50 degrees for the 2A1G case. Comparing the results of 3A1G and 2A1G, it can be seen that 2A1G configuration has larger velocity and azimuth error. This can be

explained in two ways. First, the noise bandwidth of the Doppler-aided PLL in the UT GPS/2A1G is wide (i.e. 8 Hz), resulting in more Doppler measurement noise. Second, more SVs are rejected from the navigation solution in the 2A1G case. Since the 2A1G case has more Doppler measurement noise and fewer satellites used in navigation solution, its navigation performance is degraded.

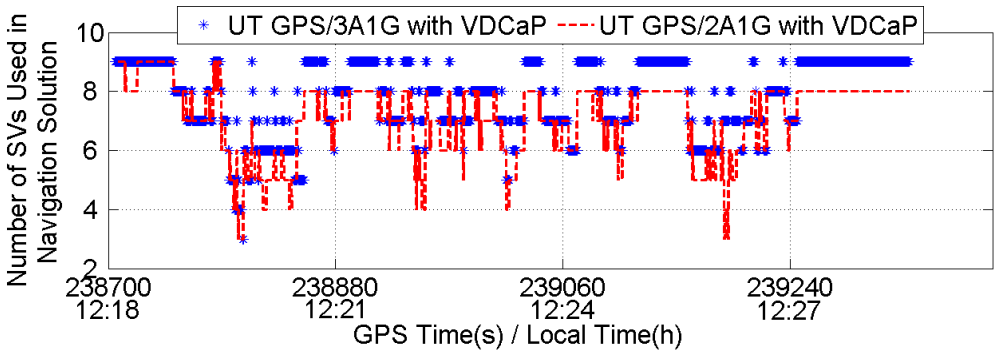

Figure 5.14 Number of SVs Used in Navigation Solution of UT GPS/RIMU (Crista) with VDCaP and Foliage Data

Table 5.4 Velocity and Attitude Error of UT GPS/RIMU (Crista) with VDCaP and Foliage Data

Integration Strategy	RMS Attitude Error (Deg)			RMS Velocity Error (m/s)		
	Pitch	Roll	Azimuth	East	North	Up
UT GPS/3A1G	0.32	0.64	2.65	0.07	0.09	0.03
UT GPS/2A1G	0.45	0.68	3.50	0.08	0.11	0.07

The analysis now compares the results of the VDCaP with those of the VDF shown in Section 5.6.1. For open sky data, Figure 5.13 shows that the VDCaP has a similar number of satellites used in the navigation solution as the VDF (the VDF always has seven SVs used in the navigation solution for both 3A1G and 2A1G). Also, both UT systems have a similar navigation performance for corresponding RIMU configurations, as shown in Table 5.1 and Table 5.3. For the foliage data, the VDF has much more SVs used in

navigation solution, as shown in Figure 5.12 and Figure 5.14. Comparing Table 5.2 and Table 5.4, it can be seen that the VDF has less velocity error than does the VDCaP for a corresponding RIMU configuration. This latter result is because there are more SVs used in navigation solution in the VDF and the Doppler measurement error of the VDCaP is not necessarily less than that of the VDF. For example, with the foliage data and 2A1G configuration, for PRN 28 (with high elevation angle), the RMS Doppler measurement error of the VDF is 0.26 Hz, but the RMS error of the VDCaP is 0.33 Hz. So, in this case, the CaPLL (still a kind of DaPLL) has more Doppler measurement error than does the VFLL. The reason is that the Doppler measurement error not only contains the Doppler thermal noise, but also contains some Doppler errors caused by the dynamic state and C/N_0 variations, especially for the CaPLL because it is a closed loop, as discussed in Section 5.1.2.1. As a result, although the theoretical analysis in Section 5.1.2.2 suggests that a DaPLL might have less Doppler measurement thermal noise than a VFLL, when other Doppler errors caused by the dynamic state and C/N_0 variations are considered, the total Doppler error of the DaPLL might be more than that of the VFLL.

5.6.3 Evaluation of GPS/RIMU with VDCaPF

Although the loop filter reset criteria of the CaPF and the CaPLL discussed in Section 5.1.2.1 are different, the VDCaPF and the VDCaP have a similar tracking performance, i.e. they have a similar number of SVs used in navigation solution for a corresponding RIMU configuration and test data. Consequently, the plots of the number of SVs used in the navigation solution of the VDCaPF are omitted herein. The statistical results of the UT GPS/RIMU with VDCaPF are summarized in Table 5.5 for open sky data, Table 5.6 for foliage data. In order to verify the CaPF approach, the test results of the UT

GPS/RIMU with VDCaP (in Figure 5.8, the output is always switched to upper branch), whose CaPLL has the same loop filter reset criteria as that of the CaPF, are summarized in Table 5.7 for open sky data, Table 5.8 for foliage data. Table 5.9 shows the statistical results of the UT GPS/RIMU with VDCaPF, ALFs and open sky data.

Table 5.5 Velocity and Attitude Error of UT GPS/RIMU (Crista) with VDCaPF and Open Sky Data

Integration Strategy	RMS Attitude Error (Deg)			RMS Velocity Error (m/s)		
	Pitch	Roll	Azimuth	East	North	Up
UT GPS/3A1G	0.65	0.58	2.70	0.04	0.04	0.03
UT GPS/2A1G	0.65	0.58	1.79	0.04	0.05	0.04

Table 5.6 Velocity and Attitude Error of UT GPS/RIMU (Crista) with VDCaPF and Foliage Data

Integration Strategy	RMS Attitude Error (Deg)			RMS Velocity Error (m/s)		
	Pitch	Roll	Azimuth	East	North	Up
UT GPS/3A1G	0.33	0.63	2.66	0.07	0.08	0.03
UT GPS/2A1G	0.43	0.65	3.16	0.08	0.11	0.06

Table 5.7 Velocity and Attitude Error of UT GPS/RIMU (Crista) with VDCaP and Open Sky Data (with Same Loop Filter Reset Criteria as CaPF)

Integration Strategy	RMS Attitude Error (Deg)			RMS Velocity Error (m/s)		
	Pitch	Roll	Azimuth	East	North	Up
UT GPS/3A1G	0.65	0.58	2.54	0.04	0.04	0.03
UT GPS/2A1G	0.65	0.58	1.76	0.04	0.05	0.04

Table 5.8 Velocity and Attitude Error of UT GPS/RIMU (Crista) with VDCaP and Foliage Data (with Same Loop Filter Reset Criteria as CaPF)

Integration Strategy	RMS Attitude Error (Deg)			RMS Velocity Error (m/s)		
	Pitch	Roll	Azimuth	East	North	Up
UT GPS/3A1G	0.32	0.62	2.60	0.07	0.08	0.03
UT GPS/2A1G	0.44	0.68	3.61	0.08	0.10	0.07

Table 5.9 Velocity and Attitude Error of UT GPS/RIMU (Crista) with VDCaPF and Open Sky Data When ALF Is Applied

Integration Strategy	RMS Attitude Error (Deg)			RMS Velocity Error (m/s)		
	Pitch	Roll	Azimuth	East	North	Up
UT GPS/3A1G	0.65	0.57	2.44	0.04	0.04	0.03
UT GPS/2A1G	0.64	0.59	2.38	0.04	0.04	0.04

Comparing Table 5.5 and Table 5.7, it can be seen that for the open sky data, the VDCaPF and the VDCaP have a similar navigation performance, although slightly different azimuth errors. For the foliage data, comparing Table 5.6 and Table 5.8, similar conclusions can be obtained as that of the open sky case. Therefore, it can be concluded that the VDCaPF (or CaPF) approach is practicable although it cannot improve the performance of the UT system obviously compared to the VDCaP (or just CaPLL) with the same loop filter reset criteria. But as a different or an innovative configuration of the carrier tracing loop, it is still attractive, and might potentially improve the performance of the UT system in other environments. Further investigation is needed to explore its potential advantages.

The reason the CaPF algorithm (or VDCaPF system) cannot improve the performance of the UT system obviously compared to the VDCaP can be explained as follows. According to the CaPF algorithm, only when the CaPLL is considered unlocked (i.e. $PLI < 0.9$) does the Doppler measurement come from the frequency discriminator. But when $PLI < 0.9$, most of Doppler measurements are not used in the navigation solution. Moreover, even if some Doppler measurements obtained from the frequency discriminator are used in the navigation solution, the Doppler measurement difference

between the CaPLL and the frequency discriminator of the CaPF (calculated with Equation (5.18)) may not be obvious. In this light, the navigation performance improvement of the CaPF is not obvious. Actually in the above tests, for both the VDCaPF and VDCaP, the Doppler measurements used in the navigation solution are controlled by the status of bit synchronization (approximately equivalent to $PLI \geq 0.9$ case). Since the CaPF can provide a reliable Doppler measurement in both carrier phase-locked (i.e. $PLI \geq 0.9$) and carrier phase-unlocked ($PLI < 0.9$) cases, the Doppler measurements of the CaPF in carrier phase-unlocked case also can be used in the navigation solution. In this light, compared to the VDCaP, the VDCaPF can have more Doppler measurements used in the navigation solution, resulting in improved navigation performance. That is why it is assumed that the VDCaPF can potentially improve the navigation performance. However more tests are needed in the future to explore this potential ablity of the VDCaPF.

Furthermore, comparing Table 5.3 to Table 5.7, and Table 5.4 to Table 5.8, it can be seen that for the two different loop filter reset criteria (i.e. one is designed in Section 5.1.2.1, the other is designed in Section 5.2 and applied in this section), the UT systems of GPS/RIMU with VDCaP have slightly different performance. Specifically, for the open sky data, the systems of VDCaP with the two different reset criteria have a similar navigation performance; for foliage data, the navigation performance of the VDCaP with the reset criteria of Section 5.2 is slightly better than that with the reset criteria of Section 5.1.2.1. This suggests that the loop filter reset criteria of Section 5.2 (used in this section) is better than that of Section 5.1.2.1.

Further comparing Table 5.5 and Table 5.9, it can be seen that for the UT GPS/RIMU with VDCaPF, the system with ALFs can achieve similar results with the system with CNBLFs having a proper noise bandwidth. This means that the ALF algorithm, discussed in Chapter Four, also can be used in the UT GPS/RIMU system.

5.6.4 Evaluation of GPS/RIMU with RTLs

In order to verify the innovative RTL algorithm, a partial GPS outage was simulated in the data. In the open sky data, a 40 s long partial GPS outage was simulated by artificially omitting some satellites from the navigation solution during post-mission processing, resulting in only two satellites – PRNs 08 and 11 – to be included in the navigation calculation. The partial outage lasted from GPS time 242290 s to 242330 s. During this time, the GPS condition is not as favourable as in other periods, i.e. before and after the simulated outage. Similarly, in the foliage data, the simulated partial GPS outage is 30 s long, and only PRNs 08 and 28 were left in the navigation calculation during the outage. The outage is from GPS time 238800 s to 238830 s. During this time, the number of SVs used in the navigation solution in normal case is low (mostly about 3-4 SVs).

5.6.4.1 Test Results with Open Sky Data

The test results of open sky data are shown in Figure 5.15 and Figure 5.16. Specifically, Figure 5.15 shows the number of SVs used in the navigation solution of UT GPS/3A1G (upper figure) and the vector tracking status (lower figure). It can be seen that during the partial GPS outage, only one or two satellites are used in the navigation solution. It is noted that although there are two SVs which are left for the navigation calculation during the partial outage, if the measurement error (i.e. pseudorange or Doppler shift error) of

one SV is too large, the SV will be rejected from the navigation solution calculation. This rejection is implemented with a GPS measurement quality control algorithm (or innovation sequence test) programmed in the navigation solution software. Accordingly, if one SV is rejected in the navigation calculation, there is only one SV used in the navigation solution during the partial outage. From Figure 5.15, it also can be seen that after the partial GPS outage, the number of SVs used in the navigation solution will recover to the normal case, i.e. without partial GPS outage case.

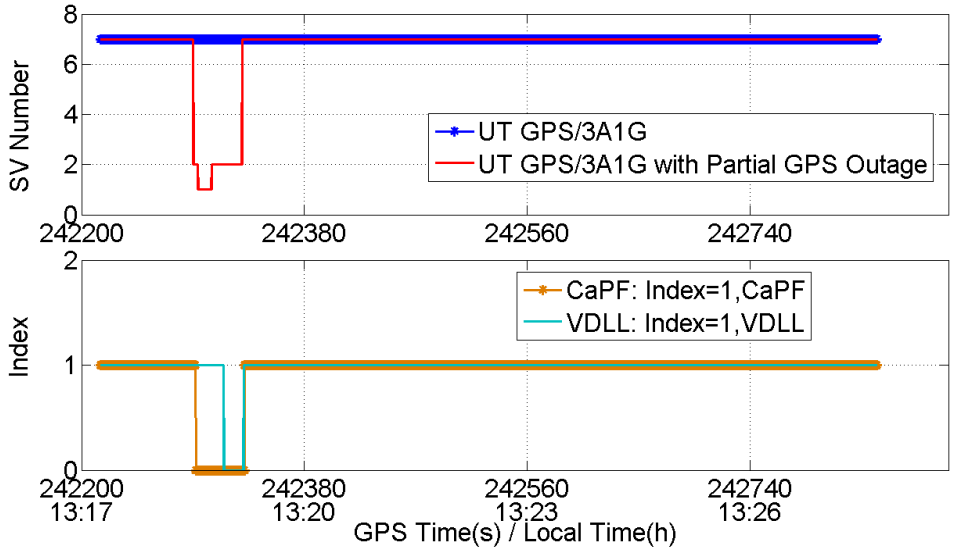

Figure 5.15 Number of SVs Used in Navigation Solution and Vector Tracking Status of UT GPS/3A1G (Crista) with RTLs and Open Sky Data

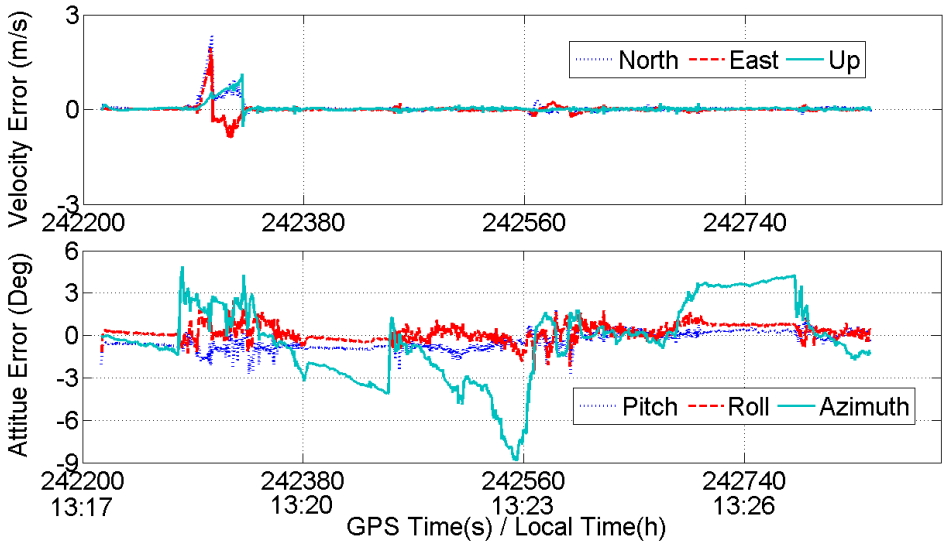

Figure 5.16 Velocity and Attitude Error of UT GPS/3A1G (Crista) with RTLs and Open Sky Data

Figure 5.15 also shows the vector tracking status (lower figure), denoted as the indices of CaPF and VDLL. If the index of CaPF is one, the carrier loop is a CaPF; if the index is zero, the carrier loop is a PLL (without Doppler aiding, a third-order loop filter and a noise bandwidth of 8 Hz). Similarly, if the index of VDLL is one, the code loop is a VDLL; if the index is zero, the loop is a DaDLL (with code Doppler aiding and a narrow noise bandwidth of 0.05 Hz). Finally, from Figure 5.15, it can be seen that when the partial GPS outage occurred, the CaPF is the first to switch to the scalar tracking loop, i.e. PLL. After the partial outage, the PLL and DLL switch back to the CaPF and VDLL, respectively.

Figure 5.16 shows the velocity and attitude errors for the UT GPS/3A1G with RTLs. From this figure, it can be seen that when the partial GPS outage occurs, both the velocity and attitude error increase, and the increase of the velocity error is more noticeable. After

the partial outage, both the velocity and attitude error decrease, as should be expected. Similar results are also obtained for the 2A1G case and are therefore not shown.

5.6.4.2 Test Results with Foliage Data

The test results of the foliage data are shown in Figure 5.17, Figure 5.18, and Figure 5.19. Figure 5.17 shows the number of SVs used in the navigation solution of UT GPS/3A1G and the vector tracking status. From this figure, it can be seen that when the partial GPS outage occurred, the CaPF is the first to switch to the scalar tracking loop. Also, after the partial GPS outage, the number of SVs used in the navigation solution recovers to the normal case, and the PLL and DLL switch back to the CaPF and VDLL, respectively, just like in the open sky case. Figure 5.18 shows the velocity and attitude error of the UT GPS/3A1G with RTLs. It shows a similar result as in the open sky case, namely that when the partial GPS outage occurs, both the velocity and attitude error increase, and, that after the partial outage, both the velocity and attitude error decrease to normal values. Figure 5.19 shows the number of SVs and the vector tracking status of the 2A1G configuration. From this figure, it can be seen that there are two partial GPS outages in the test: one is simulated and the other is naturally occurring. During the naturally occurring partial outage, only the CaPF switches to the PLL. After either of the two outages, the carrier loop and code loop switch back to the CaPF and VDLL, respectively. After the simulated outage, the DLL is the first to switch back to the VDLL. From the above results, it can be concluded that the RTL algorithm is valid, and can be used in practice. Since, with the RTLs, the SVs in view can keep tracking during partial GPS outages (and be used in the navigation solution), it is expected that the navigation performance of the integration system during the partial GPS outages can be improved

compared to the UT system without RTLs. This cannot be confirmed because the confirmation needs more tests.

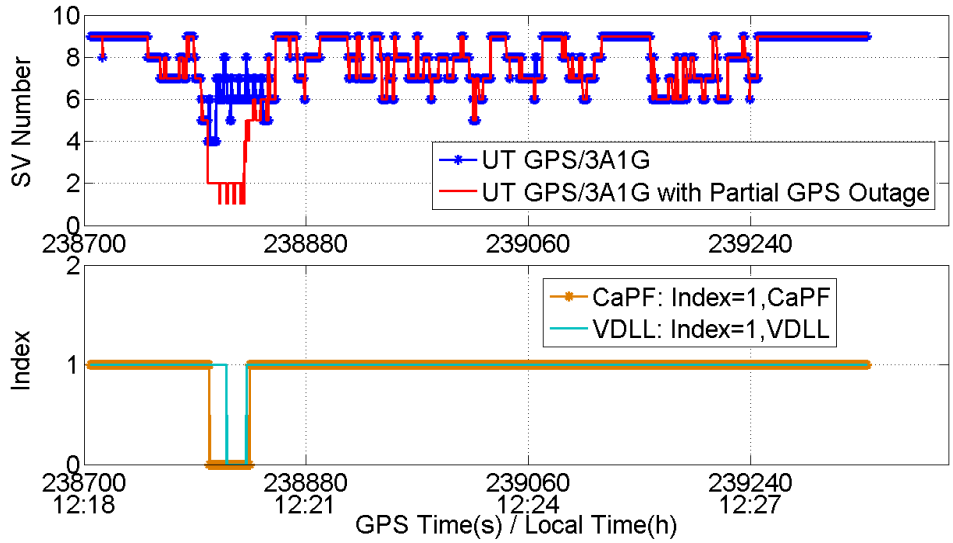

Figure 5.17 Number of SVs Used in Navigation Solution and Vector Tracking Status of UT GPS/3A1G (Crista) with RTLs and Foliage Data

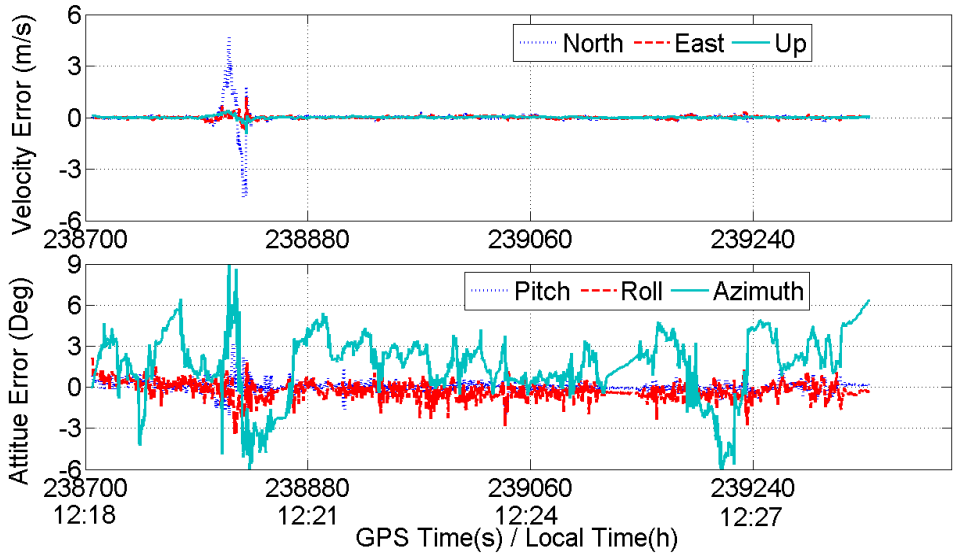

Figure 5.18 Velocity and Attitude Error of UT GPS/3A1G (Crista) with RTLs and Foliage Data

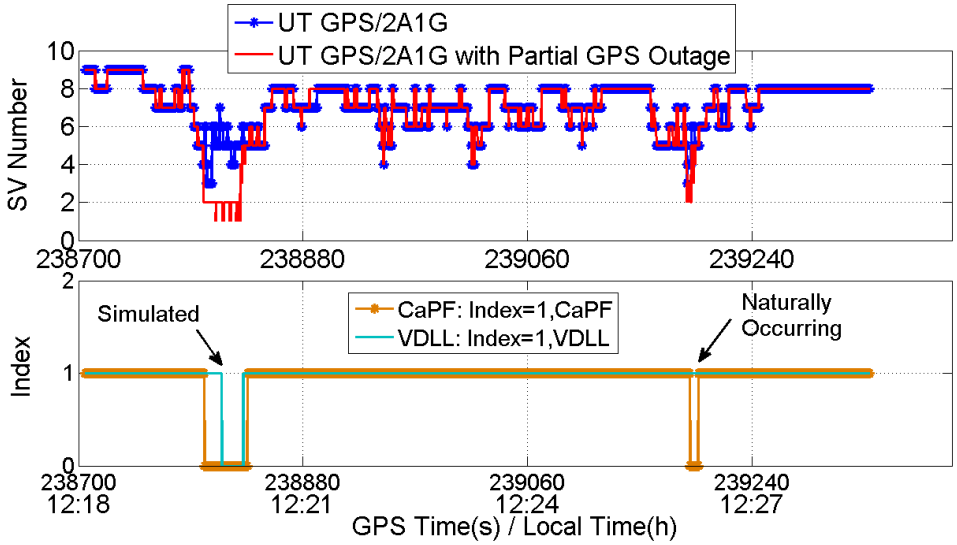

Figure 5.19 Number of SVs Used in Navigation Solution and Vector Tracking Status of UT GPS/2A1G (Crista) with RTLs and Foliage Data

5.6.4.3 Summary

From the above test results, it can be concluded that the RTL algorithm is valid. It can switch a CaPF and a VDLL into a PLL and a DLL respectively when vector-based tracking fails. Once the vector-based tracking is available, the tracking loops will switch back to the CaPF and VDLL from the PLL and DLL, respectively. This will let the satellites in view still keep tracking, thus saving the reacquisition step for those satellites, and potentially improving the navigation performance of the GPS/RIMU, especially during partial GPS outages.

5.6.5 Summary

Based on the test results presented above, the following conclusions are drawn:

- Both the GPS/RIMU with VDF and GPS/RIMU with VDCaP worked well.

- For the VDF, the velocity error in any one direction ranged between 0.03 and 0.07 m/s. Its pitch and roll error ranged between 0.34 and 0.65 degrees, respectively. And the azimuth error ranged between 1.68 and 3.04 degrees.
- For the VDCaP (with the loop filter reset criteria of Section 5.1.2.1), its velocity error ranged between 0.03 and 0.11 m/s. Its pitch and roll error ranged between 0.32 and 0.68 degrees, respectively. The azimuth error ranged between 1.78 and 3.50 degrees.
- In the open sky case, the VDF and VDCaP had a similar tracking ability (i.e. a similar number of SVs used in navigation solution) and a similar navigation performance in terms of velocity and attitude. In the foliage case, compared to the VDF, the VDCaP performed worse, i.e. its tracking ability was low (i.e. the number of SVs used in navigation solution was low), and its velocity error was large.
- The CaPF is practicable. For the same loop filter reset criteria (designed in Section 5.2), the VDCaPF and VDCaP have a similar navigation performance. Their tracking abilities are similar because their carrier tracking loops are same, i.e. both are CaPLL. Only their measurement outputs are different.
- The RTL algorithm is valid. It was shown to correctly switch a tracking loop between a VBTL and a SBTL, thus saving the reacquisition for the satellites which were in view during a partial GPS outage, and potentially improving the navigation performance of the GPS/RIMU, especially during the partial GPS outage.

It is noted that the above conclusions were obtained from the test data used in this dissertation. Further testing would be required to confidently extend these conclusions to other data sets. Further investigation is also needed to explore the potential advantages of the CaPF approach.

5.7 Evaluation of UT and TLA GPS/RIMU

In the UT and TLA system comparison, the UT GPS/RIMU with VDCaP (designed in Section 5.1.2.1) is chosen to compare with the corresponding TLA system, which is implemented with a DaDLL plus a DaPLL (see Section 4.1). The multipath alleviating comparison of the two systems is not made in this section because such an analysis would need special experiments.

5.7.1 Test Results with Open Sky Data

With the open sky data, the tracking abilities of the UT and TLA GPS/RIMU are similar. Specifically, the numbers of SVs used in the navigation solution are similar, i.e. seven SVs are used for almost the entire test. The number of SVs used in the navigation solution of the UT system is shown in Figure 5.13. The TLA system has a similar plot (not shown to save the space). The test results of the UT and TLA GPS/RIMU are summarized in Table 5.10. With reference to this table, “Azi.” is the abbreviation of “Azimuth”, and “Nor.” is the abbreviation of “North”. From Table 5.10, it can be seen that the UT and TLA systems have a similar navigation performance. Of particular interest, however, is the azimuth error of the TLA GPS/2A1G which is noticeably greater than that of the corresponding UT system.

Table 5.10 Position, Velocity, and Attitude Error of UT and TLA GPS/RIMU (Crista) with Open Sky Data

Integration Strategy	RMS Attitude Error (Deg)			RMS Velocity Error (m/s)			RMS Position Error (m)		
	Pitch	Roll	Azi.	East	Nor.	Up	East	Nor.	Up
UT GPS/3A1G	0.65	0.58	2.53	0.04	0.04	0.03	0.98	2.03	6.06
TLA GPS/3A1G	0.65	0.58	2.54	0.04	0.04	0.03	0.83	1.69	6.27
UT GPS/2A1G	0.65	0.58	1.78	0.04	0.05	0.04	0.96	2.01	6.32
TLA GPS/2A1G	0.65	0.58	2.30	0.04	0.05	0.04	0.81	1.67	6.56

5.7.2 Test Results with Foliage Data

With the foliage data, the tracking performance of the UT and TLA GPS/RIMU are shown in Figure 5.20 for 3A1G, and Figure 5.21 for 2A1G. From Figure 5.20, it can be seen that the UT and TLA GPS/3A1G system have a similar number of SVs used in navigation solution, i.e. they have a similar tracking ability. From Figure 5.21, it can be seen that the TLA GPS/2A1G has more SVs used in navigation solution than does the corresponding UT system. The UT GPS/2A1G loses one SV after the first few minutes since the maximum number of SVs used in the navigation solution is only eight after the first few minutes. Actually the SV (i.e. PRN 25, with low elevation angle, see Figure 4.13 – satellite skyplot), which is always not used in the navigation solution after the first few minutes, does not lose tracking. It is just rejected from the navigation solution calculation by a GPS measurement quality control algorithm programmed in the navigation solution software, as discussed in Section 5.6.4. This rejection happens because the measurement error (pseudorange/Doppler shift) of the SV is too large to be used in the navigation solution. In other words, it is because of the measurement quality, not the loss of the SV's

tracking that the SV is not used in the navigation solution. Actually since the rejected SV (i.e. PRN 25) has a low elevation angle (about 23 degrees), its signal is weak, resulting in a large pseudorange measurement error (about 300 km, the range of one C/A code). This large error should be caused by the integer ambiguity in the code phase, resulting from the problem in transmit time generation (e.g. in code decoding or bit synchronization). It is noted that in the TLA GPS/2A1G, the carrier loop is a CaPLL, just like in the UT system. So the difference between the UT and TLA GPS/2A1G is only in the code loop.

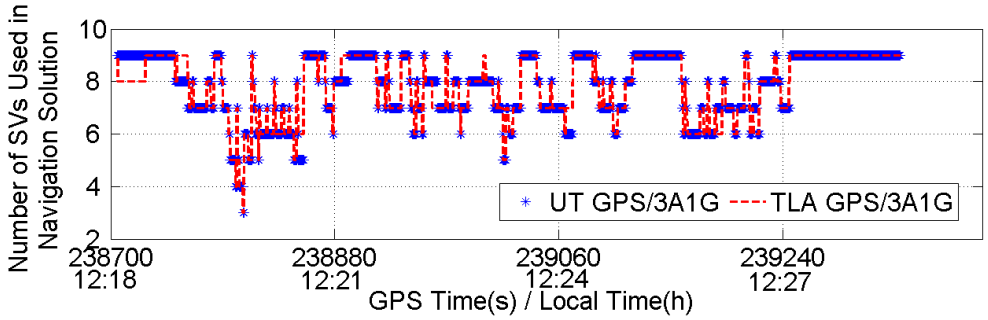

Figure 5.20 Number of SVs Used in Navigation Solution of UT and TLA GPS/3A1G (Crista) with Foliage Data

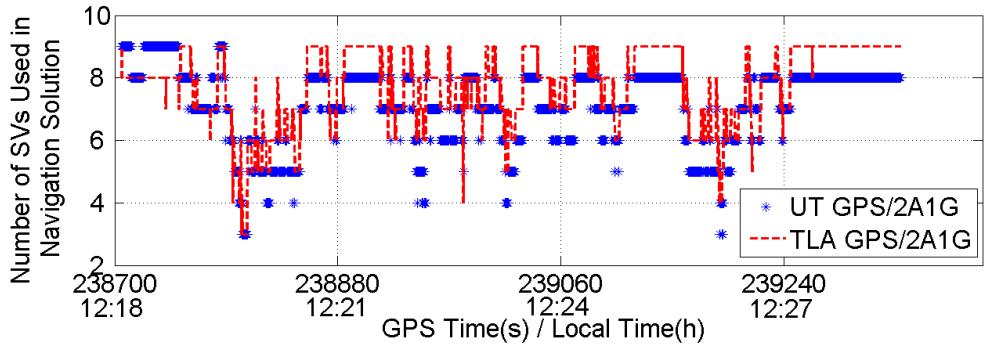

Figure 5.21 Number of SVs Used in Navigation Solution of UT and TLA GPS/2A1G (Crista) with Foliage Data

The navigation performance of the UT and TLA GPS/RIMU is summarized in Table 5.11. It can be seen that the UT and TLA system have a similar attitude error for either RIMU

configuration. For 3A1G configuration, the two systems have a similar velocity error, but their position error is slightly different. This difference is mainly caused by the transient process of the integration Kalman filter, as shown in Figure 5.22. From this figure, it can be seen that the UT and TLA system have a similar position error in each direction after the transient process. For 2A1G configuration, the TLA system has a smaller velocity error (e.g. in north and vertical direction). Specifically, the 3D RMS velocity error of TLA GPS/2A1G is reduced by 7.5% compared to the UT system. This could be caused by the fact that the TLA GPS/2A1G has more SVs used in navigation solution, as discussed above. The position error comparison of the two 2A1G systems has a similar result as the 3A1G case. In short, the UT and TLA system have a similar position and attitude error for either RIMU configuration. For 3A1G, the two systems also have a similar velocity error. For 2A1G, the 3D RMS velocity error of the TLA system is reduced by 7.5% compared to the UT system.

As discussed above, in the foliage test, the carrier loop of the TLA GPS/2A1G is implemented with a CaPLL. In other cases, the carrier loop of the TLA system is implemented with a DaPLL. In the TLA GPS/2A1G, in order to improve the system's performance in the foliage test, the PLL loop filter is reset according to a certain criterion, as discussed in Section 5.1.2.1, resulting in a CaPLL. If the carrier loop of the TLA system is implemented with a DaPLL, i.e. no loop filter reset for the DaPLL, the navigation performance of the TLA GPS/2A1G is summarized in Table 5.12. Comparing this table with the corresponding result in Table 5.11, it can be seen that with a CaPLL,

the TLA GPS/2A1G has a better navigation performance, especially in terms of velocity. This further demonstrates that the CaPLL is valid.

Table 5.11 Position, Velocity, and Attitude Error of UT and TLA GPS/RIMU (Crista) with Foliage Data

Integration Strategy	RMS Attitude Error (Deg)			RMS Velocity Error (m/s)			RMS Position Error (m)		
	Pitch	Roll	Azi.	East	Nor.	Up	East	Nor.	Up
UT GPS/3A1G	0.32	0.64	2.65	0.07	0.09	0.03	2.04	4.07	4.89
TLA GPS/3A1G	0.33	0.63	2.71	0.07	0.08	0.03	4.18	1.57	7.08
UT GPS/2A1G	0.45	0.68	3.50	0.08	0.11	0.07	1.96	4.32	4.97
TLA GPS/2A1G	0.44	0.66	3.47	0.08	0.10	0.06	4.44	1.80	7.70

Table 5.12 Position, Velocity, and Attitude Error of TLA GPS/2A1G (Crista) With a DaPLL and Foliage Data

Integration Strategy	RMS Attitude Error (Deg)			RMS Velocity Error (m/s)			RMS Position Error (m)		
	Pitch	Roll	Azi.	East	Nor.	Up	East	Nor.	Up
TLA GPS/2A1G	0.48	0.70	3.41	0.09	0.12	0.06	4.30	2.46	7.33

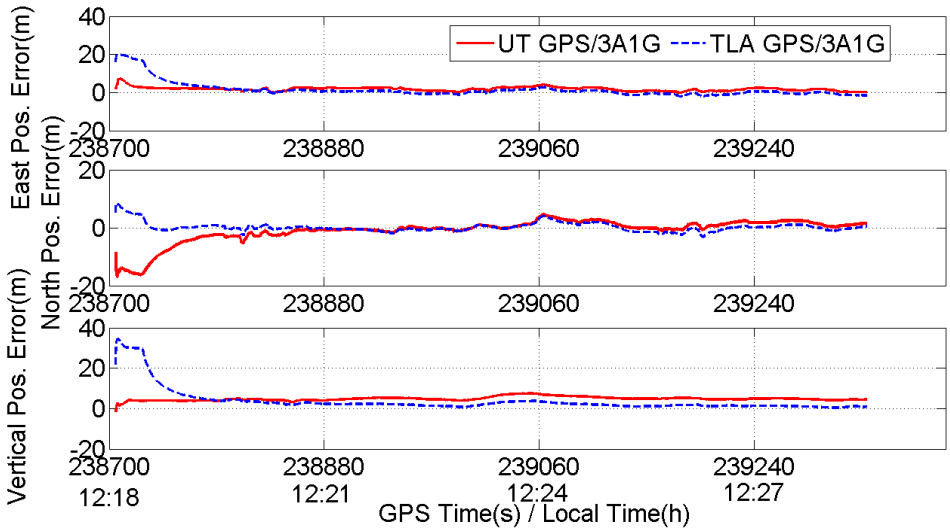

Figure 5.22 Position Error of UT and TLA GPS/3A1G (Crista) with Foliage Data

5.7.3 Summary and Discussion

Based on the above test result comparison, the following conclusions are drawn:

- The UT and TLA GPS/RIMU both have a similar tracking capability, i.e. a similar number of SVs used in the navigation solution, except that the TLA GPS/2A1G had more SVs used in navigation solution than the UT GPS/2A1G in the foliage case (i.e. weak GPS signal case). The result that UT GPS/2A1G had less SVs used in navigation solution in the foliage case should be caused by the code phase integer ambiguity in the UT system test.
- The UT and TLA GPS/RIMU both have similar navigation performance in terms of position, velocity, and attitude. The exception is that in foliage case, the 3D RMS velocity error of TLA GPS/2A1G is reduced by 7.5% compared to the UT system, resulting from the fact that the TLA GPS/2A1G had more SVs used in navigation solution in the foliage case.

For the position error comparison of the UT and TLA system, the theoretical analysis of Section 5.1.1.2 showed that a VDLL had larger pseudorange measurement thermal noise than a DaDLL, which might result in a larger position error in a UT system. However, the test results showed that the UT and TLA system had a similar position error. Thus the theoretical and the test results seem to be somewhat inconsistent. Actually the position error of the integration system might mainly come from the GPS measurement errors such as multipath and other signal delays, not from the thermal noise. In this light, although the VDLL has larger thermal noise, the UT and TLA system could still have a similar position error.

5.8 Summary

In this chapter, first the UT GPS/RIMU was introduced, specifically for the UT GPS/RIMU with VDF and UT GPS/RIMU with VDCaP. The configurations and implementations of the two UT systems were discussed. Further, the measurement thermal noises of the two systems were analyzed. Then two innovative algorithms/configurations (i.e. CaPF and RTL) were developed. Among them, the CaPF was used to improve the Doppler shift measurement, and the RTL was used to enhance the system performance during partial GPS outages. Finally from the system configuration and implementation, the UT system was compared with the corresponding TLA system to identify their differences in both tracking and navigation performance.

Following the system design and analysis, system evaluations were conducted with the vehicle test data. First the UT GPS/RIMU with VDF and UT GPS/RIMU with VDCaP were evaluated in terms of tracking ability and navigation performance. Then the UT GPS/RIMU with VDCaPF and UT GPS/RIMU with RTLs were assessed to verify these two innovative algorithms, i.e. CaPF and RTL. Finally, a comparison of UT and TLA systems was made with the test results of the two kinds of systems. In the above evaluations, two RIMU configurations, i.e. 3A1G and 2A1G, were used. From the evaluation results, the following conclusions are drawn:

- Both the GPS/RIMU with VDF and GPS/RIMU with VDCaP worked well. With VDF, the velocity error in any one direction ranged between 0.03 and 0.07 m/s. With VDCaP (designed in Section 5.1.2.1), the velocity error ranged between 0.03

and 0.11 m/s. The VDF and VDCaP had a similar attitude error for a corresponding RIMU configuration and test data.

- With strong GPS signals (i.e. open sky case), VDF and VDCaP had a similar tracking ability (i.e. a similar number of SVs used in navigation solution) and a similar navigation performance. With weak signals (i.e. foliage case), VDF outperformed VDCaP, especially in tracking ability and velocity accuracy.
- The innovative algorithm proposed herein – CaPF – is practicable. For the same loop filter reset criteria (designed in Section 5.2), the VDCaPF and VDCaP have a similar navigation performance (their tracking abilities are similar because their carrier tracking loops are same, i.e. both are CaPLL).
- The innovative algorithm proposed herein – RTL – is valid. It correctly switched a tracking loop between a VBTL and a SBTL, thus saving the reacquisition for the satellites in view during a partial GPS outage, and potentially improving the navigation performance of the GPS/RIMU during the partial GPS outage.
- The UT and TLA GPS/RIMU both had a similar tracking ability, except that the TLA GPS/2A1G had more SVs used in navigation solution than the UT GPS/2A1G in weak GPS signal case (i.e. foliage case). The result that UT GPS/2A1G had less SVs used in navigation solution in the foliage case should be caused by the code phase integer ambiguity in the UT system test.
- The UT and TLA GPS/RIMU both had a similar navigation performance, i.e. a similar position, velocity, and attitude error, except that the 3D RMS velocity error of TLA GPS/2A1G is reduced by 7.5% compared to the UT system in weak signal

case (i.e. foliage case), resulting from the fact that in weak signal case the TLA GPS/2A1G had more SVs used in the navigation solution.

Chapter Six: Conclusions and Recommendations

This dissertation presented a thorough assessment for GPS/RIMU integration systems used in land vehicle navigation. To be specific, the following approaches were investigated in detail:

- *An innovative LTP algorithm for RIMU error modeling in GPS/RIMU*: In a GPS/RIMU system, the pitch and roll cannot be calculated or observed directly from the RIMU and the navigation performance is thus affected by local terrain variations. To overcome this disadvantage, an LTP algorithm was developed for the RIMU to improve the navigation performance, resulting in a set of innovative mechanization equations and error model for RIMU. Furthermore, these equations were compared with two other types of equations (namely DR and FD type) to investigate their relative performance.
- *An innovative ALF algorithm for TLA GPS/RIMU*: In a TLA GPS/RIMU, since the PLLs of the GPS receiver are aided with the Doppler shift, the noise bandwidth of the loop filters of the PLLs can be narrowed more than in a GPS-only case, resulting in an improved navigation performance. In order to take advantage of this, an adaptive PLL loop filter whose noise bandwidth can be adjusted according to the performance of the integrated system and GPS signal C/N_0 was developed to improve the performance of the TLA GPS/RIMU.
- *Two innovative algorithms/configurations, namely CaPF and RTL, for UT GPS/RIMU*: In a UT GPS/RIMU, when the PLLs of the GPS receiver are not locked, their Doppler measurements will be degraded by the transient state of the PLLs. To overcome this disadvantage, a CaPF algorithm was developed to

provide more reliable Doppler measurement in both the “PLL locked” and “PLL unlocked” cases. On the other hand, a reconfigurable tracking loop (i.e. RTL) was developed to enhance the system performance during partial GPS outages. It can switch the tracking loops of the GPS receiver between vector and scalar tracking during partial GPS outages. In addition, two typical kinds of UT systems – VDF and VDCaP – were implemented.

To assess the above innovative algorithms, the corresponding systems such as loose, TLA, and UT GPS/RIMU were developed. Each of the above systems and innovative algorithms was implemented in software (using the University of Calgary’s GSNRx™ software as a starting point, and then the corresponding software packages were developed) and was evaluated with field vehicle test data. In the vehicle test, two different grades of IMUs were used: a tactical-grade IMU (Honeywell HG1700) and a MEMS-grade IMU (Crista). A GPS IF data collection system consisting of a NovAtel Euro-3M card was used for IF data collection. Only two RIMU configurations suitable for vehicle applications were considered: one is 3A1G, the other is 2A1G. A quite few test runs were conducted to verify the above innovative algorithms and to assess the different kinds of integrated systems (i.e. loose, TLA, and UT), thus providing useful information for practical land vehicle navigation system development.

Through the above assessment for the loose, TLA, and UT GPS/RIM, a few of conclusions were drawn. But only the major conclusions are outlined in the following section.

6.1 Conclusions

Overall, the above innovative algorithms are valid, and the three types of GPS/RIMU, namely loose, TLA, and UT, worked well in land vehicle navigation. The conclusions for the different architectures are presented below.

Reduced IMU Mechanization (i.e. loose GPS/RIMU)

1. The LTP method can improve the navigation performance of a GPS/RIMU both when GPS is available and unavailable. To be specific, with an LTP, pitch and roll were estimated, and velocity error was reduced, especially in the horizontal direction. The 3D RMS velocity error was reduced by more than 80% (from about 1.02 m/s to 0.14 m/s) compared to the case without LTP. During GPS outages, the LTP method reduced both position and velocity errors.
2. For loose GPS/RIMU integration, the 2A1G may be a better configuration when cost and performance are considered because with a vertical accelerometer, only the vertical velocity error of the GPS/3A1G was reduced (e.g. for a MEMS IMU, the vertical velocity error was reduced to 0.08 m/s from 0.09 m/s, about 11%).
3. The three types of M&E equations (i.e. LTP, DR, and FD model) are valid and can be applied in the GPS/RIMU system for land vehicle navigation. Compared to the LTP model, the DR model could achieve a similar performance only if the pitch and roll were estimated in the accelerometer bias term (i.e., a composite bias); otherwise its performance was much degraded. For the FD model, compared to the LTP, it achieved a similar performance in strong GPS signal cases (i.e., open sky case), but in weak signal cases (i.e., foliage case), its performance was inferior.

Specifically, the 3D RMS velocity error of the GPS/3A1G (Crista) with FD model was more than twice that of the system with the LTP model.

TLA GPS/RIMU

1. In both ideal and real situations, namely on the roof of a building and on a real road, the TLA GPS/RIMU performed better than the corresponding tight system in terms of tracking ability and navigation solution accuracy. Specifically, with Doppler aiding, the tracking performance of the GPS receiver was improved, with more satellites being tracked, and smaller Doppler measurement errors. In addition, with Doppler aiding, the navigation performance of the TLA GPS/RIMU was also improved. More specifically, the 3D RMS velocity error was reduced by 54% (from about 0.24 m/s to 0.11 m/s, for the foliage case), the pitch and roll error were marginally reduced, if at all, but the azimuth error was reduced clearly. Specifically in the foliage case, the RMS azimuth error of TLA GPS/3A1G (Crista) was reduced by 26% (from about 3.64 degrees to 2.71 degrees) compared to the tight GPS/3A1G (Crista).
2. The ALF algorithm can provide a proper noise bandwidth for the Doppler-aided PLL of the TLA GPS/RIMU. As a result, compared to the CNBLF case, with ALFs, the PLL tracking performance of the TLA GPS/RIMU was improved in terms of reducing the Doppler measurement error and providing better phase tracking, but some unmodeled system errors might cause phase lock degradation. Furthermore, with ALFs, the navigation performance of the TLA GPS/RIMU was improved, especially for velocity. The 3D RMS velocity error was reduced by up

to 19% (from about 0.17 m/s to 0.14 m/s). The pitch and roll error were also reduced, but only slightly. The azimuth error was reduced by 17% (from about 3.28 degrees to 2.72 degrees) for MEMS IMU and the foliage test data.

3. In TLA GPS/RIMU, the 3A1G case outperformed the 2A1G case since it allowed a narrower noise bandwidth, resulting in not only a smaller vertical velocity error but also a smaller horizontal velocity error.

Ultra-Tight GPS/RIMU

1. Both the GPS/RIMU with VDF and GPS/RIMU with VDCaP worked well. With VDF, the velocity error in any one direction ranged between 0.03 and 0.07 m/s. With VDCaP (designed in Section 5.1.2.1), the velocity error ranged between 0.03 and 0.11 m/s. The VDF and VDCaP had a similar attitude error for a corresponding RIMU configuration and test data.
2. With strong GPS signals, VDF and VDCaP had similar tracking ability and navigation performance. With weak signals, VDF outperformed VDCaP, especially in tracking ability and velocity accuracy.
3. For the CaPF, with the same loop filter reset criteria (designed in Section 5.2), the VDCaPF and VDCaP have a similar navigation performance (their tracking abilities are similar because their carrier tracking loops are same, i.e. both are CaPLL). The RTL correctly switched a tracking loop between a VBTL and a SBTL, thus saving the reacquisition for the satellites in view during a partial GPS outage, and potentially improving the navigation performance of the GPS/RIMU during the partial GPS outage.

4. UT and TLA GPS/RIMU both had similar tracking ability, except that the TLA GPS/2A1G had more SVs used in the navigation solution than the UT GPS/2A1G in a weak GPS signal case. The fact that UT GPS/2A1G had less SVs used in the navigation solution in the foliage case was caused by the code phase integer ambiguity in the UT system test. Thus, the tracking was fine, and the error could conceivably be identified and corrected using innovation sequence in the navigation solution, although this was beyond the scope of this work.
5. The UT and TLA GPS/RIMU both had similar navigation performance, except that the velocity error of TLA GPS/2A1G is reduced by 7.5% (from about 0.15 m/s to 0.14 m/s) compared to the UT system. The fact that the TLA GPS/2A1G had a smaller velocity error should result from the fact that in the weak GPS signal case the TLA GPS/2A1G had more SVs used in navigation solution.

6.2 Recommendations

Based on the research and test results obtained, it can be seen that each method or system has its own advantages and disadvantgaes. Thus, the best implementation choice depends on the most important considerations for a particular system. For example, for RIMU mechanization, compared to the LTP model, the DR model may not properly account for all roll and pitch effects but it has a smaller compuation load and can be further simplified. If the computation load and simplicity are important the DR model should be selected. However generally the LTP model should be the best because it not only can provide a similar or better performance in both strong and weak GPS signal cases, but it also has a medium computation load compared to the DR and FD models. Similar rules can be applied to the integration strategy choosing of the GPS/RIMU. Generally the

VDCaP or VDCaPF should be more preferred in land vehicle navigation because it not only has the advantages of vector tracking loops (in code loop) compared to a scalar DLL, but also has the advantages of PLL compared to an FLL.

For the future research, some recommendations can be made as follows.

Reduced IMU mechanization

1. Although the LTP algorithm is a valid attitude error model (for pitch and roll) for reduced IMU, more experiments are needed to investigate the effect of the local terrain and the GPS measurement accuracy on the navigation performance such as attitude and velocity accuracy.
2. For MEMS reduced IMU, since the gyro measurement accuracy is low (its turn on drift can be few thousands degrees per hour, see Section 3.3.1 for details), the azimuth accuracy of the GPS/RIMU closely depends on the GPS measurement accuracy and the vertical gyro's drift estimation accuracy. Thus a proper error model of the vertical gyro can benefit the performance of the GPS/RIMU. In this light, the error model of the vertical gyro in a MEMS RIMU needs to be further researched and properly modeled in the GPS/RIMU.
3. Furthermore, since in MEMS IMU, the azimuth accuracy of the GPS/RIMU depends on the GPS measurement, when GPS measurement cannot give an accurate enough azimuth estimation (i.e., within a few degrees), other on-vehicle sensors such as a steering angle sensor should benefit the azimuth estimation, especailly when the vehicle is moving slowly or is stopped. Moreover vehicle

speed sensors can mainly benefit the velocity estimation when GPS measurement is poor. As a result, more research is needed to to explore the potential benfit of the on-vehicle sensors for the proformance imporvement of the GPS/RIMU.

4. Although this dissertation conducted a thorough research on the RIMU mechanization and error model, several questions still remain in order to develop a practical GPS/RIMU system (i.e., a production system usable in all local terrain). In particular, is it necessary that the local terrain model parameters be adjusted in real time or for different local terrains and how to adjust the parameters if they needs? Does the GPS measurement noise variance necessarily need to be adjusted in real time? These topics should be further studied.

TLA GPS/RIMU

1. From the ALF results, it can be seen that some unmodeled system errors can cause phase lock degradation during short time periods. Furthermore, different models for Doppler aiding error can produce different noise bandwidth. In this light, the ALF algorithm needs further research. In particular, a more precise Doppler error model needs to be explored in the hope of further improving the performance of the TLA system. In addition, the effect of the transient process of the tracking loop and the C/N_0 variations on the noise bandwidth choosing needs to be investigated.
2. In the TLA system, an OCXO was used in the GPS receiver. Such an oscillator has a very low aging rate, high temperature stability, and low phase noise (Symmetricom 2007). But its price is quite high (few thousands US dollars). For land vehicle navigation system design, a low cost oscillator – TCXO – should be

used in practical TLA GPS/RIMU systems. Thus the performance of the TLA system with a TCXO needs to be quantified.

Ultra-Tight GPS/RIMU

1. For different UT systems such as UT GPS/RIMU with VDF and UT GPS/RIMU with VDCaP, they have different tracking and navigation performance. To further quantify their differences in performance, more experiments need to be conducted, such as experiments with different user dynamics and the experiments with different C/N_0 variations. Furthermore, the Doppler measurement errors of the VFLL and the CaPLL need to be further researched and evaluated when user dynamics and C/N_0 variations are considered.
2. Further investigation is needed to explore the potential advantages of the CaPF approach (i.e. the VDCaPF system).
3. From the above UT system research, it can be seen that in a UT system, the vector tracking loop such as the VDLL only tracks the signals whose parameters (such as time delay) can be known precisely enough. If the time delays of the tracked signals are unknown or not known precisely enough, the VDLL will fail. As a result, a VDLL not only has some advantages such as high anti-jamming and multipath alleviating ability, but also has some disadvantages such as low stability, compared to a DLL (a scalar tracking loop). In this light, innovative UT system configurations/algorithms need to be developed to overcome the UT system's disadvantages. Furthermore, some special experiments such as urban canyon

experiments are needed to quantify the multipath alleviating ability of the UT GPS/RIMU system.

References

Alban, S., D. Akos, S. Rock, and D. Gebre-Egziabher (2003) "Performance Analysis and Architectures for INS-Aided GPS Tracking Loops," in *Proceedings of ION NTM 2003*, 22-24 January, Anaheim CA, pp.611-622, U.S. Institute of Navigation, Fairfax VA

Allen, J.M., J.H. Britt, C.J. Rose, and D.M. Bevly (2009) "Intelligent Multi-Sensor Measurements to Enhance Vehicle Navigation and Safety Systems," in *Proceedings of ION ITM 2009*, 26-28 Jan., Anaheim, CA, pp. 74-83, U.S. Institute of Navigation, Fairfax VA

Axelrad, P. and R.G. Brown (1996) "GPS Navigation Algorithms," Chapter 9 of *Global Positioning System: Theory and Applications*, Volume I, B.W. Parkinson and J.J. Spilker Jr. (eds.), Washington, DC, American Institute of Aeronautics and Astronautics, Inc., p. 409-433

Babu R.and J. Wang (2005) "Analysis of INS Derived Doppler Effects on Carrier Tracking Loop," *The Journal of Navigation*, vol 58, no 3, pp. 493-507, The Royal Institute of Navigation

Benson, D. (2007) "Interference Benefits of a Vector Delay Lock Loop (VDLL) GPS Receiver," in *Proceedings of ION 63rd Annual Meeting*, 23-25 April, Cambridge, Massachusetts, pp. 749-756, U.S. Institute of Navigation, Fairfax VA

Beser, J., A. Crane, S. Rounds, and J. Wyman (2002) "TRUNAV^{TM}: A Low-Cost Guidance/Navigation Unit Integrating a SAASM-Based GPS and MEMS IMU in a Deeply Coupled Mechanization," in *Proceedings of ION GPS 2002*, 24-27 Sept., Portland, OR, pp. 545-555, U.S. Institute of Navigation, Fairfax VA

Best, R. (2007) *Phase-Locked Loops: Design, Simulation, and Applications*, Sixth Edition, McGraw Hill

Borre, K., D.M. Akos, N. Bertelsen, P. Rinder, and S. H. Jensen (2007) *A Software-Defined GPS and Galileo Receiver: A Single-Frequency Approach*, Birkhäuser

Britt, J.H. and D.M. Bevly (2009) "Lane Tracking using Multilayer Laser Scanner to Enhance Vehicle Navigation and Safety Systems," in *Proceedings of ION ITM 2009*, 26-28 Jan., Anaheim, CA, pp. 629-634, U.S. Institute of Navigation, Fairfax VA

Brown, R.G. and P. Hwang (1992) *Introduction to Random Signals and Applied Kalman Filtering*, John Wiley & Sons

Bullock, J.B., M. Foss, G.J. Geier, and M. King (2006) "Integration of GPS with Other Sensors and Network Assistance," Chapter 9 of *Understanding GPS: Principle and Applications*, Second Edition, E.D. Kaplan and C.J. Hegarty (eds.), Norwood, MA, Artech House, p.459-554

CCT (2006), *Crista Inertial Measurement Unit (IMU) Interface / Operation Document*, Cloud Cap Technology Inc., USA, March (Available at http://www.cloudcaptech.com)

Chiou, T (2005) "GPS Receiver Performance Using Inertial-Aided Carrier Tracking Loop," in *Proceedings of ION GNSS 2005*, 13-16 Sept., Long beach, CA, pp.2895-2910, U.S. Institute of Navigation, Fairfax VA

Chiou, T., J. Seo, T. Walter, and P. Enge (2008) "Performance of a Doppler-Aided GPS Navigation System for Aviation Applications under Ionospheric Scintillations," in

Proceedings of ION GNSS 2008, 16-19 Sept., Savannah, GA, pp.1139-1147, U.S. Institute of Navigation, Fairfax VA

Chiou, T., D. Gebre-Egziabher, T. Walter, and P. Enge (2007) "Model Analysis on the Performance for an Inertial Aided FLL-Assisted PLL Carrier-Tracking Loop in the Presence of Ionospheric Scintillation, " in *Proceedings of ION NTM 2007*, 22-24 Jan., San Diego, CA, pp. 1276-1295, U.S. Institute of Navigation, Fairfax VA

Chiou, T., S. Alban, S. Atwater, J.D. Gautier, S. Pullen, P. Enge, D. Akos, D. Gebre-Egziabher, and B. Pervan (2004) "Performance Analysis and Experimental Validation of a Doppler-Aided GPS/INS Receiver for JPALS Applications," in *Proceedings of ION GNSS 2004*, 21-24 Sept., Long Beach, CA, pp. 1609-1618, U.S. Institute of Navigation, Fairfax VA

Crane, R.N. (2007) "A Simplified Method for Deep Coupling of GPS and Inertial Data," in *Proceedings of ION NTM 2007*, 22-24 Jan., San Diego, CA, pp. 311-319, U.S. Institute of Navigation, Fairfax VA

Daum, P., J. Beyer, T. Köhler (1994) "Aided Inertial LAnd NAvigation System (ILANA) with a Minimum Set of Inertial Sensors," in *Proceedings of IEEE-IEE Vehicle Navigation & Information Systems Conference, Yokohama-VNIS'94,* pp. 284-291

El-Sheimy, N. (2007) *Inertial Techniques and INS/DGPS Integration*, ENGO699.64 Course Notes, Department of Geomatics Engineering, University of Calgary, Canada

Farrell, J. and M. Barth (1999) *The Global Positioning System & Inertial Navigation*, McGraw-Hill

Gao, G. (2007a) *INS-Assisted High Sensitivity GPS Receivers for Degraded Signal Navigation*, Ph.D. Dissertation, Department of Geomatics Engineering, University of Calgary, Canada (Available at http://plan.geomatics.ucalgary.ca)

Gao, J. (2007b) *Development of a Precise GPS/INS/On-Board Vehicle Sensors Integrated Vehicular Positioning System*, Ph.D. Dissertation, Department of Geomatics Engineering, University of Calgary, Canada (Available at http://plan.geomatics.ucalgary.ca)

Gao, J., M. Petovello and M.E. Cannon (2006) "Development of Precise GPS/INS/ Wheel Speed Sensor/Yaw Rate Sensor Integrated Vehicular Positioning system," in *Proceedings of ION NTM 2006*, 18-20 January, Monterey CA, pp.780-792, U.S. Institute of Navigation, Fairfax VA

Gautier, J.D. and B. Parkinson (2003) "Using the GPS/INS Generalized Evaluation Tool (GIGET) for the Comparison of Loosely Coupled, Tightly Coupled and Ultra-Tightly Coupled Integrated Navigation Systems," in *Proceedings of ION 59th AM 2003*, 23-25 June, Albuquerque, NM, pp. 65-76, U.S. Institute of Navigation, Fairfax VA

Gebre-Egziabher, D. (2007) "What is the difference between 'loose', 'tight', 'ultra-tight' and 'deep' integration strategies for INS and GNSS ?," GNSS Solutions Column, *Inside GNSS*, vol 2, no 1, pp. 28-33

Gebre-Egziabher, D., A. Razavi, P. Enge, J.D. Gautier, S. Pullen, B. Pervan, and D. Akos (2005) " Sensitivity and Performance Analysis of Doppler-Aided GPS Carrier-Tracking Loops," *Navigation*, vol 52, no 2, Summer, pp. 49-60, U.S. Institute of Navigation, Fairfax VA

Gelb, A. (1974) *Applied Optimal Estimation*, The M. I. T. Press, Massachusetts Institute of Technology, Cambridge, Massachusetts, USA

Girod, B., R. Rabenstein, and A. Stenger (2001) *Signals and Systems*, John Wiley & sons

Godha, S. (2006) *Performance Evaluation of Low Cost MEMS-Based IMU Integrated with GPS for Land Vehicle Navigation Application*, MSc Thesis, Department of Geomatics Engineering, University of Calgary, Canada (Available at http://plan.geomatics.ucalgary.ca)

Greenspan, R.L. (1996) "GPS and Inertial Integration," Chapter 7 of *Global Positioning System: Theory and Applications*, Volume II, B.W. Parkinson and J.J. Spilker Jr. (eds.), Washington, DC, American Institute of Aeronautics and Astronautics, Inc., p. 187-218

Grewal, M.S. and A.P. Andrews (2001) *Kalman Filtering: Theory and Practice Using MATLAB*, Second Edition, John Wiley & Sons, Inc.

Grewal, M.S., L.R. Weill, and A.P. Andrews (2001) *Global Positioning Systems, Inertial Navigation, and Integration*, John Wiley & Sons, Inc.

Gustafson, D., and J. Dowdle (2003) "Deeply Integrated Code Tracking: Comparative Performance Analysis," in *Proceedings of ION GPS/GNSS 2003*, 9-12 Sept., Portland, OR, pp. 2553-2561, U.S. Institute of Navigation, Fairfax VA

Hamm, C., W. Flenniken, D. Bevly, and D. Lawerence (2004) "Comparative Performance Analysis of Aided Carrier Tracking Loop Algorithms in High Noise/High Dynamic Environments," in *Proceedings of ION GNSS 2004*, 21-24 Sept., Long beach, CA, pp.523-532, U.S. Institute of Navigation, Fairfax VA

Hofmann-Wellenhof, B., K. Legat, and M. Wieser (2003) *Principles of Positioning and Guidance*, Springer-Verlag Wien, NewYork

Hsieh, M. and G. Sobelman (2005) "Clock and Data Recovery with Adaptive Loop Gain for Spread Spectrum SerDes Applications," in *Proceedings of IEEE ISCAS 2005*, 23-26, May, Kobe, Japan, pp. 4883-4886

Humphreys, T., M.L. Psiaki, P. Kintner, and B. Ledvina (2005) "GPS Carrier Tracking Loop Performance in the Presence of Ionospheric Scintillations," in *Proceedings of ION GNSS 2005*, 13-16 Sept., Long Beach CA, pp. 156-167, U.S. Institute of Navigation, Fairfax VA

Im, S., J. Song, B. Lee, G. Jee, S. Han, J. Bae, and J. Kim (2007) "Anti-Jamming Technique Performance Evaluation for GPS L1 C/A Software Receiver," in *Proceedings of ION GNSS 2007*, 25-28 Sept., Fort Worth, TX, pp. 2787-2796, U.S. Institute of Navigation, Fairfax VA

Iqbal, U., A. F. Okou, and A. Noureldin (2008) "An Integrated Reduced Inertial Sensor System -RISS / GPS for Land Vehicle," in *Proceedings of IEEE/ION PLANS 2008*, 6-8 May, Monterey, CA, pp. 1014-1021

Jwo, D. (2001) "GPS Receiver Performance Enhancement via Inertial Velocity Aiding," *The Journal of Navigation*, vol 54, no 1, Feb., pp. 105-117, The Royal Institute of Navigation

Kaplan, E.D., J.L. Leva, D. Milbert, and M.S. Pavloff (2006) "Fundamentals of Satellite Navigation," Chapter 2 of *Understanding GPS: Principle and Applications*, Second Edition, E.D. Kaplan and C.J. Hegarty (eds.), Norwood, MA, Artech House, p.21-65

Kennedy, S. and J. Rossi (2008) "Performance of a Deeply Coupled Commercial Grade GPS/INS System from KHV and NovAtel Inc.," in *Proceedings of IEEE/ION PLANS 2008*, 6-8 May, Monterey, CA, pp. 17-24

Kiesel, S., M.M. Held, G.F. Trommer (2007) "Realization of a Deeply Coupled GPS/INS Navigation System Based on INS-VDLL Integration," in *Proceedings of ION NTM 2007*, 22-24 January, San Diego CA, pp.522-531, U.S. Institute of Navigation, Fairfax VA

Kim, J., D. Hwang, and S. Lee (2007) "Performance Evaluation of INS-Aided Tracking Loop and Deeply Coupled GPS/INS Integration System in Jamming Environment," in *Proceedings of ION 63rd Annual Meeting*, 23-25 April, Cambridge, Massachusetts, pp. 742-748, U.S. Institute of Navigation, Fairfax VA

Kuchar, J. (2001) "Markov Model of Terrain for Evaluation of Ground Proximity Warning System Thresholds," *Journal of Guidance, Control, and Dynamics*, vol 24, no 3, May–June, pp.428-435

Lachapelle, G. (2006) *Navstar GPS Theory And Applications*, ENGO 625 Course Notes, Department of Geomatics Engineering, University of Calgary, Canada

Landis, D., T. Thorvaldsen, B. Fink, P. Sherman, S. Holmes (2006) "A Deeply Integration Estimator for Urban Ground Navigation" in *Proceedings of IEEE/ION PLANS 2006*, 25-27 April, San Diego CA, pp. 927-932

Lashley, M. and D. Bevly (2009a) "Vector Delay/Frequency Lock Loop Implementation and Analysis," in *Proceedings of ION ITM 2009,* 26-28 Jan., Anaheim, CA, pp. 1073-1086, U.S. Institute of Navigation, Fairfax VA

Lashley, M. and D. Bevly (2009b) "What are vector tracking loops, and what are their benefits and drawbacks?," GNSS Solutions Column, *Inside GNSS*, vol 4, no 3, pp. 16-21

Lashley, M. and D. Bevly (2008a) "Comparison of Traditional Tracking Loops and Vector Based Tracking Loops for Weak GPS Signals," in *Proceedings of ION NTM 2008*, 28-30 Jan., San Diego, CA, pp. 310-316, U.S. Institute of Navigation, Fairfax VA

Lashley, M., D. Bevly, and J. Hung (2008b) "Impact of Carrier to Noise Power Density, Platform Dynamics, and IMU Quality on Deeply Integrated Navigation," in *Proceedings of IEEE/ION PLANS 2008*, 6-8 May, Monterey, CA, pp. 9-16

Lee, K., T. Lee, and K. Song (2007) "A Study on the Tracking Loop Design for Weak Signal in High Dynamic Environment," in *Proceedings of ION 63rd Annual Meeting*, 23-25, April, Cambridge, Massachusetts, pp. 589-594, U.S. Institute of Navigation, Fairfax VA

Li, T., M.G. Petovello, G. Lachapelle, and C. Basnayake (2009) "Performance Evaluation of Ultra-tight Integration of GPS/Vehicle Sensors for Land Vehicle Navigation," in *Proceedings of ION GNSS 2009*, 22-25 Sept., Savannah, GA, pp.1785-1796, U.S. Institute of Navigation, Fairfax VA

Mandal, M., and A. Asif (2007) *Continuous and Discrete Time Signals and Systems*, Cambridge University Press, p.395-410

Mao, W., H. Tsao, and F. Chang (2004) "A New Fuzzy Bandwidth Carrier Recovery System in GPS for Robust Phase Tracking," *IEEE Signal Processing Letters*, vol 11, no 4, April, pp. 431-434

Mattern, N., R. Schubert, and G. Wanielik (2008) "Image Landmark Based Positioning in Road Safety Applications Using High Accurate Maps," in *Proceedings of IEEE/ION PLANS 2008*, 6-8 May, Monterey, CA, pp 1008-1013

Misra, P. and P. Enge (2001) *Global Positioning System: Signals, Measurements, and Performance*, Ganga-Jamuna Press

Mohamed, A.H. and K.P. Schwarz (1999) "Adaptive Kalman Filtering for INS/GPS," *Journal of Geodesy*, vol 73, pp 193-203

Nassar, S., X. Niu, P. Aggarwal, and N. El-Sheimy (2006) "INS/GPS Sensitivity Analysis Using Different Kalman Filter Approaches," in *Proceedings of ION NTM 2006*, 18-20 January, Monterey CA, pp.993-1001, U.S. Institute of Navigation, Fairfax VA

Nise, N. (2000) *Control Systems Engineering*, Third Edition, John Wiley & Sons

Niu, X., S. Nassar and N. El-Sheimy (2007a) "An Accurate Land-Vehicle MEMS IMU/GPS Navigation System Using 3D Auxiliary Velocity Updates," *Navigation*, vol 54, no 3, pp.177-188, U.S. Institute of Navigation, Fairfax VA

Niu, X., S. Nasser, C. Goodall, and N. El-Sheimy (2007b) "A Universal Approach for Processing any MEMS Inertial Sensor Configuration for Land-Vehicle Navigation," *The Journal of Navigation*, vol 60, no 2, pp.233-245, The Royal Institute of Navigation

NovAtel (2009), *SPAN™ Technology for OEMV User Manual*, NovAtel Inc., Canada, April (Available at http://www.novatel.ca)

Ochieng, W., J.W. Polak, R.B. Noland, J.Y. Park, L. Zhao, D. Briggs, J. Gulliver, A. Crookell, R. Evans, M. Walker, W. Randolph (2003) "Integration of GPS and

Dead Reckoning for Real-time Vehicle Performance and Emissions Monitoring," *GPS Solutions*, vol 6, no 4, March, pp. 229-241

Ogata, K. (1997) *Modern Control Engineering*, Third Edition, Prentice-Hill

Ohlmeyer, E. J. (2006) "Analysis of an Ultra-Tight Coupled GPS/INS System in Jamming," in *Proceedings of IEEE/ION PLANS 2006*, 25-27 April, San Diego CA, pp. 44-53

Pany, T., and B. Eissfeller (2006) "Use of a Vector Delay Lock Loop Receiver for GNSS Signal Power Analysis in Bad Signal Conditions," in *Proceedings of IEEE/ION PLANS 2006*, 25-27 April, San Diego, CA, pp. 893-903

Pany, T., R. Kaniuth, and B. Eissfeller (2005) "Deep Integration of Navigation Solution and Signal Processing," in Proceedings *of ION GNSS 2005*, 13-16 Sept., Long Beach, CA, pp. 1095-1102, U.S. Institute of Navigation, Fairfax VA

Petovello, M.G. (2003) *Real-Time Integration of a Tactical-Grade IMU and GPS for High-Accuracy Position and Navigation*, Ph.D. Dissertation, Department of Geomatics Engineering, University of Calgary, Canada (Available at http://plan.geomatics.ucalgary.ca)

Petovello, M.G., C. O'Driscoll, and G. Lachapelle (2008a) "Carrier Phase Tracking of Weak Signal Using Different Receiver Architectures," in *Proceedings of ION NTM 2008*, 28-30 Jan., San Diego, CA, pp. 781-791, U.S. Institute of Navigation, Fairfax VA

Petovello, M.G., C. O'Driscoll, G. Lachapelle, D. Borio and H. Murtaza (2008b) "Architecture and Benefits of an Advanced GNSS Software Receiver," *Journal of Global Positioning System (JGPS)*, International Association of Chinese

Professionals in Global Positioning Systems, Vol 7, No 2, pp. 156-168. Available at: http://www.gnss.com.au/JoGPS/v7n2/JoGPS_v7n2p156-168.pdf.

Petovello, M.G., D. Sun, G. Lachapelle and M.E. Cannon (2007) "Performance Analysis of an Ultra-Tightly Integrated GPS and Reduced IMU System," in *Proceedings of ION GNSS 2007*, 25-28 Sept., Fort Worth, TX, pp. 602-609, U.S. Institute of Navigation, Fairfax VA

Petovello, M.G., and G. Lachapelle (2006a) "Comparison of Vector-Based Software Receiver Implementations with Application to Ultra-Tight GPS/INS Integration," in *Proceedings of ION GNSS 2006*, 26-29 Sept., Fort Worth TX, pp.2977-2989, U.S. Institute of Navigation, Fairfax VA

Petovello, M.G., and G. Lachapelle (2006b) "An Efficient New Method of Doppler Removal and Correlation with Application to Software-Based GNSS Receivers," in *Proceedings of ION GNSS 2006*, 26-29 Sept., Fort Worth TX, pp.2407-2417, U.S. Institute of Navigation, Fairfax VA

Phuyal, B. (2004) "An Experiment for a 2-D and 3-D GPS/INS Configuration for Land Vehicle Applications," in *Proceedings of IEEE/ION PLANS 2004*, 26-29 April, Monterey CA, pp. 148-152

Psiaki, M.L. and H. Jung (2002) "Extended Kalman Filter Methods for Tracking Weak GPS Signals," in *Proceedings of ION GPS 2002*, 24-27 Sept., Portland, OR, pp. 2539-2553, U.S. Institute of Navigation, Fairfax VA

Psiaki, M.L. (2001) "Smoother-Based GPS Signal Tracking in a Software Receiver," in *Proceedings of ION GPS 2001,* 11-14 Sept., Salt Lake City UT, pp. 2900-2913, U.S. Institute of Navigation, Fairfax VA

Rana, N.C. and P.S. Joay (2006) *Classical Mechanics*, Tata McGraw-Hill

Raquet, J.F. (2004) *GPS Receiver Design*, ENGO 699.10 Course Notes, Department of Geomatics Engineering, University of Calgary, Canada

Rezaei, S. and R. Sengupta (2007) "Kalman Filter-Based Integration of DGPS and Vehicle Sensors for Localization," *IEEE TRANSACTIONS ON CONTROL SYSTEMS TECHNOLOGY*, vol 15, no 6, Nov., pp. 1080-1088

Rogers, R.M. (1999) "Integrated DR/DGPS Using Low Cost Gyro and Speed Sensor," in *Proceedings of ION NTM 1999,* 25-27 Jan., San Diego, CA, pp. 353-360, U.S. Institute of Navigation, Fairfax VA

Sivananthan, S. and J. Weitzen (2009) "Improving Optimality of Deeply Coupled Integration of GPS and INS," in *Proceedings of ION ITM 2009*, 26-28 Jan., Anaheim, CA, pp. 426-433, U.S. Institute of Navigation, Fairfax VA

Soloviev, A. (2008) "Tight Coupling of GPS, Laser Scanner, and Inertial Measurements for Navigation in Urban Environments," in *Proceedings of IEEE/ION PLANS 2008*, 6-8 May, Monterey, CA, pp. 511-525

Soloviev, A., D. Bruckner, F. van Graas, and L. Marti (2007) "Assessment of GPS Signal Quality in Urban Environments Using Deeply Integrated GPS/IMU," in *Proceedings of ION NTM 2007*, 22-24 January, San Diego, CA, pp. 815-828, U.S. Institute of Navigation, Fairfax VA

Soloviev, A., F. van Graas and S. Gunawardena (2004a) "Implementation of Deeply Integrated GPS/Low-Cost IMU for Reacquisition and Tracking of Low CNR GPS Signals," in *Proceedings of ION NTM 2004*, 26-28 January, San Diego CA, pp. 923-935, U.S. Institute of Navigation, Fairfax VA

Soloviev, A., S. Gunawardena and F. van Graas (2004b) "Deeply Integrated GPS/Low-Cost IMU for Low CNR Signal Processing: Flight Test Results and Real Time Implementation," in *Proceedings of ION GNSS 2004*, 21-24 Sept., Long Beach CA, pp.1598-1608, U.S. Institute of Navigation, Fairfax VA

Sönmez, T. and H.E. Bingöl (2008) "Modeling and Simulation of a Terrain Aided Inertial Navigation Algorithm for Land Vehicles," in *Proceedings of IEEE/ION PLANS 2008*, 6-8 May, Monterey, CA, pp. 1046-1052

Spilker Jr., J.J. (1996) "Fundamentals of Signal Tracking Theory," Chapter 7 of *Global Positioning System: Theory and Applications*, Volume I, B.W. Parkinson and J.J. Spilker Jr. (eds.), Washington, DC, American Institute of Aeronautics and Astronautics, Inc., p. 245-327

Stensby, J.L. (1997) *Phase-Locked Loops: Theory and Applications*, CRC Press

Sun, D., M.G. Petovello, and M.E. Cannon (2010) "Use of a Reduced IMU to Aid a GPS Receiver with Adaptive Tracking Loops for Land Vehicle Navigation," *GPS Solutions*, doi:10.1007/s10291-009-0159-7

Sun, D., M.G. Petovello, and M.E. Cannon (2008) "GPS/Reduced IMU with a Local Terrain Predictor in Land Vehicle Navigation," *International Journal of Navigation and Observation,* vol 2008, Article ID 813821, 15 pages, 2008. doi:10.1155/2008/813821

Syed, Z., P. Aggarwal, X. Niu, and N. El-Sheimy (2007) "Economical and Robust Inertial Sensor Configuration for a Portable Navigation System," in *Proceedings of ION GNSS 2007*, 25-28 Sept., Fort Worth TX, pp. 2129-2135, U.S. Institute of Navigation, Fairfax VA

Symmetricom (2007) "1000B Ultra-Stable Crystal Oscillator," Symmetricom Inc, USA. Available at: http://www.symmetricom.com

Titterton, D. and J. Weston (2004) *Strapdown Inertial Navigation Technology, 2nd Edition*, The Institution of Electrical Engineers

Travis, W. and D.M. Bevly (2009) "Performance Analysis of a Closely Coupled GPS/INS Relative Positioning Architecture for Automated Ground Vehicle Convoys," in *Proceedings of ION ITM 2009*, 26-28 Jan., Anaheim, CA, pp. 999-1008, U.S. Institute of Navigation, Fairfax VA

Van Dierendonck, A.J. (1996) "GPS Receivers," Chapter 8 of *Global Positioning System: Theory and Applications*, Volume I, B.W. Parkinson and J.J. Spilker Jr. (eds.), Washington, DC, American Institute of Aeronautics and Astronautics, Inc., p. 329-405

Van Dierendonck, A.J., P. Fenton, and T. Ford (1992) "Theory and Performance of Narrow Correlator Spacing in a GPS Receiver," *Navigation*, vol 39, no 3, Fall, pp. 265-283, U.S. Institute of Navigation, Fairfax VA

Vlcek, C., P. McLain, M. Murphy (1993) "GPS/Dead Reckoning for Vehicle Tracking in the 'Urban Canyon' Environment," in *Proceedings of IEEE-IEE Vehicle Navigation & Information Systems Conference*, Ottawa-VNIS'93, pp. A34-A41

Ward, P.W., J.W. Betz and C.J. Hegarty (2006) "Satellite Signal Acquisition, Tracking, and Data Demodulation," Chapter 5 of *Understanding GPS: Principle and Applications*, Second Edition, E.D. Kaplan and C.J. Hegarty (eds.), Norwood, MA, Artech House, p.153-240

Wendel, J., J. Metzger, R. Moenikes, A. Maier, and G.F. Trommer (2005) "A Performance Comparison of Tightly Coupled GPS/INS Navigation Systems Based on Extended and Sigma Point Kalman Filters," in *Proceedings of ION GNSS 2005*, 13-16 Sept., Long Beach CA, pp.456-466, U.S. Institute of Navigation, Fairfax VA

Xing, Z. and D. Gebre-Egziabher (2009) "Comparing Non-Linear Filters for Aided Inertial Navigators," in *Proceedings of ION ITM 2009*, 26-28 Jan., Anaheim, CA, pp. 1048-1053, U.S. Institute of Navigation, Fairfax VA

Yu, W. (2007) *Selected GPS Receiver Enhancements for Weak Signal Acquisition and Tracking*, MSc Thesis, Department of Geomatics Engineering, University of Calgary, Canada (Available at http://plan.geomatics.ucalgary.ca)

Zhodzishsky, M., S. Yudanov, V. Veitsel, and J. Ashjaee (1998) "Co-Op Tracking for Carrier Phase," in *Proceedings of ION GPS 1998*, 15-18 Sept., Nashville Tennessee, pp. 653-664, U.S. Institute of Navigation, Fairfax VA

Ziedan, N., J.L. Carrison (2003) "Bit Synchronization and Doppler Frequency Removal at Very Low Carrier to Noise Ratio Using a Combination of the Viterbi Algorithm with an Extended Kalman Filter," in *Proceedings of ION GPS/GNSS 2003,* 9-12 Sept., Portland, OR, pp. 616-627, U.S. Institute of Navigation, Fairfax VA

APPENDIX A: MECHANIZATION EQUATIONS AND ERROR MODEL OF FULL IMU

The navigation equations and error model of a full IMU are expressed in local level frame, and briefly introduced in the following.

A.1. Navigation Equations of Full IMU

The navigation equations of a full IMU are given by (El-Sheimy 2007; Titterton & Weston 2004)

$$\begin{cases} \dot{\mathbf{r}}^{\ell} = \mathbf{D}^{-1}\mathbf{v}^{\ell} \\ \dot{\mathbf{v}}^{\ell} = \mathbf{R}_b^{\ell}\mathbf{f}^b - (2\boldsymbol{\Omega}_{ie}^{\ell} + \boldsymbol{\Omega}_{e\ell}^{\ell})\mathbf{v}^{\ell} + \mathbf{g}^{\ell} \\ \dot{\mathbf{R}}_b^{\ell} = \mathbf{R}_b^{\ell}(\boldsymbol{\Omega}_{ib}^{b} - \boldsymbol{\Omega}_{i\ell}^{b}) \end{cases} \tag{A.1}$$

where $\boldsymbol{\Omega}_{ie}^{\ell} = \left[\boldsymbol{\omega}_{ie}^{\ell}\times\right]$, $\boldsymbol{\Omega}_{e\ell}^{\ell} = \left[\boldsymbol{\omega}_{e\ell}^{\ell}\times\right]$, $\boldsymbol{\Omega}_{ib}^{b} = \left[\boldsymbol{\omega}_{ib}^{b}\times\right]$, $\boldsymbol{\Omega}_{i\ell}^{b} = \left[\boldsymbol{\omega}_{i\ell}^{b}\times\right]$, and $\boldsymbol{\Omega}_{pq}^{a} = \left[\boldsymbol{\omega}_{pq}^{a}\times\right]$ are skew-symmetric matrices, where $\boldsymbol{\omega}_{pq}^{a}$ is a rotation rate column vector, from *q*-frame to *p*-frame, and the vector is in *a*-frame. $\mathbf{f}^b = \begin{bmatrix} f_x^b & f_y^b & f_z^b \end{bmatrix}^T$ is the measurement of accelerometers, $\boldsymbol{\omega}_{ib}^{b} = \begin{pmatrix} \omega_{ibx}^{b} & \omega_{iby}^{b} & \omega_{ibz}^{b} \end{pmatrix}^T$ is the measurement of gyros. $\mathbf{r}^{\ell} = \begin{bmatrix} \varphi & \lambda & h \end{bmatrix}^T$ is position, φ is latitude, λ is longitude, h is height. $\mathbf{v}^{\ell} = \begin{bmatrix} v_e & v_n & v_u \end{bmatrix}^T$ is velocity, v_e is velocity in east, v_n is velocity in north and v_u is in up. $\mathbf{D}^{-1}$ is a matrix, which transfers velocity in ℓ-frame into position variation rate in ℓ-frame. $\mathbf{g}^{\ell} = \begin{bmatrix} 0 & 0 & -g \end{bmatrix}^T$, g is the acceleration of gravity. $\mathbf{R}_b^{\ell}$ is a direction cosine matrix, from b-frame to ℓ-frame. For more details,

$$\boldsymbol{\omega}_{ie}^{\ell} = \begin{pmatrix} 0 \\ \omega_e \cos\varphi \\ \omega_e \sin\varphi \end{pmatrix} \tag{A.2}$$

where ω_e is the rotation rate of the earth.

$$\boldsymbol{\omega}_{e\ell}^{\ell} = \begin{bmatrix} \dfrac{-v_n}{M+h} \\ \dfrac{v_e}{N+h} \\ \dfrac{v_e \tan\varphi}{N+h} \end{bmatrix} \tag{A.3}$$

Where M is meridian radius, N is prime vertical radius.

$$\boldsymbol{\omega}_{i\ell}^{b} = \mathbf{R}_{\ell}^{b}\boldsymbol{\omega}_{i\ell}^{\ell} = \mathbf{R}_{\ell}^{b}\begin{bmatrix} \dfrac{-v_n}{M+h} \\ \dfrac{v_e}{N+h} + \omega_e \cos\phi \\ \dfrac{v_e \tan\phi}{N+h} + \omega_e \sin\phi \end{bmatrix} \tag{A.4}$$

$$\mathbf{D}^{-1} = \begin{bmatrix} 0 & \dfrac{1}{M+h} & 0 \\ \dfrac{1}{(N+h)\cos\varphi} & 0 & 0 \\ 0 & 0 & 1 \end{bmatrix} \tag{A.5}$$

A.2. Corresponding Error Model of Full IMU

The error model of a full IMU is given by (El-Sheimy 2007; Titterton & Weston 2004)

$$\begin{bmatrix} \delta\dot{\mathbf{r}}^{\ell} \\ \delta\dot{\mathbf{v}}^{\ell} \\ \dot{\boldsymbol{\varepsilon}}^{\ell} \\ \dot{\mathbf{d}} \\ \dot{\mathbf{b}} \end{bmatrix} = \begin{bmatrix} -\mathbf{D}^{-1}\mathbf{D}_r & \mathbf{D}^{-1} & \mathbf{0}_{3\times3} & \mathbf{0}_{3\times3} & \mathbf{0}_{3\times3} \\ \mathbf{A} & \mathbf{B} & -\mathbf{F}^{\ell} & \mathbf{0}_{3\times3} & \mathbf{R}_b^{\ell} \\ \mathbf{P} & \mathbf{Q} & -\boldsymbol{\Omega}_{i\ell}^{\ell} & \mathbf{R}_b^{\ell} & \mathbf{0}_{3\times3} \\ \mathbf{0}_{3\times3} & \mathbf{0}_{3\times3} & \mathbf{0}_{3\times3} & -\boldsymbol{\Gamma} & \mathbf{0}_{3\times3} \\ \mathbf{0}_{3\times3} & \mathbf{0}_{3\times3} & \mathbf{0}_{3\times3} & \mathbf{0}_{3\times3} & -\boldsymbol{\Lambda} \end{bmatrix} \begin{bmatrix} \delta\mathbf{r}^{\ell} \\ \delta\mathbf{v}^{\ell} \\ \boldsymbol{\varepsilon}^{\ell} \\ \mathbf{d} \\ \mathbf{b} \end{bmatrix} + \begin{bmatrix} \mathbf{0}_{3\times3} \\ \mathbf{R}_b^{\ell}\mathbf{W}_f \\ \mathbf{R}_b^{\ell}\mathbf{W}_{\omega} \\ \mathbf{W}_d \\ \mathbf{W}_b \end{bmatrix} \tag{A.6}$$

where $\delta\mathbf{r}^{\ell} = [\delta\varphi \quad \delta\lambda \quad \delta h]^T$ is position error, $\delta\mathbf{v}^{\ell} = [\delta v_e \quad \delta v_n \quad \delta v_u]^T$ is velocity error, $\boldsymbol{\varepsilon}^{\ell} = [\varepsilon_x^{\ell} \quad \varepsilon_y^{\ell} \quad \varepsilon_z^{\ell}]^T$ is attitude error in ℓ-frame, $\mathbf{d} = [d_x \quad d_y \quad d_z]^T$ is gyro drift in *b*-frame, $\mathbf{b} = [b_x \quad b_y \quad b_z]^T$ is accelerometer bias in *b*-frame, $\boldsymbol{\Omega}_{i\ell}^{\ell} = [\boldsymbol{\omega}_{i\ell}^{\ell} \times]$. **B** is a matrix, which transfers velocity error into velocity error varying rate in ℓ-frame. **Q** is a matrix that transfers velocity error into attitude error rate in ℓ-frame. $-\mathbf{D}^{-1}\mathbf{D}_r$, **A** and **P** are matrices defined in El-Sheimy (2007). They give the terms related to position error in position, velocity and attitude error equations. In order to simplify the error model analysis, $-\mathbf{D}^{-1}\mathbf{D}_r$, **A** and **P** are chosen as zero in this dissertation because the terms related to these three matrices are small enough (Titterton & Weston 2004). $\mathbf{F}^{\ell} = [\mathbf{f}^{\ell} \times]$, and the specific force in ℓ-frame is $\mathbf{f}^{\ell} = [f_e \quad f_n \quad f_u]^T$. $\boldsymbol{\Gamma} = diag(\alpha_x \quad \alpha_y \quad \alpha_z)$, $\boldsymbol{\Lambda} = diag(\beta_x \quad \beta_y \quad \beta_z)$, $\mathbf{0}_{3\times3}$ is a zero matrix with dimension 3×3, $\mathbf{0}_{3\times1}$ is a zero vector with dimension 3×1. $\mathbf{W}_d$ and $\mathbf{W}_b$ are driving noise. $\mathbf{W}_f$ and $\mathbf{W}_{\omega}$ are the accelerometer and gyro measurement white noise respectively. Other variables and parameters are the same with those in Equation (A.1). For more details,

$$\mathbf{B} = \begin{bmatrix} B_{11} & B_{12} & B_{13} \\ B_{21} & B_{22} & B_{23} \\ B_{31} & B_{32} & 0 \end{bmatrix} \tag{A.7}$$

where $B_{11} = \dfrac{-\dot{h} + \dot{\varphi}\tan\varphi(M+h)}{N+h}$, $B_{12} = (2\omega_e + \dot{\lambda})\sin\varphi$, $B_{13} = -(2\omega_e + \dot{\lambda})\cos\varphi$,

$B_{21} = -2(\omega_e + \dot{\lambda})\sin\varphi$, $B_{22} = -\dot{h}/(M+h)$, $B_{23} = -\dot{\varphi}$, $B_{31} = 2(\omega_e + \dot{\lambda})\cos\varphi$, $B_{32} = 2\dot{\varphi}$.

$$\mathbf{Q} = \begin{bmatrix} 0 & 1/(M+h) & 0 \\ -1/(N+h) & 0 & 0 \\ -\tan\varphi/(N+h) & 0 & 0 \end{bmatrix} \tag{A.8}$$

$$\boldsymbol{\omega}_{i\ell}^{\ell} = \begin{bmatrix} -\dot{\varphi} \\ (\omega_e + \dot{\lambda})\cos\varphi \\ (\omega_e + \dot{\lambda})\sin\varphi \end{bmatrix} \tag{A.9}$$

APPENDIX B: INDIVIDUAL PHASE ERRORS OF DOPPLER-AIDED PLL

In the following, not only the formulae of thermal noise and oscillator noise-induced phase jitters are given, but also the formulae of Doppler aiding error-induced phase errors are derived. In the formula derivation, $\xi = 0.707$ is the damping ratio of the second-order system, ω_n is undamped natural frequency, T is Kalman filter measurement update period.

B.1. Thermal Noise and Oscillator Noise-Induced Phase Jitters

PLL thermal noise jitter is given by (Ward et al 2006)

$$\sigma_{tPLL} = \frac{360}{2\pi}\sqrt{\frac{B_n}{C/N_0}\left(1+\frac{1}{2T_{PIT}C/N_0}\right)} \text{ (degrees)} \tag{B.1}$$

where B_n is carrier loop noise bandwidth (Hz), C/N_0 is carrier to noise power expressed as a ratio (Hz), T_{PIT} is predetection integration time (seconds).

Allan deviation oscillator phase jitter for a second-order loop is given by (Chiou 2005)

$$\sigma_A = 180\sqrt{\frac{4\pi^2 \cdot h_4}{\sqrt{2}\omega_n^3} + \frac{\pi \cdot h_3}{\omega_n^2} + \frac{h_2}{\sqrt{2}\omega_n}} \text{ (degrees)} \tag{B.2}$$

where h_2, h_3, and h_4 are coefficients for the oscillator, and given in Table B.1 (Chiou 2005; Gebre-Egziabher et al 2005).

Table B.1 Coefficients for Oscillator Error Models

h_k	TCXO	OCXT
h_0	5.00×10^{-8}	5.50×10^{-8}
h_1	6.19×10^{-5}	5.00×10^{-5}
h_2	9.60×10^{-4}	6.50×10^{-4}
h_3	6.00×10^{-3}	9.00×10^{-7}
h_4	6.00×10^{-4}	1.00×10^{-7}

Vibration-induced oscillator phase jitter is given by (Chiou 2005)

$$\sigma_v = \frac{180}{\pi}\int_0^\infty \left|H_e(j2\pi f_m)\right|^2 P_v(f_m)df_m \text{ (degrees)} \tag{B.3}$$

where $P_v(f_m)$ is the PSD of phase jitter, which is defined in Ward et al (2006) and Chiou (2005), and $P_v(f_m) = S_v^2(f_m)\frac{P_g(f_m)}{f_m^2}$, where $S_v(f_m)$ is oscillator vibration sensitivity, $P_g(f_m)$ is power curve of the random vibration, which is given in Table B.2 (Chiou 2005; Gebre-Egziabher et al 2005), and f_m is random vibration modulation frequency in Hz. Since the parameters of random vibration given in Table B.2 was obtained from a turbojet transport aircraft test, it should be bigger than that in a land vehicle navigation test researched in this dissertation. The transfer function is $H_e(s) = \frac{E(s)}{\delta\varphi_r(s)} = \frac{s^2}{s^2 + 2\xi\omega_n s + \omega_n^2}$, where $E(s)$ and $\delta\varphi_r(s)$ are defined in Figure 4.2.

Table B.2 Power Curve of Random Vibration (for aircraft)

$P_g(f_m) = 2.50\times10^{-3}$	$f_m \le 40$ Hz
$P_g(f_m) = 2.50\times10^{-3}\times(f/40)^{-2}$	$40 < f_m \le 100$ Hz
$P_g(f_m) = 4.00\times10^{-4}$	$100 < f_m \le 500$ Hz
$P_g(f_m) = 4.00\times10^{-4}\times(f/500)^{-2}$	500 Hz $< f_m$

B.2. Doppler Aiding Error-Induced Phase Errors

B.2.1. Random Ramp-Induced Phase Error

Random ramp-induced phase error can be obtained from the corresponding steady state error, in response to the step of frequency derivative (see Figure 4.2). And the steady state error is given by

$$e_{ss} = \lim_{t\to\infty} e(t) = \lim_{s\to 0} sE(s) = \lim_{s\to 0} \frac{-s^2}{s^2 + 2\xi\omega_n s + \omega_n^2} \Delta F_d(s) = \frac{-d(\Delta f_d(t))/dt}{\omega_n^2} \tag{B.4}$$

where $E(s) = \dfrac{-s}{s^2 + 2\xi\omega_n s + \omega_n^2} \Delta F_d(s)$.

B.2.2. First-Order GM-Induced Phase Jitter

First-order GM-induced phase jitter is derived as follows. From Equation (4.1), the PSD of phase jitter can be expressed as

$$P_{\delta\varphi}(\omega) = \left|H(j\omega)\right|^2 P_{\Delta fd}(\omega) \tag{B.5}$$

where $H(s) = \dfrac{s}{s^2 + 2\xi\omega_n s + \omega_n^2}$, $P_{\Delta fd}(\omega)$ is the PSD of first-order GM Doppler error. In sampling system, Doppler error $\Delta f_d(t) = u_1, 0 \le t < T$, $\Delta f_d(t) = u_2, T \le t < 2T, \cdots$, $\Delta f_d(t) = u_i, (i-1)T \le t < iT$,…, where u_i is a constant in $(i-1)T \le t < iT$, $i = 1, 2, 3, ..., N$. So the Fourier transform of $\Delta f_d(t)$ can be expressed as

$$\Delta F_d(j\omega) = \sum_{i=1}^{N} \int_{(i-1)T}^{iT} u_i e^{-j\omega\tau} d\tau = \frac{1 - e^{-j\omega T}}{j\omega} \sum_{i=1}^{N} u_i e^{-j\omega(i-1)T} = \frac{1 - e^{-j\omega T}}{j\omega} U(e^{j\omega T}) \tag{B.6}$$

From z-transform definition, when u_i ($i = 1, 2, 3, \cdots$) is a first-order GM sequence, $U(e^{j\omega T})$ can be expressed as (Girod 2001)

$$U(e^{j\omega T}) = \sigma_w \frac{e^{j\omega T}}{e^{j\omega T} - e^{-\alpha T}} \tag{B.7}$$

where α is the inverse of correlation time of the GM sequence, σ_w is driving noise sequence standard derivation. Since u_i is sampling random signal, its variance is $\sigma_u^2 \delta(t)$ (Mandal & Asif 2007). It can be approximated as σ_u^2 / T for its equivalent discrete signal since $\int_0^T \delta(t)dt = \int_0^T \frac{1}{T} dt = 1$. Therefore (Gelb 1974),

$$\sigma_w = \sigma_u \sqrt{(1 - e^{-2\alpha T})/T} \tag{B.8}$$

where σ_u is standard derivation of $u(t)$, where $u(t)$ is the GM process. So the PSD of $\Delta f_d(t)$ can be expressed as

$$\begin{aligned} P_{\Delta fd}(\omega) &= \left|\Delta F_d(j\omega)\right|^2 = \sigma_w^2 \frac{1}{(1 + e^{-2\alpha T}) - 2e^{-\alpha T}\cos(\omega T)} \frac{2 - 2\cos(\omega T)}{\omega^2} \\ &\approx \frac{e^{\alpha T_k} \cdot \sigma_w^2}{\omega^2 + \gamma^2} \end{aligned} \tag{B.9}$$

where $\gamma = \sqrt{e^{\alpha T}} \cdot \alpha$. Therefore, the standard derivation of phase jitter is

$$\sigma_{\delta\varphi}^2 = \frac{1}{2\pi} \int_{-\infty}^{+\infty} P_{\delta\varphi}(\omega) d\omega \approx \frac{e^{\alpha T} \cdot \sigma_w^2}{\omega_n^4 + \gamma^4} \left(\frac{\gamma^2}{2\sqrt{2}\omega_n} + \frac{\omega_n}{2\sqrt{2}} - \frac{\gamma}{2} \right) \tag{B.10}$$

If T and α are small enough, the following approximation can be made

$$\sigma_{\delta\varphi}^2 \approx \frac{\sigma_w^2}{2\sqrt{2}\omega_n^3} \tag{B.11}$$

In the derivation of Equation (B.10), the following formula is used (Chiou 2005)

$$\int_0^{+\infty} \frac{x^{m-1}}{1 + x^n} dx = \frac{\pi}{n \sin(m\pi / n)}, \; 0 < m < n \tag{B.12}$$